

Perturbative transport experiments and time-dependent modeling in Alcator C-Mod and DIII-D

by

Pablo Rodríguez Fernández

Ingeniero Superior, Universidad Politécnica de Madrid (2015)

Master of Science, Drexel University (2014)

SUBMITTED TO THE

DEPARTMENT OF NUCLEAR SCIENCE AND ENGINEERING

IN PARTIAL FULFILLMENT OF THE REQUIREMENTS FOR THE DEGREE OF

DOCTOR OF PHILOSOPHY IN NUCLEAR SCIENCE AND ENGINEERING

AT THE

MASSACHUSETTS INSTITUTE OF TECHNOLOGY

JUNE 2019

©2019 Massachusetts Institute of Technology

All rights reserved.

Author: _____

Pablo Rodríguez Fernández

Department of Nuclear Science and Engineering

May 9, 2019

Certified by: _____

Anne E. White, Ph.D.

Professor of Nuclear Science and Engineering

Thesis Supervisor

Certified by: _____

Nathan T. Howard, Ph.D.

Research Scientist, MIT Plasma Science and Fusion Center

Thesis Reader

Accepted by: _____

Ju Li, Ph.D.

Battelle Energy Alliance Professor of Nuclear Science and Engineering

Chairman, Department Committee on Graduate Theses

Perturbative transport experiments and time-dependent modeling in Alcator C-Mod and DIII-D

by Pablo Rodriguez-Fernandez

Submitted to the Department of Nuclear Science and Engineering
on May 9, 2019 in Partial Fulfillment of the Requirements for the Degree of

Doctor of Philosophy
in Nuclear Science and Engineering

Perturbative transport experiments in magnetically confined plasmas have shown, for more than 20 years, that the injection of cold pulses at the plasma edge can trigger the fast increase of core temperature. Because no single standard local transport model tried to date has been able to reproduce satisfactorily all the observed temporal behavior in the experiments, these transient transport phenomena feature prominently as an open question in the community and as a challenge for predictive capabilities in tokamak burning plasmas, such as ITER and SPARC.

For the first time after more than two decades of experimental evidence, this Thesis resolves this long-standing enigma in plasma transport, by modeling of experiments conducted on the Alcator C-Mod and DIII-D tokamaks. Predictive integrated simulations with the Trapped Gyro Landau Fluid (TGLF) quasilinear transport model demonstrate that the increase of core temperature in some regimes, and lack thereof in other regimes, can be explained by a change in dominant linear micro-instability in the plasma core. The effect of major radius, electron density and plasma current on the cold pulse are well captured by TGLF, including the relative change in position of the temperature flex point as current density changes. Linear stability analysis of simulated density and current scans in Alcator C-Mod reveals a competition between trapped electron and ion temperature gradient modes as the main driver of the core transient response. Measurements of electron density evolution during the cold-pulse propagation in DIII-D are enabled by a high time resolution density profile reflectometer. The density evolution reveals the quick propagation of a pulse from edge to core, which is the mechanism to transiently increase core temperature in low-collisionality plasmas. The work presented in this Thesis demonstrates that the existence of nonlocal heat transport phenomena is not necessary for explaining the behavior and time scales of cold-pulse experiments in tokamak plasmas.

Thesis Supervisor: Anne White

Title: Professor of Nuclear Science and Engineering

Acknowledgements

Firstly, I could not have imagined having a better mentor and advisor during my time at MIT. I would like to express my sincere gratitude to Prof. Anne White for her guidance throughout my PhD, her motivation, support and valuable insights during the development of this research work. Thanks to her exceptional mentorship, this work has already had an impact in the community, with a number of scientific publications and invited talks at international conferences. She has shown me by example what a good scientist should be.

I would like to also express my great appreciation to Dr. Nathan Howard for sharing his knowledge on transport modeling and taking the time to teach me how to use TRANSP and TGLF, among other useful tools that were essential for my research. As my reader, his feedback was very important in the development of this thesis project. Advice and feedback given by Dr. Brian Grierson have been a great help throughout this project. His extensive knowledge on both experiment and modeling were very useful to improve the quality of the scientific publications and this thesis work. My sincere thanks to Dr. John Rice for his groundbreaking experimental work in Alcator C-Mod. My research would have been impossible without it.

On the experimental side, I would like to offer my special thanks to the Alcator C-Mod and DIII-D teams for their excellent work on the experiments presented on this thesis, as well as the diagnosticians that have contributed to this thesis by procuring experimental data. In particular, this work could not have been developed without the contributions of Dr. Martin Greenwald, Dr. Jerry Hughes, Dr. Amanda Hubbard, Dr. James Irby, Dr. Gregory Wallace (Alcator C-Mod), Dr. Lei Zeng, Dr. Max Austin, Dr. Tomas Odstrcil, Dr. Terry Rhodes, Dr. Kathreen Thome and Dr. Thomas Osborne (DIII-D).

On the modeling side, I wish to acknowledge the support provided by the TRANSP team, specially Dr. Xingqiu Yuan for his help debugging predictive runs and for providing additional outputs when required. Dr. Xingqiu Yuan and Dr. Francesca Poli have also kindly reviewed the TRANSP section of this thesis, which I greatly appreciate. I thank Dr. Gary Staebler for developing TGLF and making it available for the community. Feedback provided by him was very useful to improve the quality of the paper in *Phys. Rev. Letters*, and he has kindly reviewed the TGLF

section of this thesis. An important fraction of the analysis and modeling work presented here has been greatly aided by the OMFIT framework. Special thanks goes to the OMFIT team, in particular Dr. Orso Meneghini and Dr. Sterling Smith, for the development and maintenance of OMFIT, which facilitates access to modeling and experimental data analysis tools.

I would like to thank my fellow graduate students for the stimulating discussions, feedback, contributions and, of course, friendship. Special thanks to Francesco Sciortino, whose sharpness always helps me find ways to improve my work; Dr. Alexander Creely for being a role model to succeed in graduate school; and Norman Cao for navigating with me in the beginnings of the cold-pulse research and providing high-quality data, analysis and feedback. I am also grateful to Dr. Jonathan Citrin, Dr. Clemente Angioni, Dr. Emiliano Fable and Dr. Garrard Conway for welcoming me in their institutions to promote my work and foster collaborations.

I am very grateful to Fundación Bancaria “la Caixa” for providing financial support during the first two years of my PhD with a postgraduate studies fellowship (Award LCF/BQ/AN14/ 10340041). I also enjoyed an MIT International Science and Technology Initiatives (MISTI) grant to partly cover my summer stay at the Max Planck Institute for Plasma Physics in Garching, Germany. My work in the Alcator C-Mod and DIII-D facilities has been supported by the U.S. Department of Energy, Office of Science, Office of Fusion Energy Sciences, under Awards DE-FC02-99ER54512, DE-FC02-04ER54698, DE-SC0014264 and DE-SC0017381.

Last but not least, I would like to thank my family for supporting me throughout my PhD. Most of all, thanks to my partner Gabriela for her encouragement throughout this entire journey.

List of Publications

Part of the content presented in this Thesis has already been published as peer-reviewed journal articles. Permission to reuse content from these articles has been granted. At the time of writing this Thesis, and in inverse chronological order:

- **P Rodriguez-Fernandez**, A E White, N T Howard, B A Grierson, L Zeng, X Yuan, G M Staebler, M E Austin, T Odstroil, T L Rhodes, F Sciortino, J E Rice, K Thome, C Angioni, E Fable and O Meneghini, “*Predict-First Experiments and Modeling of Perturbative Cold Pulses in DIII-D Ohmic Plasmas*” (accepted, Phys. Plasmas).

This Thesis reproduces content from this paper, with the permission of *AIP Publishing*.

- **P Rodriguez-Fernandez**, A E White, N T Howard, B A Grierson, X Yuan, G M Staebler, J E Rice, C Angioni, N M Cao, A J Creely, E Fable, M J Greenwald, A E Hubbard, J W Hughes, J H Irby and F Sciortino, “*Perturbative Transport Modeling of Cold-Pulse Dynamics in Alcator C-Mod Ohmic Plasmas*”, Nucl. Fusion **59**, 066017 (2019). <https://doi.org/10.1088/1741-4326/ab1575>

This Thesis reproduces content from this paper, with the permission of *IOP Science*.

- **P Rodriguez-Fernandez**, A E White, N T Howard, B A Grierson, G M Staebler, J E Rice, X Yuan, N M Cao, A J Creely, M J Greenwald, A E Hubbard, J W Hughes, J H Irby and F Sciortino, “*Explaining cold-pulse dynamics in tokamak plasmas using local turbulent transport models*”, Phys. Rev. Lett. **120**, 075001 (2018). <http://dx.doi.org/10.1103/PhysRevLett.120.075001>

This Thesis reproduces content from this paper, with the permission of *APS*.

- **P Rodriguez-Fernandez**, A E White, A J Creely, M J Greenwald, N T Howard, F Sciortino and J C Wright, “*VITALS: A surrogate-based optimization framework for the accelerated validation of plasma transport codes*”, Fusion Technol. **74**:1-2, 65-76 (2018). <http://dx.doi.org/10.1080/15361055.2017.1396166>

This Thesis reproduces content from this paper, with the permission of *Taylor & Francis*.

- **P Rodriguez-Fernandez**, J E Rice, N M Cao, A J Creely, N T Howard, A E Hubbard, J H Irby and A E White, “*On the correlation between “non-local” effects and intrinsic rotation reversals in Alcator C-Mod*”, Nucl. Fusion **57**, 074001 (2017). <http://dx.doi.org/10.1088/1741-4326/aa6e89>

This Thesis reproduces content from this paper, with the permission of *IOP Science*.

Contents

Abstract	3
Acknowledgements	5
List of Publications	7
Contents	9
List of Figures	13
1 Introduction	17
Bibliography	22
2 Background	29
2.1 Turbulence and Transport	29
2.2 Perturbative Transport Physics	40
2.3 On the Locality of Turbulent Transport	46
2.4 Past Work on Cold-Pulse Experiments	49
Bibliography	54
3 Experimental and Modeling Techniques	63
3.1 Alcator C-Mod tokamak	64
3.2 DIII-D tokamak	66
3.3 The Trapped Gyro-Landau Fluid (TGLF) Model	68
3.4 TRANSP Framework for Integrated Modeling of Tokamak Plasmas	74
Bibliography	82
4 Cold-Pulse Experiments in Alcator C-Mod	85
4.1 Introduction to Temperature Inversions in Alcator C-Mod	86

4.2	Cold pulses in Low and High Density Plasmas	86
4.3	Edge Cooling and Mixing Phenomena	88
4.4	Correlation of Temperature Inversions with Intrinsic Rotation	90
4.5	Other Observations in Alcator C-Mod Cold-Pulse Experiments	94
4.6	Discussion on Experiments in Alcator C-Mod Plasmas	97
	Bibliography	98
5	Modeling of Alcator C-Mod Cold Pulses	103
5.1	Propagation of Temperature Pulses	104
5.2	Transport Simulation Settings	105
5.3	Simulation Results in Low and High Density Plasmas	107
5.4	Simulation of Plasma Density Scan	114
5.5	Simulation of Plasma Current Scan	116
5.6	Combined Effect of Density and Plasma Current	119
5.7	Discussion on Modeling Results in Alcator C-Mod Plasmas	124
	Bibliography	126
6	Predict-first Cold-pulse Experiments in DIII-D	131
6.1	Predictions of Cold-Pulse Behavior in Ohmic DIII-D Plasmas	132
6.2	Experiments in Ohmic DIII-D Plasmas	133
6.3	Postdictive Modeling of DIII-D Cold-Pulses	139
6.4	Discussion on Modeling Results in DIII-D Plasmas	144
	Bibliography	145
7	Conclusions and Future Work	149
7.1	Future Work	151
7.2	Final Remarks	152
	Bibliography	153
A	Derivations	159
A.1	Definitions of Stiffness	159
A.2	1.5D Governing Equations for Transport Codes	162

Bibliography	166
Appendices	159
B Steady-State Transport Model Validation	167
B.1 Motivation: Difficulties in Transport Model Validation	168
B.2 VITALS Fundamentals	169
B.3 Optimization Framework	170
B.4 Validation Metrics	175
B.5 Application to Study Validation of Quasilinear Transport Models	177
B.6 Conclusions and Future Work	181
Bibliography	183
C Code Workflows	187
Bibliography	187

List of Figures

1.1	Conceptual fusion power plant	18
1.2	Temperature inversion in Alcator C-Mod	19
1.3	Diagram of local v.s. nonlocal transport	20
2.1	Drift-wave turbulence flowchart	30
2.2	Turbulence suppression via flow shearing	32
2.3	Fluctuation-induced transport	33
2.4	Power balance v.s. perturbative diffusivities	43
2.5	Stiffness in LOC and SOC plasmas	45
2.6	Core v.s. edge temperature behavior in Alcator C-Mod	49
2.7	Example of flex-point in temperature profile	50
3.1	Illustrations of the Alcator C-Mod tokamak.	64
3.2	LBO Diagram	65
3.3	Illustrations of the DIII-D tokamak.	66
3.4	Alcator C-Mod and DIII-D plasmas overlaid	67
3.5	Example of TGLF linear growth rates and frequencies	70
3.6	Example of zonal flow mixing in TGLF-SAT1	72
3.7	Gradient-driven TGLF to evolve profiles	73
3.8	TRANSP spatial discretization	77
3.9	TRANSP numerical scheme	79
3.10	Schematic of temperature evolution using PRIMA	80
3.11	Example of simplified perturbation	81
4.1	Relative change in core electron temperature for low and high density plasmas	87
4.2	Cold pulses during density scan exhibit opposite behavior in plasma core	88
4.3	Scan of amount of ablated impurities	89

4.4	Temperature inversion for opposite core toroidal rotation	91
4.5	Relative core temperature change as a function of density and collisionality	92
4.6	Effect of rotation reversal on temperature inversion	92
4.7	Opposite core temperature behavior for co-current toroidal rotation	93
4.8	Temperature inversions in locked-mode plasmas	94
4.9	Effect of magnetic configuration on cold-pulse behavior	95
4.10	Correlation of temperature inversion and incremental diffusivity	96
5.1	Schematic of inward cold-pulse propagation	104
5.2	Perturbations in density and radiation profiles at low density	107
5.3	Simulations results: steady-state and perturbative transport	108
5.4	Physics of cold-pulse effect on core temperature at low density	110
5.5	Physics of cold-pulse effect on core temperature at high density	111
5.6	Comparison of TGLF models	113
5.7	Simulations with different density perturbations	114
5.8	Simulation of density scan	115
5.9	Simulation of current scan	117
5.10	Simulation of combined density and current scan	118
5.11	Simulation of combined current and density scan	119
5.12	Metric TEM v.s. ITG and temperature inversions	121
5.13	Quasilinear analysis of low-density case	121
5.14	Quasilinear analysis of high-density case	122
5.15	Quasilinear analysis of high-current case	123
6.1	Predict-first simulations in DIII-D	132
6.2	Low and high density plasmas in DIII-D	134
6.3	Measured density pulse in DIII-D	135
6.4	Time evolution of DBS turbulence measurements	136
6.5	Profile of DBS turbulence measurements	137
6.6	Inward propagation of impurities in DIII-D	138
6.7	Prediction of steady-state profiles in DIII-D	139

6.8	Prediction of perturbative transport in DIII-D	140
6.9	Quasilinear analysis of perturbative transport in DIII-D	142
6.10	Quasilinear analysis of perturbative transport in DIII-D for two models	143
B.1	General workflow for inverse problem	170
B.2	VITALS workflow	173
B.3	VITALS example in Alcator C-Mod L-mode plasma	178
B.4	Trust-region logic in Alcator C-Mod L-mode plasma	179
B.5	VITALS application for different saturation rules	180

Chapter 1

Introduction

*“I would like nuclear fusion to become a practical power source.
It would provide an inexhaustible supply of energy,
without pollution or global warming.”*

S. W. Hawking, *Time Magazine*, 2010

Fusion works by combining two light nuclei to form heavier elements, releasing vast amounts of energy in the process. Fusion reactions take place readily in the core of stars, where the massive gravitational pull keeps the nuclei together close and long enough for fusion reactions to take place.

On earth, fusion energy could be used to generate virtually unlimited amounts of reliable, sustainable and environmentally-friendly energy with no long-term radiative waste. The quest for harnessing controlled nuclear fusion is sometimes termed as the holy grail of energy production, for its many advantages and practically no downsides. This very appealing picture is what has motivated scientists, researchers and engineers around the world for many decades.

In magnetic confinement fusion energy, a gas composed by hydrogen isotopes is heated up to very high temperatures and contained inside a vacuum chamber. At the temperatures required for fusion, charge particles live in a state called “plasma”, and magnetic field coils are used to constraint their motion inside the vacuum chamber. Energy from fusion reactions is released in form of kinetic energy of the products, typically a charged particle and a neutron. Because neutrons are not affected by magnetic fields, they leave the plasma, and can be captured to produce heat. This heat can be used to heat up water and thus generate electricity in a thermodynamic cycle. A nuclear fusion power plant based on the magnetic confinement fusion concept is displayed conceptually in [Figure 1.1](#).

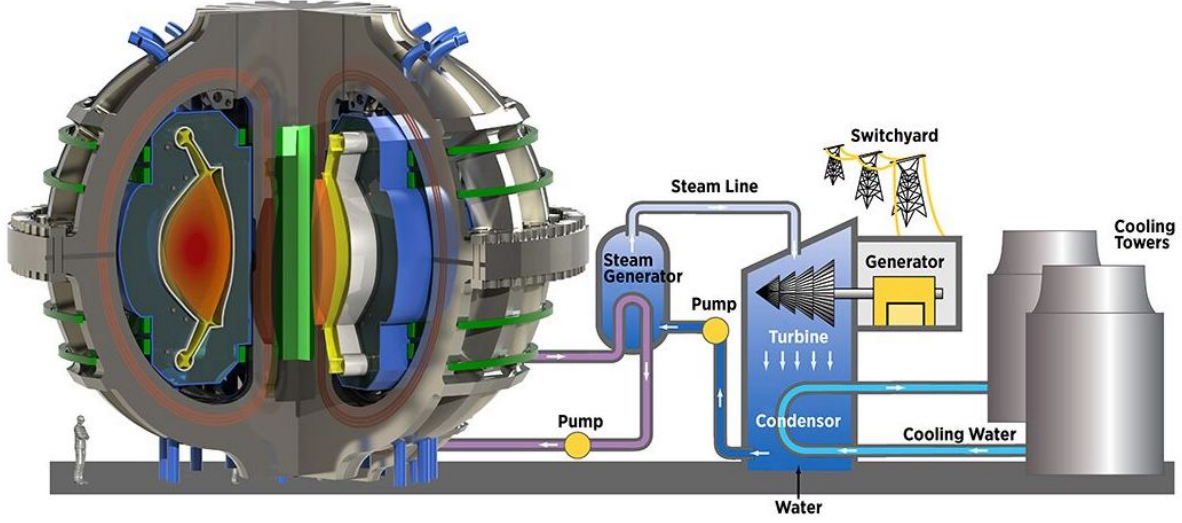


Figure 1.1: Conceptual picture of a fusion power plant based on the ARC reactor [1]. Figure from *MIT News* (Image courtesy of PSFC, adapted from Wikimedia Commons).

At the time of writing this Thesis, no fusion machine in the world has yet been able to generate more energy that it consumes in heating and sustaining the hot plasma. This is due, for the most part, to the quality of confinement, which in turn is associated with the physics of core transport. On a perfectly quiescent and isolated system, one could simply provide external energy to heat the plasma core up to the desired temperature for fusion. However, in the real world, part of that heat will inevitably leave the system due to collisions and convective flows that are inherent to the nature of plasmas. Understanding the processes that are responsible for the energy exhaust in plasma systems thus becomes critical for the optimization of fusion experiments, and the overall development of fusion as an energy source.

In plasma physics for fusion research, a metric called *global energy confinement time*, τ_E , represents the characteristic relaxation time of the plasma energy, and is used to assess how well energy is confined within the plasma. Therefore, the energy confinement time gives information on the transport processes that are responsible for the energy exhaust. Formally, this can be expressed as follows:

$$\int_A \vec{q} \cdot d\vec{A} = \frac{W}{\tau_E} \quad (1.1)$$

where W is the plasma energy, \vec{q} is the total heat flux, and \vec{A} is the surface vector of the plasma.

At this point, one may wonder how energy transport (and, in particular, the energy confinement time) is related to fusion performance of magnetically-confined plasmas. To illustrate this relationship, the circulating power quality factor, Q_f , can be defined as the ratio of the net thermonuclear power (P_f) to the input power required to sustain the plasma (P_h). In principle, one wants to design and operate a fusion machine that generates more energy that it consumes, i.e. $Q_f \equiv P_f/P_h > 1$

(“breakeven”¹). Simple power balance calculations, neglecting radiation, lead to a modified Lawson criterion of the form [2]:

$$n\tau_E = \frac{12T}{\langle\sigma v\rangle Y_c} \frac{1}{1 + 5/Q_f} \quad (1.2)$$

Because the fusion reactions rate coefficient $\langle\sigma v\rangle$ is approximately proportional to T^2 in the range of interest for fusion, and the fusion reaction yield in charge particles Y_c is constant, it turns out that $p\tau_E \propto (1 + 5/Q_f)^{-1}$. In other words, $p\tau_E$ emerges as an important metric for fusion performance, and indicates that plasmas benefit from both high pressure, p , and high energy confinement, τ_E .

In consequence of the stability and engineering limits that restrict plasma pressure, achieving good energy confinement in tokamaks (low energy transport) has been one of the pillars of fusion energy research for many decades. In order to design, build, and operate a fusion device, one needs first to understand and be able to predict core transport. Immense progress has been made towards this goal, but some fundamental questions remain open up to this day.

An example of one of the prominent fundamental questions in core transport research was acknowledged as early as 1995 by Professor K.W. Gentle at the University of Texas at Austin. Prof. Gentle and his team performed experiments in the TEXT tokamak [3], which showed evidence of what it seemed to indicate the existence of unknown, long-range interactions between plasma core and edge during transient perturbations.

These phenomena were observed during the propagation of intentional edge temperature perturbations, in the form of cold pulses, that exhibit a temperature “reversal” as they propagate through the plasma. In short, and as illustrated in Figure 1.2, these experiments manifest a sudden increase in core temperature as a result of cooling of the plasma edge. These unexplained effects have been reproduced in more than ten fusion machines to date [4–14], and no first-principle, validated model of energy transport has been successful so far in explaining many of the qualitative features of these experiments, even less a quantitative match of the magnitude and time-scale of these phenomena.

Various models have been proposed to shed some light on this issue and elucidate whether ex-

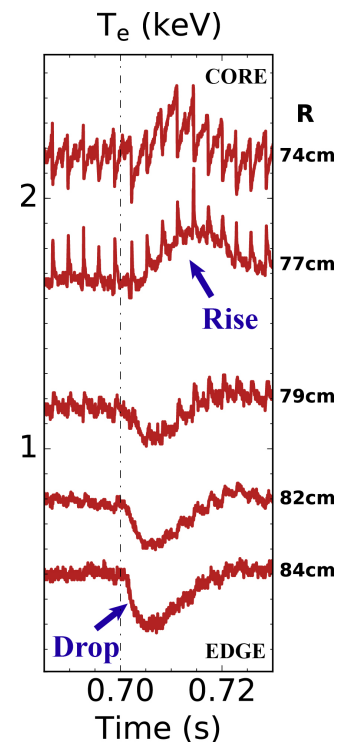


Figure 1.2: Electron temperature at five radial locations in the Alcator C-Mod tokamak, showing peculiar temperature reversal.

¹Naturally, fusion power plants would operate with Q_f well above 1, to account for thermodynamic and nuclear engineering efficiencies (i.e. $Q_{eng} > 1$). However, reaching $Q_f = 1$ is nonetheless an important milestone in the quest for fusion energy.

otic, long-range, nonlocal interactions are required to study and predict plasma behavior. Figure 1.3 displays, schematically, the difference between local and nonlocal interactions. In a local-transport framework, heat fluxes are described as a function of local plasma parameters alone, and therefore changes in background profiles define radial heat flux levels. This way, edge perturbations in the temperature profile propagate in a continuous manner through the plasma. Nonlocal transport, however, allows distant portions to interact, and changes in heat flux could be triggered without changes in local parameters.

Most of the models proposed to explain the inversion of temperature perturbation (as in Figure 1.2) were phenomenological [3, 4, 15–18], i.e. use experimental observations of the phenomenon to inform what transport coefficients would be needed to explain it. However, these models generally ignore the underlying mechanisms that result in energy transport, and oftentimes allow interactions between distant portions of the plasma without a thorough physics understanding to support them [19]. In other words, phenomenological transport coefficients might be inconsistent with the physics of neoclassical and turbulence theories as we know them, and may be incompatible with predictions of stationary plasmas. These predictions have been more extensively validated, and thus it becomes imperative that models proposed to explain perturbative transport events are also consistent with the paradigm of turbulence and neoclassical theory.

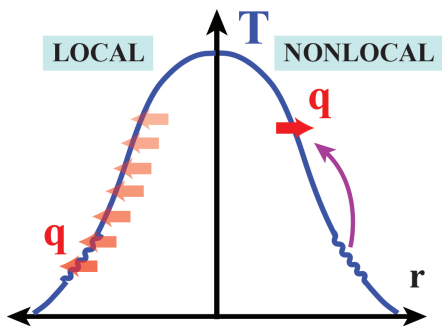


Figure 1.3: Example of local v.s. nonlocal interactions between plasma edge and core.

Turbulence-physics-based transport models were also tested in the past [7, 8, 20], revealing that the core temperature increase could be explained by multichannel interactions and collisional equilibration between plasma species. These pioneering studies established the basis for the work presented here but, as we will demonstrate for the first time in this Thesis, the models at the time were lacking important physics, that led to simulation results that underpredicted the magnitude and time-scale of the temperature inversion if experimentally-relevant edge perturbations were used. Important qualitative features of the temperature inversion effect, such as the trends with density and plasma current, were also not fully ad-

ressed in these first studies.

The importance of solving this long-standing mystery cannot be overstated. Most of our current predictive capabilities for future burning plasmas are fundamentally based on the assumption that heat flux, \vec{q} , can be described by local plasma parameters alone. Predictions have been made for burning plasmas in ITER, SPARC and future reactors that rely on the local transport paradigm [21–31], and the operation of such machines is being prepared based on these predictions. The significance of this topic is such that it has been featured in plasma physics books [32, 33], review articles have been written on this specific question [19, 34], and it is recognized in the ITER physics

basis [35] as an outstanding issue in core transport research.

This Thesis provides, for the first time, a first-principles explanation for these “seemingly nonlocal” effects based on the widely accepted and extensively validated [36, and references therein] paradigm of drift-wave turbulence physics [37, 38]. Nonlinear gyrokinetic theory of drift-wave turbulence and transport, as encapsulated by modern codes such as GYRO [39] and GENE [40], is the leading model and also the most extensively validated in steady-state [41–55]. So much so, that the codes have been used successfully to design new experiments and predict changes in turbulence before measurements are available [56–58]. To reduce computational cost, reduced theory-based models have been developed to match nonlinear simulations by resorting to quasilinear theory and saturation rules fitted to nonlinear gyrokinetics. Such models, like TGLF [59] and QuaLiKiz [60], among others, are widely used to predict plasma performance and profiles in ITER and future reactors [21–31], and have been also extensively validated against steady-state experiments [25, 61–65].

The model presented here is able to capture the dynamics of core electron temperature during cold-pulse experiments. It provides a quantitative match of the experimental response within error bars, and is able to resolve all qualitative trends of cold-pulse experiments that have been tested so far. These results provides the strongest evidence to date that local transport simulations are enough to reproduce core responses to edge perturbations, thus providing confidence that local transport modeling is sufficient to explain cold-pulse propagation and associated phenomenology.

This important conclusion is achieved in this Thesis by means of novel experiments in two world-class fusion machines, state-of-the-art transport models and integrated simulation frameworks, and new modeling ideas based on multi-channel interactions in trapped-electron-mode-driven turbulence regimes. The outline of this Thesis is as follows. Chapter 2 introduces turbulence and associated transport phenomena, as well as important perturbative transport physics concepts. It also provides a discussion on the concept of locality in core transport. Chapter 3 describes the experimental set-up in Alcator C-Mod and DIII-D tokamaks used to study perturbative transport experiments, as well as the modeling techniques that are employed to simulate plasma dynamics.

Next, Chapter 4 presents the set of cold-pulse experiments that exhibit the seemingly nonlocal response. It describes parametric dependences of cold-pulse behavior in Alcator C-Mod and discusses the apparent connection with momentum transport. It follows Chapter 5, which presents novel simulations of perturbative transport in Alcator C-Mod that confirm that local models are sufficient to reproduce cold-pulse dynamics. New predict-first experiments in DIII-D are introduced in Chapter 6, which support and further validate the model thanks to novel experimental measurements. Finally, a conclusion is presented in Chapter 7, with remarks on the significance of this work and expected future steps.

Bibliography

- [1] B.N. Sorbom et al. Arc: A compact, high-field, fusion nuclear science facility and demonstration power plant with demountable magnets. *Fusion Engineering and Design*, 100:378 – 405, 2015. ISSN 0920-3796. doi: <https://doi.org/10.1016/j.fusengdes.2015.07.008>. URL <http://www.sciencedirect.com/science/article/pii/S0920379615302337>.
- [2] J.P. Freidberg. *Plasma Physics and Fusion Energy*. Cambridge University Press, 2008. ISBN 9781139462150. URL <https://books.google.com/books?id=Vyoe88GEVz4C>.
- [3] K. W. Gentle et al. Strong nonlocal effects in a tokamak perturbative transport experiment. *Phys. Rev. Lett.*, 74:3620–3623, 1995. URL <https://link.aps.org/doi/10.1103/PhysRevLett.74.3620>.
- [4] M.W. Kissick et al. Non-local component of electron heat transport in tfr. *Nucl. Fusion*, 36(12): 1691, 1996. URL <http://stacks.iop.org/0029-5515/36/i=12/a=I09>.
- [5] T. Dudok de Wit et al. Self-consistent removal of sawtooth oscillations from transient plasma data by generalized singular value decomposition. *Phys. Plasmas*, 5(5):1360–1368, 1998. URL <https://doi.org/10.1063/1.872796>.
- [6] P. Mantica et al. Nonlocal transient transport and thermal barriers in rijnhuizen tokamak project plasmas. *Phys. Rev. Lett.*, 82:5048–5051, 1999. URL <https://link.aps.org/doi/10.1103/PhysRevLett.82.5048>.
- [7] F. Ryter et al. Propagation of cold pulses and heat pulses in asdex upgrade. *Nucl. Fusion*, 40(11): 1917, 2000. URL <http://stacks.iop.org/0029-5515/40/i=11/a=311>.
- [8] P Mantica et al. Perturbative transport experiments in jet low or reverse magnetic shear plasmas. *Plasma Phys. Control. Fusion*, 44(10):2185, 2002. URL <http://stacks.iop.org/0741-3335/44/i=10/a=308>.
- [9] S. Inagaki et al. Observation of long-distance radial correlation in toroidal plasma turbulence. *Phys. Rev. Lett.*, 107:115001, 2011. URL <https://link.aps.org/doi/10.1103/PhysRevLett.107.115001>.
- [10] X.R. Duan et al. Overview of experimental results on hl-2a. *Nucl. Fusion*, 49(10):104012, 2009. URL <http://stacks.iop.org/0029-5515/49/i=10/a=104012>.
- [11] J.E. Rice et al. Non-local heat transport, rotation reversals and up/down impurity density asymmetries in alcator c-mod ohmic l-mode plasmas. *Nucl. Fusion*, 53(3):033004, 2013. URL <http://stacks.iop.org/0029-5515/53/i=3/a=033004>.

- [12] Y.J. Shi et al. Intrinsic rotation reversal, non-local transport, and turbulence transition in kstar l-mode plasmas. *Nuclear Fusion*, 57(6):066040, 2017. URL <http://stacks.iop.org/0029-5515/57/i=6/a=066040>.
- [13] Yuejiang Shi et al. Observation of multi-channel non-local transport in j-text plasmas. *Nuclear Fusion*, 58(4):044002, 2018. URL <http://stacks.iop.org/0029-5515/58/i=4/a=044002>.
- [14] Yong Liu et al. Dynamics of cold pulses induced by super-sonic molecular beam injection in the EAST tokamak. *Nuclear Fusion*, 59(4):044005, mar 2019. doi: 10.1088/1741-4326/ab0665. URL <https://doi.org/10.1088%2F1741-4326%2Fab0665>.
- [15] K. W. Gentle et al. An experimental counter-example to the local transport paradigm. *Phys. Plasmas*, 2(6):2292–2298, 1995. URL <http://dx.doi.org/10.1063/1.871252>.
- [16] K. W. Gentle et al. The evidence for nonlocal transport in the texas experimental tokamak. *Phys. Plasmas*, 4(10):3599–3613, 1997. URL <http://dx.doi.org/10.1063/1.872255>.
- [17] G M D Hogeweyj et al. Recording non-local temperature rise in the RTP tokamak. *Plasma Physics and Controlled Fusion*, 42(10):1137–1144, oct 2000. doi: 10.1088/0741-3335/42/10/310. URL <https://doi.org/10.1088%2F0741-3335%2F42%2F10%2F310>.
- [18] C. Gao et al. Non-local heat transport in alcator c-mod ohmic l-mode plasmas. *Nucl. Fusion*, 54(8):083025, 2014. URL <http://stacks.iop.org/0029-5515/54/i=8/a=083025>.
- [19] J D Callen and M W Kissick. Evidence and concepts for non-local transport. *Plasma Phys. Control. Fusion*, 39(12B):B173, 1997. URL <http://stacks.iop.org/0741-3335/39/i=12B/a=014>.
- [20] J. E. Kinsey et al. Theoretical transport modeling of ohmic cold pulse experiments. *Phys. Plasmas*, 5(11):3974–3981, 1998. URL <http://dx.doi.org/10.1063/1.873117>.
- [21] R.V. Budny et al. Predictions of h-mode performance in iter. *Nuclear Fusion*, 48(7):075005, 2008. URL <http://stacks.iop.org/0029-5515/48/i=7/a=075005>.
- [22] F Wagner et al. On the heating mix of iter. *Plasma Physics and Controlled Fusion*, 52(12):124044, 2010. URL <http://stacks.iop.org/0741-3335/52/i=12/a=124044>.
- [23] M. Murakami et al. Integrated modelling of steady-state scenarios and heating and current drive mixes for iter. *Nuclear Fusion*, 51(10):103006, 2011. URL <http://stacks.iop.org/0029-5515/51/i=10/a=103006>.
- [24] A.H. Kritz et al. Integrated modelling for prediction of optimized iter performance. *Nuclear Fusion*, 51(12):123009, 2011. URL <http://stacks.iop.org/0029-5515/51/i=12/a=123009>.

- [25] J.E. Kinsey et al. Iter predictions using the gyro verified and experimentally validated trapped gyro-landau fluid transport model. *Nuclear Fusion*, 51(8):083001, 2011. URL <http://stacks.iop.org/0029-5515/51/i=8/a=083001>.
- [26] K Besseghir et al. Achieving and sustaining advanced scenarios in iter modelled by cronos and dina-ch. *Plasma Physics and Controlled Fusion*, 55(12):125012, 2013. URL <http://stacks.iop.org/0741-3335/55/i=12/a=125012>.
- [27] V. Parail et al. Self-consistent simulation of plasma scenarios for iter using a combination of 1.5d transport codes and free-boundary equilibrium codes. *Nuclear Fusion*, 53(11):113002, 2013. URL <http://stacks.iop.org/0029-5515/53/i=11/a=113002>.
- [28] R.V. Budny et al. Core fusion power gain and alpha heating in jet, tftr, and iter. *Nucl. Fusion*, 56(5):056002, 2016. URL <http://stacks.iop.org/0029-5515/56/i=5/a=056002>.
- [29] O. Meneghini et al. Integrated fusion simulation with self-consistent core-pedestal coupling. *Physics of Plasmas*, 23(4):042507, 2016. doi: 10.1063/1.4947204. URL <https://doi.org/10.1063/1.4947204>.
- [30] C. Chrystal et al. Predicting rotation for iter via studies of intrinsic torque and momentum transport in diii-d. *Physics of Plasmas*, 24(5):056113, 2017. doi: 10.1063/1.4979194. URL <https://doi.org/10.1063/1.4979194>.
- [31] Jiale Chen et al. Self-consistent modeling of cfetr baseline scenarios for steady-state operation. *Plasma Physics and Controlled Fusion*, 59(7):075005, 2017. URL <http://stacks.iop.org/0741-3335/59/i=7/a=075005>.
- [32] M. Kikuchi et al. *Fusion Physics*. International Atomic Energy Agency, Vienna, 2012. URL <http://www-pub.iaea.org/books/IAEABooks/8879/Fusion-Physics>.
- [33] R. Balescu. *Aspects of Anomalous Transport in Plasmas*. CRC Press, 2005. ISBN 9780750310307. doi: 10.1201/9781420034684. URL <https://doi.org/10.1201/9781420034684>.
- [34] K. Ida et al. Towards an emerging understanding of non-locality phenomena and non-local transport. *Nucl. Fusion*, 55(1):013022, 2015. URL <http://stacks.iop.org/0029-5515/55/i=1/a=013022>.
- [35] E.J. Doyle et al. Chapter 2: Plasma confinement and transport. *Nucl. Fusion*, 46:B557–B574, 2007. URL <http://stacks.iop.org/0029-5515/47/i=6/a=S02>.
- [36] A. E. White. Validation of nonlinear gyrokinetic transport models using turbulence measurements. *Journal of Plasma Physics*, 85(1):925850102, 2019. doi: 10.1017/S0022377818001253. URL <https://doi.org/10.1017/S0022377818001253>.
- [37] W. Horton. Drift waves and transport. *Rev. Mod. Phys.*, 71:735–778, 1999.

- [38] J. Weiland. *Collective Modes in Inhomogeneous Plasmas: Kinetic and Advanced Fluid Theory*. Series in Plasma Physics and Fluid Dynamics. Taylor & Francis, 1999. ISBN 9780750305891. URL <https://books.google.com/books?id=cDNKgCqDh6UC>.
- [39] J. Candy and R.E. Waltz. An eulerian gyrokinetic-maxwell solver. *Journal of Computational Physics*, 186(2):545 – 581, 2003. ISSN 0021-9991. doi: [https://doi.org/10.1016/S0021-9991\(03\)00079-2](https://doi.org/10.1016/S0021-9991(03)00079-2). URL <http://www.sciencedirect.com/science/article/pii/S0021999103000792>.
- [40] F. Jenko et al. Electron temperature gradient driven turbulence. *Phys. Plasmas*, 7(5):1904–1910, 2000. doi: 10.1063/1.874014. URL <http://dx.doi.org/10.1063/1.874014>.
- [41] A. Casati et al. Turbulence in the tore supra tokamak: Measurements and validation of nonlinear simulations. *Phys. Rev. Lett.*, 102:165005, 2009. doi: 10.1103/PhysRevLett.102.165005. URL <https://link.aps.org/doi/10.1103/PhysRevLett.102.165005>.
- [42] A. E. White et al. Measurements of core electron temperature and density fluctuations in diii-d and comparison to nonlinear gyrokinetic simulations. *Phys. Plasmas*, 15(5):056116, 2008. doi: 10.1063/1.2895408. URL <http://dx.doi.org/10.1063/1.2895408>.
- [43] C. Holland et al. Implementation and application of two synthetic diagnostics for validating simulations of core tokamak turbulence. *Phys. Plasmas*, 16(5):052301, 2009. doi: 10.1063/1.3085792. URL <http://dx.doi.org/10.1063/1.3085792>.
- [44] T.L. Rhodes et al. L-mode validation studies of gyrokinetic turbulence simulations via multi-scale and multifield turbulence measurements on the DIII-d tokamak. *Nuclear Fusion*, 51(6):063022, may 2011. doi: 10.1088/0029-5515/51/6/063022. URL <https://doi.org/10.1088/0029-5515/51/6/063022>.
- [45] C. Holland et al. Progress in GYRO validation studies of DIII-d h-mode plasmas. *Nuclear Fusion*, 52(11):114007, oct 2012. doi: 10.1088/0029-5515/52/11/114007. URL <https://doi.org/10.1088/0029-5515/52/11/114007>.
- [46] N.T. Howard et al. Quantitative comparison of experimental impurity transport with nonlinear gyrokinetic simulation in an alcator c-mod l-mode plasma. *Nucl. Fusion*, 52(6):063002, 2012. URL <http://stacks.iop.org/0029-5515/52/i=6/a=063002>.
- [47] D. Told et al. Characterizing turbulent transport in asdex upgrade l-mode plasmas via nonlinear gyrokinetic simulations. *Phys. Plasmas*, 20(12):122312, 2013. doi: 10.1063/1.4858899. URL <http://dx.doi.org/10.1063/1.4858899>.
- [48] J. Citrin et al. Ion temperature profile stiffness: non-linear gyrokinetic simulations and comparison with experiment. *Nuclear Fusion*, 54(2):023008, feb 2014. doi: 10.1088/0029-5515/54/2/023008. URL <https://doi.org/10.1088/0029-5515/54/2/023008>.

- [49] A R Field et al. Comparison of BES measurements of ion-scale turbulence with direct gyrokinetic simulations of MAST l-mode plasmas. *Plasma Physics and Controlled Fusion*, 56(2): 025012, jan 2014. doi: 10.1088/0741-3335/56/2/025012. URL <https://doi.org/10.1088/2F0741-3335%2F56%2F2%2F025012>.
- [50] T. Goerler et al. A flux-matched gyrokinetic analysis of diii-d l-mode turbulence. *Phys. Plasmas*, 21(12):122307, 2014. doi: 10.1063/1.4904301. URL <http://dx.doi.org/10.1063/1.4904301>.
- [51] C. Sung et al. Quantitative comparison of electron temperature fluctuations to nonlinear gyrokinetic simulations in c-mod ohmic l-mode discharges. *Phys. Plasmas*, 23(4):042303, 2016. doi: 10.1063/1.4945620. URL <http://dx.doi.org/10.1063/1.4945620>.
- [52] A. J. Creely et al. Validation of nonlinear gyrokinetic simulations of l- and i-mode plasmas on alcator c-mod. *Phys. Plasmas*, 24(5):056104, 2017. doi: 10.1063/1.4977466. URL <http://dx.doi.org/10.1063/1.4977466>.
- [53] F van Wyk et al. Ion-scale turbulence in MAST: anomalous transport, subcritical transitions, and comparison to BES measurements. *Plasma Physics and Controlled Fusion*, 59(11):114003, sep 2017. doi: 10.1088/1361-6587/aa8484. URL <https://doi.org/10.1088/2F1361-6587%2Faa8484>.
- [54] S. J. Freethy et al. Validation of gyrokinetic simulations with measurements of electron temperature fluctuations and density-temperature phase angles on asdex upgrade. *Physics of Plasmas*, 25(5):055903, 2018. doi: 10.1063/1.5018930. URL <https://doi.org/10.1063/1.5018930>.
- [55] N T Howard et al. Multi-scale gyrokinetic simulations of an alcator c-mod, ELM-y h-mode plasma. *Plasma Physics and Controlled Fusion*, 60(1):014034, 2017. doi: 10.1088/1361-6587/aa9148. URL <https://doi.org/10.1088/2F1361-6587%2Faa9148>.
- [56] A E White et al. Feasibility study for a correlation electron cyclotron emission turbulence diagnostic based on nonlinear gyrokinetic simulations. *Plasma Phys. Control. Fusion*, 53(11): 115003, 2011. URL <http://stacks.iop.org/0741-3335/53/i=11/a=115003>.
- [57] A. E. White et al. Measurements of the cross-phase angle between density and electron temperature fluctuations and comparison with gyrokinetic simulations. *Phys. Plasmas*, 17(5): 056103, 2010. doi: 10.1063/1.3323084. URL <http://dx.doi.org/10.1063/1.3323084>.
- [58] S. Leerink et al. Multiscale investigations of drift-wave turbulence and plasma flows: Measurements and total-distribution-function gyrokinetic simulations. *Phys. Rev. Lett.*, 109:165001, Oct 2012. doi: 10.1103/PhysRevLett.109.165001. URL <https://link.aps.org/doi/10.1103/PhysRevLett.109.165001>.
- [59] G. M. Staebler et al. A theory-based transport model with comprehensive physics. *Phys. Plasmas*, 14(5):055909, 2007. URL <http://dx.doi.org/10.1063/1.2436852>.

- [60] C. Bourdelle et al. A new gyrokinetic quasilinear transport model applied to particle transport in tokamak plasmas. *Phys. Plasmas*, 14(11):112501, 2007. doi: 10.1063/1.2800869. URL <http://dx.doi.org/10.1063/1.2800869>.
- [61] Hyun-Tae Kim et al. Statistical validation of predictive transp simulations of baseline discharges in preparation for extrapolation to jet d-t. *Nucl. Fusion*, 57(6):066032, 2017. URL <http://stacks.iop.org/0029-5515/57/i=6/a=066032>.
- [62] J Citrin et al. Tractable flux-driven temperature, density, and rotation profile evolution with the quasilinear gyrokinetic transport model qualikiz. *Plasma Physics and Controlled Fusion*, 59(12):124005, 2017. URL <http://stacks.iop.org/0741-3335/59/i=12/a=124005>.
- [63] O. Meneghini et al. Self-consistent core-pedestal transport simulations with neural network accelerated models. *Nuclear Fusion*, 57(8):086034, 2017. URL <http://stacks.iop.org/0029-5515/57/i=8/a=086034>.
- [64] P. Rodriguez-Fernandez et al. Vitals: A surrogate-based optimization framework for the accelerated validation of plasma transport codes. *Fusion Science and Technology*, 74(1-2):65–76, 2018. doi: 10.1080/15361055.2017.1396166. URL <https://doi.org/10.1080/15361055.2017.1396166>.
- [65] O. Linder et al. Flux-driven integrated modelling of main ion pressure and trace tungsten transport in asdex upgrade. *Nuclear Fusion*, 59(1):016003, 2019. URL <http://stacks.iop.org/0029-5515/59/i=1/a=016003>.

Chapter 2

Background

“Turbulence is the most important unsolved problem of classical physics.”

R. P. Feynman, *The Feynman Lectures on Physics*, 1964

The work presented in this Thesis focuses on the physics of turbulence and associated transport phenomena. Special emphasis is placed on multi-channel interactions during perturbative transport experiments, i.e. the interactions between particle, momentum and energy transport during transients. This Chapter presents the broad concept of turbulence and fluctuation-induced transport (Section 2.1), together with an introduction to perturbative transport (Section 2.2) and a discussion on the meaning of “local” and “diffusive” transport (Section 2.3). This Chapter ends with a discussion of relevant experimental observations of cold-pulse propagation and modeling attempts found in the literature for several fusion devices (Section 2.4).

2.1 Turbulence and Transport

One of the main challenges that tokamaks have faced since they were first conceived was to understand the physics of transport, in order to predict and control the confinement of particles, momentum and energy in the plasma core.

The **classical** and most fundamental mechanism of transport is the diffusion of particles, momentum and energy via collisional processes. These individual particle collisions have been thoroughly studied, and led to the development of the **neoclassical** theory that takes into account curved and inhomogeneous magnetic fields (i.e. applied to magnetically-confined toroidally-shaped plasmas). However, in most situations, neoclassical predictions were significantly below experimentally

observed transport levels. The term “**anomalous**” transport was then coined to refer to these unexplained phenomena, such that total transport fluxes are the sum of neoclassical and anomalous contributions, $\vec{q} = \vec{q}_{neo.} + \vec{q}_{an.}$. Now, thanks mostly to developments in the gyrokinetic theory [1] and increased computational power, the understanding within the fusion community is that anomalous transport is, in great part, caused by turbulence and associated transport phenomena [2].

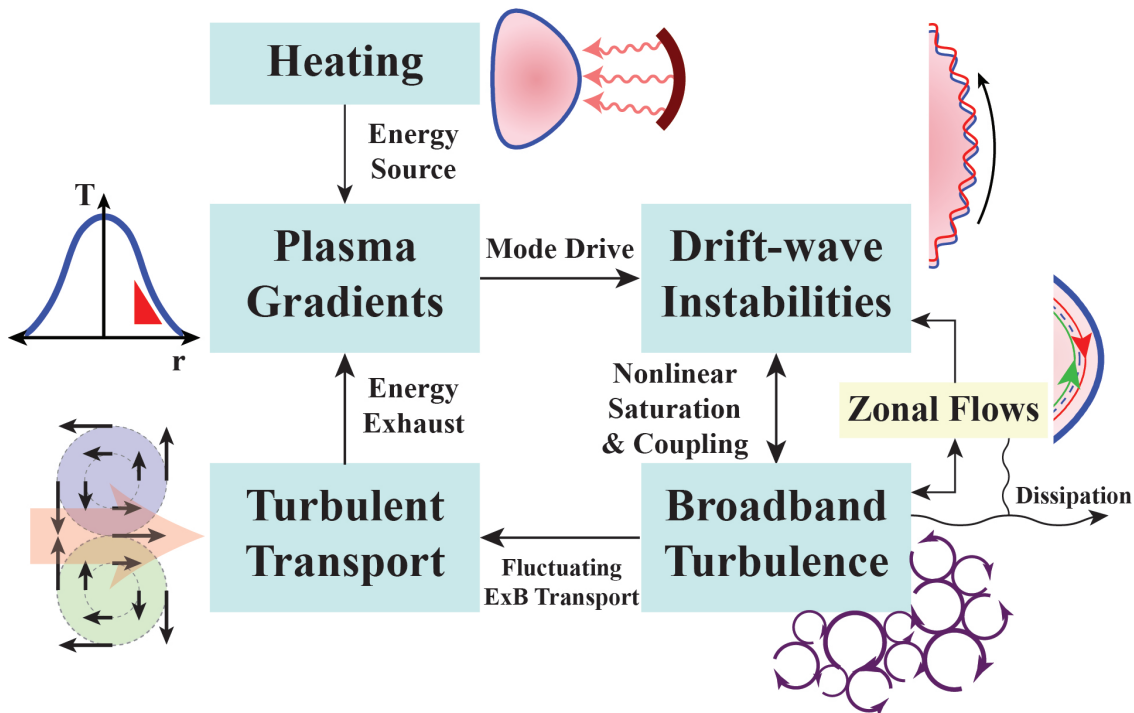


Figure 2.1: Drift-wave turbulence flowchart. Heating of the plasma provides a source of energy for the development of radial gradients, which in turn drive various drift-wave modes unstable. These linear modes eventually saturate via nonlinear three-wave processes and lead to broadband turbulent structures. The combination of fluctuating $E \times B$ velocity and pressure fluctuations contributes to enhanced radial transport of particles, momentum and energy. Inspired from Refs. [3, 4].

In the following, an introduction of the basics of turbulence and transport in tokamak plasmas is presented. The pedagogical concepts provided in this Section have been compiled from different sources, especially from Refs. [3, 5–11]. Figure 2.1 displays schematically the interactions among the several aspects that contribute to turbulence and transport in magnetically-confined plasmas. Firstly, Section 2.1.1 briefly introduces the concept of plasma turbulence and the most common drift-wave-type pressure gradient driven instabilities. Section 2.1.2 provides a link of plasma turbulence to fluctuation-induced (i.e. turbulent) transport. Section 2.1.3 introduces the plasma kinetic equation, which describes the exact evolution of the plasma in phase-space, and the gyrokinetic theory as a simplified and alternative model to the plasma kinetic equation. Lastly, Section 2.1.4 presents the quasilinear approximation to turbulent transport, which is used in the rest of this Thesis to model plasma transport phenomena.

2.1.1 Plasma Turbulence

Plasma turbulence can be understood as the result of the nonlinear evolution of a number of collective modes [5]. These modes are the result of instabilities that are excited by some free energy in the plasma and converted into kinetic energy and fluctuating electromagnetic fields. In magnetic confinement devices, large temperature and density gradients form as a consequence of having a hot and dense plasma core in proximity of reactor walls. Therefore, tokamak plasmas are unstable to a variety of modes that are excited by the free energy contained in the gradients and that need to be understood to accurately predict performance of burning plasmas. Fundamental understanding of these micro-instabilities is necessary to project new regimes, develop high-performance scenarios, and control burning plasmas in future fusion devices.

The collective modes that are primarily responsible for the anomalous transport in tokamak plasmas are the so-called drift waves. The common feature of these waves is the phase velocity, which is equal to the diamagnetic drift velocity of the plasma species, and the finite parallel wavenumber. These modes grow to a saturation state and form broadband turbulent structures via nonlinear three-wave processes [3], with very long parallel wavelengths and small radial and poloidal wavelengths. Tokamak plasmas typically experience the following types of electrostatic¹ drift-wave instabilities, which respond in different ways to plasma conditions but have drift-wave-like nature [3]:

- **Ion Temperature Gradient (ITG) driven instability** [12, and references therein]

ITG modes get their free energy from the ion temperature gradient, ∇T_i , and in tokamak plasmas are mostly driven unstable in the bad curvature region (low-field side, where $\nabla p \cdot \nabla B > 0$), although they may also occur in slab geometry via ion acoustic wave coupling [13].

ITG modes are unstable at long wavelengths, typically larger than the ion Larmor radius $k_\theta \rho_i < 1$, and rotate in the direction of the ion diamagnetic drift velocity. Here, k_θ refers to the poloidal wavenumber, typically defined as $k_\theta = n \frac{q}{r}$, where n is the toroidal wavenumber. ρ_i is the ion Larmor radius, $\rho_i = \frac{\sqrt{m_i T_i}}{qB}$.

These modes exhibit a threshold in normalized ion temperature gradient, a/L_{T_i} , which in turn depends on the normalized density gradient a/L_n and temperatures ratio T_i/T_e . They dominantly drive ion heat transport, but are also responsible for particle, momentum and electron heat transport.

- **Trapped Electron Mode (TEM) instability** [14, and references therein]

TEMs get their free energy from electron pressure gradients, ∇n and ∇T_e , and are driven unstable because of the presence of trapped electrons in the bad curvature region (slow average motion along the field line due to trapping). These modes are unstable at long

¹Generally speaking, electromagnetic effects can be ignored in the limit of low $\beta \equiv 2\mu_0 p/B^2$ [6].

wavelengths, typically of the order of the ion Larmor radius $k_\theta \rho_i \sim 1$, and usually rotate in the direction of the electron diamagnetic drift velocity.

These modes exhibit a threshold in normalized electron temperature gradient, a/L_{T_e} , which in turn depends on the normalized density gradient a/L_{n_e} and the fraction of trapped electrons f_t . They also drive particle, momentum, ion heat and, especially, electron heat transport. TEMs are strongly stabilized by collisions, which lead to de-trapping.

- **Electron Temperature Gradient (ETG) driven instability** [15, and references therein]
ETG modes are the analogous of the ITG but their free energy is contained in the electron temperature gradient, ∇T_e , their spatial scale is in the order of the electron Larmor radius $k_\theta \rho_e > 1$, and usually rotate in the direction of the electron diamagnetic drift velocity.

Turbulence is the result of the interaction and balance between driving terms that are source of free energy (e.g. gradients) and stabilizing terms (e.g. magnetic and velocity shear) [6]. Interactions of modes in the plasma eventually leads to energy dissipation at the high wavenumber range via collisional processes and the formation of large scale plasma flows at low wavenumbers, which are comparable to the plasma flows and intrinsic $E \times B$ velocity [3]. These self-generated zonal flows (perpendicular to the background driving gradients) act as a regulation mechanism for turbulence itself. The shear in background plasma flows also contributes to turbulence suppression, as turbulent “eddy”-like structures are sheared radially, as depicted schematically in Figure 2.2. More details on these nonlinear saturation processes will be presented in Section 3.3.2, where the turbulence model used in this work, TGLF, is discussed.

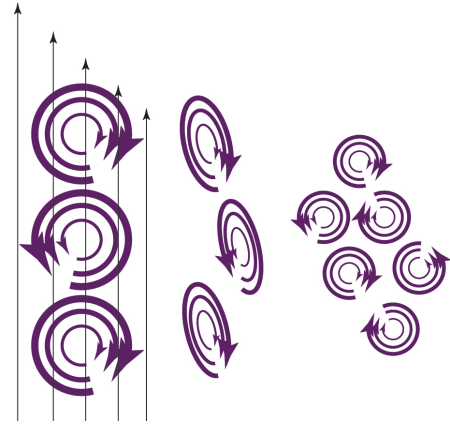


Figure 2.2: Schematic of turbulence suppression via decorrelation by sheared flows. Circular eddies are distorted by large scale flows and eventually broke up. Inspired from Ref. [16].

This nonlinear interplay between different scales of turbulence, dissipation and flows eventually leads to a saturated state where turbulent fluctuations (with frequencies much smaller than the gyromotion and perpendicular spatial scales much smaller than the system size [10]) are present with constant magnitude.

2.1.2 Fluctuation-induced Transport

In the previous section it was described how a number of saturated modes (primarily driven by radial pressure gradients) give rise to turbulent fluctuations [3]. These turbulent fluctuations in numerous fields (\tilde{n} , \tilde{T} , $\tilde{\phi}$, \tilde{A}_\parallel ...) that develop from the drift-wave-type turbulence result in

time-averaged cross-field particle, momentum and heat fluxes. As schematically depicted in Figure 2.3, electric potential fluctuations produce an $E \times B$ drift velocity (“ $E \times B$ velocity eddies”) that, combined with pressure fluctuations, may result in cross-field transport.

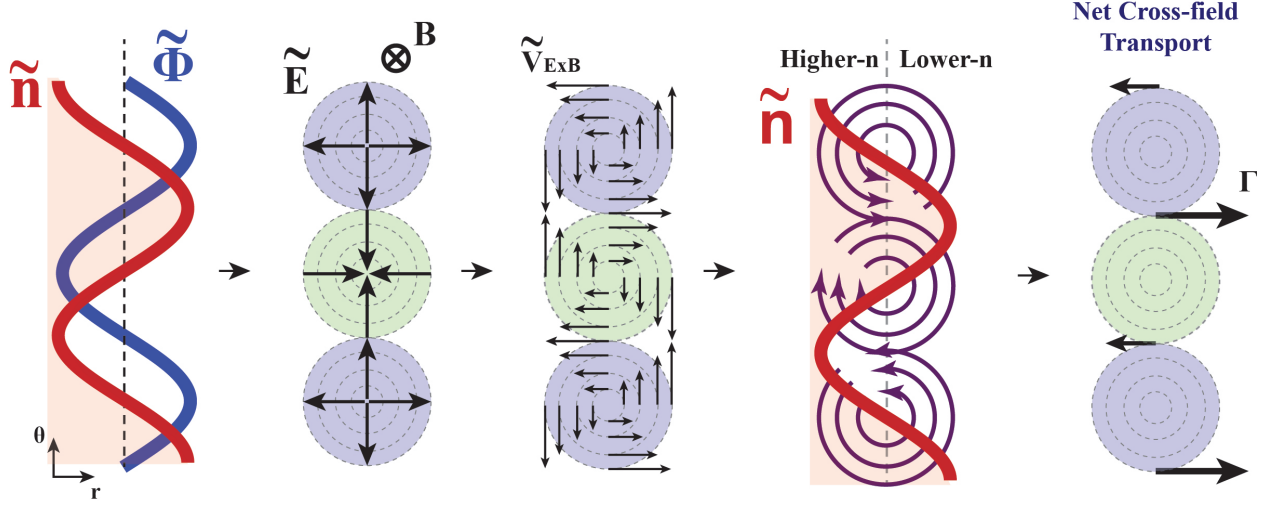


Figure 2.3: Schematic of fluctuation-induced cross-field transport. Potential fluctuations, $\tilde{\phi}$, result in $E \times B$ velocity eddies, which induce net cross-field particle transport, Γ , depending on the relative phase to the density fluctuations, \tilde{n} .

In this section, we provide intuition of what this fluctuation-induced transport looks like from a one-dimensional fluid model perspective. The general expressions for the radial particle and heat fluxes of species α are given by:

$$\Gamma_\alpha = \left\langle \int_\omega \omega_{r,\alpha} f_\alpha d^3 \vec{\omega} \right\rangle \quad (2.1)$$

$$Q_\alpha = \left\langle \int_\omega \left(\frac{1}{2} m_\alpha \omega^2 \right) \omega_{r,\alpha} f_\alpha d^3 \vec{\omega} \right\rangle \quad (2.2)$$

where we define the thermal component of the velocity as $\vec{\omega} = \vec{v} - \vec{u}_\alpha$ (where \vec{u}_α is the flow velocity for species α), and $\langle \cdot \rangle$ is the ensemble average². The fluctuation-induced particle and effective total energy fluxes (as presented in Ref. [17]) can be then written as:

$$\Gamma_\alpha^{turb} = \langle \tilde{n}_\alpha \tilde{v}_r \rangle \quad (2.3)$$

$$Q_\alpha^{turb} = \left\langle \frac{3}{2} \tilde{p}_\alpha \tilde{v}_r \right\rangle \quad (2.4)$$

In the case of low-frequency fluctuations, the radial velocity fluctuation can be written as [18] $\tilde{v}_r \simeq \frac{\tilde{E}_\theta}{B_0} + v_\parallel \frac{\tilde{B}_r}{B_0}$, which for electrostatic fluctuations reduces simply to $\tilde{v}_r \simeq \frac{\tilde{E}_\theta}{B_0}$. With these

²Here, ensemble average indicates the average over time-scales longer than the period of the fluctuating quantity but short compared to transport time-scale, and a flux-surface average

assumptions we can write:

$$\Gamma_\alpha^{turb} = \frac{1}{B_0} \langle \tilde{n}_\alpha \tilde{E}_\theta \rangle \quad (2.5)$$

$$Q_\alpha^{turb} = \frac{3}{2} \frac{1}{B_0} \langle \tilde{p}_\alpha \tilde{E}_\theta \rangle = \frac{3}{2} T_\alpha \Gamma_\alpha^{turb} + \frac{3}{2} \frac{1}{B_0} n_\alpha \langle \tilde{T}_\alpha \tilde{E}_\theta \rangle \quad (2.6)$$

where the average of the fluctuating quantities, $\langle \tilde{A} \rangle = 0$, vanishes and only the correlation between them matters.

From Equation 2.6 one can identify that the fluctuation-induced (i.e. *turbulent*) heat flux is a function of density, temperature and potential fluctuations, as well as the correlation (i.e. phase) between density and potential and temperature and potential fluctuations. Modeling accurately the evolution of the fluctuating plasma quantities is thus critical to predict turbulent transport and kinetic profiles in magnetically-confined plasmas.

2.1.3 Plasma Modeling

The most complete description of a plasma starts from the definition of a single particle as a classical point in phase space. Considering an ensemble of particles and assuming that the only long-range forces acting on individual particles are the electromagnetic (Lorentz) forces, then the plasma kinetic equation can be derived (as in Ref. [7]). The plasma kinetic equation for the evolution of the distribution function, $f_\alpha(\vec{x}, \vec{v}, t)$, can be then written as:

$$\frac{df_\alpha}{dt} \equiv \frac{\partial f_\alpha}{\partial t} + \vec{v} \cdot \nabla_x f_\alpha + \frac{q_\alpha}{m_\alpha} \left(\vec{E} + \frac{\vec{v} \times \vec{B}}{c} \right) \cdot \nabla_v f_\alpha = \left(\frac{\partial f_\alpha}{\partial t} \right)_c \quad (2.7)$$

Equation 2.7 is sometimes referred to as Boltzmann kinetic model, and should be coupled to Maxwell's equations to describe a plasma system. This plasma model (with real and velocity space dimensions), although complete, is not tractable from the point of view of solving for the plasma evolution, since, generally, the dimensionality of the problem is too high to be handled by a computer simulation. Nonetheless, the plasma kinetic equation is the starting point for the development of simplifying models that make reasonable assumptions depending on the problem of interest. For instance, the assumptions made by the gyrokinetic model (which will be described next) are reasonable for the study of turbulence, whereas the stronger assumptions made by the fluid model (with the right closure) are enough for the study of plasma dynamics over transport time scales and plasma discharges.

Gyrokinetic Description

Given the difficulty of solving the 6D plasma kinetic equation in a direct way, the gyrokinetic theory has been developed to study plasma phenomena [8, 19–21]. The basic idea of gyrokinetics in

magnetized plasmas is to neglect the fast gyromotion of particles around equilibrium magnetic field lines with respect to turbulence timescales. In this way, we define “pseudo-particles” as charged rings described by their gyrocenter coordinates. The gyroangle coordinate then becomes ignorable and the guiding center magnetic moment, μ , is treated as a adiabatic invariant ($\frac{d\mu}{dt} = 0$) [8], which also leads to parallel/perpendicular scale separation [9].

The plasma kinetic equation can be written specifically for the gyrocenter with position \vec{X} and parallel velocity \vec{v}_{\parallel} . Using the parallel/perpendicular scale separation, we can write the most general nonlinear gyrokinetic equation that describes the evolution of the gyro-averaged distribution function, \bar{f}_{α} , as [11]:

$$\frac{\partial \bar{f}_{\alpha}(\vec{X}, \vec{v}_{\parallel}, t; \mu)}{\partial t} + (\vec{v}_{E \times B} + \vec{v}_{\nabla B} + \vec{v}_{\kappa}) \cdot \nabla_{\perp} \bar{f}_{\alpha} + \vec{v}_{\parallel} \cdot \nabla_{\parallel} \bar{f}_{\alpha} + \dot{\vec{v}}_{\parallel} \cdot \nabla_{v_{\parallel}} \bar{f}_{\alpha} = \left\langle \left(\frac{\partial f_{\alpha}}{\partial t} \right)_c \right\rangle \quad (2.8)$$

where $\left\langle \left(\frac{\partial f_{\alpha}}{\partial t} \right)_c \right\rangle$ represents the gyro-averaged collision operator, and $\vec{v}_{E \times B}$, $\vec{v}_{\nabla B}$ and \vec{v}_{κ} are the $E \times B$, ∇B and curvature drifts.

Equation 2.8, along with the appropriate field equations from Maxwell [10] represents a set of nonlinear, 5D equations capable of capturing the dynamics of plasma turbulence that is generally accepted to drive the majority of transport in the core of tokamaks. This is the standard approach to study plasma turbulence in recent years, and numerous codes have been developed to do so, which differ in the physics they include (plasma species, electromagnetic fluctuations, collisional operators, treatment of shear $E \times B$ flows, etc.).

Typically, one can simplify the full nonlinear gyrokinetics by assuming a frozen background, i.e. by neglecting the feedback of turbulence on the equilibrium [9]. This approximation is usually called the “ δf ”-approximation, as only the perturbed distribution function is solved. The δf framework is the basis of gradient-driven simulations, where we intend to solve for the transport levels in a given background state. Another standard simplification is the local approximation [22], where only one flux-tube elongated along a magnetic field is simulated and the plasma quantities are linearized and evaluated at the center of the flux-tube, so that variations of the kinetic profiles across the simulation domain is ignored. However, for situations that involve studying plasma dynamics over energy confinement times (such that for profile predictions), solving the nonlinear gyrokinetic equation is still too computationally expensive.

2.1.4 The Quasilinear Approximation

A further approximation that can be made to simplify the simulation of transport in magnetically confined plasmas is the quasilinear approximation. The quasilinear approximation makes use of the idea that the saturated turbulence state can be described, in part, from linear characteristics. Typically, it is assumed that the cross-phase between fluctuating quantities are given by the linear response, while the saturation amplitude is modeled via saturation rules, which are simple formulas

constructed from linear properties that aim at capturing the physics of nonlinear gyrokinetic simulations.

In this quasilinear approximation, the solution can be written as the superposition of waves that evolve independently of each other (i.e. eigenmodes), which are obtained from the eigenvalue problem of a linear operator [23]. The eigenvalues are generally complex, with a form that contains a real frequency (oscillation) and imaginary frequency (growth rate), $\omega(\vec{k}) + i\gamma(\vec{k})$. These modes are unstable if $\gamma(\vec{k}) > 0$, a case in which their amplitude grows exponentially in time. To deal with the final turbulence state, nonlinear contributions need to be included, i.e. the exponentially growing amplitudes of the unstable linear modes become larger and larger until the linear approximation is not valid anymore and the system is dominated by wave-wave and wave-particle interactions.

In the derivation of turbulent heat fluxes, we explored that the time and flux-surface average of the electrostatic part of the heat flux (Equation 2.6) can be written as $Q_\alpha = \langle \frac{3}{2} \tilde{p}_\alpha \tilde{v}_r \rangle$. Assuming electrostatic microturbulence, we can write:

$$Q_\alpha = \left\langle \frac{3}{2} \tilde{p}_\alpha \tilde{v}_r \right\rangle = \left\langle \frac{3}{2} \tilde{p}_\alpha \frac{\nabla \tilde{\phi} \times \mathbf{B}}{B^2} \right\rangle \quad (2.9)$$

By Fourier expansion of the fluctuating quantities, $\tilde{a} \propto e^{-i(\omega t - \mathbf{k} \cdot \mathbf{x})}$, we identify that $\nabla \tilde{\phi} \approx ik_\theta \tilde{\phi}$, where k_θ is defined as $k_\theta = \frac{nq}{r}$, with n as the toroidal wavenumber. By using normalized electrostatic potential fluctuations, $\tilde{\Phi} = \frac{e\tilde{\phi}}{T_e}$, normalized wavenumber, $k_y = k_\theta \rho_s$, and $\rho_s c_s = T_e/eB$, we can write the flux for each of the Fourier components (modes) as:

$$Q_{\alpha,k} = \frac{3}{2} \Re \left\langle \tilde{p}_\alpha \frac{ik_\theta \tilde{\phi}}{B} \right\rangle = c_s \frac{3}{2} \Re \langle ik_y \tilde{p}_\alpha \tilde{\Phi} \rangle \quad (2.10)$$

We define the quasilinear weights³ as the fluxes for a single mode divided by the mode intensity, as follows:

$$Q_{\alpha,ql} = \frac{1}{|\tilde{\Phi}|^2 c_s n_e T_e} Q_{\alpha,k} = \left(\frac{3}{2} \frac{1}{n_e T_e} \right) \frac{\Re \langle ik_y \bar{\Phi}^* \bar{p}_\alpha \rangle}{\langle \bar{\Phi}^* \bar{\Phi} \rangle} \quad (2.11)$$

where the gyro-reduced norms $\bar{\Phi}^2 = \tilde{\Phi}^2 / \rho_*^2$ and $\bar{p}_\alpha = \tilde{p}_\alpha / \rho_*$ were used, with $\rho_* \equiv \rho_s / a$.

Quasilinear transport solvers assume that the total flux can be written as the sum over k (independent) contributions of the most unstable linear modes, such that $Q_\alpha = \sum_k Q_{\alpha,k}$. We can then write the gyroBohm-normalized flux as:

$$Q_\alpha^{GB} = \sum_{k_y} \bar{\Phi}^2 Q_{\alpha,ql} \quad (2.12)$$

where the heat flux in real units is given by $Q_\alpha = n_e T_e c_s \rho_*^2 \sum_{k_y} \bar{\Phi}^2 Q_{\alpha,ql}$. The factor $n_e T_e c_s \rho_*^2$ is called the gyroBohm normalization.

³Note that quasilinear weights notation in Ref [24] use moments of the perturbed distribution function normalized to their equilibrium values, while I prefer to use absolute fluctuations here.

Then, the quasilinear approach for the total heat flux leads to a summation of (non-interacting) contributions of the linear response (represented by the quasilinear weight of each mode) and the saturated electrostatic potential at each wavenumber:

$$Q_{\alpha}^{GB} = \underbrace{\left(\frac{3}{2} \frac{1}{n_e T_e}\right)}_{\text{Dimensionality Factor}} \cdot \sum_{k_y} \left[\frac{\Re \langle ik_y \tilde{\Phi}^* \tilde{p}_{\alpha} \rangle}{\underbrace{\langle \tilde{\Phi}^* \tilde{\Phi} \rangle}_{\text{Linear Response}}} \cdot \underbrace{\overline{\Phi}^2}_{\text{Saturated Potential}} \right] \quad (2.13)$$

In derivation of quasilinear fluxes, an important assumption is made: the phase difference and the relative amplitude of pressure, \tilde{p}_{α} , and potential, $\tilde{\phi}$, fluctuations are given by the solution of the linearized equations. The system of linear equations that results from a gyrokinetic or gyrofluid framework lead to an eigenvalue problem of the form $D(\omega, k) = 0$. Solutions of the dispersion relation of unstable modes ($\gamma > 0$) will provide the required relation between fluctuating kinetic quantities, such as \tilde{p}_{α} , and the fluctuating electrostatic potential through the corresponding eigenmode solution. This way, the factor $\Re \langle ik_y \tilde{\Phi}^* \tilde{p}_{\alpha} \rangle / \langle \tilde{\Phi}^* \tilde{\Phi} \rangle$ is determined simply from the **linearized set of equations** that govern the system. Such set of equations depends on the quasilinear code in hand. The trapped-gyro-Landau-fluid (TGLF) model [25], which will be presented in detail in Section 3.3, solves a system of fluid moments of the linearized gyrokinetic equation, while the QuaLiKiz model [26] works directly with the linearized gyrokinetic equation.

Furthermore, the saturated electrostatic potential, $\overline{\Phi}$, cannot be obtained from linear physics. Therefore a model for the saturated level of turbulence based on linear features must be chosen. This is what is commonly referred to as **saturation rule**, and it also depends on each quasilinear code. Typically, the saturated electrostatic potential is given by a heuristic mixing-length estimate for the heat flux contribution from each wavenumber. Basically this argument states that, at saturation, the growth of the linear mode is balanced by turbulent diffusion [13]. If the characteristic time-step is given by $1/\gamma_k$ and the spatial extend by $1/k$, we can estimate:

$$D_k \sim \frac{(\Delta x)^2}{\Delta t} \sim \frac{\gamma_k}{k^2} \sim |\tilde{\phi}| \quad (2.14)$$

More details about the linear response and saturation rule needed for the evaluation of the quasilinear fluxes will be presented in Section 3.3, where the TGLF model is introduced. Validation of the quasilinear approximation and saturation rule against experiment is very important to build confidence in the models. It is only by careful verification and experimental validation exercises when one can assess the accuracy of present models to predict performance of future fusion devices. Section 2.1.5 and Appendix B address this issue by presenting a validation workflow for quasilinear transport models.

2.1.5 Validation of Transport Models in Steady-State: the VITALS framework

In general, quasilinear models provide transport fluxes at low computational cost, and thus can be used to predict profiles and performance of fusion machines (which typically require many iterations of gradient-based models). Nonetheless, before using them to inform experiments and design new machines, one needs first to validate these models with data from current experiments.

Experimental measurements of plasma parameters are subject to diagnostic uncertainties, and in the case of temperature and density gradients these uncertainties can be very high (typically 15% – 30%) which complicates the validation process of transport models. Furthermore, because of the high sensitivity of transport fluxes with respect to plasma parameters and to reduce the possibility of fortuitous agreement, one should validate the transport model against multiple quantities, ideally at different levels of the primacy hierarchy. As stated in Refs. [27, 28], the primacy hierarchy in plasma transport validation indicates how measured quantities (e.g. density fluctuations) affect or produce other measured quantities (e.g. fluxes). Due to this, and because many plasma parameters affect transport, validation then becomes a very computationally intensive problem, even with reduced quasilinear models.

As part of this Thesis work, a new framework has been developed to reduce the computational intensity of this problem, by resorting to smart techniques for exploring the high-dimensional parameter space. The “**Validation via Iterative Training of Active Learning Surrogates**” (VITALS) framework exploits the speed of computation afforded by quasilinear transport models, surrogate strategies and a genetic-algorithm-based optimizer to test whether a combination of plasma parameters exists such that experimental transport measurements are captured by a transport model. A detailed description of VITALS is out of the scope of this Thesis, which focuses on the physics of perturbative transport. Here, only a high-level summary of this methodology is provided, and further details can be found in Appendix B and in Ref. [29].

In short, VITALS aims at solving the inverse problem of finding the set of input plasma parameters to a given transport model (like TGLF) that provides measured transport levels. Because validation is the focus of VITALS, input parameters can only vary within experimental error bars. As a differentiating feature with other flux-matching tools such as TGYRO [30], VITALS is able to include as many transport metrics as available in the experiment. That is, VITALS makes use of multi-channel transport fluxes, turbulence measurements (e.g. fluctuation levels and cross-phase angles) and transport characteristics (e.g. stiffness and D and V impurity transport coefficients) to validate transport models.

VITALS is very computationally efficient in performing this task. First, the input-parameters space is randomly sampled, and single combinations of input parameters are evaluated in parallel with the transport code. Surrogate models are constructed using the set of inputs and corresponding outputs, and the inverse problem on the surrogates is solved by minimizing the difference with respect to experimental outputs. This minimization problem is solved using genetic algorithms,

which are heuristic methods suited for multi-variable, nonlinear, non-convex problems.

Thanks to its flexibility, VITALS has been successfully implemented to study Alcator C-Mod, ASDEX Upgrade, DIII-D and JET plasmas. Both TGLF and QuaLiKiz reduced transport models have been included. For the interested reader, [Appendix B](#) includes a detailed description of the techniques and application of VITALS for transport model validation.

2.2 Perturbative Transport Physics

In this section, we introduce the concept of perturbative transport. In steady-state, a phenomenological description of transport fluxes as $Q = -n\chi^{eff}\nabla T$ is always mathematically correct (because an effective thermal diffusivity can always be defined from steady-state fluxes and gradients as $\chi^{eff} \equiv -Q/n\nabla T$), but might be physically meaningless because the heat flux may have no dependence on the gradients that χ^{eff} is evaluated with. In order to understand the dependence of local fluxes to changes in gradients, small perturbations can be introduced experimentally to probe the relationship between fluxes and gradients.

Over the years, there has been strong evidence that suggests that the idealized description of transport as diffusive (only diagonal fluxes) is too simple to explain plasma phenomena [31]. This is particularly important in particle transport studies, where there is significant experimental evidence for diffusive and convective contributions to the particle flux [32, and references therein]. A detailed discussion on the topic of diffusive v.s. non-diffusive transport will be presented in Section 2.3.1, but here we introduce the concept of transport matrix as a more accurate phenomenological description of transport experiments. The introduction of transport matrices to describe transport originated from the need of explaining anomalously high heat transport responses in some machines [33, and references therein]. The addition of convective pinches and off-diagonal terms to the transport flux-relation can help explain some of these discrepancies. Equation 2.15 shows an example of a transport matrix where diffusive and convective terms for several transport channels are specified.

$$\underbrace{\begin{bmatrix} \frac{\Gamma_e}{n_e} \\ \frac{Q_e}{n_e T_e} \\ \frac{Q_i}{n_i T_i} \\ \frac{\Pi}{(m_i n_i v_\phi)} \end{bmatrix}}_{\text{Fluxes}} = - \underbrace{\begin{bmatrix} D & \cdot & \cdot & \cdot & V \\ \cdot & \chi_e & \cdot & \cdot & V_e \\ \cdot & \cdot & \chi_i & \cdot & V_i \\ \cdot & \cdot & \cdot & \chi_\phi & V_\phi \end{bmatrix}}_{\text{Transport Coefficients}} \cdot \underbrace{\begin{bmatrix} \frac{1}{n_e} \nabla n_e \\ \frac{1}{T_e} \nabla T_e \\ \frac{1}{T_i} \nabla T_i \\ \frac{\nabla(m_i n_i v_\phi)}{(m_i n_i v_\phi)} \\ 1 \end{bmatrix}}_{\text{Thermodynamic Drives}} \quad (2.15)$$

In the following, we provide a discussion of standard analyses of experimental perturbative transport phenomena, putting special emphasis on the definition of temperature profile stiffness, which will be very useful to understand the fast propagation of temperature pulses in tokamak plasmas.

2.2.1 Electron Thermal Incremental Diffusivity, χ^{inc}

In perturbative transport studies, the concept of incremental diffusivity is of great importance to understand the difference between steady-state and transient behavior. Incremental diffusivity is then related to the widely-known concept of stiff transport and therefore can be linked to profile

consistency observed in tokamaks. The derivation presented here makes use of the method derived by Ref. [34]. The process starts by modeling the equilibrium heat flux with diffusion and convection terms:

$$Q = -n\chi\nabla T + VnT \quad (2.16)$$

Here, χ is the power balance heat diffusivity (sometimes referred as D^{PB} or χ^{PB}), and V is the convection velocity. It is assumed that negative values of V represent inward convection. It is important to note that, in order for the term VnT not to be “diffusive-like”, the convective velocity cannot depend on ∇T . This type of transport modeling is called “interpretive” or “phenomenological” and it is a vestige of classical transport theory that suggested that temperature gradients and plasma flows have the most significant contribution to the heat flux [35]. Temperature gradients give rise to conductive components, whereas the convective part does not have a form *a priori* nor it needs to be related to mean plasma flows when turbulent transport is assumed.

The linearized heat flux due to small perturbations around the equilibrium value can be determined by perturbing and expanding Equation 2.16 up to first-order:

$$\tilde{Q} = -(\tilde{n}\chi\nabla T + n\tilde{\chi}\nabla T + n\chi\nabla\tilde{T}) + \tilde{V}nT + V\tilde{n}T + Vn\tilde{T} \quad (2.17)$$

Expressions for the perturbed transport coefficients, $\tilde{\chi}$ and \tilde{V} , can be found by applying the chain rule and assuming that the diffusivity only depends on temperature, density and their gradients, $\chi = \chi(T, \nabla T, n, \nabla n)$, whereas the convective velocity cannot depend on the temperature gradient, $V = V(T, n, \nabla n)$ as described above:

$$\tilde{\chi} = \nabla\tilde{n}\frac{\partial\chi}{\partial\nabla n} + \tilde{n}\frac{\partial\chi}{\partial n} + \nabla\tilde{T}\frac{\partial\chi}{\partial\nabla T} + \tilde{T}\frac{\partial\chi}{\partial T} \quad (2.18)$$

$$\tilde{V} = \nabla\tilde{n}\frac{\partial V}{\partial\nabla n} + \tilde{n}\frac{\partial V}{\partial n} + \tilde{T}\frac{\partial V}{\partial T} \quad (2.19)$$

Therefore, combining Equation 2.16 with these expressions for the perturbed transport coefficient, an expression for the linearized perturbed heat flux can be derived:

$$\begin{aligned} \tilde{Q} = & -\left(\tilde{n}\chi\nabla T + n\left[\nabla\tilde{n}\frac{\partial\chi}{\partial\nabla n} + \tilde{n}\frac{\partial\chi}{\partial n} + \nabla\tilde{T}\frac{\partial\chi}{\partial\nabla T} + \tilde{T}\frac{\partial\chi}{\partial T}\right]\nabla T + n\chi\nabla\tilde{T}\right) + \\ & + \left[\nabla\tilde{n}\frac{\partial V}{\partial\nabla n} + \tilde{n}\frac{\partial V}{\partial n} + \tilde{T}\frac{\partial V}{\partial T}\right]nT + V\tilde{n}T + Vn\tilde{T} \end{aligned} \quad (2.20)$$

This expression for the linearized perturbed heat flux can be casted by grouping terms with $\nabla\tilde{T}$, \tilde{T} and density perturbations separately, getting to the final simplifying form:

$$\tilde{Q} = -n\chi^{inc}\nabla\tilde{T} + nV^{inc}\tilde{T} + \tilde{\xi} \quad (2.21)$$

In this expression, the diffusive part of the perturbed heat transport is defined as $-n\chi^{inc}\nabla\tilde{T} = -n\left(\chi + \frac{\partial\chi}{\partial\nabla T}\nabla T\right)\nabla\tilde{T}$. Therefore, we can define the incremental diffusivity, sometimes called

perturbative, heat pulse or modulated diffusivity, as:

$$\chi^{inc} = \chi + \frac{\partial \chi}{\partial \nabla T} \nabla T = \frac{\partial}{\partial \nabla T} (\chi \nabla T) \quad (2.22)$$

In Equation 2.21, V^{inc} represents the velocity related to the convection part of the perturbed heat flux, while $\tilde{\zeta}$ groups the remaining terms, those that are driven by perturbations in density and its gradient. $\tilde{\zeta}$ is usually called the coupling term and, unlike χ^{inc} and V^{inc} , it is a complex quantity. Both convection V^{inc} and coupling $\tilde{\zeta}$ will not be treated in this derivation and the interested reader is invited to read Refs. [36, 37].

If we now use again the assumptions that T , ∇T and n are independent variables and that V does not depend on ∇T we can write Equation 2.22 as:

$$\chi^{inc} = \frac{\partial}{\partial \nabla T} (-Q/n + VT) = -\frac{1}{n} \frac{\partial Q}{\partial \nabla T} \quad (2.23)$$

Therefore, accounting for the sign convention of heat flux and temperature gradient we get the final expression for the incremental electron thermal diffusivity:

$$\boxed{\chi^{inc} = \frac{1}{n} \left| \frac{\partial Q}{\partial \nabla T} \right|} \quad (2.24)$$

The incremental diffusivity defined by Equation 2.24 is a very important metric to characterize turbulent transport. In general, the incremental diffusivity is the real slope of the $Q/n-\nabla T$ curve, which then characterizes how much heat flux is exhausted with small changes in temperature gradient.

χ_{inc} can also be used to separate diffusion and convection. Using Equation 2.22, the value of the power-balance diffusivity can be obtained by integrating the incremental diffusivity as a function of the equilibrium gradients:

$$\chi = \frac{1}{\nabla T} \int_0^{\nabla T} \chi^{inc} d\nabla T \quad (2.25)$$

Consequently, we can write an expression for power-balance convection, V , as follows:

$$\left. \begin{aligned} Q &= -n\chi \nabla T + nVT \\ \chi &= \frac{1}{\nabla T} \int_0^{\nabla T} \chi^{inc} d\nabla T \end{aligned} \right\} \Rightarrow V = \frac{Q}{nT} + \frac{1}{T} \int_0^{\nabla T} \chi^{inc} d\nabla T \quad (2.26)$$

Equation 2.26 is used to determine the convective component of the equilibrium heat flux. With only power balance calculations it is not possible to determine the components of the heat flux and therefore perturbative experiments become essential to determine the nature of plasma transport.

For a better understanding of these concepts, Figure 2.4 reflects the differences between power-balance and incremental electron heat diffusivity during an electron temperature gradient scan in the core of an Alcator C-Mod L-mode plasma. This scan was performed using the TGLF-SAT1

model, which will be described in detail in Chapter 3, but that follows the same workflow as general quasilinear models, which were discussed in Section 2.1.4.

The top plot shows the evolution of the electron turbulent heat flux, Q_e , as a function of the electron temperature gradient, ∇T_e . It also shows the evolution of the linear growth rate of electron-diamagnetic-direction modes at $k_\theta \rho_s = 0.6$ (TEM mode), as seen by the sudden increase of γ at the critical gradient. Electron heat flux exhibits a critical gradient behavior, which coincides with the destabilization of a TEM mode at $k_\theta \rho_s = 0.6$. The bottom plot shows the evolution of power balance (χ_e), effective (χ_e^{eff}) and incremental (χ_e^{inc}) diffusivities, as well as the power balance convective velocity. The latter does not change during the scan (except for numerical artifacts due to simple numerical derivation and integration) because we assumed that $V = V(T, n, \nabla n) \neq V(\nabla T)$. Above the critical gradient $\chi_e^{inc} \gg \chi_e$, which corresponds to a strongly nonlinear increase of the heat flux. At high gradient, it is also observed that $\chi_e \approx \chi_e^{eff}$, whereas at low gradient we see that $\chi_e^{eff} > \chi_e$. This is because $\chi_e^{eff} = \chi_e + \frac{V T_e}{\nabla T_e}$ and hence $\lim_{\nabla T_e \rightarrow \infty} \chi_e^{eff} = \chi_e$ for constant T_e . As displayed in the bottom plot of Figure 2.4, incremental diffusivity exhibits a clearer jump than for the heat flux or χ_e^{eff} . For this reason, χ_e^{inc} has been used to determine critical gradients in tokamak experiments [38].

It is important to understand the difference between steady-state and perturbative transport coefficients. Typically, cold-pulse experiments have been regarded as evidence of non-local transport on the basis that the propagation from edge to core happens faster than the diffusive time-scale (i.e. τ_E). However, diffusive times are calculated from steady-state (effective) diffusion coefficients and do not consider what happens when driving gradients and background profiles are abruptly perturbed. The variation in heat flux with changes in gradients, which really delimits how

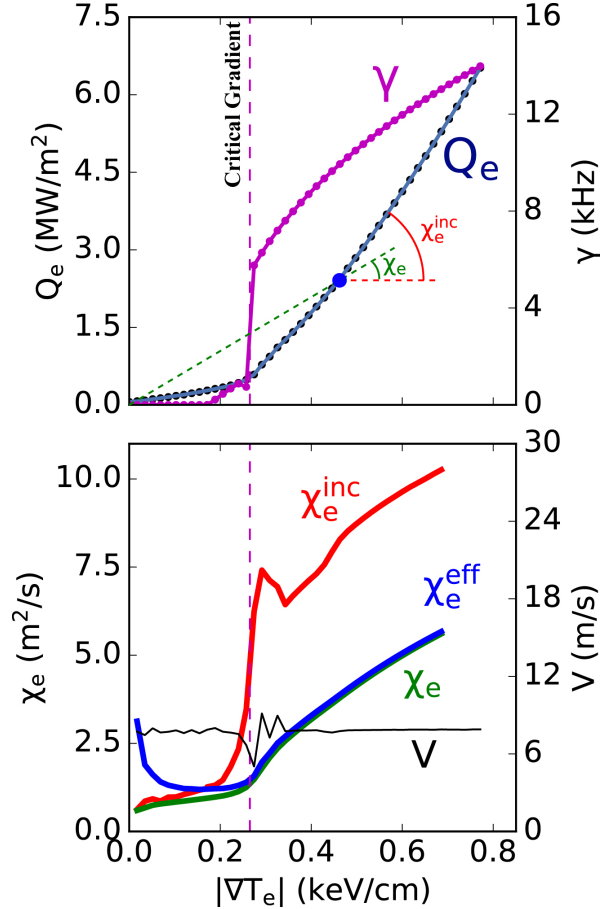


Figure 2.4: Scan of electron temperature gradient in a quasilinear turbulent transport simulation (using the TGLF-SAT1 model, to be described in Chapter 3) for the core ($\rho_N = 0.8$) of an L-mode plasma in Alcator C-Mod. (top) Evolution of the electron heat flux Q_e and linear growth rate γ of a mode with $k_\theta \rho_s = 0.6$ propagating in the electron diamagnetic direction. (bottom) Incremental, effective and power balance electron heat diffusivities, and power balance convective velocity.

fast a perturbation in temperature propagates, may be much larger than predicted from steady-state diffusion (as seen in Figure 2.4). However, fast propagation due to stiff profiles (high χ_e^{inc}) does not imply nonlocality, as it will be discussed in Section 2.3.

2.2.2 Stiff Transport

In the bottom plot of Figure 2.4, we can see that χ_e^{inc} takes very high values above the critical gradient. These high values indicate that small changes to the electron temperature gradient lead to large variations in electron heat flux. This is typically referred to as stiff transport, and a metric called “stiffness” illustrates this concept. The departure from purely “diffusive” behavior into stiff regions of the heat-flux-curve will be exceptionally important when studying the propagation of perturbations in the temperature profile.

In the following, a list of possible definitions of stiffness are provided. For detailed information on the derivation of each of them, please refer to Appendix A.1.

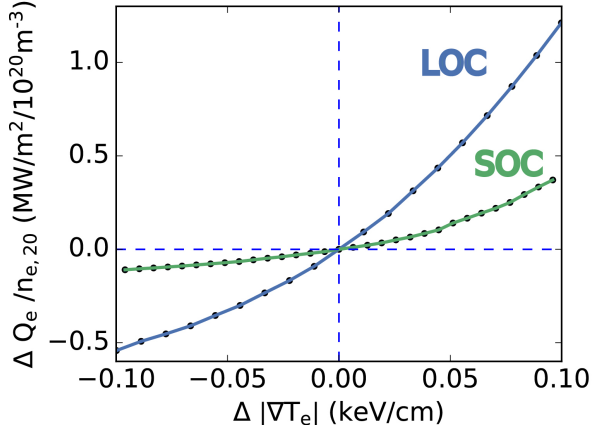
- Incremental diffusivity as a measure of stiffness: $\chi^{inc} = \frac{1}{n} \left| \frac{\partial Q}{\partial \nabla T} \right|$
- Departure from steady-state diffusivity: $S_\chi = \frac{\chi^{inc} - \chi}{\chi} = \frac{\partial \ln(Q/n - VT)}{\partial \ln \nabla T}$
- Relative flux increase: $S_T = \frac{\chi^{inc}}{\chi_{eff}} = \frac{\partial \ln Q}{\partial \ln \nabla T}$
- Normalized incremental diffusivity: $S^* = \frac{\partial Q_{GB}}{\partial a/L_T} = \chi_{GB} \cdot S_T$

As an application of these definitions, Figure 2.5 depicts the difference in simulated stiffness between two Ohmic plasmas in Alcator C-Mod. At low density the plasma is in the Linear Ohmic Confinement (LOC) regime, while at high density it is in the Saturated Ohmic Confinement (SOC) regime. These names refer to the dependence of confinement time on density (linear in LOC, following neo-Alcator scaling, and nearly constant in SOC). It is expected that SOC plasmas exhibit a higher confinement time⁴, which is consistent with these simulations because ($\chi_{SOC}^{eff} < \chi_{LOC}^{eff}$). Incremental diffusivity is significantly higher at low density, consistent with experimental work [38, 39], and all stiffness metrics exhibit this same trend.

Since the first fusion experiments, it was observed that plasmas exhibit some sort of “profile consistency”, i.e. kinetic profiles do not vary with significant changes in external heating. Generally, this suggests that transport is stiff above critical gradients and, as a consequence, kinetic profiles live near marginal stability (i.e. no matter how much input power is injected into the plasma, gradient will remain nearly unaltered).

Another direct implication of profile consistency is the core sensitivity to changes in the edge boundary condition. This is part of the motivation for this Thesis, which explores the experimental

⁴Sometimes a degradation of confinement is observed at very high densities.



Metric	LOC	SOC	$\frac{LOC}{SOC}$
χ^{eff} (m^2/s)	3.49	1.05	3.32
χ^{inc} (m^2/s)	5.17	1.13	4.58
χ (m^2/s)	2.74	0.71	3.86
V (m/s)	16.62	6.32	2.63
S_χ -	0.89	0.59	1.51
S_T -	1.48	1.07	1.38
S^* (GB)	25.02	9.43	2.65

Figure 2.5: Scan of electron temperature gradient in a quasilinear turbulent transport simulation (using the TGLF-SAT1 model, to be described in Chapter 3) for the core ($\rho_N = 0.7$) of two Ohmic plasmas in Alcator C-Mod: #1120607008 (LOC, low-density) and #1120607011 (SOC, high-density). Evolution of electron heat flux is plotted against the relative change in electron temperature gradient, and different stiffness metrics are computed and displayed in the table.

observation of edge cold pulses quickly changing core transport. If transport is very stiff, exceptionally small variations in the driving gradients can significantly increase or decrease the heat flux. This Thesis explores the possibility of capturing these fast core responses with transport models that only invoke local plasma parameters and gradients.

2.3 On the Locality of Turbulent Transport

Fast responses have been observed in a number of perturbative experiments in tokamak plasmas, and nonlocal models have been proposed to explain them. The question of whether or not nonlocal effects may be important to determine transport phenomena is essential for our understanding of magnetically-confined plasmas. The rest of this Thesis will focus on this topic, and therefore it is important to clarify the terminology used within the transport community.

Subsection 2.3.1 discusses the terminology used when referring to processes that resemble Brownian motion, even when the diffusion assumptions are not met. Subsection 2.3.2 defines the concept of locality in the transport description, and thus motivates the rest of this Thesis.

2.3.1 Diffusive *v.s.* Non-diffusive Transport

Throughout the derivation presented here and the rest of this Thesis, diffusive transport is the terminology given to transport characterized by a relationship of the form: $Q = -n\chi\nabla T$, where the heat diffusion coefficient χ is considered to be independent of the gradient ∇T and only represents a constant of proportionality ($Q \propto \nabla T$). It is important to be aware that this definition is only used here for historical reasons and that, strictly speaking, actual diffusion almost never happens in tokamak plasmas.

Diffusion is a stochastic transport process based on Brownian (random walk) motion. The basic restriction to this motion, and hence the main feature of a diffusive process, is that both the individual displacement of particles and the time steps are small, which provides the local character of diffusive processes in time and space. This idea of diffusion is, in principle, equivalent to Fourier's law of conduction, $Q = -\kappa\nabla T$, widely used in engineering and materials applications. Here, the conductivity κ can depend on the material properties and the conditions, but not on the temperature gradient.

In plasma physics, $\chi = \kappa/n$ is used as the effective heat diffusion coefficient. However, transport in tokamak plasmas is not governed by purely collisional processes. Instead, fluctuation-induced transport (based on drift-wave-type turbulence) is known to carry most of the energy exhausted in magnetically-confined plasmas. As described in Section 2.1.2, temperature and density gradients are sources of free energy for the development of instabilities that, in turn, lead to a saturated turbulence state where energy, momentum and particles are transported out of the plasma. In the description of the transport matrix given in Section 2.2, diffusion could only happen if the matrix represented in Equation 2.15 has only diagonal terms. However, we know that there are certain instabilities in magnetically confined plasmas that are excited by multiple drive terms, e.g. density gradient driven trapped electron modes (TEMs). Therefore, transport fluxes could be expected to be a function of a number of gradients that give rise to the flux, the turbulence drive and the nonlinear saturation [31]. Typically, the transport that arises from the diagonal terms in the transport matrix

is called the diffusive contribution, while the off-diagonal terms are referred to as the non-diffusive transport [40]. Likewise, the dependence of Q_e on ∇T_e is nonlinear, even when neglecting the off-diagonal terms in the transport matrix. In experiments, it has long been observed that turbulent transport exhibits a threshold-like behavior, featuring a critical gradient for the development of the drift-wave instabilities (e.g. Figure 2.4). Gyrokinetic simulations also showed that, after the critical gradient, Q_e does not exhibit a linear behavior with respect to ∇T_e .

All these observations suggest that, strictly speaking, turbulent transport in plasmas is non-diffusive, as strong non-linearities are present in the transport fluxes v.s. thermodynamic drives relation. Nevertheless, turbulent transport can provide an effective diffusion coefficient (ratio of heat flux to gradient) analogous to diffusion, i.e. random-walk estimates of transport based on collisions, when the radial correlation lengths are small compared to the system size (on the order of the ion gyro-radius) [41]. In these cases the term “diffusive transport” is sometimes used in magnetically-confined plasmas to refer to as such transport processes.

2.3.2 Local v.s. Nonlocal Transport

One of the restrictive assumptions of the diffusive transport paradigm is locality, which assumes that separated regions of the plasma do not interact, at least significantly, with each other. In this framework, local gradients are responsible for the observed heat fluxes and there is little to no influence from distant regions of the plasma. Perturbative transport phenomena are typically classified as dominated by local or nonlocal mechanisms based on the speed of propagation. This is a common misconception of the concept of locality, which does not claim anything on the promptness of the plasma response. Local transport implies that the transport state at a given position only varies with changes in the local thermodynamic variables, i.e. for nonlocal effects to exist, transport should be changed at a given position without changes in the plasma parameters at the same position and at the same time. This concept of nonlocality links back to the discussion on stiffness (and observed profile consistency) at the end of Section 2.2.2. Any transport model can yield prompt responses at long distances, but stiffness provides a mechanism for those responses to have large magnitude when changes in plasma parameters are so small that cannot be measured by actual diagnostic systems.

The formal consequence of locality in the transport description is the possibility to write an expression for the heat flux as:

$$q(x) = -\chi_{(B(x,L_c))}^{eff} n_{(B(x,L_c))} \nabla_x T_{(B(x,L_c))} \quad (2.27)$$

where L_c is the radial correlation length of transport and we have defined a ball centered at \bar{x} with radius ϵ as the set $B(\bar{x}, \epsilon) \equiv \{x \mid \|x - \bar{x}\| \leq \epsilon\}$. Measurements and simulation of radial correlation lengths in tokamak plasmas have consistently shown that the turbulence structure size scales as 5 – 10 times the ion gyroradius, ρ_i [42]. In a typical L-mode Alcator C-Mod plasma ($a \approx 22$ cm), this would suggest that $L_c < 0.5$ cm. Then $B(x, L_c) \rightarrow x$ for most core transport processes of interest

(see Ref. [22] for extensive discussion on the local limit of gyrokinetic turbulence simulations), and therefore we recover the usual expression for the heat flux as: $q_{(x)} = -\chi_{(x)}^{eff} n_{(x)} \nabla_x T_{(x)}$.

If the transport correlation length is of the order of the system's size, then Equation 2.27 breaks down and new formal expressions for the heat flux must be defined. In Ref. [43], an example of how such a description of the heat flux would look like in one dimension:

$$q = -\chi n \frac{\partial}{\partial x} \int K(x-y) T(y) dy \quad (2.28)$$

where K represents the transport kernel and accounts for the nonlocal contribution of the temperature at point y to the flux at point x .

It is important to note that the diffusive transport paradigm requires locality and short-range correlations. However, other restrictive assumptions based on Gaussianity and linearity are also needed for the standard-diffusion paradigm [44]. Because of this, non-diffusive transport (as defined in the previous section) does not necessarily imply nonlocality. If we assume that transport processes based on micro-turbulence only depend on local quantities, Equation 2.27 still holds, and the underlying transport mechanisms invoked in local gyrokinetics and quasilinear models are enough to understand and predict plasma performance.

This Thesis explores the question of whether or not nonlocal transport effects are required to explain the behavior of cold pulses. Simulations using a gradient-driven quasilinear turbulent transport model, fundamentally based on the local assumption, will reveal that nonlocal mechanisms are indeed not needed to capture the seemingly nonlocal propagation of cold pulses in tokamak plasmas.

2.4 Past Work on Cold-Pulse Experiments

Impurity injections at the edge of magnetically confined plasmas have been widely used for trace impurity transport studies [45–48], where a small number of foreign neutral particles is deposited at the periphery of the plasma and transported inwards via processes that can be modeled as diffusion and convective particle pinches. An increase in the number of injected particles can cause a sharp drop in edge electron temperature [49], predominantly driven by enhanced line-radiation of partially ionized states that live at the edge of the plasma shortly after the injection [50]. Early experiments in the TEXT tokamak [51] revealed a very fast core electron temperature increase as a result of the edge temperature drop (as shown as an example in Figure 2.6).

This seemingly exotic effect, characteristic of low collisionality plasmas [52], was readily reproduced in several other tokamaks [51–61] and helical devices [62], suggesting that the phenomenology of these effects could, in principle, be explained by robust fundamental mechanisms. In this Thesis, these phenomena will be referred to as *temperature inversions*, whereas the lack thereof will be referred to as *standard core drop*, since the expected response of the plasma core to an edge cold-pulse would be, if purely diffusive transport applies, a time-delayed temperature decrease.

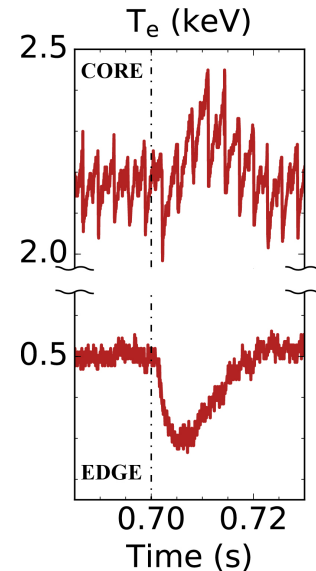


Figure 2.6: Electron temperature following edge impurity injection at low collisionality in C-Mod.

2.4.1 Relevant Experimental Observations

In the following, a summary of the main experimental observations relevant to this Thesis is presented. To the author’s knowledge, temperature inversions have been documented in TEXT [51, 63, 64], TFTR [53, 65], Tore Supra [54, 66], RTP [55, 67, 68], ASDEX Upgrade [56], JET [57], LHD [62, 69–75], HL-2A [58, 76–81], Alcator C-Mod [52, 82], KSTAR [59], J-TEXT [60, 83] and EAST [61]. Extended reviews of these phenomena and interpretations can also be found in Refs. [33, 84, 85].

Effects of Density and Plasma Current

The most commonly observed feature of temperature inversions since their discovery is the robust effect of electron density on the magnitude and threshold of the core temperature increase. At low enough density, the core electron temperature increases following the edge temperature drop, but this effect gets weaker as density increases, until it eventually disappears and the core temperature drops at higher densities.

Oftentimes, the threshold density had to be normalized to the core electron temperature to include plasmas with auxiliary heating in the same parametric scaling. In particular, experimental work in TFTR [65] first revealed a critical value of $n_e/\sqrt{T_e}$ to observe the effects for all their plasma conditions and heating input powers⁵. Later on, cold-pulse propagation studies in RTP [67] showed a clear scaling of the magnitude of the temperature inversion with electron density, which was later confirmed by experiments in ASDEX Upgrade [56]. ASDEX Upgrade experiments also noted that a correlation of the form $n_e/\sqrt{T_e}$ helped include cases with higher plasma current and electron cyclotron heating. Experiments in LHD [62, 69, 70] showed the same scaling for the amplitude of the core temperature change, and it was found that the core response exhibited a higher time delay as density increased.

On the other hand, experiments in Tore Supra [66] and Alcator C-Mod [52, 82] noted that the threshold was better described by the introduction of plasma current rather than core temperature. In Tore Supra, a threshold of the form $n_e/\sqrt{I_p}$ was determined (along with a threshold in the relative density variation), whereas $n_e \cdot q_{95}$ was preferred in Alcator C-Mod. The scaling in Alcator C-Mod came about because the reduction of the core inversion at high densities and low temperatures suggested a link with collisionality. This can be formalized with the ratio of electron-ion collision frequency and the bounce frequency [38, 86]:

$$\nu^* = \frac{\nu_{ei}}{\epsilon\omega_{be}} \propto \frac{qRZ_{eff}n_e}{T_e^2\epsilon^{3/2}} \propto n_e q R \quad (2.29)$$

where the last proportionality is constructed under the assumption that ϵ and the factor (Z_{eff}/T_e^2) do not strongly vary in the plasmas under investigation [82]. For a single device, the scaling indicates that temperature inversions have a threshold at a particular $n_e \cdot q$ value, which is found in Alcator C-Mod to include plasmas with different plasma currents [52, 82].

Another important observation relevant to this work is that cold-pulse experiments in several machines (RTP [55, 67, 68], ASDEX-U [56] and Alcator C-Mod [52]) revealed that the electron temperature “flex point” (the radial location where the electron temperature remains the same

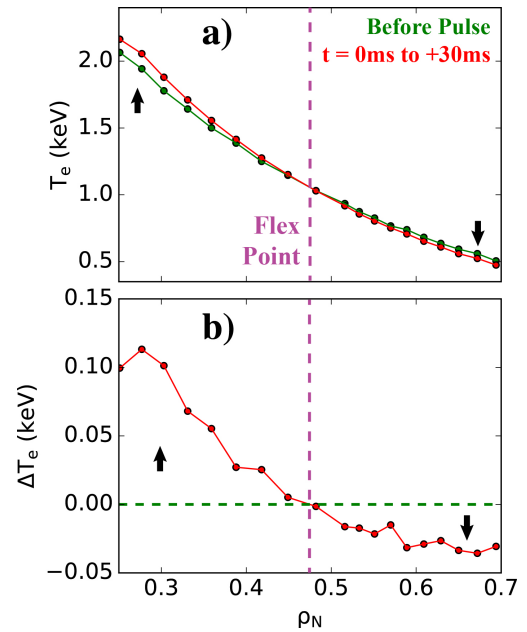


Figure 2.7: Example of flex-point in temperature profile following cold-pulse injection in DIII-D. (a) Electron temperature profile before and averaged after the cold-pulse injection, and (b) local change in electron temperature with respect to steady-state. Magenta vertical dashed line indicates location of flex-point.

⁵Interestingly, plasmas that contained Tritium exhibited an extended density range, which could not be included in the same scaling [33].

before and during the cold-pulse propagation, as shown in Figure 2.7) was linked to the safety factor profile, and that the location moves along with the rational surfaces, suggesting a connection with the current density profile.

Effects of Heating

Temperature inversions are extensively observed in Ohmic plasmas, but the effect of different auxiliary heating scenarios has also been widely studied. Early experiments in the TEXT tokamak [64] indicated that the magnitude of the relative core temperature change gets weaker with the addition of ECH input power. Experiments with addition of neutral beam power (NBI) in TFTR [65] and JET [57] showed that no inversions were observed in the NBI-heated plasmas. In contrast to TEXT and TFTR observations, experiments in Tore Supra had the opposite effect: an extended range for existence of core temperature inversions are observed in plasmas heated with Lower Hybrid waves [66]. Following the same behavior as in Tore Supra and contrary to past studies, observations in ASDEX-U [56] and HL-2A [77, 78] indicated that ECH-heated plasmas exhibited stronger edge cooling and core temperature increase. Recent experiments in KSTAR [59] also confirm that the cut-off density (density above which temperature inversions cease to be observed) is proportional to the ECH input power.

Past studies [33] noted that the temperature inversion appears when the ratio of collisional electron-ion power transfer to electron heat conduction is sufficiently small. This means that these phenomena take place when electrons and ions are thermally decoupled. This was confirmed in experiments in RTP [67], which indicated that a threshold in electron density can be found because it is then when the electrons to ions power transfer is comparable to the electron heat conduction. The importance of the ratio of electron to ion heating was also speculated after experiments in JET [57].

Connection with Intrinsic Rotation

Ohmic L-mode and RF-heated plasmas with no external net momentum input are known to exhibit intrinsic toroidal rotation. This rotation, observed in many devices [87], can be theoretically generated by interactions of turbulent residual stresses in the plasma [88]. Interestingly, work in Alcator C-Mod found that plasmas that intrinsically rotate exhibit an abrupt reversal of the rotation direction (from co-current to counter-current) at a given value of average electron density [89]. Changes in turbulence regimes, ohmic energy confinement (LOC/SOC transition) and up/down impurity density asymmetries are speculated to occur at the intrinsic rotation reversal density [52, 90].

A major experimental observation relevant to this Thesis was found in Alcator C-Mod [52] (Ohmic plasmas) and confirmed in KSTAR [59] (ECH-heated plasmas): temperature inversions disappear above the intrinsic toroidal rotation reversal density, suggesting a connection between

heat and momentum transport in perturbative experiments.

2.4.2 Modeling with Local Turbulent Transport Models

As expressed in Chapter 1, most models proposed in the literature to explain temperature inversions were phenomenological [51, 53, 63, 64, 68, 82]. However, turbulence-physics-based transport models were also suggested in past studies. These studies revealed that the core temperature increase could be explained somehow by multichannel interactions and collisional equilibration between plasma species, even though the magnitude and speed the phenomenon could not be reproduced using experimental inputs. Because these pioneering studies established the basis for the work presented in this Thesis, a brief summary of the relevant findings with these models is presented.

[Kinsey et al.](#) first proposed the use of stiff critical gradient models to simulate the fast core response to peripheral temperature perturbations. Temperature inversions in the TEXT tokamak were reproduced qualitatively by the IFS-PPPL model [92]. Electron edge cold pulses were initiated by reducing the edge boundary condition, and core electron temperature inverted in the simulations as a consequence of electron-ion equilibration and T_i/T_e effects on ITG stability. However, the magnitude of temperature inversion was smaller and significantly more delayed than in experiment. It is worth mentioning that, probably due to the lack of TEM physics in the model, steady-state predictions needed a significant enhancement of neoclassical transport to match steady-state profiles.

[Ryter et al.](#) carried out modeling of ASDEX Upgrade plasmas using the IFS-PPPL model as well, reaching qualitative agreement with experimental observations of cold-pulse behavior. However, in order to match the experimental magnitude of the core electron temperature increase, the edge perturbation was much larger in simulation than experiment. This modeling study also required a very large inwardly-propagating ion heat pulse, inconsistent with measurements of neutron rates.

[Mantica et al.](#) studied cold pulses in JET discharges, yielding similar results as previous works. Temperature inversions could be qualitatively reproduced, but the ion dynamics had to be manually altered for the effects to take place. In simulations with IFS-PPPL, ion temperature had to increase over the whole plasma in order to observe the effect on the electron temperature. Despite the importance of this modeling work, study of temperature inversions at JET has been exceptionally complicated, and the magnitude of the core temperature increase is rather small and very delayed in the few cases that was achieved.

2.4.3 Summary and Motivation for this Thesis based on Previous Work

Most experimental observations seem to indicate that core temperature inversions get stronger as direct electron heating is higher, either via electron cyclotron heating or via increased Ohmic power. In such cases, electron-ion equilibration is low, and therefore the electron channel is the main exhaust mechanism in these plasmas. Low-collisionality, electron-heated plasmas are frequently dominated by trapped electron mode (TEM) turbulence, which is strongly affected by de-trapping collisions. Hence, the scaling with normalized collisionality would be consistent with the paradigm of temperature inversions being stronger in TEM-dominated regimes.

Local modeling studies indicate that seemingly nonlocal effects could take place with stiff critical gradient models, and point to multichannel interactions as an important ingredient to reproduce these effects. However, electron dynamics as provided by ITG in these low-collisionality plasmas was not enough to reproduce both steady-state and transient behavior. TEM turbulence dynamics might be the missing piece of physics in past modeling attempts to explain temperature inversions, which is also suggested by experimental observations.

Therefore, modeling of cold-pulse dynamics will be revisited in this Thesis with the recent Trapped-Gyro-Landau-Fluid (TGLF) model, which includes trapped particle dynamics [25] and has been very successful in reproducing energy transport in steady-state [93]. Nonetheless, experiments in Alcator C-Mod [52] and KSTAR [59] suggested that temperature inversions may be related to intrinsic rotation reversals, and therefore to changes in momentum transport. Hence, this Thesis first addresses the question of whether the correlation between temperature inversions and rotation reversals is a result of actual multi-channel transport processes or is only coincidental, as discussed in the next Chapter.

Bibliography

- [1] J. Candy and R. E. Waltz. Anomalous transport scaling in the diii-d tokamak matched by supercomputer simulation. *Phys. Rev. Lett.*, 91:045001. doi: 10.1103/PhysRevLett.91.045001. URL <https://link.aps.org/doi/10.1103/PhysRevLett.91.045001>.
- [2] A J Wootton et al. Fluctuations and anomalous transport (in tokamaks, particularly TEXT). *Plasma Physics and Controlled Fusion*, 30(11):1479–1491, oct 1988. doi: 10.1088/0741-3335/30/11/010. URL <https://doi.org/10.1088/0741-3335/30/11/010>.
- [3] G D Conway. Turbulence measurements in fusion plasmas. *Plasma Physics and Controlled Fusion*, 50(12):124026, 2008. URL <http://stacks.iop.org/0741-3335/50/i=12/a=124026>.
- [4] P H Diamond et al. Zonal flows in plasma-a review. *Plasma Physics and Controlled Fusion*, 47(5): R35, 2005. URL <http://stacks.iop.org/0741-3335/47/i=5/a=R01>.
- [5] Patrick H. Diamond, Sanae-I. Itoh, and Kimitaka Itoh. *Modern Plasma Physics*, volume 1. Cambridge University Press, 2010. doi: 10.1017/CBO9780511780875. URL <https://doi.org/10.1017/CBO9780511780875>.
- [6] X. Garbet et al. Physics of transport in tokamaks. *Plasma Physics and Controlled Fusion*, 50(4): 043002, 2004. URL <http://stacks.iop.org/pp/46/B557>.
- [7] D.R. Nicholson. *Introduction to plasma theory*. Wiley series in plasma physics. Wiley, 1983. ISBN 9780471090458. URL <https://books.google.com/books?id=fyRRAAAAMAAJ>.
- [8] A. J. Brizard and T. S. Hahm. Foundations of nonlinear gyrokinetic theory. *Rev. Mod. Phys.*, 79: 421–468, Apr 2007. doi: 10.1103/RevModPhys.79.421. URL <https://link.aps.org/doi/10.1103/RevModPhys.79.421>.
- [9] Y. Camenen. Modern challenges in the gyrokinetic modeling of turbulent transport in tokamak plasmas. *ESF Exploratory Workshop*, 2013. URL <https://www.ipp.mpg.de/2058340/Camenen.pdf>.
- [10] F. Jenko. Turbulence in fusion plasmas. *HEPP Guest Lecture*, 2013. URL http://www.physics.ucla.edu/~jenko/turbulence_fusion.html.
- [11] A. Casati. A quasi-linear gyrokinetic transport model for tokamak plasmas. *PhD Thesis Universite de Provence, Aix-Marseille*, 2009. URL <https://arxiv.org/abs/1204.3254>.
- [12] H. Nordman and J. Weiland. Transport due to toroidal etai-mode turbulence in tokamaks. *Nuclear Fusion*, 29(2):251–263, feb 1989. doi: 10.1088/0029-5515/29/2/008. URL <https://doi.org/10.1088/0029-5515/29/2/008>.

- [13] J W Conner and H R Wilson. Survey of theories of anomalous transport. *Plasma Physics and Controlled Fusion*, 36(5):719, 1994. URL <http://stacks.iop.org/0741-3335/36/i=5/a=002>.
- [14] C. A. Primmerman, L. M. Lidsky, and P. A. Politzer. Trapped-electron mode in cylindrical geometry. *Phys. Rev. Lett.*, 33:957–960, Oct 1974. doi: 10.1103/PhysRevLett.33.957. URL <https://link.aps.org/doi/10.1103/PhysRevLett.33.957>.
- [15] A. Hirose. Electron temperature gradient modes in tokamaks. *Physics of Fluids B: Plasma Physics*, 2(4):850–853, 1990. doi: 10.1063/1.859272. URL <https://doi.org/10.1063/1.859272>.
- [16] P. Manz et al. Physical mechanism behind zonal-flow generation in drift-wave turbulence. *Phys. Rev. Lett.*, 103:165004, Oct 2009. doi: 10.1103/PhysRevLett.103.165004. URL <https://link.aps.org/doi/10.1103/PhysRevLett.103.165004>.
- [17] D W Ross. On standard forms for transport equations and quasilinear fluxes. *Plasma Physics and Controlled Fusion*, 34(2):137, 1992. URL <http://stacks.iop.org/0741-3335/34/i=2/a=001>.
- [18] Paulett C. Liewer. Measurements of microturbulence in tokamaks and comparisons with theories of turbulence and anomalous transport. *Nuclear Fusion*, 25(5):543–621, may 1985. doi: 10.1088/0029-5515/25/5/004. URL <https://doi.org/10.1088%2F0029-5515%2F25%2F5%2F004>.
- [19] P J Catto. Linearized gyro-kinetics. *Plasma Physics*, 20(7):719–722, jul 1978. doi: 10.1088/0032-1028/20/7/011. URL <https://doi.org/10.1088%2F0032-1028%2F20%2F7%2F011>.
- [20] T. S. Hahm. Nonlinear gyrokinetic equations for tokamak microturbulence. *The Physics of Fluids*, 31(9):2670–2673, 1988. doi: 10.1063/1.866544. URL <https://aip.scitation.org/doi/abs/10.1063/1.866544>.
- [21] Felix I Parra and Ivan Calvo. Phase-space lagrangian derivation of electrostatic gyrokinetics in general geometry. *Plasma Physics and Controlled Fusion*, 53(4):045001, feb 2011. doi: 10.1088/0741-3335/53/4/045001. URL <https://doi.org/10.1088%2F0741-3335%2F53%2F4%2F045001>.
- [22] J. Candy et al. The local limit of global gyrokinetic simulations. *Physics of Plasmas*, 11(5):L25–L28, 2004. doi: 10.1063/1.1695358. URL <https://doi.org/10.1063/1.1695358>.
- [23] R. Balescu. *Aspects of Anomalous Transport in Plasmas*. CRC Press, 2005. ISBN 9780750310307. doi: 10.1201/9781420034684. URL <https://doi.org/10.1201/9781420034684>.
- [24] G. M. Staebler et al. A theory-based transport model with comprehensive physics. *Phys. Plasmas*, 14(5):055909, 2007. URL <http://dx.doi.org/10.1063/1.2436852>.
- [25] G. M. Staebler et al. Gyro-landau fluid equations for trapped and passing particles. *Phys. Plasmas*, 12(10), 2005. URL <http://dx.doi.org/10.1063/1.2044587>.

- [26] C. Bourdelle et al. A new gyrokinetic quasilinear transport model applied to particle transport in tokamak plasmas. *Phys. Plasmas*, 14(11):112501, 2007. doi: 10.1063/1.2800869. URL <http://dx.doi.org/10.1063/1.2800869>.
- [27] P. W. Terry et al. Validation in fusion research: Towards guidelines and best practices. *Phys. Plasmas*, 15(6), 2008. URL <http://dx.doi.org/10.1063/1.2928909>.
- [28] Martin Greenwald. Verification and validation for magnetic fusion. *Phys. Plasmas*, 17(5):058101, 2010. doi: 10.1063/1.3298884. URL <http://dx.doi.org/10.1063/1.3298884>.
- [29] P. Rodriguez-Fernandez et al. Vitals: A surrogate-based optimization framework for the accelerated validation of plasma transport codes. *Fusion Science and Technology*, 74(1-2):65–76, 2018. doi: 10.1080/15361055.2017.1396166. URL <https://doi.org/10.1080/15361055.2017.1396166>.
- [30] J. Candy et al. Tokamak profile prediction using direct gyrokinetic and neoclassical simulation. *Phys. Plasmas*, 16(6):060704, 2009. doi: 10.1063/1.3167820. URL <http://dx.doi.org/10.1063/1.3167820>.
- [31] N J Lopes Cardozo. Perturbative transport studies in fusion plasmas. 37(8):799–852, aug 1995. doi: 10.1088/0741-3335/37/8/001. URL <https://doi.org/10.1088/0741-3335/37/8/001>.
- [32] C Bourdelle. Turbulent particle transport in magnetized fusion plasma. *Plasma Physics and Controlled Fusion*, 47(5A):A317–A326, apr 2005. doi: 10.1088/0741-3335/47/5a/023. URL <https://doi.org/10.1088/0741-3335/47/5a/023>.
- [33] J D Callen and M W Kissick. Evidence and concepts for non-local transport. *Plasma Phys. Control. Fusion*, 39(12B):B173, 1997. URL <http://stacks.iop.org/0741-3335/39/i=12B/a=014>.
- [34] R. E. Stockdale et al. *Bull. Am. Phys. Soc.*, 31(1535), 1986.
- [35] J.D. Callen et al. Modelling of temperature profiles and transport scaling in auxiliary heated tokamaks. *Nucl. Fusion*, 27(11):1857, 1987. URL <http://stacks.iop.org/0029-5515/27/i=11/a=010>.
- [36] J. C. DeBoo et al. Electron profile stiffness and critical gradient studies. *Physics of Plasmas*, 19(8):082518, 2012. doi: 10.1063/1.4750061. URL <https://doi.org/10.1063/1.4750061>.
- [37] M. W. Brookman et al. Experimental measurement of ech deposition broadening: Beyond anomalous transport. *EPJ Web Conf.*, 147:03001, 2017. doi: 10.1051/epjconf/201714703001. URL <https://doi.org/10.1051/epjconf/201714703001>.

- [38] F. Ryter et al. Experimental study of trapped-electron-mode properties in tokamaks: Threshold and stabilization by collisions. *Phys. Rev. Lett.*, 95:085001, Aug 2005. doi: 10.1103/PhysRevLett.95.085001. URL <https://link.aps.org/doi/10.1103/PhysRevLett.95.085001>.
- [39] A.J. Creely et al. Validation study of gene on asdex upgrade using perturbative thermal diffusivity measured with partial sawtooth heat pulses. *Nuclear Fusion*, 58(12):126001, 2018. URL <http://stacks.iop.org/0029-5515/58/i=12/a=126001>.
- [40] M. Kikuchi et al. *Fusion Physics*. International Atomic Energy Agency, Vienna, 2012. URL <http://www-pub.iaea.org/books/IAEABooks/8879/Fusion-Physics>.
- [41] T.C. Luce et al. Experimental challenges to stiffness as a transport paradigm. *Nuclear Fusion*, 58(2):026023, jan 2018. doi: 10.1088/1741-4326/aa9af7. URL <https://doi.org/10.1088/2F1741-4326%2Faa9af7>.
- [42] T. L. Rhodes et al. Comparison of turbulence measurements from diiii-d low-mode and high-performance plasmas to turbulence simulations and models. *Physics of Plasmas*, 9(5):2141–2148, 2002. doi: 10.1063/1.1464544. URL <https://doi.org/10.1063/1.1464544>.
- [43] D. del Castillo-Negrete et al. Fractional diffusion models of non-local perturbative transport: numerical results and application to jet experiments. *Nuclear Fusion*, 48(7):075009, 2008. URL <http://stacks.iop.org/0029-5515/48/i=7/a=075009>.
- [44] D. del Castillo-Negrete et al. Nondiffusive transport in plasma turbulence: A fractional diffusion approach. *Phys. Rev. Lett.*, 94:065003, Feb 2005. doi: 10.1103/PhysRevLett.94.065003. URL <https://link.aps.org/doi/10.1103/PhysRevLett.94.065003>.
- [45] J. F. Friichtenicht. Laser-generated pulsed atomic beams. *Review of Scientific Instruments*, 45(1): 51–56, 1974. doi: 10.1063/1.1686447. URL <https://doi.org/10.1063/1.1686447>.
- [46] E. S. Marmor et al. System for rapid injection of metal atoms into plasmas. *Review of Scientific Instruments*, 46(9):1149–1154, 1975. doi: 10.1063/1.1134432. URL <https://doi.org/10.1063/1.1134432>.
- [47] N. T. Howard et al. Characterization of impurity confinement on alcator c-mod using a multi-pulse laser blow-off system. *Rev. Sci. Instrum*, 82(3), 2011. URL <http://dx.doi.org/10.1063/1.3565448>.
- [48] J.E. Rice et al. Core impurity transport in alcator c-mod l-, i- and h-mode plasmas. *Nucl. Fusion*, 55(3):033014, 2015. URL <http://stacks.iop.org/0029-5515/55/i=3/a=033014>.
- [49] M.W. Kissick et al. Transient electron heat diffusivity obtained from trace impurity injection on tftr. *Nucl. Fusion*, 34(3):349, 1994. URL <http://stacks.iop.org/0029-5515/34/i=3/a=I03>.
- [50] T. S. Pedersen et al. Edge x-ray imaging measurements of plasma edge in alcator c-mod. *Rev. Sci. Instrum*, 70(1):586–590, 1999. URL <http://dx.doi.org/10.1063/1.1149487>.

- [51] K. W. Gentle et al. Strong nonlocal effects in a tokamak perturbative transport experiment. *Phys. Rev. Lett.*, 74:3620–3623, 1995. URL <https://link.aps.org/doi/10.1103/PhysRevLett.74.3620>.
- [52] J.E. Rice et al. Non-local heat transport, rotation reversals and up/down impurity density asymmetries in alcator c-mod ohmic l-mode plasmas. *Nucl. Fusion*, 53(3):033004, 2013. URL <http://stacks.iop.org/0029-5515/53/i=3/a=033004>.
- [53] M.W. Kissick et al. Non-local component of electron heat transport in tftr. *Nucl. Fusion*, 36(12):1691, 1996. URL <http://stacks.iop.org/0029-5515/36/i=12/a=I09>.
- [54] T. Dudok de Wit et al. Self-consistent removal of sawtooth oscillations from transient plasma data by generalized singular value decomposition. *Phys. Plasmas*, 5(5):1360–1368, 1998. URL <https://doi.org/10.1063/1.872796>.
- [55] P. Mantica et al. Nonlocal transient transport and thermal barriers in rijnhuizen tokamak project plasmas. *Phys. Rev. Lett.*, 82:5048–5051, 1999. URL <https://link.aps.org/doi/10.1103/PhysRevLett.82.5048>.
- [56] F. Ryter et al. Propagation of cold pulses and heat pulses in asdex upgrade. *Nucl. Fusion*, 40(11):1917, 2000. URL <http://stacks.iop.org/0029-5515/40/i=11/a=311>.
- [57] P Mantica et al. Perturbative transport experiments in jet low or reverse magnetic shear plasmas. *Plasma Phys. Control. Fusion*, 44(10):2185, 2002. URL <http://stacks.iop.org/0741-3335/44/i=10/a=308>.
- [58] H.J. Sun et al. Observation of non-local transport phenomena with SMBI in HL-2a. *Chinese Physics Letters*, 24(9):2621–2623, aug 2007. doi: 10.1088/0256-307x/24/9/044. URL <https://doi.org/10.1088/0256-307x/24/9/044>.
- [59] Y.J. Shi et al. Intrinsic rotation reversal, non-local transport, and turbulence transition in kstar l-mode plasmas. *Nuclear Fusion*, 57(6):066040, 2017. URL <http://stacks.iop.org/0029-5515/57/i=6/a=066040>.
- [60] Yuejiang Shi et al. Observation of multi-channel non-local transport in j-text plasmas. *Nuclear Fusion*, 58(4):044002, 2018. URL <http://stacks.iop.org/0029-5515/58/i=4/a=044002>.
- [61] Yong Liu et al. Dynamics of cold pulses induced by super-sonic molecular beam injection in the EAST tokamak. *Nuclear Fusion*, 59(4):044005, mar 2019. doi: 10.1088/1741-4326/ab0665. URL <https://doi.org/10.1088/1741-4326/ab0665>.
- [62] N. Tamura et al. Observation of core electron temperature rise in response to an edge cooling in toroidal helical plasmas. *Physics of Plasmas*, 12(11):110705, 2005. doi: 10.1063/1.2131047. URL <https://doi.org/10.1063/1.2131047>.

- [63] K. W. Gentle et al. An experimental counter-example to the local transport paradigm. *Phys. Plasmas*, 2(6):2292–2298, 1995. URL <http://dx.doi.org/10.1063/1.871252>.
- [64] K. W. Gentle et al. The evidence for nonlocal transport in the texas experimental tokamak. *Phys. Plasmas*, 4(10):3599–3613, 1997. URL <http://dx.doi.org/10.1063/1.872255>.
- [65] M.W. Kissick et al. Conditions and behaviour related to non-local electron heat transport on tfttr. *Nucl. Fusion*, 38(6):821, 1998. URL <http://stacks.iop.org/0029-5515/38/i=6/a=304>.
- [66] X L Zou et al. *Plasma Physics and Controlled Fusion*, 42(10):1067–1076, oct 2000. doi: 10.1088/0741-3335/42/10/305. URL <https://doi.org/10.1088%2F0741-3335%2F42%2F10%2F305>.
- [67] P Galli et al. Non-local response of rtp ohmic plasmas to peripheral perturbations. *Nuclear Fusion*, 39(10):1355–1368, oct 1999. doi: 10.1088/0029-5515/39/10/301. URL <https://doi.org/10.1088%2F0029-5515%2F39%2F10%2F301>.
- [68] G M D Hogeweij et al. Recording non-local temperature rise in the RTP tokamak. *Plasma Physics and Controlled Fusion*, 42(10):1137–1144, oct 2000. doi: 10.1088/0741-3335/42/10/310. URL <https://doi.org/10.1088%2F0741-3335%2F42%2F10%2F310>.
- [69] S Inagaki et al. Abrupt reduction of core electron heat transport in response to edge cooling on the large helical device. *Plasma Phys. Control. Fusion*, 48(5A):A251, 2006. URL <http://stacks.iop.org/0741-3335/48/i=5A/a=S23>.
- [70] N. Tamura et al. Impact of nonlocal electron heat transport on the high temperature plasmas of lhd. *Nucl. Fusion*, 47(5):449, 2007. URL <http://stacks.iop.org/0029-5515/47/i=5/a=009>.
- [71] N. Tamura et al. Edge-core interaction revealed with dynamic transport experiment in lhd (exc/p8-16). *International Atomic Energy Agency (IAEA), (IAEA-CN-180)*, 2010. URL http://www-pub.iaea.org/MTCD/Meetings/PDFplus/2010/cn180/cn180_BookOfAbstracts.pdf.
- [72] S Inagaki et al. Characterization of bifurcation induced by long distance correlation between heat flux and temperature gradient in toroidal plasmas. *Plasma Physics and Controlled Fusion*, 52(7):075002, may 2010. doi: 10.1088/0741-3335/52/7/075002. URL <https://doi.org/10.1088%2F0741-3335%2F52%2F7%2F075002>.
- [73] S. Inagaki et al. Observation of long-distance radial correlation in toroidal plasma turbulence. *Phys. Rev. Lett.*, 107:115001, 2011. URL <https://link.aps.org/doi/10.1103/PhysRevLett.107.115001>.
- [74] R O Dendy et al. Modelling the measured local time evolution of strongly nonlinear heat pulses in the large helical device. *Plasma Physics and Controlled Fusion*, 55(11):115009, oct 2013. doi: 10.1088/0741-3335/55/11/115009. URL <https://doi.org/10.1088%2F0741-3335%2F55%2F11%2F115009>.

- [75] H. Zhu et al. A quantitative model for heat pulse propagation across large helical device plasmas. *Physics of Plasmas*, 22(6):062308, 2015. doi: 10.1063/1.4923307. URL <https://doi.org/10.1063/1.4923307>.
- [76] X.R. Duan et al. Overview of experimental results on hl-2a. *Nucl. Fusion*, 49(10):104012, 2009. URL <http://stacks.iop.org/0029-5515/49/i=10/a=104012>.
- [77] Hong-Juan Sun et al. Experiment of non-local effect with smbi on hl-2a. *Plasma Phys. Control. Fusion*, 52(4):045003, 2010. URL <http://stacks.iop.org/0741-3335/52/i=4/a=045003>.
- [78] H.J. Sun et al. Experimental evidence of the non-local response of transport to peripheral perturbations. *Nuclear Fusion*, 51(11):113010, oct 2011. doi: 10.1088/0029-5515/51/11/113010. URL <https://doi.org/10.1088/0029-5515/51/11/113010>.
- [79] O. Pan et al. Evidence of enhanced self-organized criticality (soc) dynamics during the radially non-local transient transport in the hl-2a tokamak. *Nucl. Fusion*, 55(11):113010, 2015. URL <http://stacks.iop.org/0029-5515/55/i=11/a=113010>.
- [80] W. Chen et al. Dynamics between the fishbone instability and nonlocal transient transport in hl-2a nbi plasmas. *Nucl. Fusion*, 56(4):044001, 2016. URL <http://stacks.iop.org/0029-5515/56/i=4/a=044001>.
- [81] X Q Ji et al. On the interplay between neoclassical tearing modes and nonlocal transport in toroidal plasmas. *Scientific Reports*, 6:32697, 2016. URL <https://www.nature.com/articles/srep32697>.
- [82] C. Gao et al. Non-local heat transport in alcator c-mod ohmic l-mode plasmas. *Nucl. Fusion*, 54(8):083025, 2014. URL <http://stacks.iop.org/0029-5515/54/i=8/a=083025>.
- [83] Y. J. Shi et al. Observation of non-local effects in ion transport channel in j-text plasmas. *arXiv:1810.07529*, 2018. URL <https://arxiv.org/abs/1810.07529>.
- [84] V D Pustovitov. Nonlocal effects in energy balance in an equilibrium plasma during its fast heating/cooling in tokamaks and stellarators. *Plasma Physics and Controlled Fusion*, 54(12):124036, nov 2012. doi: 10.1088/0741-3335/54/12/124036. URL <https://doi.org/10.1088/0741-3335/54/12/124036>.
- [85] K. Ida et al. Towards an emerging understanding of non-locality phenomena and non-local transport. *Nucl. Fusion*, 55(1):013022, 2015. URL <http://stacks.iop.org/0029-5515/55/i=1/a=013022>.
- [86] G.D. Conway et al. Observations on core turbulence transitions in asdex upgrade using doppler reflectometry. *Nuclear Fusion*, 46(9):S799, 2006. URL <http://stacks.iop.org/0029-5515/46/i=9/a=S15>.

- [87] J.E. Rice et al. Inter-machine comparison of intrinsic toroidal rotation in tokamaks. *Nuclear Fusion*, 47(11):1618–1624, oct 2007. doi: 10.1088/0029-5515/47/11/025. URL <https://doi.org/10.1088/0029-5515/47/11/025>.
- [88] P.H. Diamond et al. Physics of non-diffusive turbulent transport of momentum and the origins of spontaneous rotation in tokamaks. *Nuclear Fusion*, 49(4):045002, mar 2009. doi: 10.1088/0029-5515/49/4/045002. URL <https://doi.org/10.1088/0029-5515/49/4/045002>.
- [89] J.E. Rice et al. Observations of core toroidal rotation reversals in alcator c-mod ohmic l-mode plasmas. *Nuclear Fusion*, 51(8):083005, jun 2011. doi: 10.1088/0029-5515/51/8/083005. URL <https://doi.org/10.1088/0029-5515/51/8/083005>.
- [90] C. Angioni et al. Intrinsic toroidal rotation, density peaking, and turbulence regimes in the core of tokamak plasmas. *Phys. Rev. Lett.*, 107:215003, Nov 2011. doi: 10.1103/PhysRevLett.107.215003. URL <https://link.aps.org/doi/10.1103/PhysRevLett.107.215003>.
- [91] J. E. Kinsey et al. Theoretical transport modeling of ohmic cold pulse experiments. *Phys. Plasmas*, 5(11):3974–3981, 1998. URL <http://dx.doi.org/10.1063/1.873117>.
- [92] M. Kotschenreuther et al. Quantitative predictions of tokamak energy confinement from first-principles simulations with kinetic effects. *Physics of Plasmas*, 2(6):2381–2389, 1995. doi: 10.1063/1.871261. URL <https://doi.org/10.1063/1.871261>.
- [93] J.E. Kinsey et al. Iter predictions using the gyro verified and experimentally validated trapped gyro-landau fluid transport model. *Nuclear Fusion*, 51(8):083001, 2011. URL <http://stacks.iop.org/0029-5515/51/i=8/a=083001>.

Chapter 3

Experimental and Modeling Techniques

“In general we look for a new law by the following process. First we guess it. Then we compute the consequences of the guess to see what would be implied if this law that we guessed is right. Then we compare the result of the computation to nature, with experiment or experience, compare it directly with observation, to see if it works. If it disagrees with experiment it is wrong. In that simple statement is the key to science. It does not make any difference how beautiful your guess is. It does not make any difference how smart you are, who made the guess, or what his name is - if it disagrees with experiment it is wrong.”

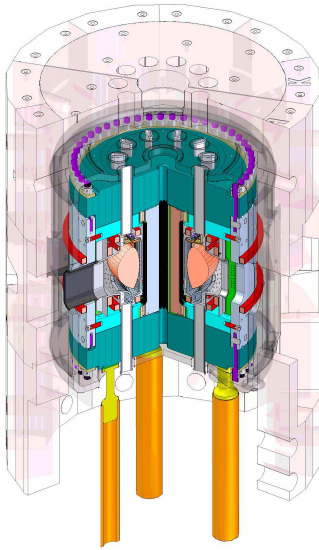
R. P. Feynman, 1964

This Thesis addresses the question of whether multi-channel interactions and stiff transport models are capable of reproducing the seemingly exotic behavior of cold-pulse propagation in magnetically-confined plasmas. In order to do so, perturbative transport experiments were first performed in the Alcator C-Mod tokamak, and cold-pulse behavior was characterized. Then, simulations were performed with the quasilinear TGLF reduced transport model and the TRANSP integrated modeling suite. Once a model of perturbation was found consistent with observations in C-Mod, predictions were performed for a different machine, DIII-D. New experiments were designed and run in DIII-D to test these predictions and further validate and answer open questions in the model.

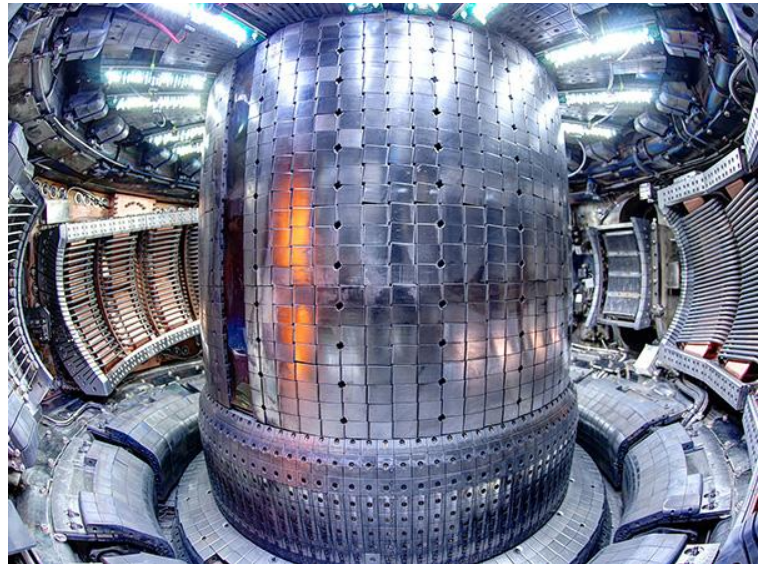
This Chapter introduces the experimental set-up, i.e. the Alcator C-Mod (Section 3.1) and DIII-D (Section 3.2) tokamaks, with emphasis on the laser blow-off technique used to introduce perturbations at the edge of the plasma. The quasilinear TGLF reduced transport model [1–3] is then described in Section 3.3, and the TRANSP integrated modeling framework [4, 5] is presented in Section 3.4. The chapter ends with a description of the specific techniques used to run perturbative transport simulations in TRANSP.

3.1 Alcator C-Mod tokamak

The Alcator C-Mod tokamak [6] is a diverted, high-field, compact, experimental fusion device with major radius $R = 0.67$ m and typical minor radius $a \approx 0.22$ m. Alcator C-Mod is the last of a series of high-field compact devices at the Massachusetts Institute of Technology, and, among many breakthroughs, it achieved world record plasma pressure in its last day of operation in 2016, with volume average core plasma pressure of $\langle p \rangle \approx 2.1$ atm [7]. Alcator C-Mod has high-Z materials (molybdenum and tungsten) for plasma facing components. Figure 3.1 sketches the Alcator C-Mod tokamak.



(a) Engineering diagram. Source: [Wikimedia Commons](#).



(b) Interior of Alcator C-Mod. Source: [Wikimedia Commons](#).

Figure 3.1: Illustrations of the Alcator C-Mod tokamak.

All experiments reported here were performed with deuterium L-mode plasmas with toroidal magnetic field $B_T = 5.4$ T, although Alcator C-Mod could run magnetic fields up to $B_T = 8.0$ T. It could run with plasma currents up to $I_p = 2.0$ MA, and auxiliary power systems included ion cyclotron heating ($F_{ICH} = 50 - 80$ MHz) up to $P_{ICH} = 6$ MW, and lower hybrid ($F_{LH} = 4.6$ GHz) up to $P_{LH} = 1$ MW. Densities in Alcator C-Mod ranged from $\bar{n}_e = 0.2 \cdot 10^{20} \text{m}^{-3}$ up to $\bar{n}_e = 5.0 \cdot 10^{20} \text{m}^{-3}$.

3.1.1 Relevant Diagnostic Systems in Alcator C-Mod

In the work presented in this Thesis, electron temperature traces were measured with a fast time-resolution ECE grating polychromator (GPC) with 9 spatial channels [8]. Despite lower time resolution, electron temperature measurements from a Thomson Scattering (TS) system [9] were also used to reconstruct temperature profiles. The same Thomson Scattering diagnostic provided

localized electron density measurements, and average electron densities were determined from line-integrated measurements of a 10-channel two-color interferometer (TCI) [10]. Ion (argon) temperature and toroidal rotation profiles were measured by a high-resolution imaging x-ray spectrometer (XICS) system [11, 12]. Soft x-ray emission is collected using four soft x-ray arrays (SXR) of 38 chords with high spatial and temporal resolution [13], and high time resolution total radiated power was measured by an absolute extreme ultraviolet (AXUV) bolometer [14].

Cold pulses are produced in the edge of Alcator C-Mod plasmas using a laser blow-off (LBO) system [15] that is able to introduce non-recycling impurities that abruptly decrease the edge temperature of the plasma by radiative cooling, facilitating perturbative transport studies. Spatial and temporal localization of the source of impurities is ensured by the use of non-recycling materials [15]. The LBO system used in Alcator C-Mod is comprised by a Nd:YAG pulsed laser (1064 nm, 680 mJ) with a rate up to 10 Hz, coupled with a remotely steerable piezo-electric mirror mount to inject multiple times in the same plasma discharge. The amount of neutral impurity particles that reach the plasma is controlled with an optical iris and a translational stage. In the Alcator C-Mod experiments presented here, calcium fluoride (CaF_2) was used as the LBO impurity.

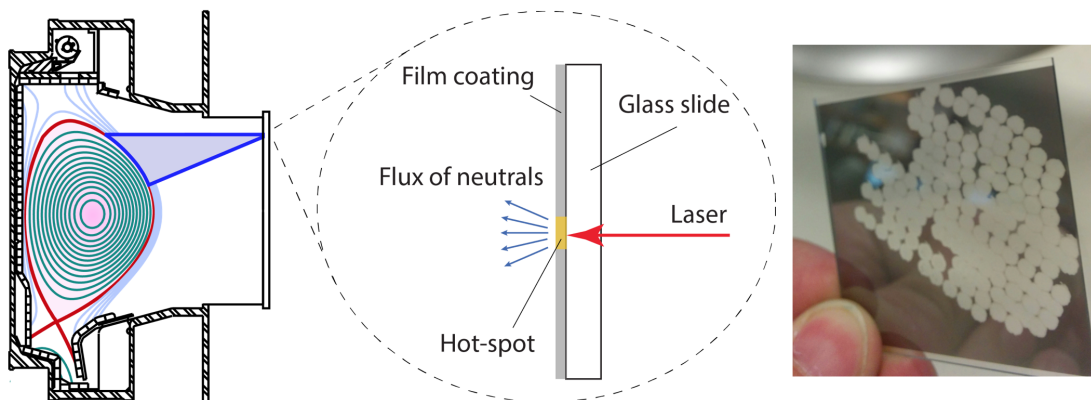


Figure 3.2: Diagram of laser blow-off operation in Alcator C-Mod. First, a laser is used to ablate a thin coating on a glass slide, which creates a flux of neutral particles directed towards the edge of the plasma. Many ablations can be performed on the same slide, allowing the injection of various cold pulses during the same discharge, limited to the laser firing rate (10 Hz in Alcator C-Mod).

Figure 3.2 summarizes the general operation of LBO. Typically, laser blow-off systems are used for impurity transport studies, where only trace amounts of non-intrinsic impurities are introduced at the edge of the plasma. Inferences of impurity confinement times and transport coefficients are made by running impurity transport simulations (like the STRAHL code [16]) until measured and simulated radiation signals match. In such experiments, only non-perturbative trace amounts of impurities are introduced ($< 10\%$ change in electron temperature and density [15]), so as to ensure that measured properties are an indication of the background, un-perturbed plasma. In perturbative transport experiments (such as those performed in this Thesis), large amounts of impurities are introduced in order to locally perturb the electron temperature (and inevitably also

density), hence generating a cold pulse at the edge via radiative cooling.

3.2 DIII-D tokamak

The DIII-D tokamak [17] is a diverted, medium-size, moderate-field experimental device with major radius $R = 1.67$ m and typical minor radius $a \approx 0.67$ m. Following the success of the Doublet magnetic fusion experiments series, DIII-D started operation at General Atomics in 1986, and continues to operate as of 2019. It has an all-carbon wall. Figure 3.3 sketches the DIII-D tokamak.

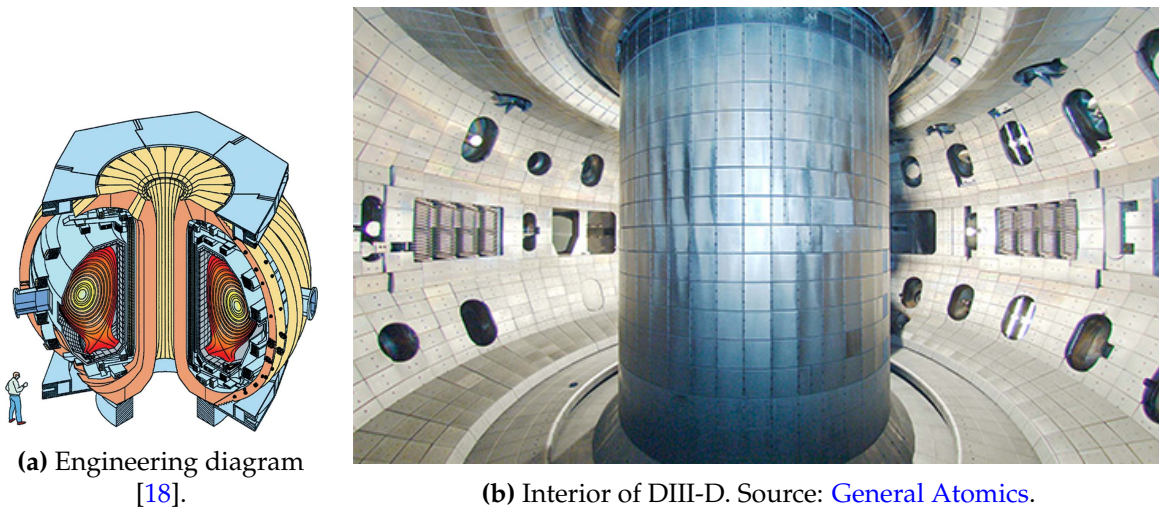


Figure 3.3: Illustrations of the DIII-D tokamak.

All experiments reported here were performed with deuterium L-mode plasmas with toroidal magnetic field $B_T = 2.0$ T, although DIII-D can typically operate up to $B_T = 2.2$ T. The maximum plasma current achievable is limited by hardware constraints to $I_p = 3.0$ MA. Auxiliary power in DIII-D is commonly provided by neutral beams (up to $P_{NBI} = 20$ MW) and electron cyclotron heating (up to $P_{ECH} = 6$ MW). However, in the DIII-D experiments presented in this Thesis, no auxiliary power was used. The interested reader is encouraged to read more about the DIII-D tokamak in Ref. [17].

3.2.1 Relevant Diagnostic Systems in DIII-D

Electron temperature traces were measured with a fast time-resolution ECE radiometer [19]. High time resolution electron density traces were measured with a density profile reflectometer [20]. Ion (carbon) temperature, impurity density and toroidal rotation profile were measured with a charge exchange recombination (CER) system [21, 22]. Electron density fluctuations and perpendicular velocity are measured by a multi-channel Doppler backscattering (DBS) system [23].

To trigger cold pulses, and in the same way as in Alcator C-Mod tokamak experiments, a laser

blow-off (LBO) system is used to introduce non-intrinsic non-recycling impurities to reduce the edge electron temperature. In the DIII-D experiment, aluminum (Al) is chosen as the LBO impurity.

3.2.2 Remarks on Differences between Alcator C-Mod and DIII-D Tokamaks

Cold-pulse propagation studies were performed in both Alcator C-Mod and DIII-D plasmas, which exhibit very different features. In terms of size, Alcator C-Mod is a small, compact device with total plasma volume $V_p \approx 1.0 \text{ m}^3$. DIII-D, instead, is a medium-size tokamak with $V_p \approx 20.0 \text{ m}^3$. The differences in size and geometry are displayed in Figure 3.4. Plasma-facing materials are also quite different between the two devices: high-Z (molybdenum and tungsten) in C-Mod, and low-Z (carbon) in DIII-D.

Low-collisionality experiments to study cold pulses in Alcator C-Mod will be performed with $B_T = 5.4 \text{ T}$ and $\bar{n}_e \approx 8.0 \cdot 10^{19} \text{ m}^{-3}$. On the other hand, DIII-D experiments will have $B_T = 2.0 \text{ T}$ and $\bar{n}_e \approx 1.0 \cdot 10^{19} \text{ m}^{-3}$. Because of the different sizes compensating the differences in line-average densities, both experiments will operate with the same Greenwald fraction of $f_G \approx 0.15$. Safety factors will be $q_{95} \approx 5.1$ in DIII-D and $q_{95} \approx 4.3$ in Alcator C-Mod at the time of the laser blow-off injections. Energy confinement times in the Ohmic low-collisionality L-mode experiments performed in this work were measured to be $\tau_E \approx 25 \text{ ms}$ in Alcator C-Mod and $\tau_E \approx 60 \text{ ms}$ in DIII-D.

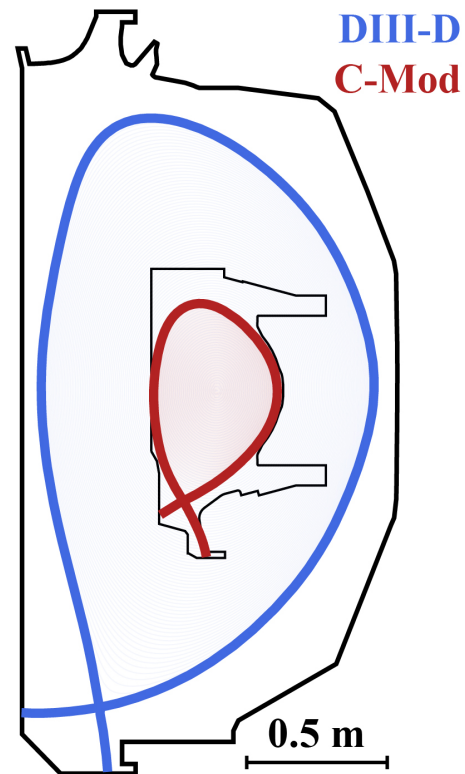


Figure 3.4: Equilibrium reconstructions of Alcator C-Mod and DIII-D tokamaks and vacuum vessel layouts.

3.3 The Trapped Gyro-Landau Fluid (TGLF) Model

In the transport simulations presented in Chapter 5 and Chapter 6, to study cold-pulse propagation dynamics, a quasilinear transport approach is taken. Section 2.1.4 introduced the quasilinear approximation, and derived a convenient form of quasilinear fluxes as:

$$Q_\alpha^{ql} = \left(\frac{3}{2} \frac{1}{n_e T_e} \right) \cdot \sum_{k_y} \left[\frac{\Re \langle i k_y \tilde{\Phi}^* \tilde{p}_\alpha \rangle}{\langle \tilde{\Phi}^* \tilde{\Phi} \rangle} \cdot \bar{\Phi}^2 \right] \quad (3.1)$$

where $Q_\alpha^{ql} = Q_\alpha / Q_{unit}^{GB}$ represents the quasilinear gyro-reduced flux for each species α , normalized by the gyro-Bohm unit $Q_{unit}^{GB} = n_e T_e c_s (\rho_s / a)^2$. The gyro-reduced intensity of the electrostatic potential fluctuations is defined as $\bar{\Phi}^2 = \tilde{\Phi}^2 / (\rho_s / a)^2 = (e\tilde{\phi} / T_e)^2 / (\rho_s / a)^2$.

The first term in the summation corresponds to the linear response of a mode with normalized poloidal wavenumber k_y , and can be cast, along with constant pre-factors, as $\mathcal{L}_{k_y}(\tilde{\Phi}, \tilde{p}_\alpha)$. Therefore the energy fluxes for electron and ion species result:

$$\begin{aligned} Q_e^{ql} &= \sum_{k_y} \mathcal{L}_{k_y}(\tilde{\Phi}, \frac{\tilde{p}_e}{p_e}) \cdot \bar{\Phi}^2 \\ Q_i^{ql} &= \frac{p_i}{p_e} \cdot \sum_{k_y} \mathcal{L}_{k_y}(\tilde{\Phi}, \frac{\tilde{p}_i}{p_i}) \cdot \bar{\Phi}^2 \end{aligned} \quad (3.2)$$

Hence, in order to evaluate the quasilinear heat fluxes as given by Equations 3.2, one needs to calculate the linear responses $\mathcal{L}_{k_y}(\tilde{\Phi}, \frac{\tilde{p}_\alpha}{p_\alpha})$, as well as the saturated intensity of potential fluctuations, $\bar{\Phi}^2$. In the following, descriptions of the linear problem and saturation rule in the Trapped-Gyro-Landau-Fluid (TGLF) model are provided. The following discussion about TGLF does not intend to be exhaustive and is a summary of what is found in Refs. [1, 2, 24–26].

3.3.1 Linear problem in TGLF

The TGLF model approximates the linear eigenmodes for gyrokinetic drift-wave instabilities by solving a system of velocity moments of the gyro-averaged kinetic equation [1]. It includes finite Larmor radius effects (hence the ‘‘gyro’’ in the name) and it captures unstable trapped ion and electron modes (TIM, TEM), ion and electron temperature gradient modes (ITG, ETG) and kinetic-ballooning modes (KBM). As indicated in Section 2.4, inclusion of comprehensive trapped electron mode physics in TGLF is crucial to reproduce cold-pulse dynamics (in particular, temperature inversions observed in low collisionality conditions).

The derivation of the TGLF moment equations starts from the linearized electrostatic gyrokinetic equation, which can be written for the fluctuating gyroaveraged distribution function \tilde{f} as [1]:

$$\left(\frac{\partial}{\partial t} + v_\parallel \nabla_\parallel + i\omega_{dv} \right) \tilde{f} = \left(-v_\parallel \nabla_\parallel - i\omega_{dv} + i\omega_*^T \right) f_0 J_0 \frac{e\tilde{\phi}}{T} \quad (3.3)$$

where f_0 is the equilibrium distribution function, J_0 is a Bessel function that accounts for finite Larmor radius (FLR) effects, ω_{dv} represents perpendicular curvature and centrifugal drifts, and ω_*^T contains the driving pressure gradients.

At the time of writing this thesis, TGLF uses 6 moments of Equation 3.3 for each circulating species (density n , parallel velocity u_{\parallel} , parallel pressure p_{\parallel} , total pressure p , parallel energy flux Q_{\parallel} and total energy flux Q) for the entire velocity space and for the trapped region only, and 3 for trapped species (n^t , p_{\parallel}^t , p^t). This results in 15 moments for each plasma species, which make use of the ballooning transformation and are detailed in Ref. [1]. This system of velocity moments is closed by expressing the higher moments as linear combinations of the lower moments, which is similar to the method presented in Ref. [27]. Kinetic effects, like Landau damping, are retained in this gyro-fluid formulation by fitting the closure coefficients to the exact kinetic response. In TGLF, because trapped particles are included, the closure coefficients are functions of the trapped fraction and, compared to its predecessor GLF23, it requires a more exact treatment of the finite Larmor radius effects to be valid for all wavenumbers. As discussed in Section 2.4, and as will be shown in later chapters, these corrections to treat trapped particle physics and kinetic effects (that differentiate TGLF from past models) will provide the physics needed for the temperature inversion effect to be captured in simulations.

These equations are transformed into a linear eigenmode system and solved using a finite series of Hermite polynomials with complex coefficients to expand the velocity moments and the electrostatic potential. Solution of this eigenvalue problem provides growth rates (γ) and real frequencies (ω) at each normalized poloidal wavenumber (k_y) for the unstable modes in the plasma. Figure 3.5 shows an example of TGLF linear growth rate and real frequency spectra in the core ($\rho_N = 0.4$) of a modified¹ Alcator C-Mod plasma.

As expected, drift-wave-type unstable modes live at the scale of electron and ion gyroradii, and propagate with frequencies of the order of the diamagnetic frequency. This plasma in particular exhibits ITG (ion scale, ion-direction propagating mode), TEM (ion scale, electron-direction propagating mode) and ETG (electron scale, electron-direction propagating mode) branches.

By solving the eigenvalue problem of the linear set of gyrofluid equations, TGLF also calculates the eigenmode associated with each unstable root. With this information, TGLF calculates the linear response contribution to the heat flux, $\mathcal{L}_{k_y}(\tilde{\Phi}, \tilde{p}_{\alpha})$, in Equation 3.2. In particular, the cross-phase angle between density and potential and temperature and potential fluctuations are the missing pieces to determine $\mathcal{L}_{k_y}(\tilde{\Phi}, \tilde{p}_{\alpha})$.

¹Here, we used a flux-matched case in Alcator C-Mod with artificially reduced a/Ln by 50% and a/LT_i by 20% so that the high-k ETG peak gets above low-k TEM and ITG for better visualization of effect of the multiscale saturation rule.

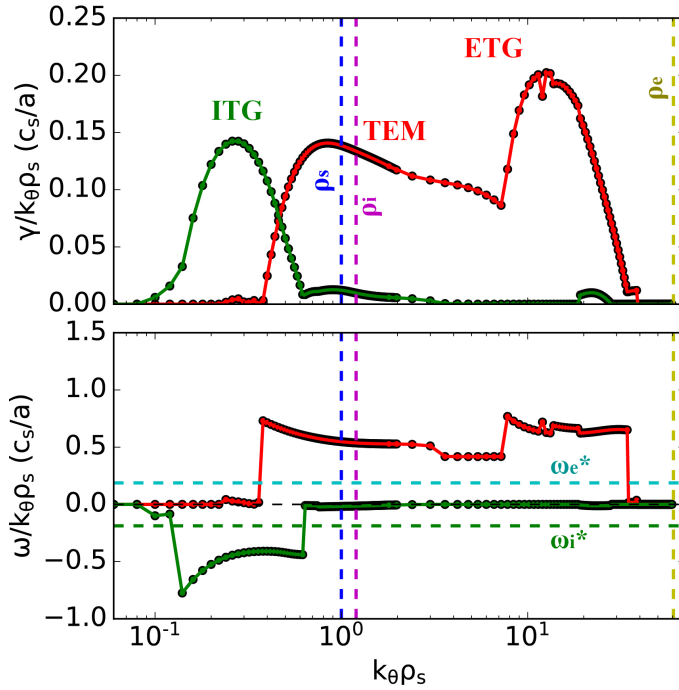


Figure 3.5: (top) Linear growth rate and (bottom) frequency spectra using TGLF in the core ($\rho_N = 0.4$) of a modified Alcator C-Mod Ohmic high-density plasma. Positive (negative) frequency indicates modes propagating in the electron (ion) diamagnetic direction. Ion and electron Larmor radii and diamagnetic frequencies are plotted for visualization purposes.

3.3.2 Saturation rule in TGLF-SAT1

As posed in Section 2.1.4, quasilinear transport codes require the calculation of the saturated electrostatic potential from linear characteristics by resorting to rules that are built to fit nonlinear gyrokinetics. In particular, SAT1 [3, 26] has been developed to account for interactions that happen between ion and electron scales of turbulence, observed only in expensive multiscale nonlinear gyrokinetic simulations [28, 29]. As a consequence of the new saturation rule in SAT1, the nonlinear upshift of the critical gradient (Dimits shift) is also captured by TGLF. In this section, we provide some intuition about the mechanisms that result in nonlinear saturation, as well as details on the implementation of these ideas in TGLF-SAT1.

Considering the existence of a collection of modes in the plasma, the evolution of a mode is affected by linear growth and nonlinear advection, and can be approximated as follows:

$$\frac{\partial \tilde{f}(\vec{k})}{\partial t} = \gamma \tilde{f}(\vec{k}) + \sum_{\vec{k}=\vec{k}'+\vec{k}''} \tilde{v}(\vec{k}') \cdot \nabla \tilde{f}(\vec{k}'') = \gamma \tilde{f}(\vec{k}) + \sum_{\vec{k}'} (\vec{k}' \times \vec{k}) \cdot \hat{z} \cdot \tilde{\phi}(\vec{k}') \tilde{f}(\vec{k} - \vec{k}') \quad (3.4)$$

Therefore in 2D slab geometry and in gyro-Bohm units we can write (making explicit the

contribution from axisymmetric zonal modes, $k'_y = 0$) [3]:

$$\begin{aligned} \frac{\partial \tilde{f}(k_x, k_y)}{\partial t} = & \underbrace{\gamma \tilde{f}(k_x, k_y) + \sum_{k'_x} \sum_{k'_y \neq 0} (k'_x k_y - k'_y k_x) \tilde{\Phi}(k'_x, k'_y) \tilde{f}(k_x - k'_x, k_y - k'_y)}_{\text{Drif-Wave Mixing, } \sim -\gamma_{DWM} \tilde{f}(k_x, k_y)} \\ & + \underbrace{k_y \sum_{k'_x} k'_x \tilde{\Phi}(k'_x, 0) \tilde{f}(k_x - k'_x, k_y)}_{\text{Zonal Flow Mixing, } \sim -\gamma_{ZFM} \tilde{f}(k_x, k_y)} \end{aligned} \quad (3.5)$$

In Equation 3.5, the linear growth rate drive must be balanced by nonlinear $E \times B$ advection, either by zonal flow ($k_y = 0$) mixing or by other finite k_y -mode ($k_y > 0$) electric field fluctuations. Nonlinear gyrokinetic simulations [3] indicate that the zonal flow mixing rate γ_{ZFM} is the only one comparable to the linear growth rates at all scales and therefore it is the only one that can be an effective saturation mechanism. For this to happen, it is hypothesized [26] that the zonal flow velocity saturates at the maximum of the linear growth at ion scales: $V_{ZF} \equiv \gamma_{ZFM}/k_y \sim \max_{ion-scale} (\gamma/k_y)$.

TGLF-SAT1 [3, 26] defines an “effective growth rate” at each wavenumber using the zonal flow mixing velocity. At ion scales, $k_y < k_{max}$, it is found that zonal flow mixing is always damping, and grows linearly with the wavenumber distance to k_{max} . At high-k, it delimits a constant baseline except when the high-k (γ/k_y) peak is larger than at low-k, in which case an excess is included. These observations can be expressed by a simple model for the two parts of the spectrum:

$$\gamma^{model} = \begin{cases} \max [\gamma - c_2^{ZF} V_{ZF} (k_{max} - k_y), 0] & \text{for } k_y \leq k_{max} \\ \sum_{k'_y > k_{max}} (c_1^{ZF} k_{max} V_{ZF} + \max [\gamma - c_1^{ZF} V_{ZF} k'_y, 0]) \Delta k'_y W_{(k'_y, k_y, c_{k_y})} & \text{for } k_y > k_{max} \end{cases} \quad (3.6)$$

where it has been taken into account the broadening of the peak at high-k due to non-linear drift-wave mixing with the Lorentzian weight function $W_{(k'_y, k_y, c_{k_y})}$, with c_{k_y} as a free parameter.

Another consideration taken in TGLF-SAT1 is the anisotropy of the eddies (i.e. ratio of radial to poloidal wavelengths, k_x/k_y). Multiscale nonlinear simulations indicate that poloidal correlation length is about half of the radial correlation length at low-k, but that anisotropy increases as the poloidal wavelength is reduced (i.e. eddies get more radially elongated at high-k: “streamers”), typically proportional to $\sqrt{k_y}$. Taking this into account, a model for the effective growth rate can be written as:

$$\gamma^{eff} = \gamma^{model} \max \left[\sqrt{\frac{k_y}{k_{ETG}}}, 1.0 \right] \quad (3.7)$$

Figure 3.6 depicts these concepts. In the top plot, γ_{max} and k_{max} at low-k are found from the spectrum of the most unstable mode at each k_y (blue circle). A zonal flow mixing rate $\gamma_{ZFM} = k_y V_{ZF}$ is constructed and used to build γ^{model} for each part of the spectrum. The bottom plot shows γ^{model} ,

which exhibits a bump at high- k because the high- k γ/k_y peak from linear stability is above the low- k γ/k_y peak, an important result from multiscale nonlinear gyrokinetic simulations. The effective growth rate, γ^{eff} , is also enhanced as the result of eddies anisotropy at high- k .

The effective growth rate given by Equation 3.7 takes only into account saturation by drift-wave and zonal flow mixing. However, background flows also contribute nonlinearly to the suppression of turbulence and must also be modeled. The method in TGLF not only accounts for the reduction of amplitude, but it also uses an analytical model for the shift in the peak of the radial wavenumber spectrum, resulting in a finite spectral average radial wavenumber, $\langle k_x \rangle$. It is found that the nonlinear spectrum of electric potential fluctuation amplitude can be fitted by [24]:

$$\Phi_{k_y} = \frac{\gamma^{eff} / \left(1 + (a_x \langle k_x \rangle / k_y)^4\right)}{\left(c_y k_y^2 + c_x \langle k_x \rangle^2 + c_x (k_x - \langle k_x \rangle)^2\right)} \quad (3.8)$$

where the spectral shift $\langle k_x \rangle$ can be estimated from a fit to nonlinear gyrokinetic simulations (Equation 14 in Ref. [25]) so that it is only a function of k_y , the $E \times B$ shearing rate $\gamma_{E \times B}$, and growth rate γ_{k_y} at $k_x = 0$.

Taken this into consideration, a model for the intensity of the normalized electrostatic potential fluctuations at the peak of the spectrum that is used to calculate the quasilinear transport fluxes is given by:

$$\bar{\Phi}_{k_y}^2 = c_{norm} \left(\frac{\gamma^{eff} / k_y^2}{\left(1 + (a_x \langle k_x \rangle / k_y)^4\right) \left(1 + a_y (\langle k_x \rangle / k_y)^2\right)} \right)^2 \quad (3.9)$$

In this derivation, various factors were left undefined. In particular, TGLF-SAT1 needs to fit c_{norm} , c_2^{ZF} , c_1^{ZF} , c_{k_y} and k_{ETG} . A database of nonlinear GYRO runs, including multi-scale GYRO simulations [28, 29], were used to fit these parameters.

3.3.3 Final remarks about transport modeling with TGLF

In conclusion, solving for the linear dynamics of drift-wave-type instabilities (taking moments of Equation 3.3), and using a model for the saturated level of potential fluctuations (Equations 3.6,

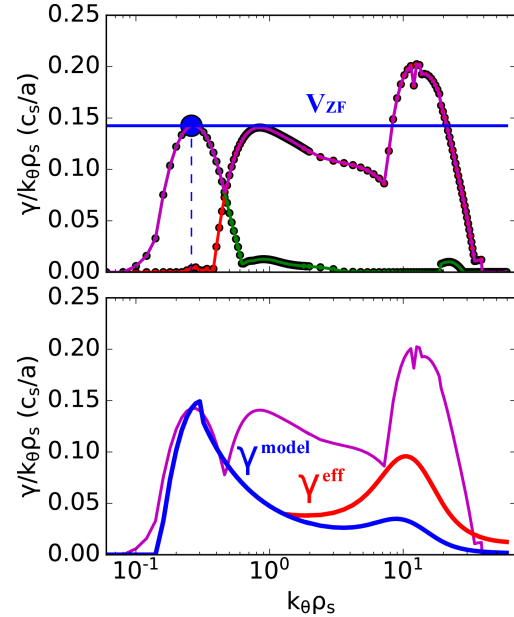


Figure 3.6: Illustration of saturation rule in TGLF-SAT1. In top figure: (red) electron, (green) ion and (magenta) most unstable mode spectrum. In bottom figure: Model and effective growth rates due to zonal flow mixing and eddies anisotropy, along with (magenta) most unstable mode spectrum.

3.7 and 3.9) that accounts for $E \times B$ mean field shearing and zonal flow mixing physics consistent with nonlinear gyrokinetics, we can provide transport fluxes (combining all this in Equation 3.2) as:

$$\begin{aligned} Q_e &= c_0 \cdot \sum_{k_y} \mathcal{L}_{k_y}(\tilde{\Phi}, \frac{\tilde{p}_e}{p_e}) \cdot \overline{\Phi}_{((k_x))}^2 \\ Q_i &= c_0 \cdot \frac{p_i}{p_e} \cdot \sum_{k_y} \mathcal{L}_{k_y}(\tilde{\Phi}, \frac{\tilde{p}_i}{p_i}) \cdot \overline{\Phi}_{((k_x))}^2 \end{aligned} \quad (3.10)$$

where c_0 is also a constant to be fitted to nonlinear gyrokinetic simulations, and the heat fluxes are given in gyro-Bohm units.

This approach, although nonlocal in wavenumber (because the zonal flow mixing saturation mechanism links low- to high- k), it is fully local in real space, and thus it represents a very convenient method to study the validity of the local-transport paradigm in cold-pulse propagation experiments. Reduced models like TGLF are fundamentally gradient-driven, and need an integrated modeling framework to predict background profiles, as shown schematically in Figure 3.7. Next section describes TRANSP, the tool used to accomplish this goal, which also ensures locality when evolving background profiles and defining heating sources.

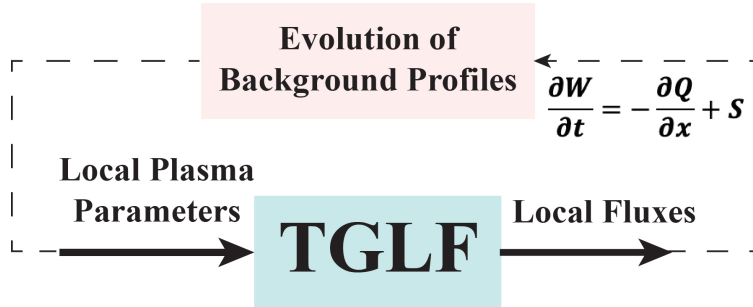


Figure 3.7: Diagram for a gradient-driven transport code like TGLF to evolve background profiles, provided sources.

3.4 TRANSP Framework for Integrated Modeling of Tokamak Plasmas

The study of transport physics and plasma phenomena requires the solution of the fully nonlinear equations that describe the plasma evolution over time. In Section 2.1.3, we saw that the study of turbulence and associated transport phenomena can be very computationally expensive. The solution of the dynamic plasma evolution over an energy confinement time or discharge duration thus become intractable. In Section 3.3, the quasilinear TGLF reduced transport model was introduced, which allows the calculation of linear stability and transport fluxes in a quick manner (core-seconds per TGLF evaluation rather than thousands of core-hours typical of gyrokinetic studies). However, TGLF is based on a gradient-driven framework, i.e. given plasma parameters, it provides transport fluxes, and thus are not coupled to the evolution of the plasma equilibrium.

In order to study plasma dynamics over transport time scales one can implement quasilinear models within an integrated modeling framework that evolves plasma profiles. Typically, the local transport model is run over a radial grid to compute the particle, momentum and energy fluxes (or a subset of them), which are used by the integrated modeling framework to evolve the equilibrium profiles, as we saw schematically in Figure 3.7. These new profiles can then be used again as inputs to the transport model, thus reaching convergence after a number of iterations. These integrated modeling frameworks, generally, do not properly model global effects and thus only local physics can be tested.

Given that quasilinear transport models only provide an approximation to the fluctuation-induced transport, the integrated modeling framework must couple other models that capture collisional transport, such as neoclassical models. Furthermore, in order to properly couple such models to the profile evolution, integrated modeling frameworks usually consider a fluid-like description of the plasma, where conservation laws for mass, momentum and energy are satisfied. Consequently, these frameworks are sometimes called “power balance” codes. In these equations, which will be described next, one must provide sources and sinks, as well as a proper geometry description and electromagnetic fields evolution (i.e. current diffusion). This can be achieved by the introduction of equilibrium reconstruction codes and the coupling with codes that solve for the energy and particle deposition for different heating and gas puffing schemes.

First of all, given the interest in studying tokamak plasma physics, we focus on toroidally symmetric systems, and therefore no variations with respect to the toroidal angle are expected in the fundamental plasma parameters. A second assumption comes from basic magnetohydrodynamic arguments: kinetic quantities and other parameters of interest are constant on flux surfaces. Hence, plasma profiles are virtually solved as 1D quantities (in terms of a radial-like coordinate) and are eventually mapped to a full 2D equilibrium reconstruction when needed. Because of this, power balance codes that follow these characteristics are typically referred to as “1.5D” codes.

Appendix A.2 provides a derivation of the set of governing equations that are solved within most transport models in a moving spatial grid. Generally, this set involves particle, momentum

and energy conservation equations. However, given that this Thesis focuses on phenomena associated with heat transport, special emphasis is put here on energy conservation equations. Because particle and momentum transport will not be modeled in here, details on their governing equations are outside the scope of this Thesis. The final set of equations for electrons and ions that we will consider is given by:

$$\begin{aligned} \frac{1}{V'} \left[\frac{\partial}{\partial t} \Big|_{\rho} \left(\frac{3}{2} \langle n_e T_e \rangle V' \right) + \langle n_e T_e \rangle \frac{\partial V'}{\partial t} \right] &= - \frac{1}{V'} \frac{\partial}{\partial \rho} \left(\left[\langle \vec{q}_e \cdot \nabla \rho \rangle + \frac{5}{2} \langle T_e \Gamma_e \cdot \nabla \rho \rangle \right] V' \right) - \langle Q_{ei} \rangle + \langle S_{E,e} \rangle \\ \frac{1}{V'} \left[\frac{\partial}{\partial t} \Big|_{\rho} \left(\frac{3}{2} \langle n_i T_i \rangle V' \right) + \langle n_i T_i \rangle \frac{\partial V'}{\partial t} \right] &= - \frac{1}{V'} \frac{\partial}{\partial \rho} \left(\left[\langle \vec{q}_i \cdot \nabla \rho \rangle + \frac{5}{2} \langle T_i \Gamma_i \cdot \nabla \rho \rangle \right] V' \right) + \langle Q_{ei} \rangle + \langle S_{E,i} \rangle \end{aligned} \quad (3.11)$$

where ρ is an absolute spatial coordinate with arbitrary normalization ($\rho = \frac{\sqrt{\phi}}{\pi B_0}$). Equations 3.11 are general for any transport model, but in the following, we will particularize to the case of TRANSP [4, 5, 30]. In the work presented in this Thesis, plasma equilibrium is solved with fixed boundary, and therefore Equations 3.11 also apply for a normalized radial coordinate $\zeta = \rho / \rho_{lim}$. Details on how Equations 3.11 are modified when using free-boundary solvers are outside the scope of this thesis. The interested reader is invited to read Ref. [30].

Electron energy transport

In the case of electron energy sources and sinks, $S_{E,e}$ includes radiative losses (P_{rad}), power loss by ionization of neutrals (P_{ioniz}) and auxiliary heating. Auxiliary power here refers to Ohmic heating (P_{OH}), along with heating of electrons from beams ($P_{NB,e}$), ICRF ($P_{ICRH,e}$), ECRF ($P_{ECRH,e}$) and LH ($P_{LH,e}$) waves. Fast ion heating of electrons from fusion reactions is also included ($P_{fus,e}$). TRANSP also defines a variable called EHEAT that is defined as the sum of compressional and auxiliary power, and a variable EETR_OBS that is defined as the sum of convective and conducted powers (PCNVE and PCNDE in the equation below, respectively).

All these considerations can be summarized in the following equation for electron energy conservation equation in TRANSP:

$$\begin{aligned} \underbrace{\frac{1}{V'} \frac{\partial}{\partial t} \Big|_{\rho} \left(\frac{3}{2} \langle n_e T_e \rangle V' \right)}_{\text{GAINE}} &= - \underbrace{\left(\frac{1}{V'} \frac{\partial}{\partial \rho} \left(\langle \vec{q}_e \cdot \nabla \rho \rangle V' \right) + \frac{1}{V'} \frac{\partial}{\partial \rho} \left(\frac{5}{2} \langle T_e \Gamma_e \cdot \nabla \rho \rangle V' \right) \right)}_{\text{EETR_OBS}} - \underbrace{\langle Q_{ei} \rangle}_{\text{QIE}} - \underbrace{\langle P_{rad} \rangle}_{\text{PRAD}} \\ &= - \underbrace{\left(\underbrace{\langle P_{ioniz} \rangle}_{\text{PION}} + \underbrace{\left(- \frac{1}{V'} \langle n_e T_e \rangle \frac{\partial V'}{\partial t} \right)}_{\text{PCMPE}} + \underbrace{\langle P_{OH} \rangle}_{\text{POH}} + \underbrace{\langle P_{NB,e} \rangle}_{\text{PBE}} + \underbrace{\langle P_{ICRH,e} \rangle}_{\text{PEICH}} + \underbrace{\langle P_{ECRH,e} \rangle}_{\text{PEECH}} + \underbrace{\langle P_{LH,e} \rangle}_{\text{PELH}} + \underbrace{\langle P_{fus,e} \rangle}_{\text{PFE}} \right)}_{\text{EHEAT}} \end{aligned} \quad (3.12)$$

Ion energy transport

On the other hand, $S_{E,i}$ for ions includes charge-exchange losses (P_{CX}), and RF and NBI auxiliary power: heating of ions from beams ($P_{NB,i}$), ICRF ($P_{ICRH,i}$) and LH ($P_{LH,i}$) waves. Fast ion heating of ions from fusion reactions is also included ($P_{fus,i}$). Other sources related to ion friction, power source from ionization of neutrals, minority transport, etc, might be also taken into account (P_{others}).

Similarly to electrons, the equation for ion energy conservation in TRANSP is given by:

$$\begin{aligned}
 \underbrace{\frac{1}{V'} \frac{\partial}{\partial t} \Big|_{\rho} \left(\frac{3}{2} \langle n_i T_i \rangle V' \right)}_{\text{GAIN}} = & - \overbrace{\left(\underbrace{\frac{1}{V'} \frac{\partial}{\partial \rho} (\langle \vec{q}_i \cdot \nabla \rho \rangle V')}_{\text{PCOND}} + \underbrace{\frac{1}{V'} \frac{\partial}{\partial \rho} \left(\frac{5}{2} \langle T_i \Gamma_i \cdot \nabla \rho \rangle V' \right)}_{\text{PCONV}} \right)}_{\text{IETR_OBS}} + \underbrace{\langle Q_{ei} \rangle}_{\text{QIE}} - \underbrace{\langle P_{CX} \rangle}_{\text{P0NET}} \\
 & + \overbrace{\left(\underbrace{-\frac{1}{V'} \langle n_i T_i \rangle \frac{\partial V'}{\partial t}}_{\text{PCMPI}} + \underbrace{\langle P_{NB,i} \rangle}_{\text{PBI}} + \underbrace{\langle P_{ICRH,i} \rangle}_{\text{PIICH}} + \underbrace{\langle P_{LH,i} \rangle}_{\text{PILH}} + \underbrace{\langle P_{fus,i} \rangle}_{\text{PFI}} + \langle P_{others} \rangle \right)}_{\text{IHEAT}}
 \end{aligned} \tag{3.13}$$

3.4.1 Interpretive TRANSP runs

Transport simulations can generally be of two types, depending on the problem unknowns: interpretive and predictive². On the one hand, **interpretive** power balance codes are used for analysis of experimental plasma discharges, where a set of plasma parameters are measured and we wish to further understand the behavior and performance of the confined plasma, particularly the cross-field heat fluxes for each of the plasma species.

Given a typical discharge, one should expect to measure parameters such as $n_e(R, t)$, $T_e(R, t)$ and $P_{rad}(R, t)$. Furthermore, most machines nowadays can measure or infer $T_i(R, t)$ and $Z_{eff}(R, t)$, which then allows to estimate P_{OH} and Q_{ei} by assuming an expression for the resistivity. Experimental profiles, which are typically measured as a function of the physical coordinates, R , can be mapped into normalized coordinates, ρ , to be used by TRANSP. Knowledge of the total deposited power, along with a model for the different heating schemes, permits to separate the electron and ion auxiliary power, $P_{aux} = P_{aux,e} + P_{aux,i}$, and information about neutrals provides P_{ioniz} . Lastly, one should also expect to be able to calculate the volumetric and wall particle sources. Therefore, given a well-diagnosed plasma, the electron and ion conservation equations given by Equations 3.12 and 3.13 become algebraic, and the cross-field heat fluxes can be calculated. Nevertheless, this procedure is not as trivial as it may seem from this simplified explanation. In auxiliary-heated plasmas, the deposited power for given plasma conditions must be calculated, which involves, e.g.,

²Even though throughout this Thesis we have used the terms “power balance” and “integrated modeling frameworks” interchangeably, power balance codes are typically referred to interpretive simulations and integrated modeling frameworks to predictive simulations

running expensive wave-particle interaction codes for RF heating (e.g. TORIC [31]) or Monte Carlo simulations for NBI deposition (e.g. NUBEAM [32]).

In the following, we provide some intuition on how to deal with accumulation integral of the divergence of the conducted and convective electron heat fluxes, PCNDE and PCNVE. Same process applies for ion energy channel.

Equations 3.11 were derived over a grid defined on flux surfaces and with surface averaged plasma quantities, but it is still a differential equation that needs to be discretized in the coordinate ζ in order to perform numerical implementation. For instance, given a grid of N discrete radial zones ($\{\zeta_j\}_1^N$), we can define a zone volume $\Delta V_j = \int_{\zeta_j}^{\zeta_{j+1}} V' d\zeta$ and a surface area $S_j = 2\pi \oint R dl_\rho$ that will be used to integrate energy densities and divergence of the cross-field flux respectively [30], using quantities from the equilibrium reconstruction. By definition of the total heat flux throughout the flux-surface, Q_e , we can write:

$$\text{PCNDE} = \frac{1}{V'} \frac{\partial}{\partial \zeta} (\langle \vec{q}_e \cdot \nabla \zeta \rangle V') = \frac{1}{V'} \frac{\partial Q_e}{\partial \zeta} \quad (3.14)$$

Then:

$$Q_e(\zeta) = \int_0^\zeta \text{PCNDE}(\zeta) V'(\zeta) d\zeta \Rightarrow q_e(\zeta) = \frac{1}{S(\zeta)} \int_0^\zeta \text{PCNDE}(\zeta) V'(\zeta) d\zeta \quad (3.15)$$

where q_e now is the heat flux per unit area (in real units).

If we now discretize the grid and realize that $V' d\zeta = \frac{dV}{d\zeta} d\zeta = dV$, we have that:

$$q_{e,j} = \frac{1}{S_j} \sum_{k=1}^j \text{PCNDE}_k \cdot \Delta V_k \quad (3.16)$$

where ΔV_k and S_j are provided as outputs of TRANSP as the zone volume DVOL, and flux surface area SURF, and whose meaning is indicated schematically in Figure 3.8.

When comparing to heat fluxes provided by (neoclassical and turbulent) transport codes in validation studies, the total heat flux as given by the sum of “conducted” and “convective” contributions must be used:

$$q_{e,j}^{turb.} + q_{e,j}^{neo.} = \frac{1}{S_j} \sum_{k=1}^j (\text{PCNDE}_k + \text{PCNVE}_k) \cdot \Delta V_k \quad (3.17)$$

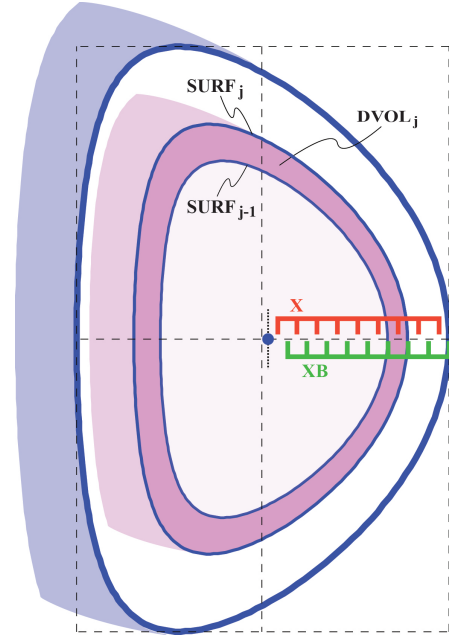


Figure 3.8: Schematic of TRANSP discretization. X and XB indicate “body” and “boundary” grids, respectively. Both grids are given in square root of normalized toroidal flux, $\zeta = \sqrt{\Phi/\Phi_{lim}}$. Surface quantities are evaluated in the boundary grid.

3.4.2 Predictive TRANSP runs

Predictive transport codes are used to predict plasma profiles (typically any combination of electron temperature, ion temperature, density and toroidal rotation). Given an initial set of plasma profiles, a reduced transport code provides the cross-field transport fluxes. These frameworks aim at reaching a solution where transport and the rest of power balance terms are consistent (i.e. converged solution). Of course, predictive models are significantly more expensive to run than interpretive codes, given that electron and ion energy equations and density equations are strongly coupled.

In Appendix A.2, we see that $\langle \vec{q} \cdot \nabla \rho \rangle V' = - \langle \chi_{eff} n \frac{\partial T}{\partial \rho} \|\nabla \rho\|^2 \rangle V'$ if a diffusive form of the flux is assumed. We could generalize this expression by assuming a convective-diffusive form, which is typically used in transport solvers, resulting in $\langle \vec{q} \cdot \nabla \rho \rangle V' = \langle n \|\nabla \rho\|^2 \left(v_T T - \chi \frac{\partial T}{\partial \rho} \right) \rangle V'$.

Including the classical convective contribution to the flux inside $\langle \vec{q} \cdot \nabla \rho \rangle V'$, dropping $\langle \cdot \rangle$ for simplification (plasma parameters in the equations represent flux-averaged quantities), and grouping ion-electron exchange with the sources, we can write energy conservation equations from Equation 3.11 as:

$$\boxed{\frac{1}{(V')^{2/3}} \frac{\partial}{\partial t} \Big|_{\rho} \left(\frac{3}{2} n T (V')^{5/3} \right) + \frac{\partial}{\partial \rho} \left(n \|\nabla \rho\|^2 \left(v_T T - \chi \frac{\partial T}{\partial \rho} \right) V' \right) = S_E V'} \quad (3.18)$$

The transport solver within TRANSP (PT_SOLVER [33]) simulates plasma dynamics by advancing the transport equations given in Equation 3.18. By taking into account the geometric factors that can be evaluated with an equilibrium solver, we can write a general transport equation, using an implicit backward time scheme³:

$$\frac{\partial T}{\partial t} = - \frac{\partial}{\partial x} \left(D \frac{\partial T}{\partial x} - VT \right) + S(T) \quad (3.19)$$

$$T^{n+1} = T^n - \Delta t \frac{\partial}{\partial x} \left(D^{n+1} \frac{\partial T^{n+1}}{\partial x} - V^{n+1} T^{n+1} \right) + \Delta t S(T^{n+1}) \quad (3.20)$$

where n indicates current step and $\frac{\partial}{\partial x}$ represents a general derivative operator. To solve explicitly for T^{n+1} , we need transport coefficients evaluated at the future iteration, D^{n+1} and V^{n+1} , as well as the sources, $S(T^{n+1})$, which can also depend on the future temperature.

Transport coefficients as provided by transport models like TGLF have a non-analytic dependence on temperature and gradients and may be strongly nonlinear, which complicates the convergence of standard numerical schemes. These features arise from the calculation of microinstabilities and subsequent fluctuation-induced transport fluxes, as explained in Section 2.1, such as critical gradients. The interested reader is invited to read Ref. [34] about this topic. The numerical scheme within TRANSP to work around this problem operates as follows. One can generate an

³An implicit scheme is only written here for the purpose of simplicity, but one could develop a Crank-Nicholson scheme with an implicitness parameter θ .

index m that indicates the so-called **Newton iterations** for each time step, and write:

$$T^{n+1,m} = T^n - \Delta t \overbrace{\frac{\partial}{\partial x} \left(D^{n+1,m-1} \frac{\partial}{\partial x} T^{n+1,m-1} - V^{n+1,m-1} T^{n+1,m-1} \right)}^{\text{Sinks at previous iteration}} + \overbrace{\Delta t S(T^{n+1,m-1})}^{\text{Sources at previous iteration}} \quad (3.21)$$

here, we can explicitly solve for $T^{n+1,m}$ because we can evaluate transport coefficients and sources at $m - 1$, and therefore sinks and sources are readily available. An iterative process is applied from $[n + 1, m = 0] (\equiv n)$ to $[n + 1, m = M] (\equiv n + 1)$, where M is a sufficiently high number of iterations so that convergence is reached. A relaxation factor for the temperature evolution may be added to ease convergence during Newton iterations.

These are called Newton iterations, and the convergence of the solver is determined by the difference between the power from sources, S , and the exhausted power, $\frac{\partial}{\partial x} \left(D \frac{\partial}{\partial x} T - VT \right)$, at the last Newton iteration. Figure 3.9 displays schematically the process of advancing in time by Newton iterations. In this framework, a convergence criteria based on a minimum relative variation of predicted variables is also used, $(T^{m+1} - T^m) / \min [T^{m+1}, T^m]$.

In TRANSP, the variable EETR_OBS refers to the divergence of electron energy flux as observed (EETR_OBS = GAIN - SOURCES), while EETR_MOD is the divergence of electron energy flux provided by TGLF (same applies for ions, with variables IETR_OBS and IETR_MOD). At every real-time-iteration, one wants to get a situation where EETR_OBS = EETR_MOD⁴, and must always be checked before interpreting predictive results. This is particularly important for the TGLF transport model, which sometimes provides discontinuous fluxes, causing convergence issues.

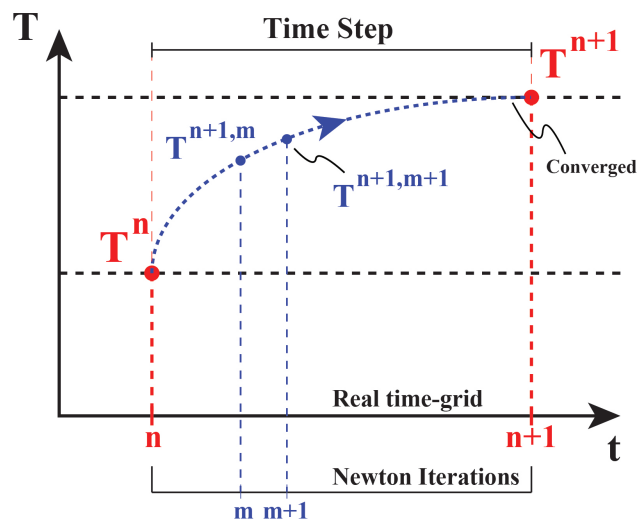


Figure 3.9: Newton iterations advancing real time step in TRANSP predictive simulations. Here, the final value of T^{n+1} is not reached until a number of iterations because transport coefficients and sources depend on T , and the difference between sources and sinks gets larger for larger T , until saturation.

⁴Please note that, by definition, EETR_OBS = EETR_MOD for every Newton iteration, but if convergence is not reached at M iterations, then the energy gain will not be equal to the difference between sources and sinks for the real time-step.

3.4.3 PRIMA Methodology and Techniques

In this Thesis, a workflow to launch and study cold pulses in integrated modeling TRANSP simulations has been developed. For the rest of this Thesis, this workflow will be referred as “PRIMA” (*Perturbative Response Integrated Modeling Analysis*), and the specifics of the implementation, codes and libraries used can be found in detail in Appendix C.

As illustrated schematically in Figure 3.10, the methodology used in PRIMA follows a number of steps. First, one must identify a portion of a plasma discharge with reasonably well measured parameters to study perturbative transport. As with most transport analysis workflows, one reconstructs magnetic equilibrium (e.g. EFIT) and fits profiles. At this stage, electron and ion edge temperatures are very important to measure accurately, as they will be used as boundary conditions in later predictive simulations. Using a reasonable time average for the measurements, one runs an interpretive TRANSP simulation⁵ that will be used as the starting point of the predictive analysis.

Electron and ion temperature evolution is enabled with a proper transport model (e.g. TGLF) and boundary conditions. It is important to use exactly the same transport model and settings as later in the perturbative transport prediction phase. One ensures that steady-state is reached in the simulation by allowing an extended amount of time (usually ~ 5 energy confinement times). After a converged (EETR_OBS = EETR_MOD) steady-state solution has been obtained, the profiles are extracted and a perturbation in radiation and density are introduced (which are consistent with the measured changes observed during the cold-pulse experiment). A final predictive TRANSP simulation is run.

Simplified Perturbation Model

Simplified perturbations to radiation and electron and impurity density profiles are introduced during the last stage of the simulated plasma discharge. Because such perturbation is constrained by experimental measurements, a very general (but still simplistic) perturbation shape with free parameters is implemented. Here, we implement pulses as skewed-Gaussians in both space and

⁵One could perform iterations for kinetically-constrained EFIT reconstructions if needed.

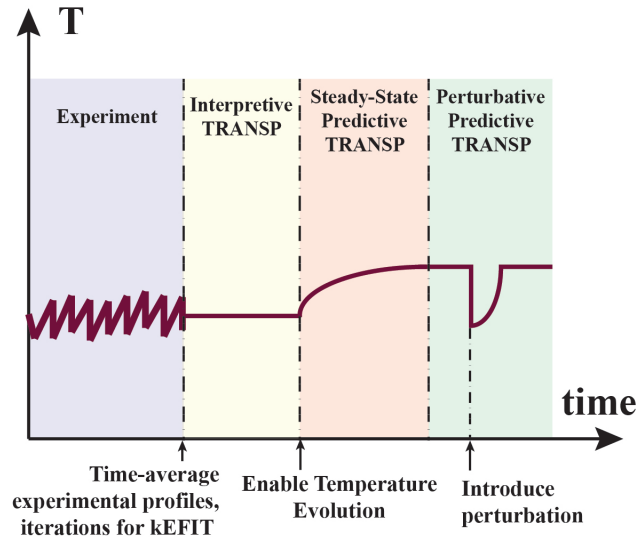


Figure 3.10: Schematic of temperature evolution using PRIMA workflow.

time:

$$A(\rho, t) = A_0 \cdot \left[e^{\frac{(\rho - \tilde{\rho}_0)^2}{2\sigma_\rho^2}} \cdot \operatorname{erfc} \left(-\frac{\alpha_\rho (\rho - \tilde{\rho}_0)}{\sqrt{2}\sigma_\rho} \right) \right] \cdot \left[e^{\frac{(t - t_0)^2}{2\sigma_t^2}} \cdot \operatorname{erfc} \left(-\frac{\alpha_t (t - t_0)}{\sqrt{2}\sigma_t} \right) \right] \quad (3.22)$$

where erfc is the complementary error function, and the mean spatial location is allowed to move with a given propagation speed v_ρ , such that $\tilde{\rho}_0 = \rho_0 - v_\rho t$.

Here, A_0 represents the magnitude of the perturbation, σ_ρ and σ_t provide spatial and temporal variances, α_ρ and α_t are the skewness parameters, and ρ_0 and t_0 are the initial location in space and time. In this way, the modeled perturbation includes 8 free parameters, usually enough to meet experimental constraints. Once an experimentally-relevant perturbation is constructed, one can introduce it to the model in order to mimic the effect of a cold-pulse injection.

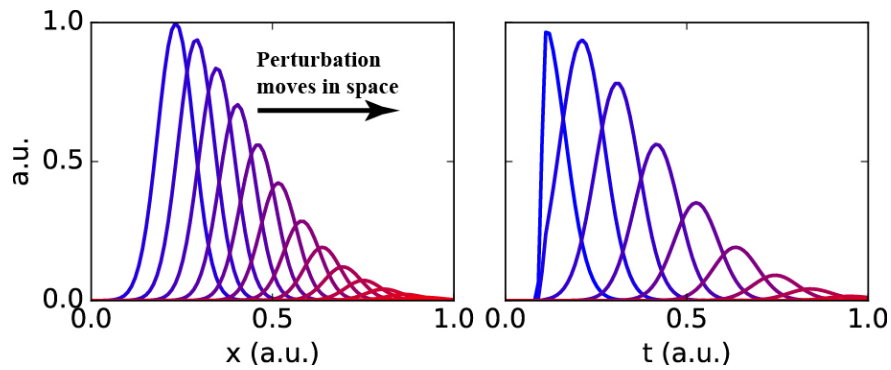


Figure 3.11: Modeled perturbation as skewed-Gaussian in space and time. (left) Spatial perturbation at different times. (right) Temporal perturbation at different locations.

Bibliography

- [1] G. M. Staebler et al. Gyro-landau fluid equations for trapped and passing particles. *Phys. Plasmas*, 12(10), 2005. URL <http://dx.doi.org/10.1063/1.2044587>.
- [2] G. M. Staebler et al. A theory-based transport model with comprehensive physics. *Phys. Plasmas*, 14(5):055909, 2007. URL <http://dx.doi.org/10.1063/1.2436852>.
- [3] G. M. Staebler et al. The role of zonal flows in the saturation of multi-scale gyrokinetic turbulence. *Phys. Plasmas*, 23(6):062518, 2016. URL <http://dx.doi.org/10.1063/1.4954905>.
- [4] R. J. Hawryluk. An empirical approach to tokamak transport. *Physics of Plasmas Close to Thermonuclear Conditions*, 1:19–46, 1980. URL <http://www.sciencedirect.com/science/article/pii/B9781483283852500091>.
- [5] Joshua Breslau et al. Transp. [Computer Software] <https://doi.org/10.11578/dc.20180627.4>, jun 2018. URL <https://doi.org/10.11578/dc.20180627.4>.
- [6] M. Greenwald et al. 20 years of research on the alcator c-mod tokamak. *Phys. Plasmas*, 21(11), 2014. URL <http://dx.doi.org/10.1063/1.4901920>.
- [7] J.W. Hughes et al. Access to pedestal pressure relevant to burning plasmas on the high magnetic field tokamak alcator c-mod. *Nuclear Fusion*, 58(11):112003, sep 2018. doi: 10.1088/1741-4326/aabc8a. URL <https://doi.org/10.1088%2F1741-4326%2Faabc8a>.
- [8] P.J.L O’Shea et al. In *Proc. 11th Conf. on Radio Frequency Power in Plasmas*, volume 403 (AIP), page 89, 1997.
- [9] J. W. Hughes et al. Thomson scattering upgrades on alcator c-mod. *Review of Scientific Instruments*, 74(3):1667–1670, 2003. doi: 10.1063/1.1532764. URL <https://doi.org/10.1063/1.1532764>.
- [10] J. H. Irby et al. Two-color interferometer system for alcator c-mod. *Rev. Sci. Instrum*, 59(8): 1568–1570, 1988. URL <http://dx.doi.org/10.1063/1.1140199>.
- [11] M. L. Reinke et al. X-ray imaging crystal spectroscopy for use in plasma transport research. *Rev. Sci. Instrum*, 83(11), 2012. URL <http://dx.doi.org/10.1063/1.4758281>.
- [12] A. Ince-Cushman et al. Spatially resolved high resolution x-ray spectroscopy for magnetically confined fusion plasmas. *Rev. Sci. Instrum*, 79(10):10E302, 2008. URL <http://dx.doi.org/10.1063/1.2968707>.
- [13] T. S. Pedersen et al. Edge x-ray imaging measurements of plasma edge in alcator c-mod. *Rev. Sci. Instrum*, 70(1):586–590, 1999. URL <http://dx.doi.org/10.1063/1.1149487>.

- [14] R. L. Boivin et al. High resolution bolometry on the alcator c-mod tokamak (invited). *Rev. Sci. Instrum*, 70(1):260–264, 1999. doi: 10.1063/1.1149309. URL <http://dx.doi.org/10.1063/1.1149309>.
- [15] N. T. Howard et al. Characterization of impurity confinement on alcator c-mod using a multi-pulse laser blow-off system. *Rev. Sci. Instrum*, 82(3), 2011. URL <http://dx.doi.org/10.1063/1.3565448>.
- [16] R. Dux. Report ipp 9/82. *MPI fur Plasmaphysik, Garching*, 2007.
- [17] J.L. Luxon. A design retrospective of the diiii-d tokamak. *Nuclear Fusion*, 42(5):614, 2002. URL <http://stacks.iop.org/0029-5515/42/i=5/a=313>.
- [18] Y. Ou et al. Receding-horizon optimal control of the current profile evolution during the ramp-up phase of a tokamak discharge. *Control Engineering Practice*, 19(1):22 – 31, 2011. ISSN 0967-0661. doi: <https://doi.org/10.1016/j.conengprac.2010.08.006>. URL <http://www.sciencedirect.com/science/article/pii/S0967066110001875>.
- [19] M. E. Austin and J. Lohr. Electron cyclotron emission radiometer upgrade on the diiii-d tokamak. *Review of Scientific Instruments*, 74(3):1457–1459, 2003. doi: 10.1063/1.1530387. URL <https://doi.org/10.1063/1.1530387>.
- [20] L. Zeng et al. Fast automated analysis of high-resolution reflectometer density profiles on diiii-d. *Nuclear Fusion*, 46(9):S677, 2006. URL <http://stacks.iop.org/0029-5515/46/i=9/a=S03>.
- [21] P. Gohil et al. High spatial and temporal resolution visible spectroscopy of the plasma edge in diiii-d. *Review of Scientific Instruments*, 61(10):2949–2951, 1990. doi: 10.1063/1.1141786. URL <https://doi.org/10.1063/1.1141786>.
- [22] C. Chrystal et al. Improved edge charge exchange recombination spectroscopy in diiii-d. *Review of Scientific Instruments*, 87(11):11E512, 2016. doi: 10.1063/1.4958915. URL <https://aip.scitation.org/doi/abs/10.1063/1.4958915>.
- [23] W. A. Peebles et al. A novel, multichannel, comb-frequency doppler backscatter system. *Review of Scientific Instruments*, 81(10):10D902, 2010. doi: 10.1063/1.3464266. URL <https://doi.org/10.1063/1.3464266>.
- [24] G. M. Staebler et al. New paradigm for suppression of gyrokinetic turbulence by velocity shear. *Phys. Rev. Lett.*, 110:055003, Jan 2013. doi: 10.1103/PhysRevLett.110.055003. URL <https://link.aps.org/doi/10.1103/PhysRevLett.110.055003>.
- [25] G.M. Staebler et al. A new paradigm for exb velocity shear suppression of gyro-kinetic turbulence and the momentum pinch. *Nuclear Fusion*, 53(11):113017, 2013. URL <http://stacks.iop.org/0029-5515/53/i=11/a=113017>.

- [26] Gary M Staebler et al. A model of the saturation of coupled electron and ion scale gyrokinetic turbulence. *Nucl. Fusion*, 2017. URL <http://iopscience.iop.org/10.1088/1741-4326/aa6bee>.
- [27] M. A. Beer and G. W. Hammett. Toroidal gyrofluid equations for simulations of tokamak turbulence. *Physics of Plasmas*, 3(11):4046–4064, 1996. doi: 10.1063/1.871538. URL <https://doi.org/10.1063/1.871538>.
- [28] N. T. Howard et al. Synergistic cross-scale coupling of turbulence in a tokamak plasma. *Phys. Plasmas*, 21(11), 2014. URL <http://dx.doi.org/10.1063/1.2928909>.
- [29] N.T. Howard et al. Multi-scale gyrokinetic simulation of tokamak plasmas: enhanced heat loss due to cross-scale coupling of plasma turbulence. *Nucl. Fusion*, 56(1):014004, 2016. URL <https://doi.org/10.1088/0029-5515/56/1/014004>.
- [30] B.A. Grierson. Basic transp equations. 2017. URL <https://drive.google.com/file/d/0B3rL-PK3cq03cmU2WTNpWlFOVvk/view>.
- [31] M Brambilla. Numerical simulation of ion cyclotron waves in tokamak plasmas. *Plasma Physics and Controlled Fusion*, 41(1):1–34, jan 1999. doi: 10.1088/0741-3335/41/1/002. URL <https://doi.org/10.1088/0741-3335/41/1/002>.
- [32] Alexei Pankin et al. The tokamak monte carlo fast ion module nubeam in the national transport code collaboration library. *Computer Physics Communications*, 159(3):157 – 184, 2004. ISSN 0010-4655. doi: <https://doi.org/10.1016/j.cpc.2003.11.002>. URL <http://www.sciencedirect.com/science/article/pii/S0010465504001109>.
- [33] X. Yuan et al. Parallel computing aspect in TRANSP with PT-SOLVER. In *APS Meeting Abstracts*, page JP8.119, October 2013. URL <http://adsabs.harvard.edu/abs/2013APS..DPPJP8119Y>.
- [34] S.C. Jardin et al. On 1d diffusion problems with a gradient-dependent diffusion coefficient. *Journal of Computational Physics*, 227(20):8769 – 8775, 2008. ISSN 0021-9991. doi: <https://doi.org/10.1016/j.jcp.2008.06.032>. URL <http://www.sciencedirect.com/science/article/pii/S0021999108003616>.

Chapter 4

Cold-Pulse Experiments in Alcator C-Mod

“[...] Experimental evidence has been accumulated regarding the breakdown of a local expression of the flux-gradient relation [...] One example of such non-locality phenomena is the spontaneous increase of core temperature associated with edge cooling by small impurity and hydrogen pellets which are observed both in tokamak and helical plasmas.”

[Ida et al.](#), *Nuclear Fusion*, 2015

Understanding the physical mechanisms limiting confinement in fusion devices is important for realizing the dream of a fusion power plant. To understand the limitation on confinement, considerable effort has been applied towards understanding possible violations of the local closure of the transport relation [1], which states that the local fluxes are described in terms of local plasma parameters (see Section 2.3 for details on local v.s. nonlocal transport).

The possibility of “non-local agents” being the dominant transport mechanism poses an important challenge to our understanding of plasma processes. As presented in Section 2.2, perturbative transport experiments are useful tools to identify possible non-localities in the transport description [2]. As first presented in Section 2.4, one of the most provocative observations that is speculated to violate the local closure is the rapid rise in core temperature following sharp edge cooling of the plasma. This “temperature inversion” phenomenon occurs when the edge suffers an intense cooling, intentionally produced via impurity injections [3]. This Chapter explores the phenomenology of temperature inversions on Alcator C-Mod. Special emphasis is placed on the effect of plasma density on temperature inversions and the relationship with intrinsic toroidal rotation in Ohmic and ICRF-heated plasmas.

4.1 Introduction to Temperature Inversions in Alcator C-Mod

To the author's knowledge, temperature inversions have been documented in TEXT [4–6], TFTR [7, 8], Tore Supra [9, 10], RTP [11–13], ASDEX Upgrade [14], JET [15], LHD [16–23], HL-2A [24–30], Alcator C-Mod [31, 32], KSTAR [33], J-TEXT [34, 35] and EAST [36]. Despite the reproducibility of these phenomena in very different plasma conditions, the underlying mechanism of the core response is still unclear. Many explanations favor a non-local mechanism [1, and references therein], while others suggest that a local transport model may explain qualitatively the observed behavior [14, 15, 37].

Past work in low-current Ohmic plasmas in Alcator C-Mod [31] and in ECH-heated plasmas in KSTAR [33] found that these transient heat transport effects—the temperature inversions—disappear above the intrinsic toroidal rotation reversal density, suggesting a connection between heat and momentum transport. Changes in turbulence regimes, ohmic energy confinement (LOC/-SOC transition) and up/down impurity density asymmetries are also speculated to occur at the intrinsic rotation reversal density [31, 38].

By tracking the change in the core temperature in response to the edge cold pulses in a variety of different plasma conditions—particularly in Ohmic L-mode I_p scans, ICRF heated L-mode plasmas, and plasmas with zero toroidal rotation due to the presence of locked modes—the absence of the correlation between temperature inversions and intrinsic rotation is demonstrated in this Chapter. All experiments reported here were performed in Alcator C-Mod with deuterium L-mode plasmas with $B_t = 5.4$ T. As indicated in more detail in Section 3.1, electron temperature traces were measured with an ECE Grating PolyChromator (GPC) [39], and average electron densities were determined using a two-color interferometer [40]. Impurity toroidal rotation profile was measured by a high-resolution imaging x-ray spectrometer system [41, 42].

4.2 Cold pulses in Low and High Density Plasmas

Cold pulses are introduced in the edge of Alcator C-Mod plasmas via the injection of CaF_2 impurities. The expected response, if local diffusive processes are dominating the transport, would be a temperature decrease at all radial locations, as shown in Figure 4.1a. Such a decrease in temperature following impurity injection is observed in high density plasmas ($B_T = 5.4$ T, $I_p = 0.8$ MA, $\langle n_e \rangle = 1.12 \cdot 10^{20} \text{m}^{-3}$). In principle, the very fast propagation of the cold-pulse could be explained in terms of high incremental diffusivity, which has been documented in past work in Alcator C-Mod [43, and references therein].

In contrast, the transient temperature inversion characterized by the rapid (much faster than τ_E , the energy confinement time) temperature rise in the core following a sharp edge cooling is shown in Figure 4.1b. This response is common in low density ($B_T = 5.4$ T, $I_p = 0.8$ MA,

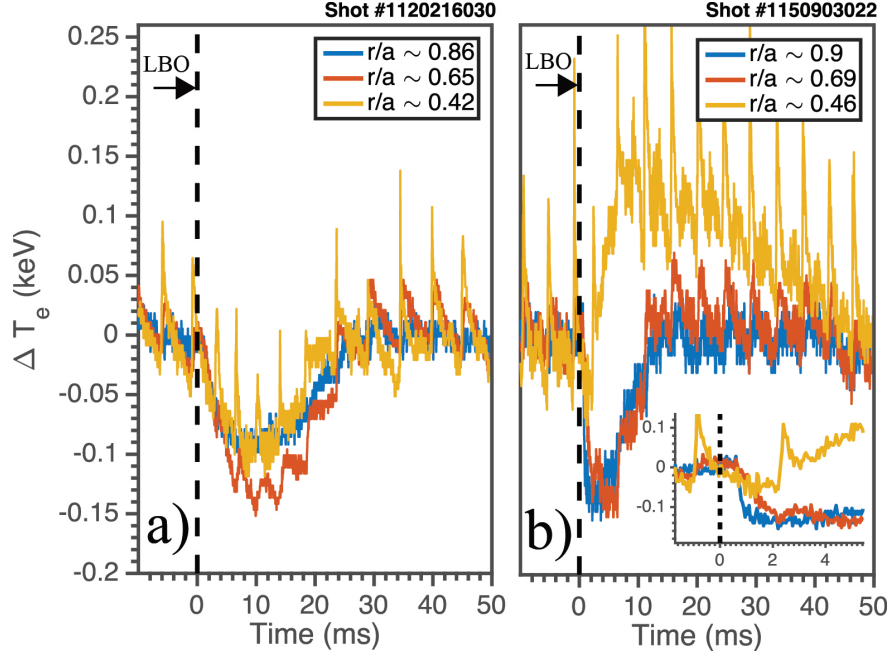


Figure 4.1: Temperature traces following LBO injections for: (a) high-density plasma (USN, Ohmic, $I_p = 0.8$ MA, $\langle n_e \rangle = 1.12 \cdot 10^{20} \text{ m}^{-3}$), and (b) low-density plasma (USN, Ohmic, $I_p = 0.8$ MA, $\langle n_e \rangle = 0.62 \cdot 10^{20} \text{ m}^{-3}$). The temperature inversion effect is clearly observed at low density, but it disappears at high density. Relaxation time of the edge temperature (red and blue traces) is longer at high density than at low density.

($\langle n_e \rangle = 0.62 \cdot 10^{20} \text{ m}^{-3}$) plasmas. As shown in Figure 4.1b, the rapid temperature inversion is often preceded by an even more rapid drop in the core temperature ($r/a \sim 0.5$) following the LBO injection. This first rapid drop is coincident with the minimum of the edge temperature at $t \sim 2$ ms after the injection. The core temperature starts to rise, peaking at $t \sim 8$ ms, still faster than an energy confinement time. The edge cold pulse decays until the temperature reaches its initial value at $t \sim 13$ ms at the edge, whereas the core temperature takes a much longer time to return to the original value, up to $t \sim 50$ ms.

It is noteworthy that the time-scale of the entire cold-pulse propagation and core temperature dynamics is much shorter than the energy confinement time ($\tau_E \sim 25 - 30$ ms) for both the high and low density plasmas shown in Figure 4.1. In the past, temperature inversions have been referred to as “non-local” effects, based on the fast time scale of these phenomena and the apparent lack of a definite plasma parameter changing in the core of the plasma prior to the temperature increase. However, previous modeling studies [14, 15, 37] suggested that a local transport model could reproduce the observed temperature inversions, because of the existence of high stiffness, critical gradients and the T_i/T_e stabilization of turbulence.

Thanks to the capabilities of the laser blow-off system in Alcator C-Mod [44], cold pulses can also be introduced in the same shot during density scans. Next, cold-pulses are introduced at the edge of an Ohmic L-mode plasma ($B_T = 5.5$ T, $I_p = 0.8$ MA) during a controlled density

ramp, as shown in Figs. 4.2a and 4.2b. As density increase, this discharge transitions from LOC (Linear Ohmic Confinement regime) to SOC (Saturated Ohmic Confinement regime). Line-averaged density and total radiated power (Figure 4.2b), electron temperature, T_e , and ion temperature, T_i , (Figure 4.2c) are perturbed by the impurity injection. At this plasma current, the controlled density ramp covers the transition from temperature inversion to “standard” transport behavior (disappearance of temperature inversion) in both electron and ion channels, as shown in Figure 4.2c. Core inversions of T_e and T_i , as well as an edge T_i inversion, are only observed in the low-density portion of the discharge.

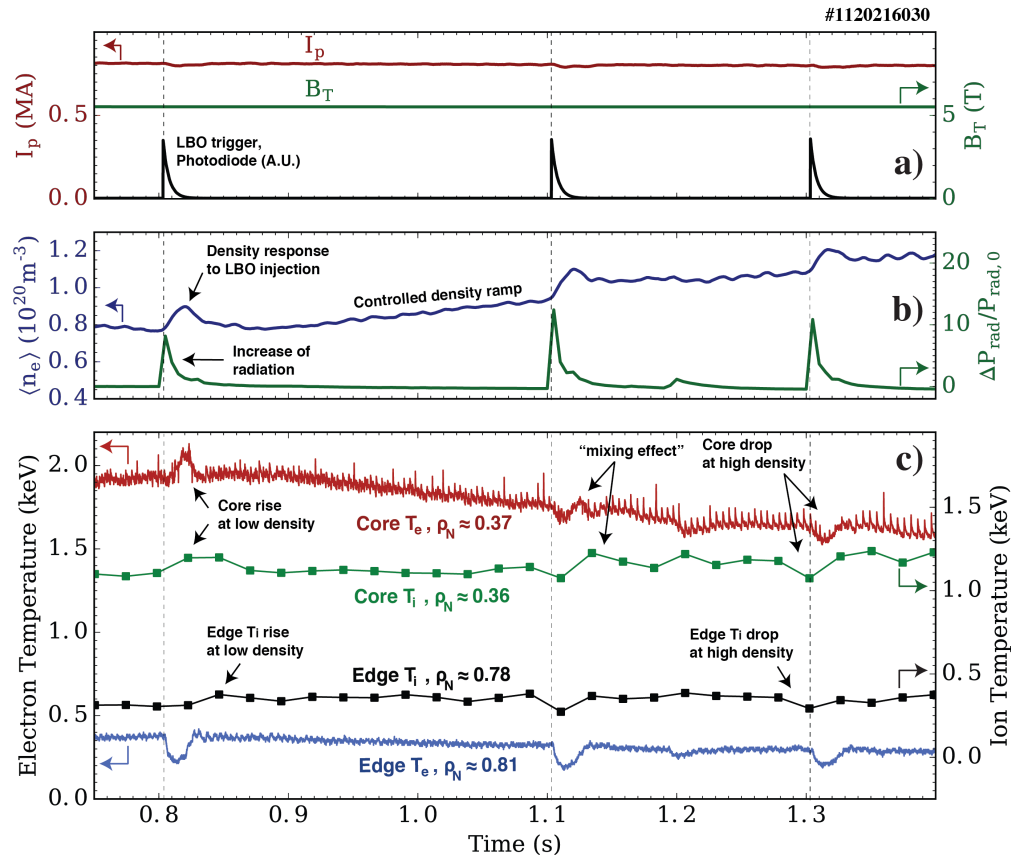


Figure 4.2: Experimental parameters. (a) Plasma current, toroidal field and LBO injection times; (b) line-averaged density and total radiated power normalized to pre-cold pulses time; (c) core and edge electron and ion temperatures. Details on diagnostic systems can be found in Refs. [31, 32].

4.3 Edge Cooling and Mixing Phenomena

In Alcator C-Mod, varying the amount of injected impurities¹ helped to reveal “mixing effects” that motivated a new parameterization of the cold pulse propagation and core temperature dynamics. The results of the controlled injection experiment show that the core temperature re-

¹In this experiment, the amount of impurities was varied by carefully overlapping with the previously ablated spot of the laser blow-off slide.

sponse is nearly independent of the initial edge perturbation, as evidenced in Figure 4.3, where multiple injections with increasing amounts of ablated impurities were introduced in an Ohmic low-density plasma. The smallest injection ($t = 0.8$ s) does not have a strong effect on the edge electron temperature and hence the core effect is weak. The edge perturbation grows as the amount of impurities injected gets larger, but the core temperature increase does not. For small edge perturbations (case at $t = 0.9$ s), the temperature rises in the core without an earlier drop, whereas for large injections ($t = 1.4$ s) there is an early drop before the onset of the temperature rise. This controlled injection experiment shows the existence of a mixing process in Alcator C-Mod where the inwardly-propagating edge cold-pulse mixes with an independent core heat pulse and delays its effect. A “mixing effect” such as this has been alluded to in past work [10, 14].

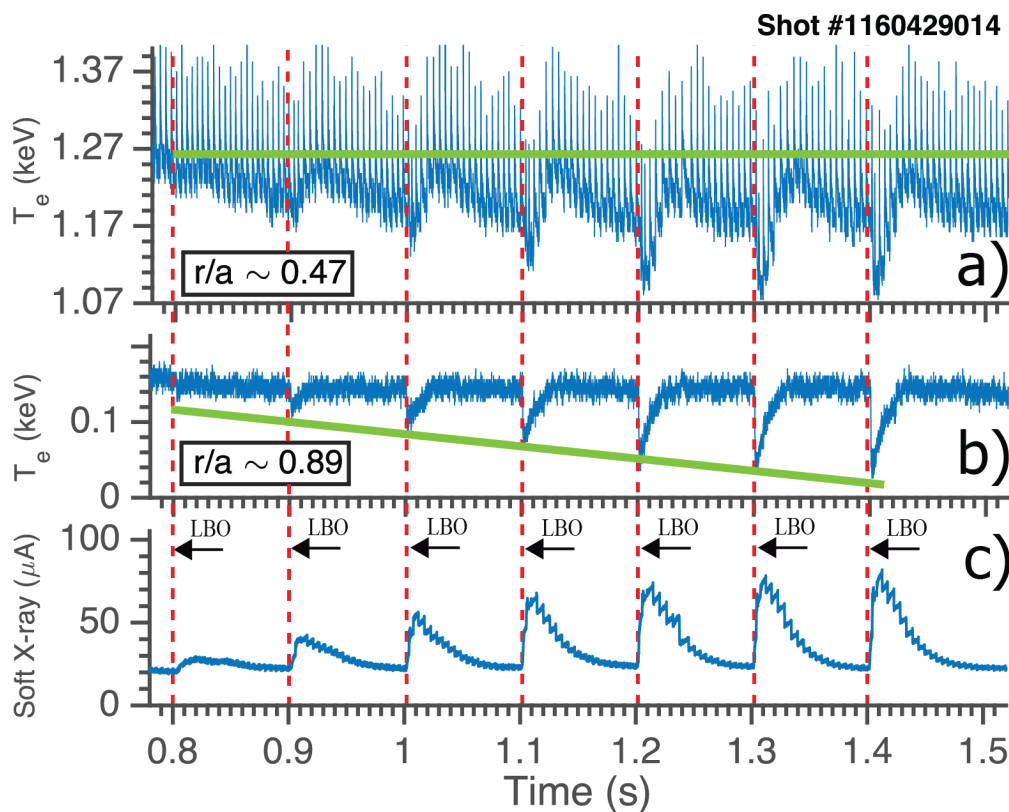


Figure 4.3: ECE temperature time-traces in the core *a*) and edge *b*) showing LBO injection times for a LSN, Ohmic plasma with $I_p = 0.8$ MA $\langle n_e \rangle \sim 1.0 \cdot 10^{20} \text{m}^{-3}$. After the LBO injection at $t = 0.9$ s, there is a small temperature drop prior to the inversion. At $t = 1.4$ s, the same magnitude of the temperature inversion is seen but a larger drop in temperature prior, evidence of increased mixing effects. *c*) Soft x-ray brightness time-trace showing LBO injection times.

Accounting for the possibility of two merging heat pulses and the existence of a mixing process is important in studies of the temperature inversion effect. A new parameterization of the cold pulse is used to analyze the data, where any earlier drop in temperature (before the temperature rise but after the LBO injection) is ignored and only the absolute change in core temperature is tracked, regardless of the speed of the phenomenon.

4.4 Correlation of Temperature Inversions with Intrinsic Rotation

Ohmic L-mode plasmas and RF heating plasmas with no external net momentum input are known to exhibit intrinsic toroidal rotation. This rotation, observed in many devices [45], can be theoretically generated by interactions of turbulent residual stresses in the plasma [46]. Past work in Alcator C-Mod found that plasmas that intrinsically rotate exhibit an abrupt reversal of the rotation direction (from co-current to counter-current) at a given value of average electron density [47]. In RF heating scenarios, full reversal does not usually occur and, instead, only a hollowing of the rotation profile takes place [48, 49], suggesting competing effects when ICRF heating is added.

Past work in Alcator C-Mod [31] found that, in low-current Ohmic L-mode plasmas, rotation reversal at high density is concomitant with the disappearance of core temperature inversions. This strong link between the two unexplained phenomena suggested that energy and momentum transport are connected by mechanisms that are still not well understood. Changes in energy confinement and turbulence regimes are also reported to happen at the intrinsic rotation reversal density in the ASDEX Upgrade tokamak [38]. Recent work in KSTAR [33] found that this correlation between temperature inversions and rotation reversals is also observed with the addition of ECH input power. In Ref. [33], the authors suggest that a change of the dominant micro-turbulence mode could explain both the intrinsic rotation reversal and the cut-off density for the temperature inversions.

In this section, the correlation between the disappearance of temperature inversions and the reversal of intrinsic rotation is revisited. New cold-pulse experiments with high plasma current, ICRF heating and locked modes reveal that the direction of core rotation and its reversal do not affect the heat transport behavior of the temperature inversion effect.

4.4.1 Temperature Inversions at High Plasma Current in Ohmic L-mode Plasmas

The link between rotation reversals and temperature inversions was already recognized to be unclear for the higher current cases analyzed in Alcator C-Mod [31]. The analysis presented here uses a different parameterization of the core temperature response, accounting for the possibility of a “mixing process”, to show that the correlation between rotation reversals and temperature inversions does not hold at high current in Ohmic L-mode plasmas.

Figure 4.4 depicts one example of the breakdown of the rotation reversals and temperature inversions correlation for high-current Ohmic plasmas ($I_p = 1.1$ MA). In Figure 4.4c, it is observed that the case with lower density exhibits a rotation profile that is co-current and with no noticeable hollowing of the core rotation at mid-radius, whereas the higher density case presents a reversed counter-current rotation profile, which is consistent with past work on rotation reversals in Ohmic L-mode C-Mod plasmas [50]. Although strong sawtooth activity is present, core temperature inversions following edge cold-pulse injections are observed for both plasmas, as depicted in

Figures 4.4a and 4.4b. This example shows that, at high current, the rotation profile can fully reverse but temperature inversions during cold pulse propagation persist at higher densities.

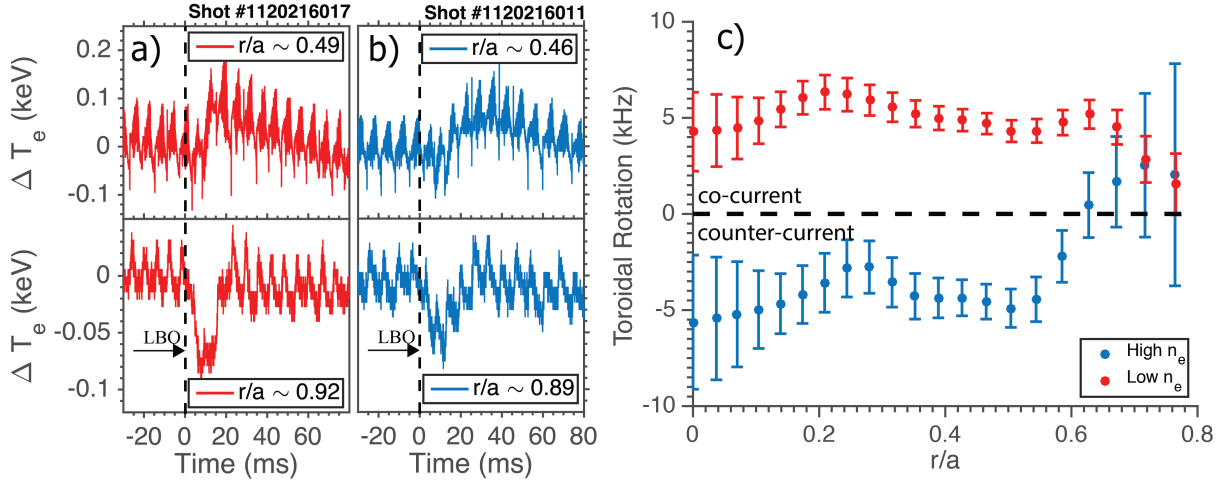


Figure 4.4: Edge and core temperature traces for two LSN, Ohmic, $I_p = 1.1$ MA plasmas at different densities: (a) $\langle n_e \rangle = 1.10 \cdot 10^{20} \text{m}^{-3}$ and (b) $\langle n_e \rangle = 1.35 \cdot 10^{20} \text{m}^{-3}$. (c) Intrinsic toroidal rotation profiles for the same shots. Temperature inversions are observed with both co-current and counter-current rotation, breaking the correlation between temperature inversion effects and rotation reversals.

The correlation between temperature inversions and intrinsic rotation reversals is recovered for low and medium current Ohmic plasmas in the I_p scan. Figure 4.5 shows the relative change in core temperature after LBO injections as a function of line-average density and collisionality ($\nu^* \propto n_e \cdot q_{95}$ [31, 32]) for different sets of plasma currents in Ohmic plasmas. These examples show that plasma current has a very strong effect on the cut-off density, which is consistent with past work [10, 31, 32]. In Figure 4.5, rotation reversal densities are depicted with vertical lines, evidencing that temperature inversions ($\Delta T_e / T_e > 0$) persist at high density and collisionality, when the intrinsic rotation has reversed.

Figure 4.6a depicts the core temperature time-trace for a medium-current ($I_p = 0.8$ MA) plasma, showing that the reversal of the rotation is concomitant to the disappearance of the core temperature rise. Nevertheless, Figure 4.6b further emphasizes that the rotation reversal does not have an effect on the transient heat transport behavior in high current ($I_p = 1.1$ MA) plasmas: after the rotation reversal, core temperature still robustly increases following the cold-pulse injection. Figure 4.6c shows the weak effect that density has on the core response in the high-current plasmas, since the core exhibits a very strong temperature rise even at very high densities ($\langle n_e \rangle \sim 1.40 \cdot 10^{20} \text{m}^{-3}$) in Alcator C-Mod.

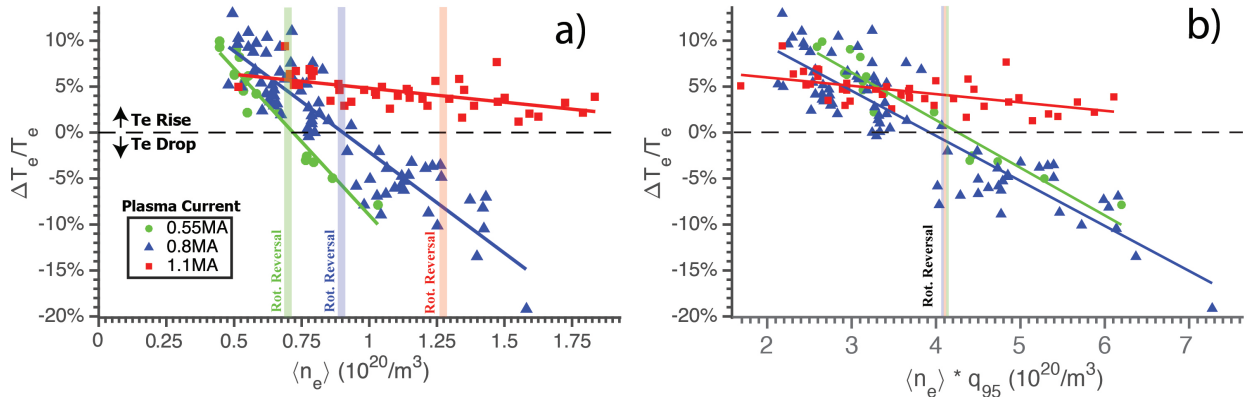


Figure 4.5: Relative core temperature change as a function of (a) line-average density $\langle n_e \rangle$ and (b) the product $\langle n_e \rangle \cdot q_{95}$ at three different plasma currents. For the low current cases (green, blue), the rotation reversal correlates with the disappearance of the temperature inversion effect and both transitions happen at a similar collisionality. At high current (red), the rotation reversal occurs but the inversion effect does not disappear. Solid lines are linear fits to the data.

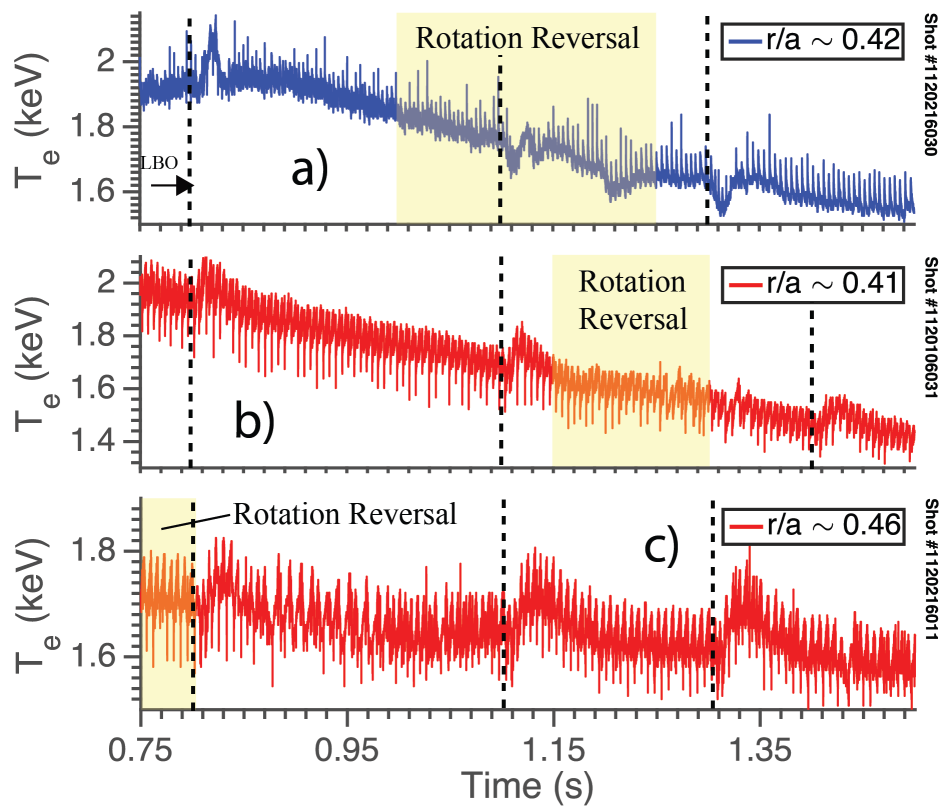


Figure 4.6: Core temperature time-traces during density scan for three LSN, Ohmic plasmas: a) $I_p = 0.8 \text{ MA}$, $\langle n_e \rangle = 0.80 - 1.18 \cdot 10^{20} \text{ m}^{-3}$, b) $I_p = 1.1 \text{ MA}$, $\langle n_e \rangle = 0.76 - 1.16 \cdot 10^{20} \text{ m}^{-3}$, and c) $I_p = 1.1 \text{ MA}$, $\langle n_e \rangle = 1.21 - 1.40 \cdot 10^{20} \text{ m}^{-3}$

4.4.2 Temperature Inversions in ICRF-heated L-mode Plasmas

Cold-pulse propagation experiments in Alcator C-Mod in ICRF-heated L-mode plasmas also show the absence of the correlation between changes in the rotation profile and the disappearance of the temperature inversion effect. At high density, the intrinsic rotation profile in Alcator C-Mod hollows in ICRF-heated plasmas, but does not tend to reverse direction [48].

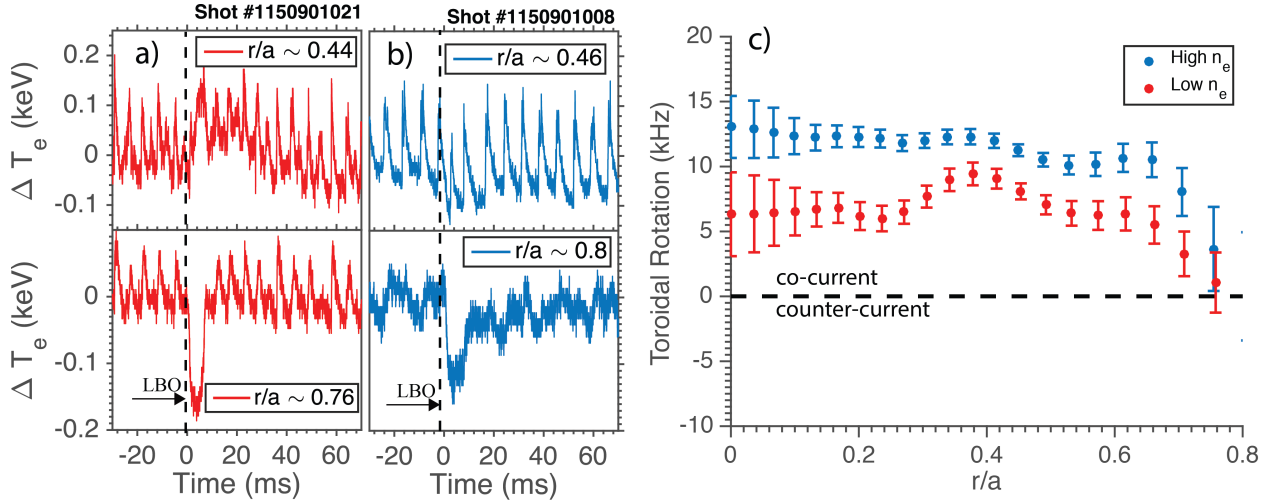


Figure 4.7: Edge and core temperature traces for two USN, $P_{RF} = 1.2$ MW, $I_p = 0.8$ MA plasmas at different densities: (a) $\langle n_e \rangle = 0.76 \cdot 10^{20} \text{ m}^{-3}$ and (b) $\langle n_e \rangle = 1.29 \cdot 10^{20} \text{ m}^{-3}$. (c) Intrinsic toroidal rotation profiles for the same shots. Both plasmas have co-current rotation but different core temperature behavior.

Figure 4.7 shows the relative change in edge and core electron temperature traces for two ICRF-heated plasmas ($P_{RF} = 1.2$ MW). A clear core temperature inversion following edge cold-pulse injection is observed for the low-density ICRF L-mode plasma denoted in Figure 4.7a. Surprisingly, at the time of the injection, the intrinsic rotation exhibits a profile with slight core hollowing, contrary to past results and at a somehow lower density than expected (Figure 4.7c). On the other hand, a higher-density ICRF L-mode plasma is displayed in Figure 4.7b, with a co-current peaked rotation profile (Figure 4.7c) and absence of core temperature inversion. This example also contradicts the correlation between occurrence of temperature inversions and changes in the rotation profile, in this case, a hollowing rather than a full inversion.

4.4.3 Temperature Inversions in Zero-rotation Plasmas

Locked modes are magnetic field perturbations in Alcator C-Mod that result in intrinsic rotation braking ($V_{tor} \sim 0$ kHz), degraded confinement, and sawtooth disappearance [51]. Cold pulses were injected into Ohmic (Figure 4.8a) and ICRF-heated (Figure 4.8b) locked-mode plasmas. In contrast to typical sawtoothing plasmas with finite intrinsic rotation, the core temperature inversions were quite large, on the order of 10% and significantly larger than the edge perturbation. This contrasts

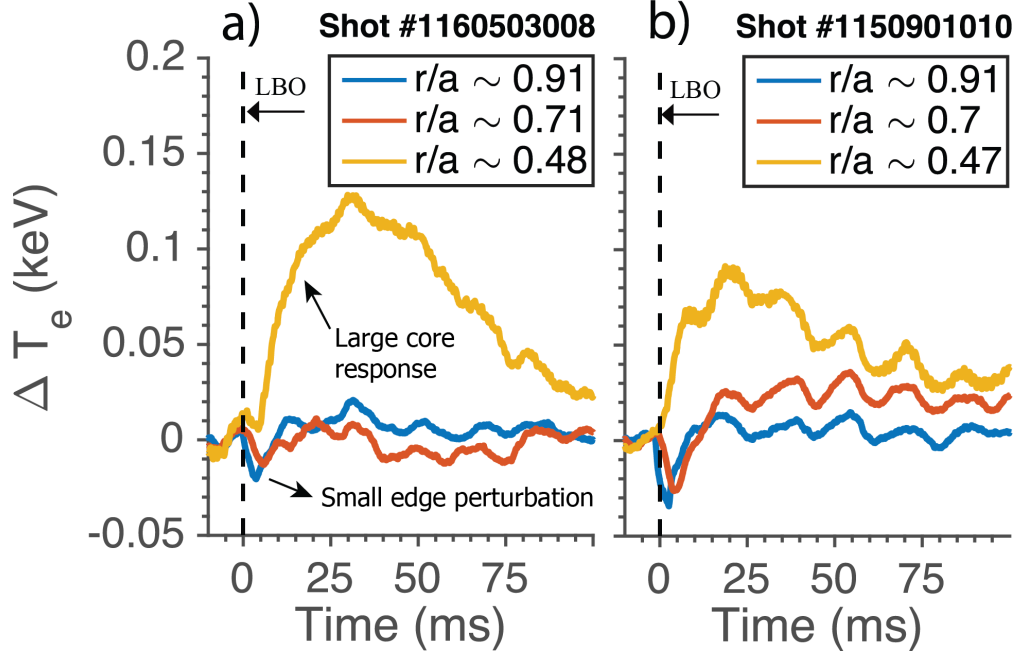


Figure 4.8: Temperature inversion effects in locked mode plasmas with similar densities and different RF heating power are shown. (a) LSN, Ohmic, $I_p = 0.8$ MA, $\langle n_e \rangle = 0.63 \cdot 10^{20} \text{m}^{-3}$, (b) USN, $P_{RF} = 1.2$ MW, $I_p = 0.8$ MA, $\langle n_e \rangle = 0.69 \cdot 10^{20} \text{m}^{-3}$. Large temperature inversions are observed in these shots, which have zero rotation.

with past results in JET [15], where it was reported that the temperature inversion phenomenon disappears in the absence of rotation in low or reversed magnetic shear plasmas in the core region. These new observations from Alcator C-Mod in the locked mode plasmas are intriguing but leave many open questions and will be part of future work to further study the interaction of the heat and momentum channels in these plasmas.

4.5 Other Observations in Alcator C-Mod Cold-Pulse Experiments

4.5.1 Effect of Magnetic Configuration

In Alcator C-Mod, it has been observed that, for the same given plasma parameters (density, net plasma current, input power) and same edge perturbation amplitude (controlled by the size of the ablated spot or number of impurities that go into the plasma) the physics of the perturbative transport in upper-single-null (USN) and lower-single-null (LSN) geometries are different. Figure 4.9a shows the different plasma geometry between two shots in Alcator C-Mod that are otherwise equal to each other ($\bar{n}_{e,104} \sim 0.6 \cdot 10^{20} \text{m}^{-3}$, $I_p = 0.8$ MA).

The change in line-averaged density (Figure 4.9b) and soft x-ray emission (Figure 4.9c) are different in USN and LSN configurations, suggesting that magnetic geometry affect the propagation of particles in these plasmas. Figure 4.9e shows that, for USN, the recovery of the edge temperature

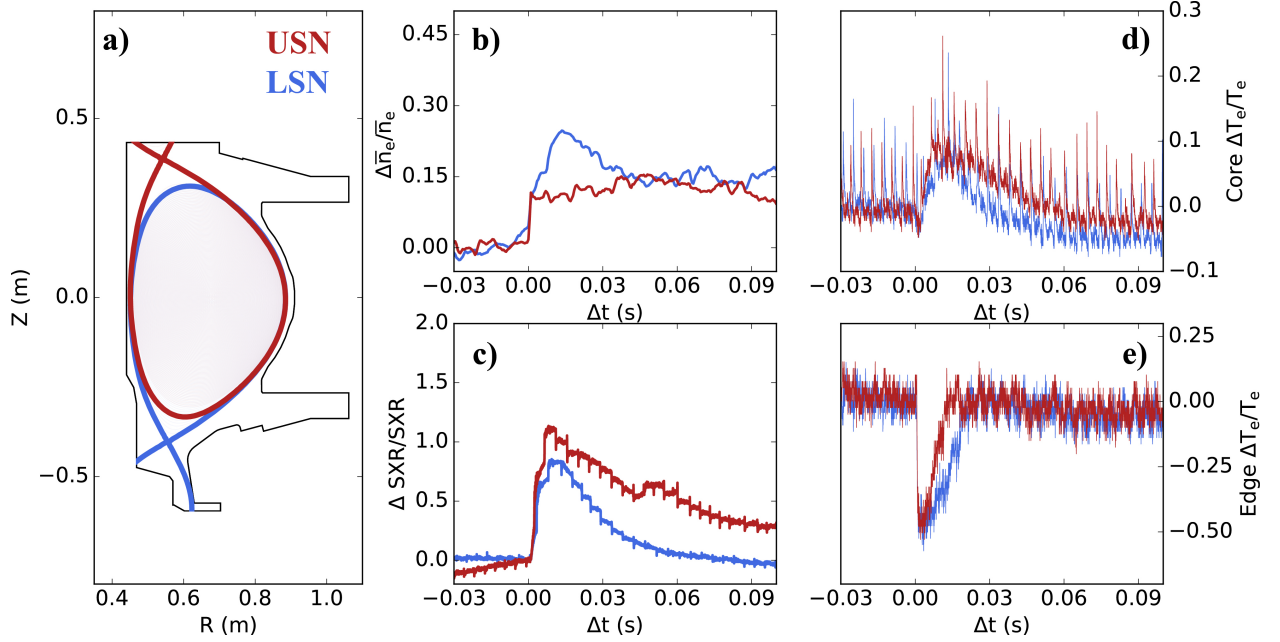


Figure 4.9: Comparison of perturbed quantities for pair of shots #1150903021 (LSN) and #1150903022 (USN). Both plasmas are ohmic, with $\langle n_e \rangle_{104} \sim 0.6 \cdot 10^{20} \text{m}^{-3}$, $I_p = 0.8 \text{ MA}$.

is slower (15 ms vs 25 ms in LSN). In Figure 4.9d we observe that both plasmas display a similar temperature increase, but a slower relaxation is observed in USN.

These observations in different magnetic geometry seem to indicate that the propagation of impurities and electron density perturbation affect the dynamics of the temperature inversion effect.

4.5.2 Effect of Incremental Diffusivity

Early modeling attempts to recreate cold-pulse propagation scenarios [37] suggested that temperature reversals could indeed be exhibited if electron and ion energy channels are characterized by stiff transport models. As described in Section 2.2.2, profile stiffness is usually pictured as an incremental thermal diffusivity, χ_e^{inc} , and perturbative transport techniques allow to determine this value during transient processes. In this case, incremental diffusivity (χ_e^{inc}) has been measured on Alcator C-Mod by tracking the propagation of heat pulses that originate from partial sawtooth crashes [43].

Figure 4.10 shows how the cases that present temperature inversions have higher values of χ_e^{inc} , further confirming that this phenomenon might be due to the nature of turbulent transport. A high-stiffness model was needed in Ref. [37] to reproduce an inversion of core temperature following the edge temperature drop, and this experimental evidence shows, for the first time, that measured stiffness is also correlated with the temperature inversion effect.

Work in ASDEX Upgrade [52] has recently showed that perturbative diffusivity, χ_e^{inc} , is in-

versely proportional to collisionality, which is consistent with the trend of temperature inversions presented here (Figure 4.5). A possible explanation of the reduction of perturbative diffusivity with collisionality is the damping of trapped electron modes and increase in dominance of ion temperature gradient modes. At low collisionality, trapped electron modes are the dominant heat exhaust mechanism for electrons and are driven by both density and electron temperature gradients. As a consequence, changes in electron temperature gradients affect electron heat flux more strongly when trapped electron mode turbulence is dominance, i.e. at low collisionality.

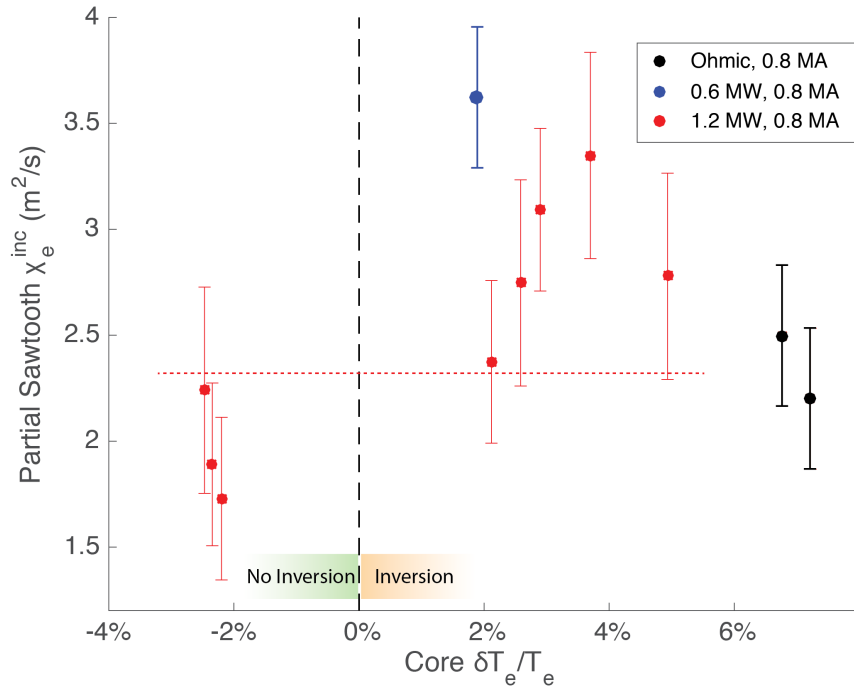


Figure 4.10: Incremental electron thermal diffusivity (χ_e^{inc}) as a function of relative magnitude of core electron temperature perturbation ($\delta T_e / T_e$) following cold-pulse injection for several Alcator C-Mod plasmas.

4.6 Discussion on Experiments in Alcator C-Mod Plasmas

These new results with high-current Ohmic and RF-heated L-mode plasmas challenge the established picture that temperature inversions are correlated with intrinsic rotation reversals. This work also reports observations of temperature inversions in ICRF-heated plasmas and locked-mode plasmas, and shows that this unexplained, often referred to as “non-local” heat transport behavior, will occur with hollow rotation profiles and in plasmas with zero rotation.

This finding raises the question of whether the correlation between temperature inversions and rotation reversals found in low-current Ohmic L-mode plasmas [31] and ECH-heated L-mode plasmas [33] is a result of actual multi-channel transport processes or is only coincidental. Figure 4.5 shows that temperature inversions can exist at very high densities and that there is a decrease in the magnitude of the temperature inversion that is roughly proportional to the line-average density. These observations, along with the abruptness that characterizes the rotation reversals [47] and the existence of large temperature inversions in zero-rotation scenarios (Figure 4.8) suggest that these heat and momentum transport effects may be driven by different mechanisms.

As a result of these experimental observations, modeling of cold-pulse dynamics will be performed in the next chapter by ignoring the prediction of momentum transport and thus the evolution of rotation during the simulated cold-pulse propagation. In practice, the intrinsic rotation profile before the cold pulse will be imposed from experimental measurements in Alcator C-Mod, and assumed constant in the simulation.

Bibliography

- [1] K. Ida et al. Towards an emerging understanding of non-locality phenomena and non-local transport. *Nucl. Fusion*, 55(1):013022, 2015. URL <http://stacks.iop.org/0029-5515/55/i=1/a=013022>.
- [2] N J Lopes Cardozo. Perturbative transport studies in fusion plasmas. 37(8):799–852, aug 1995. doi: 10.1088/0741-3335/37/8/001. URL <https://doi.org/10.1088%2F0741-3335%2F37%2F8%2F001>.
- [3] M.W. Kissick et al. Transient electron heat diffusivity obtained from trace impurity injection on tftr. *Nucl. Fusion*, 34(3):349, 1994. URL <http://stacks.iop.org/0029-5515/34/i=3/a=I03>.
- [4] K. W. Gentle et al. Strong nonlocal effects in a tokamak perturbative transport experiment. *Phys. Rev. Lett.*, 74:3620–3623, 1995. URL <https://link.aps.org/doi/10.1103/PhysRevLett.74.3620>.
- [5] K. W. Gentle et al. An experimental counter-example to the local transport paradigm. *Phys. Plasmas*, 2(6):2292–2298, 1995. URL <http://dx.doi.org/10.1063/1.871252>.
- [6] K. W. Gentle et al. The evidence for nonlocal transport in the texas experimental tokamak. *Phys. Plasmas*, 4(10):3599–3613, 1997. URL <http://dx.doi.org/10.1063/1.872255>.
- [7] M.W. Kissick et al. Non-local component of electron heat transport in tftr. *Nucl. Fusion*, 36(12):1691, 1996. URL <http://stacks.iop.org/0029-5515/36/i=12/a=I09>.
- [8] M.W. Kissick et al. Conditions and behaviour related to non-local electron heat transport on tftr. *Nucl. Fusion*, 38(6):821, 1998. URL <http://stacks.iop.org/0029-5515/38/i=6/a=304>.
- [9] T. Dudok de Wit et al. Self-consistent removal of sawtooth oscillations from transient plasma data by generalized singular value decomposition. *Phys. Plasmas*, 5(5):1360–1368, 1998. URL <https://doi.org/10.1063/1.872796>.
- [10] X L Zou et al. *Plasma Physics and Controlled Fusion*, 42(10):1067–1076, oct 2000. doi: 10.1088/0741-3335/42/10/305. URL <https://doi.org/10.1088%2F0741-3335%2F42%2F10%2F305>.
- [11] P. Mantica et al. Nonlocal transient transport and thermal barriers in rijnhuizen tokamak project plasmas. *Phys. Rev. Lett.*, 82:5048–5051, 1999. URL <https://link.aps.org/doi/10.1103/PhysRevLett.82.5048>.
- [12] P Galli et al. Non-local response of rtp ohmic plasmas to peripheral perturbations. *Nuclear Fusion*, 39(10):1355–1368, oct 1999. doi: 10.1088/0029-5515/39/10/301. URL <https://doi.org/10.1088%2F0029-5515%2F39%2F10%2F301>.

- [13] G M D Hogewei et al. Recording non-local temperature rise in the RTP tokamak. *Plasma Physics and Controlled Fusion*, 42(10):1137–1144, oct 2000. doi: 10.1088/0741-3335/42/10/310. URL <https://doi.org/10.1088/0741-3335/42/10/310>.
- [14] F. Ryter et al. Propagation of cold pulses and heat pulses in asdex upgrade. *Nucl. Fusion*, 40(11):1917, 2000. URL <http://stacks.iop.org/0029-5515/40/i=11/a=311>.
- [15] P Mantica et al. Perturbative transport experiments in jet low or reverse magnetic shear plasmas. *Plasma Phys. Control. Fusion*, 44(10):2185, 2002. URL <http://stacks.iop.org/0741-3335/44/i=10/a=308>.
- [16] N. Tamura et al. Observation of core electron temperature rise in response to an edge cooling in toroidal helical plasmas. *Physics of Plasmas*, 12(11):110705, 2005. doi: 10.1063/1.2131047. URL <https://doi.org/10.1063/1.2131047>.
- [17] S Inagaki et al. Abrupt reduction of core electron heat transport in response to edge cooling on the large helical device. *Plasma Phys. Control. Fusion*, 48(5A):A251, 2006. URL <http://stacks.iop.org/0741-3335/48/i=5A/a=S23>.
- [18] N. Tamura et al. Impact of nonlocal electron heat transport on the high temperature plasmas of lhd. *Nucl. Fusion*, 47(5):449, 2007. URL <http://stacks.iop.org/0029-5515/47/i=5/a=009>.
- [19] N. Tamura et al. Edge-core interaction revealed with dynamic transport experiment in lhd (exc/p8-16). *International Atomic Energy Agency (IAEA)*, (IAEA-CN–180), 2010. URL http://www-pub.iaea.org/MTCD/Meetings/PDFplus/2010/cn180/cn180_BookOfAbstracts.pdf.
- [20] S Inagaki et al. Characterization of bifurcation induced by long distance correlation between heat flux and temperature gradient in toroidal plasmas. *Plasma Physics and Controlled Fusion*, 52(7):075002, may 2010. doi: 10.1088/0741-3335/52/7/075002. URL <https://doi.org/10.1088/0741-3335/52/7/075002>.
- [21] S. Inagaki et al. Observation of long-distance radial correlation in toroidal plasma turbulence. *Phys. Rev. Lett.*, 107:115001, 2011. URL <https://link.aps.org/doi/10.1103/PhysRevLett.107.115001>.
- [22] R O Dendy et al. Modelling the measured local time evolution of strongly nonlinear heat pulses in the large helical device. *Plasma Physics and Controlled Fusion*, 55(11):115009, oct 2013. doi: 10.1088/0741-3335/55/11/115009. URL <https://doi.org/10.1088/0741-3335/55/11/115009>.
- [23] H. Zhu et al. A quantitative model for heat pulse propagation across large helical device plasmas. *Physics of Plasmas*, 22(6):062308, 2015. doi: 10.1063/1.4923307. URL <https://doi.org/10.1063/1.4923307>.

- [24] H.J. Sun et al. Observation of non-local transport phenomena with SMBI in HL-2a. *Chinese Physics Letters*, 24(9):2621–2623, aug 2007. doi: 10.1088/0256-307x/24/9/044. URL <https://doi.org/10.1088%2F0256-307x%2F24%2F9%2F044>.
- [25] X.R. Duan et al. Overview of experimental results on hl-2a. *Nucl. Fusion*, 49(10):104012, 2009. URL <http://stacks.iop.org/0029-5515/49/i=10/a=104012>.
- [26] Hong-Juan Sun et al. Experiment of non-local effect with smbi on hl-2a. *Plasma Phys. Control. Fusion*, 52(4):045003, 2010. URL <http://stacks.iop.org/0741-3335/52/i=4/a=045003>.
- [27] H.J. Sun et al. Experimental evidence of the non-local response of transport to peripheral perturbations. *Nuclear Fusion*, 51(11):113010, oct 2011. doi: 10.1088/0029-5515/51/11/113010. URL <https://doi.org/10.1088%2F0029-5515%2F51%2F11%2F113010>.
- [28] O. Pan et al. Evidence of enhanced self-organized criticality (soc) dynamics during the radially non-local transient transport in the hl-2a tokamak. *Nucl. Fusion*, 55(11):113010, 2015. URL <http://stacks.iop.org/0029-5515/55/i=11/a=113010>.
- [29] W. Chen et al. Dynamics between the fishbone instability and nonlocal transient transport in hl-2a nbi plasmas. *Nucl. Fusion*, 56(4):044001, 2016. URL <http://stacks.iop.org/0029-5515/56/i=4/a=044001>.
- [30] X Q Ji et al. On the interplay between neoclassical tearing modes and nonlocal transport in toroidal plasmas. *Scientific Reports*, 6:32697, 2016. URL <https://www.nature.com/articles/srep32697>.
- [31] J.E. Rice et al. Non-local heat transport, rotation reversals and up/down impurity density asymmetries in alcator c-mod ohmic l-mode plasmas. *Nucl. Fusion*, 53(3):033004, 2013. URL <http://stacks.iop.org/0029-5515/53/i=3/a=033004>.
- [32] C. Gao et al. Non-local heat transport in alcator c-mod ohmic l-mode plasmas. *Nucl. Fusion*, 54(8):083025, 2014. URL <http://stacks.iop.org/0029-5515/54/i=8/a=083025>.
- [33] Y.J. Shi et al. Intrinsic rotation reversal, non-local transport, and turbulence transition in kstar l-mode plasmas. *Nuclear Fusion*, 57(6):066040, 2017. URL <http://stacks.iop.org/0029-5515/57/i=6/a=066040>.
- [34] Yuejiang Shi et al. Observation of multi-channel non-local transport in j-text plasmas. *Nuclear Fusion*, 58(4):044002, 2018. URL <http://stacks.iop.org/0029-5515/58/i=4/a=044002>.
- [35] Y. J. Shi et al. Observation of non-local effects in ion transport channel in j-text plasmas. *arXiv:1810.07529*, 2018. URL <https://arxiv.org/abs/1810.07529>.
- [36] Yong Liu et al. Dynamics of cold pulses induced by super-sonic molecular beam injection in the EAST tokamak. *Nuclear Fusion*, 59(4):044005, mar 2019. doi: 10.1088/1741-4326/ab0665. URL <https://doi.org/10.1088%2F1741-4326%2Fab0665>.

- [37] J. E. Kinsey et al. Theoretical transport modeling of ohmic cold pulse experiments. *Phys. Plasmas*, 5(11):3974–3981, 1998. URL <http://dx.doi.org/10.1063/1.873117>.
- [38] C. Angioni et al. Intrinsic toroidal rotation, density peaking, and turbulence regimes in the core of tokamak plasmas. *Phys. Rev. Lett.*, 107:215003, Nov 2011. doi: 10.1103/PhysRevLett.107.215003. URL <https://link.aps.org/doi/10.1103/PhysRevLett.107.215003>.
- [39] P.J.L O’Shea et al. In *Proc. 11th Conf. on Radio Frequency Power in Plasmas*, volume 403 (AIP), page 89, 1997.
- [40] J. H. Irby et al. Two-color interferometer system for alcator c-mod. *Rev. Sci. Instrum*, 59(8): 1568–1570, 1988. URL <http://dx.doi.org/10.1063/1.1140199>.
- [41] M. L. Reinke et al. X-ray imaging crystal spectroscopy for use in plasma transport research. *Rev. Sci. Instrum*, 83(11), 2012. URL <http://dx.doi.org/10.1063/1.4758281>.
- [42] A. Ince-Cushman et al. Spatially resolved high resolution x-ray spectroscopy for magnetically confined fusion plasmas. *Rev. Sci. Instrum*, 79(10):10E302, 2008. URL <http://dx.doi.org/10.1063/1.2968707>.
- [43] A.J. Creely et al. Perturbative thermal diffusivity from partial sawtooth crashes in alcator c-mod. *Nucl. Fusion*, 56(3):036003, 2016. URL <https://doi.org/10.1088/0029-5515/56/3/036003>.
- [44] N. T. Howard et al. Characterization of impurity confinement on alcator c-mod using a multi-pulse laser blow-off system. *Rev. Sci. Instrum*, 82(3), 2011. URL <http://dx.doi.org/10.1063/1.3565448>.
- [45] J.E. Rice et al. Inter-machine comparison of intrinsic toroidal rotation in tokamaks. *Nuclear Fusion*, 47(11):1618–1624, oct 2007. doi: 10.1088/0029-5515/47/11/025. URL <https://doi.org/10.1088/0029-5515/47/11/025>.
- [46] P.H. Diamond et al. Physics of non-diffusive turbulent transport of momentum and the origins of spontaneous rotation in tokamaks. *Nuclear Fusion*, 49(4):045002, mar 2009. doi: 10.1088/0029-5515/49/4/045002. URL <https://doi.org/10.1088/0029-5515/49/4/045002>.
- [47] J.E. Rice et al. Observations of core toroidal rotation reversals in alcator c-mod ohmic l-mode plasmas. *Nuclear Fusion*, 51(8):083005, jun 2011. doi: 10.1088/0029-5515/51/8/083005. URL <https://doi.org/10.1088/0029-5515/51/8/083005>.
- [48] M L Reinke et al. Density sensitivity of intrinsic rotation profiles in ion cyclotron range of frequency-heated l-mode plasmas. *Plasma Physics and Controlled Fusion*, 55(1):012001, dec 2012. doi: 10.1088/0741-3335/55/1/012001. URL <https://doi.org/10.1088/0741-3335/55/1/012001>.

- [49] A. E. White et al. Multi-channel transport experiments at alcator c-mod and comparison with gyrokinetic simulations. *Physics of Plasmas*, 20(5):056106, 2013. doi: 10.1063/1.4803089. URL <https://doi.org/10.1063/1.4803089>.
- [50] J. E. Rice et al. Rotation reversal bifurcation and energy confinement saturation in tokamak ohmic *l*-mode plasmas. *Phys. Rev. Lett.*, 107:265001, Dec 2011. doi: 10.1103/PhysRevLett.107.265001. URL <https://link.aps.org/doi/10.1103/PhysRevLett.107.265001>.
- [51] S. M. Wolfe et al. Nonaxisymmetric field effects on alcator c-mod. *Physics of Plasmas*, 12(5):056110, 2005. doi: 10.1063/1.1883665. URL <https://doi.org/10.1063/1.1883665>.
- [52] A.J. Creely et al. Validation study of gene on asdex upgrade using perturbative thermal diffusivity measured with partial sawtooth heat pulses. *Nuclear Fusion*, 58(12):126001, 2018. URL <http://stacks.iop.org/0029-5515/58/i=12/a=126001>.

Chapter 5

Modeling of Alcator C-Mod Cold Pulses

“Transient transport phenomena have also posed a significant challenge to be explained by the theory and modelling community. [...] In perturbative experiments with cold edge pulses, the observed fast radial propagation of the pulses from the plasma edge to the core has been a challenge to be explained by local diffusive transport models.”

Doyle et al., *Nuclear Fusion*, (ITER Physics Basis), 2007

Chapter 4 presented an enigmatic but universal transient transport phenomenon in fusion plasmas that has challenged the standard local model of transport: an increase of core temperature associated with edge cooling on timescales faster than the energy confinement time [2, 3]. In Chapter 2, the ideas behind turbulent transport were discussed, leading to the conclusion that drift-wave-type turbulence, generally found to be the main mechanism of cross-field transport in tokamaks, should follow a local closure and diffusive-like behavior. Therefore, it is of vital importance to understand whether temperature inversions after cold-pulse injections can be explained with local models or nonlocal dynamics need to be explored.

This Chapter demonstrates that cold-pulse phenomena in tokamak plasmas can be explained by local transport models, including the disappearance of the core temperature inversions at high density and the effect of plasma current. While nonlocal effects may exist in some fusion devices, the study of cold pulse behavior in tokamaks will be shown to be well reproduced by local transport models. The quasilinear transport models considered are widely applied for predictions of equilibrium pressure profiles [4, 5]. Specifically, we use the recently developed Trapped-Gyro-Landau-Fluid model (TGLF), which contains a rule for the turbulence saturation (TGLF-SAT1) where the zonal flow mixing, rather than shearing, is the primary saturation mechanism of both ion and electron scale turbulence [6, 7], as explained in detail in Section 3.3.

5.1 Propagation of Temperature Pulses

When a temperature pulse propagates through the plasma, the turbulence state and transport characteristics at every radial position are important. Figure 5.1 schematically depicts the physics of an inward cold-pulse propagation. A drop in electron temperature at the edge of the plasma (e.g. due to a localized increase in radiated power losses) causes an increase in normalized electron temperature gradient in the inward portion of the pulse, which will be referred to as the “propagating front”. Such increase in a driving gradient destabilizes turbulence and could potentially trigger instabilities that were marginally stable before the cold-pulse was injected, thus enhancing the electron heat flux via the mechanisms discussed in Section 2.1.2. Such quick enhancement of cross-field electron heat transport reduces the electron stored energy for constant input power, thus causing the drop in temperature in the propagating front region.

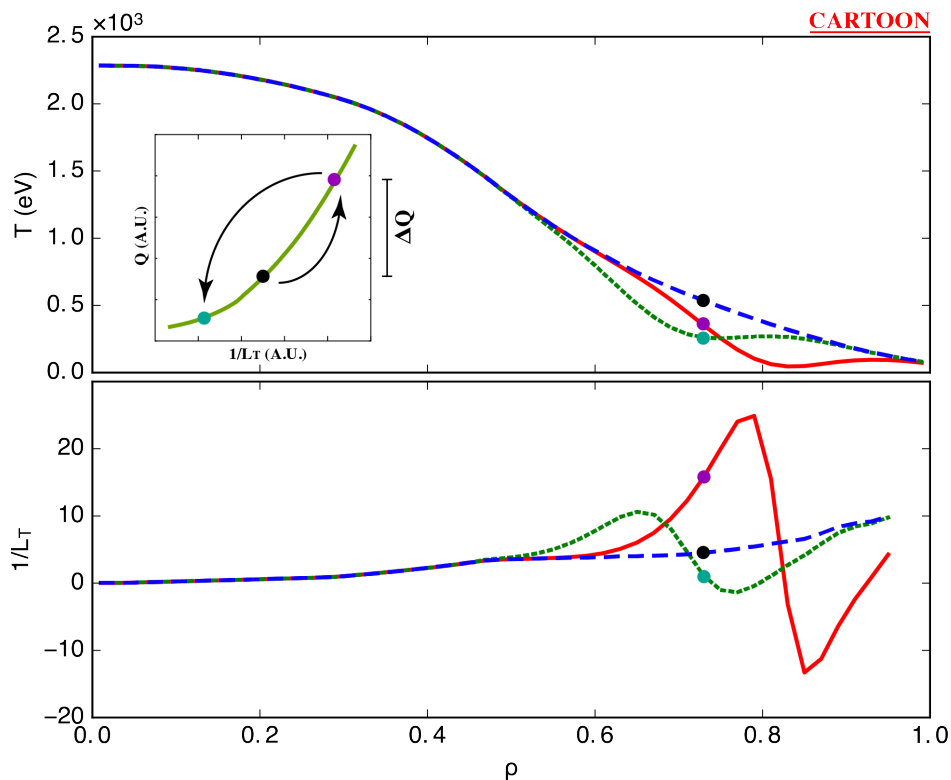


Figure 5.1: Schematic of inward cold-pulse propagation. Perturbation in (top) temperature profile and (bottom) inverse temperature gradient scale length. Subplot in top figure shows the typical form of gradient-driven heat flux curve. Color points indicate same radial location at different times.

This process happens all over the plasma profile, thus resembling the propagation of a cold-pulse from edge to core. Given the fast decorrelation time of plasma turbulence ($\sim 1/\gamma \sim 10 \mu\text{s}$), the heat flux profile quickly responds to changes in the gradients. If the plasma is very stiff (i.e. high χ_e^{inc}), the heat flux increases significantly with small changes in the driving gradients, allowing for the seemingly very fast propagation of cold pulses.

The goal of this Chapter is to introduce artificial perturbations (but consistent with experiment) to otherwise steady-state temperature profiles in integrated modeling simulations. In the next section, the specific details on how to run these perturbative transport simulations are presented.

5.2 Transport Simulation Settings

Here we describe modeling of one dedicated experiment at Alcator C-Mod [8], which exhibits the cold-pulse phenomena observed ubiquitously in fusion plasmas. Such experiment was described in Chapter 4, specifically in Figure 4.2. In following subsections, numerical experiments are also performed based on the low-density condition reported in Figure 4.2. Around this condition, scans of electron density and plasma current are performed, to resolve whether the model captures the observed trends of temperature inversions with changes in electron density, plasma current and safety factor profile. Following the literature [8], plasma current effects will be tested for $I_p = 0.55$ MA (low), 0.8 MA (medium) and 1.1 MA (high). Likewise, volume-averaged density will cover a range $\langle n_e \rangle \approx 0.5 - 1.5 \cdot 10^{20} \text{m}^{-3}$, which is close to the observed cold-pulse transition for Alcator C-Mod plasmas. For these scans, poloidal field diffusion will be self-consistently solved, along with the introduction of sawteeth crashes to prevent current peaking and unrealistic on-axis temperature profiles.

In the simulations, implicit transport equations are solved using the PT_SOLVER numerical scheme [9] integrated with the TRANSP power balance code [10, 11]. The time dependent evolution of the highly non-linear and stiff equations for electron and ion temperatures are solved using Newton iterations over 200 equally spaced radial zones and adaptive time-steps. Neoclassical transport is estimated using the Chang-Hinton analytic model [12], and turbulent transport fluxes are calculated using the Trapped Gyro-Landau Fluid (TGLF) quasilinear model [13, 14], with a saturation rule that accounts for cross-scale coupling physics (TGLF-SAT1) [6, 7]. The experimental ion and electron temperatures at radial position $\rho_N = 0.9$ (square root of the normalized toroidal flux), taken prior to the cold-pulse injection, are used as boundary conditions for the transport model. We have made sure that this choice does not compromise convergence of the transport solver in the outer radii when plasma parameters vary. No transport enhancement factors are included, in order to test the actual transport physics within the model. The poloidal wavenumber grid (k_θ) normalized at each radius by the ion acoustic gyroradius (ρ_s) for the turbulent transport simulations is chosen from $k_\theta \rho_s \approx 0.1$ up to $k_\theta \rho_s \approx 24.0$.

The MHD equilibrium is solved using the TEQ library [15], with fixed plasma boundary. This is motivated by the fact that changes in plasma position or magnetic flux surfaces due to impurity injections were demonstrated experimentally to be too small to affect the core temperature response or measurement [16, 17].

As the cold pulse propagates, total plasma current and applied magnetic field are kept constant in time. Because the inward propagation of the density perturbation is constrained in this work

by the line-average density alone, propagation speed of cold pulses is not addressed here. Recent work at ASDEX Upgrade [18] has been devoted to investigating this issue, confirming that the density pulse propagation is indeed captured in TGLF simulations. Work in DIII-D, which will be presented in Chapter 6 also explores the propagation of density pulses from the experimental standpoint, confirming the existence of fast, inwardly-propagating electron density perturbation.

As indicated in Section 4.6 following the conclusions from Chapter 4, the intrinsic rotation profile before the cold pulse will be imposed from experimental measurements. This is motivated by the observations that the core transport behavior (temperature inversion *v.s.* standard drop) does not change during rotation reversals and hollowing, or in zero rotation scenarios.

Specific Assumptions and Settings for Density and Current Scans

Simulations of density and net current scans (Sections 5.4, 5.5 and 5.6) require additional assumptions. To limit the complexity of the simulations and ease the interpretation of the results, the ion effective charge Z_{eff} is assumed unchanged during the density and current ramps, as well as the impurity fractional content and the density gradient inverse scale lengths a/L_n (except at the cold-pulse injection times, when impurities are injected and travel inwards, as will be explained in Section 5.2.1). During parameter scans, intrinsic rotation is assumed co-current and unchanged during cold-pulse injections and parameter scans. In terms of the intrinsic rotation, Section 4.4 showed no changes in the core response during rotation reversals, and suggested that momentum transport may not play a role in the phenomenology of temperature inversions. Recent work in J-TEXT [19] has showed that plasma rotation can change as a consequence of the cold-pulse injection, but it is likely a consequence of the change in dominant micro-instability and core turbulence state as the cold pulse travels inwards, rather than a cause of the temperature inversion.

5.2.1 Perturbations after Laser Blow-Off Injections

Once the steady-state temperature profiles are obtained, we introduce a time-evolving cold-pulse in the simulation by accounting for two major effects observed in the experiment: enhanced radiation losses and impurity density perturbation. Both effects are introduced as inputs with the simplified perturbation model described in Section 3.4.3 (Figure 5.2a), using the experimental constraints of the measured total radiated power and line-averaged density, as shown in Figure 5.2b. The radiative sink is localized at the periphery of the plasma (peaked at $\rho_N \simeq 0.95$), in order to reproduce the experimentally measured increase in total radiated power. The impurity density evolution is modeled as an inwardly propagating skewed-Gaussian, by self-consistently varying Z_{eff} and electron density profiles, such that main ion density remains constant during the injection. This technique for introducing the cold-pulse in the simulation is used in order to self-consistently model the onset of the electron and ion temperature perturbations. This is a critical difference with past work using quasilinear models [20, 21], in which the edge temperatures were often manually

adjusted outside of experimentally relevant ranges to produce the desired amplitude of the core temperature inversion.

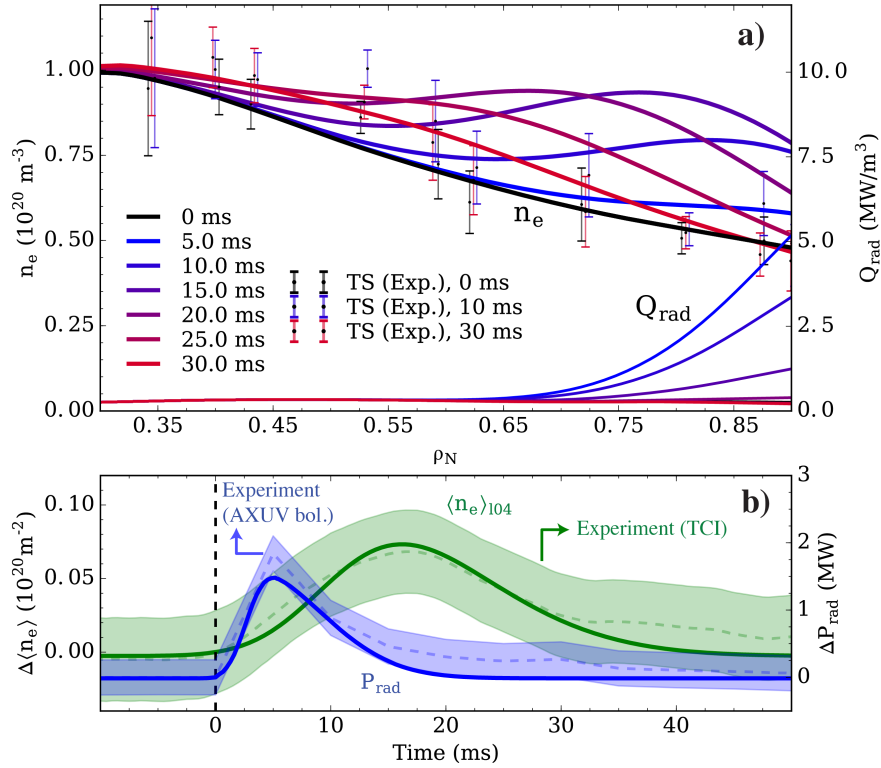


Figure 5.2: Low-density plasma. (a) Density perturbation and radiative sink introduced to model cold-pulse injection. (b) Simulated and experimental changes in line-integrated density (error bar calculated from low frequency subtraction errors) and total radiated power (error bar estimated from Ref. [22]). Density profile was measured using a Thomson scattering (TS) system. Line-integrated density was determined from a two-color interferometer (TCI). Total radiated power was measured by an absolute extreme ultraviolet (AXUV) bolometer.

Using the simulation settings presented earlier in this section, along with the perturbations from Figure 5.2, the propagation physics of cold pulses in low and high density is studied. Next section presents the results from these simulations, including scans in plasma current and density.

5.3 Simulation Results in Low and High Density Plasmas

Figs. 5.3a and 5.3b show simulated electron and ion temperatures in steady-state at low and high density, $\langle n_e \rangle \simeq 0.8 \cdot 10^{20} \text{ m}^{-3}$ and $\langle n_e \rangle \simeq 1.1 \cdot 10^{20} \text{ m}^{-3}$, respectively. In this simulation, turbulent transport is modeled using TGLF-SAT1, with a standard $k_{\theta} \rho_s$ -grid to account for contributions up to $k_{\theta} \rho_s = 24.0$. At the position of interest, $\rho_N \approx 0.36$ (where experimental measurements show the inversion behavior), both electron and ion temperature steady-state profiles are within two-sigma experimental error bars.

First, we investigate the low-density condition, where the core temperature inversion is observed

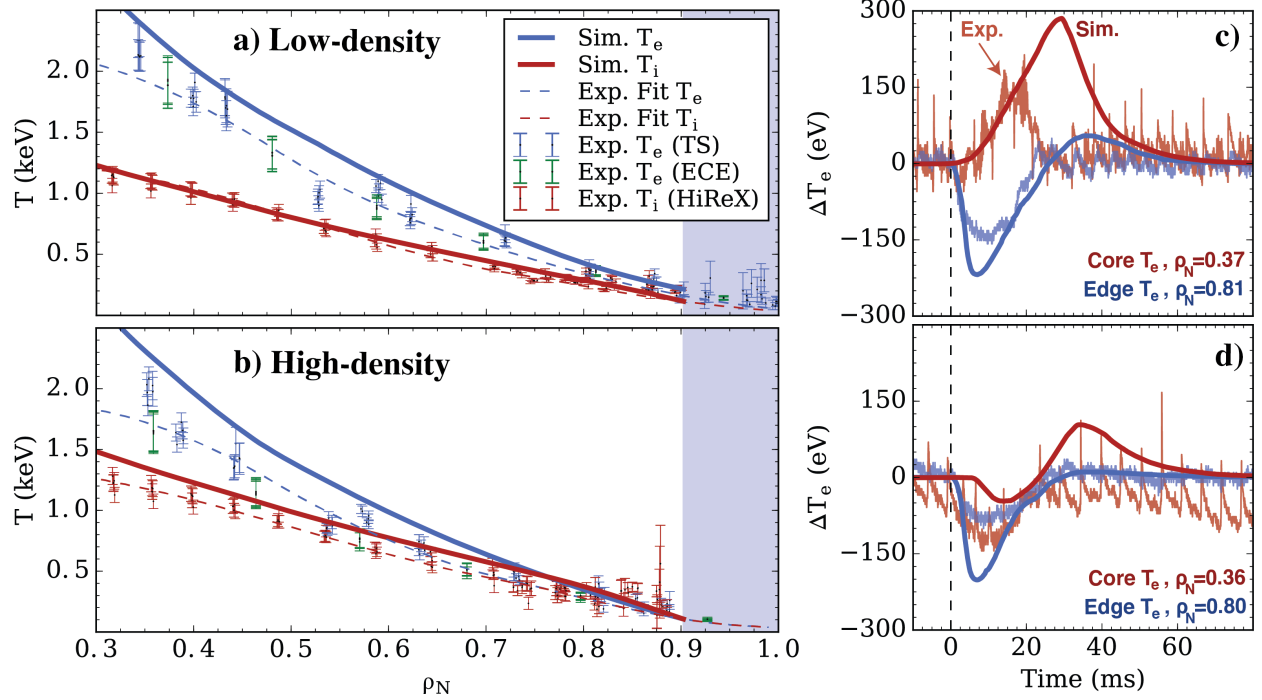


Figure 5.3: Steady-state ion and electron temperature profiles in experiment and simulation (TGLF-SAT1) for (a) low-density and (b) high-density. Evolution of edge and core electron temperature after cold-pulse injection for (c) low-density and (d) high-density. Experimental electron and ion temperature traces were determined from electron cyclotron emission (ECE) and a high-resolution imaging x-ray spectrometer (HiReX) system, respectively.

experimentally, by comparing the simulated transient behavior of the electron temperature after the cold-pulse injection to the experiment, using TGLF-SAT1 (Figure 5.3c). To be conservative, we define an onset time for the core temperature (in both the simulation and the experiment) to be the time at which the mean value has increased by more than one experimental standard deviation (27 eV). The experimental onset time is 7 ms, and the experimental energy confinement time is 22 ms. The onset time is also calculated in the simulation to be 7 ms, but the energy confinement time is 39 ms (due to the systematic overprediction of steady-state electron temperature). Hence, the simulation captures the “prompt” response (faster than energy confinement time¹) of the core temperature to the edge perturbation. Past work [20] using several quasilinear transport models, including GLF23 [23] the predecessor to TGLF, was unable to create core temperature inversions of high enough magnitude to match the observed peak temperature.

In our case, predictions for the core temperature evolution reach the experimental peak value at 16 ms, and continue to rise higher than the peak experimental value. Because the background equilibrium predicted by the simulation (see Figure 5.3a) is at a lower collisionality due to the overpredicted electron temperature for fixed density, it causes the simulated inversion to achieve

¹Direct comparison between transient phenomena and steady-state properties (diffusive time-scales) is only mentioned here for historical reasons. As posed in Section 2.2, incremental and power balance diffusivities can be very different from each other.

higher peak values before decay, and to last longer, consistent with experimental trends [24]. The edge temperature drop is overpredicted, outside error bars, in the simulations. We have run cases in which the modeled edge drop and core inversion are forced to match the experiment. In these cases, the density perturbation and the radiated power are inconsistent with the experimental measurements. Next, detail investigation of the low and high density plasmas is presented, in order to understand what turbulence physics is relevant to the temperature inversion effect.

5.3.1 Detailed Investigation of Low-Density Plasma

In order to interpret these results and understand the origin of the cold-pulse phenomena, we consider the changes in electron and ion transport and subsequent changes in the power balance terms in the TGLF-SAT1 simulation. Collisional equilibration comes into play as a source or sink of stored energy for ions and electrons, but our modeling shows that it is not the dominant contribution in the low collisionality plasmas where the core temperature inversions appear. This is one of the main differences with respect to past integrated modeling approaches [20, 21, 25], where the collisional equilibration was a dominant mechanism in creating an inversion. Instead, these results show that **core turbulence stabilization due to a reduction of the driving gradients** plays the dominant role. Given that heat fluxes can be driven by a variety of micro-instabilities that can have dependencies on electron temperature (a/L_{T_e}), ion temperature (a/L_{T_i}) and density (a/L_n) gradients, the three channels are coupled.

Figure 5.4a duplicates Figure 5.3c, with dashed lines indicating time points of interest, and Figure 5.4b shows the time evolution of edge and core ion temperature. Figures 5.4c and 5.4d depict the evolution of the core gradients and their effect on the total conducted power profile, respectively. Drops in both a/L_n and a/L_{T_i} stabilize turbulence and therefore reduce the conducted power losses. Such a drop in the conducted power leads to a transient increase in the stored energy, as shown in Figure 5.4e. The time-derivative of the electron stored energy, $\frac{\partial W}{\partial t}$ (where $W = \frac{3}{2}n_e T_e$), traces the opposite evolution to the conducted power density, $\nabla \cdot \vec{q}_e$, which means that changes in transport dominate the time behavior. This interplay between channels depends on the turbulence at each radial position during the propagation of the cold-pulse. Figure 5.4f depicts the reduction of the growth rates of the most unstable mode at the core of the plasma following the cold-pulse arrival. In this case, the plasma core is observed to be dominated by trapped electron modes, which are stabilized by the a/L_n reduction. It is worth pointing out that the onset time of core T_e , although faster than the energy confinement time, is slow compared to the turbulence decorrelation time, estimated as $1/\gamma_{low-k} \sim 6.5\mu s$ from TGLF at the low-k maximum ($k_\theta \rho_s \sim 0.7$). We note that this peak is consistent with strong TEM activity.

Simulated ion response is also qualitatively consistent with experimental observations here and previously at C-Mod [26]. The simulations recover a small, late increase in the core T_i (Figure 5.4b), as well as an increase in T_i at the edge, which arises due to the stabilization of turbulence. In contrast to the electron temperature, which is measured in the experiment with a time resolution of 0.05 ms,

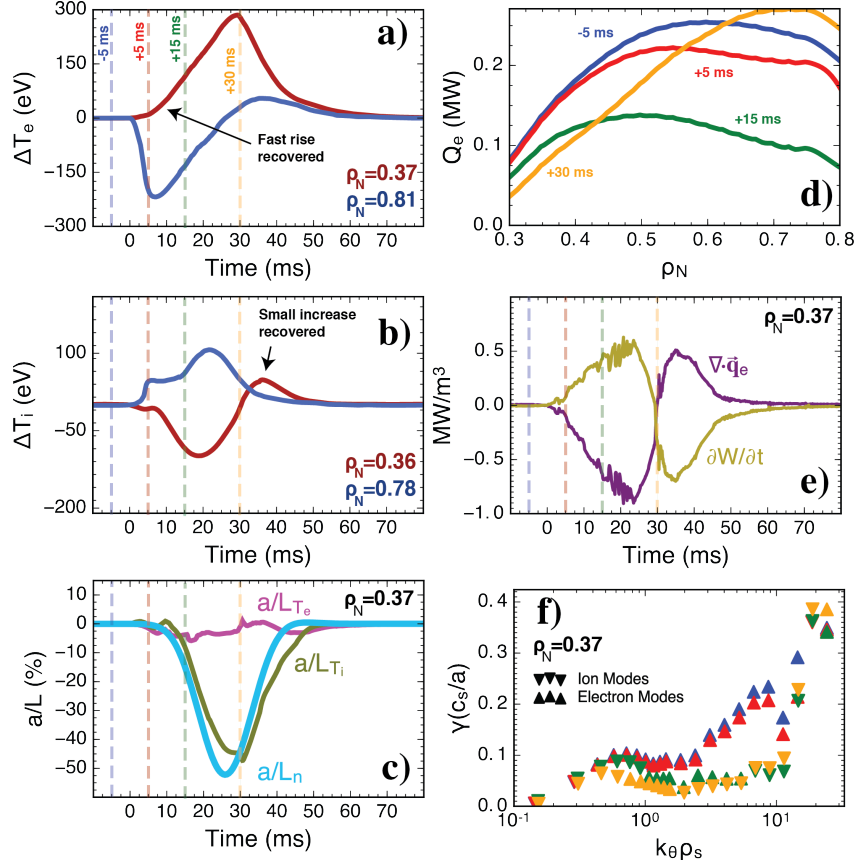


Figure 5.4: Simulation results at low-density. (a) Edge and core electron temperature; (b) Edge and core ion temperature; (c) Normalized gradient scale lengths; (d) Volume-integrated electron heat flux at different times after the injection; (e) Change in conducted electron power density and rate of increase of stored energy; (f) Growth rates of most unstable mode (same color code as in (d)).

the time resolution of the measured ion temperature was 24 ms, making it challenging to perform direct comparison of timing of core and edge ion temperature rises. This work, however, does show that a large core ion temperature increase is not needed to recover the electron temperature inversion, contrary to past modeling work [20] and consistent with the fact that a temperature increase in the electron channel is observed in other experiments regardless of the ion response [21, 27], especially in such regimes with de-coupled ions and electrons.

5.3.2 Detailed Investigation of High-Density Plasma

Having shown the cold pulse dynamics associated with a temperature inversion, next we test the model for high for the “standard” diffusive response (Figure 5.3d). In the experimental discharge, the density was increased by 37%, and a second cold-pulse was injected, which leads to the standard core drop (Figure 4.2c). Figures 5.5a and 5.5b show the simulation time histories of electron and ion temperature, respectively, with times of interest marked again by dashed lines. The simulated drop in the core (red trace) in Figure 5.5a is lower than the experimental core drop

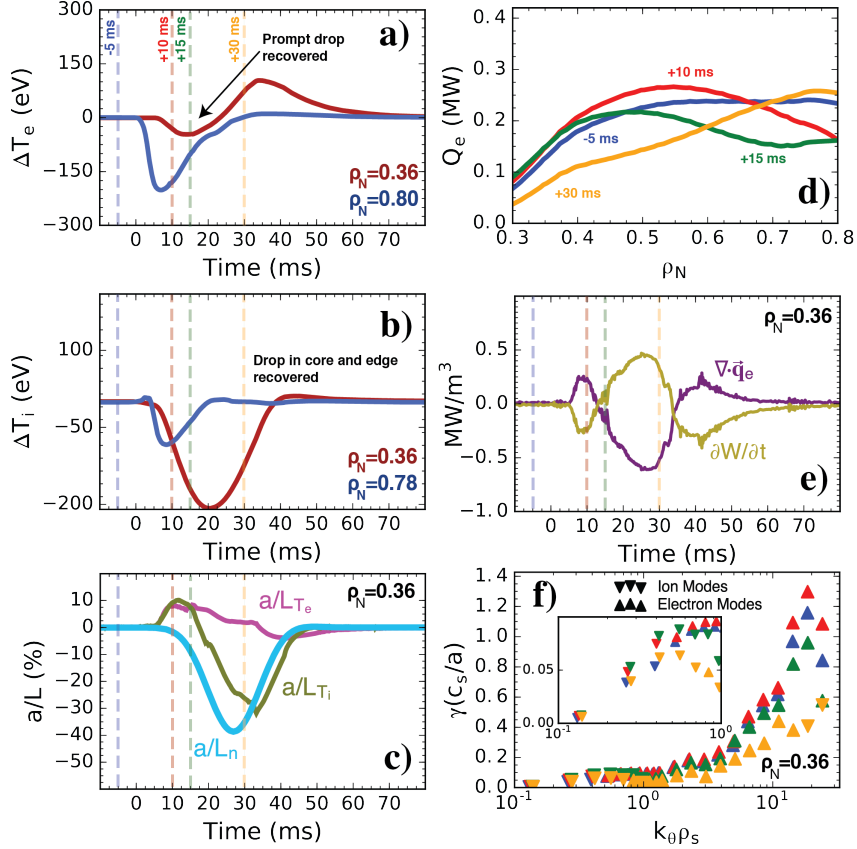


Figure 5.5: Simulation results at high-density. (a) Edge and core electron temperature; (b) Edge and core ion temperature; (c) Normalized gradient scale lengths; (d) Volume-integrated electron heat flux at different times after the injection; (e) Change in conducted electron power density and rate of increase of stored energy; (f) Growth rates of most unstable mode.

(Figure 5.3d), outside of error bars. The minimum core temperature occurs 14 ms after the injection in the simulation, and 10 ms in the experiment. The simulated drop in the edge (blue trace) in Figure 5.5a is larger than the experimental drop. The minimum edge temperature occurs 7 ms after the injection in the simulation, and 10 ms in the experiment. Hence, the simulation at high-density does not capture quantitatively the experimental magnitudes and time-scales. It does, however, reproduce qualitatively the disappearance of the prompt core temperature increase, as well as the ion temperature drop. A later electron temperature rise is observed in the simulation (peak at 35 ms), not present in the experiment. This feature can be explained, again, by the underprediction of collisionality resulting from slightly overpredicted electron temperature profiles. Given the trends found in past work [24], the plasma at the simulated collisionality approaches the “transition regime” and therefore a “mixing effect” (drop followed by a rise) is present. We have run simulations at higher density, past the transition regime, and the mixing effect is no longer present, and only the standard diffusive response (a drop in the core electron temperature) is observed.

At higher density, the disappearance of temperature inversions, in both the ion and the electron channels, Figs. 5.5a and 5.5b, respectively, is attributable to a stronger effect of the ion temperature

gradient scale length on electron and ion heat transport, characteristic of SOC plasmas [28]. Furthermore, the higher edge collisional coupling causes the edge ion temperature to drop along with the electron temperature, causing the propagation of an ion cold-pulse and subsequent increase in a/L_{Ti} , as shown in Figure 5.5c. As depicted in Figure 5.5f, low-k ion modes are destabilized on a fast time-scale and the conducted heat flux is increased (Figure 5.5d), causing the fast reduction of electron stored energy (Figure 5.5e). Past experimental work suggested that the disappearance of temperature inversions could be connected to the TEM/ITG paradigm [8], which is consistent with the results presented here. This conclusion supports the idea of an TEM to ITG transition as the driver for the transition from the LOC to SOC confinement transition [29–31].

The simulations and physics interpretation presented in Sections 5.3.1 and 5.3.2 used the new saturation rule in TGLF (TGLF-SAT1) that accounted for drift-wave instabilities from short to long wavelength. Next section investigates the importance of saturation rule physics and wavenumber spectrum in capturing the temperature inversion effect.

5.3.3 Effect of TGLF Saturation Rule and Wavenumber Spectrum

The new saturation rule in the TGLF model (TGLF-SAT1) came about as a consequence of cross-scale coupling physics, first identified in high-fidelity, realistic mass ratio multiscale nonlinear gyrokinetic simulations [32] (details were described in Section 3.3). However, the original saturation rule (TGLF-SAT0) [14] does not include cross-scale coupling. TGLF-SAT1 gives a larger amplitude to intermediate-k modes than in TGLF-SAT0, and is also able to capture the nonlinear upshift (Dimits shift) of the critical ion temperature gradient at low-k [7]. Furthermore, experimental electron temperature profile stiffness is underpredicted with TGLF-SAT0, but can be matched by the higher stiffness TGLF-SAT1 model [33].

Figure 5.6 depicts the evolution of core ($\rho_N = 0.4$) and edge ($\rho = 0.8$) electron temperature for the low-density condition, normalized to pre-injection values. TGLF-SAT1 simulations with only ion scale turbulence, $k_{\theta}\rho_s \leq 3.0$ (“low-k”), can reproduce experiment as well as simulations that include multi-scale turbulence. This indicates that multi-scale interactions and cross-scale energy transport recently discovered in nonlinear gyrokinetic simulations [32, 34] play a subdominant role in determining the cold-pulse dynamics in these experiments.

However, TGLF-SAT0 underpredicts the onset time of the core response and reached a smaller peak amplitude than TGLF-SAT1. Furthermore, TGLF-SAT0 strongly overpredicted the steady-state electron and ion temperatures outside two-sigma experimental error bars. In addition to the higher stiffness and critical gradient, the new saturation rule in TGLF-SAT1 gives a larger amplitude to intermediate-k modes than in TGLF-SAT0, which likely enhances the impact of the TEM on the fluxes. Unlike the TGLF-SAT1 simulations, TGLF-SAT0 did not recover an ion temperature increase at the plasma core. We therefore conclude that the physics in the new saturation rule in TGLF based on zonal flow mixing (resulting in cross-scale effects, Dimits shift and enhanced TEM activity) is

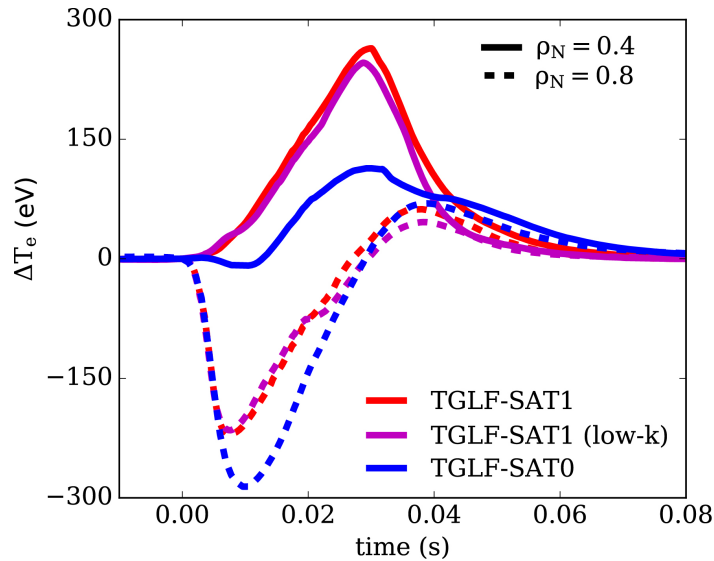


Figure 5.6: Evolution of core ($\rho_N = 0.4$) and edge ($\rho = 0.8$) electron temperature for the low-density condition, using (a) TGLF-SAT1 full spectrum, (b) TGLF-SAT1 only at low-k ($k_{\theta}\rho_s \leq 3.0$), and (c) TGLF-SAT0.

likely a better description for turbulent transport in the core of tokamak plasmas.

The simulations and physics interpretation presented in this chapter points to the density pulse as the most important ingredient to capture the temperature inversion effect. Next section investigates the sensitivity to the magnitude of the density perturbation that drives the experimentally observed temperature increase.

5.3.4 Sensitivity of Magnitude of Density Perturbation

A sensitivity scan of the magnitude of the density perturbation (outside of experimental error bars) was performed for low-density condition. We find that temperature inversions still occur and the time to peak remains the same for the cases with a finite density perturbation. However, the magnitude of the temperature increase gets somewhat reduced (10x smaller density perturbation produces a ~ 3.7 smaller temperature increase). No temperature inversion is found when the density perturbation is removed altogether, further confirming the importance of TEM stabilization by changes in density gradients.

These results are qualitatively consistent with the experimental observations in Alcator C-Mod (Section 4.3), where the amount of ablated impurities was varied (see Figure 4.3), but still an inversion of temperature was observed in all cases. In the simulations presented here, changes in radiation and speed of inward propagation of density perturbation have not been performed and are left for future work. In particular, the increase in edge radiation with different amount of impurities would affect the magnitude of the drop in edge temperature, which would in turn delay the core temperature increase (as observed experimentally, Figure 4.3). This delay would result

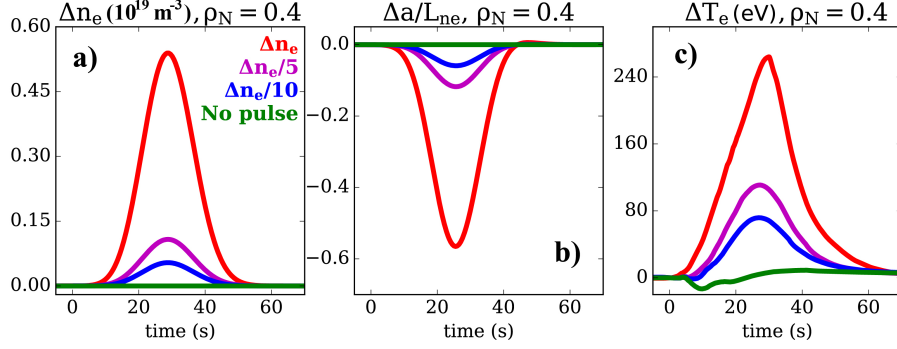


Figure 5.7: Evolution of core ($\rho_N = 0.4$) (a) density, (b) normalized density gradient scale length, and (c) electron temperature for the low-density condition. Variations in the strength of density perturbations are indicated with different colors.

from the competition between flattening of density gradient and increase in electron temperature gradient (larger for stronger edge perturbation).

Having shown that TGLF-SAT1 is able to capture the temperature inversion effect with a density pulse that is consistent with experimental line-averaged measurements, next section further investigates the effect of background density on the magnitude of the temperature inversion.

5.4 Simulation of Plasma Density Scan

Motivated by the clear experimental results, that demonstrate that scanning the density dramatically alters the cold pulse behavior, we performed a simulated density scan starting from the low density condition reported in the previous section. As before, cold pulses are introduced by artificial changes to the radiation and impurity density profiles, while temperatures are allowed to evolve self-consistently. These perturbations are the same for all cold pulses in this numerical experiment, an assumption made here to simplify the interpretation of the phenomena. Section 5.3.4 demonstrated that temperature inversions still occur and the time to peak remains the same when the magnitude of the density perturbation is scanned. Detailed study of the changes in density and its gradient for different plasma conditions is left for future work, which requires self-consistent evolution of particle transport following cold-pulse injections.

The most commonly observed feature of the temperature inversion effect since its discovery [16] is its disappearance at high densities. Experimentally, it was proposed [8] that the temperature inversion effect takes place in plasmas with dominance of collisionless trapped electron mode turbulence, which disappears at densities where the ion temperature gradient turbulence becomes important. This observation was consistent with the confinement saturation paradigm, since it has long been considered that the transition from linear Ohmic confinement (LOC) to saturated Ohmic confinement (SOC) regimes happens concomitant with the destabilization of ITG at higher densities [35].

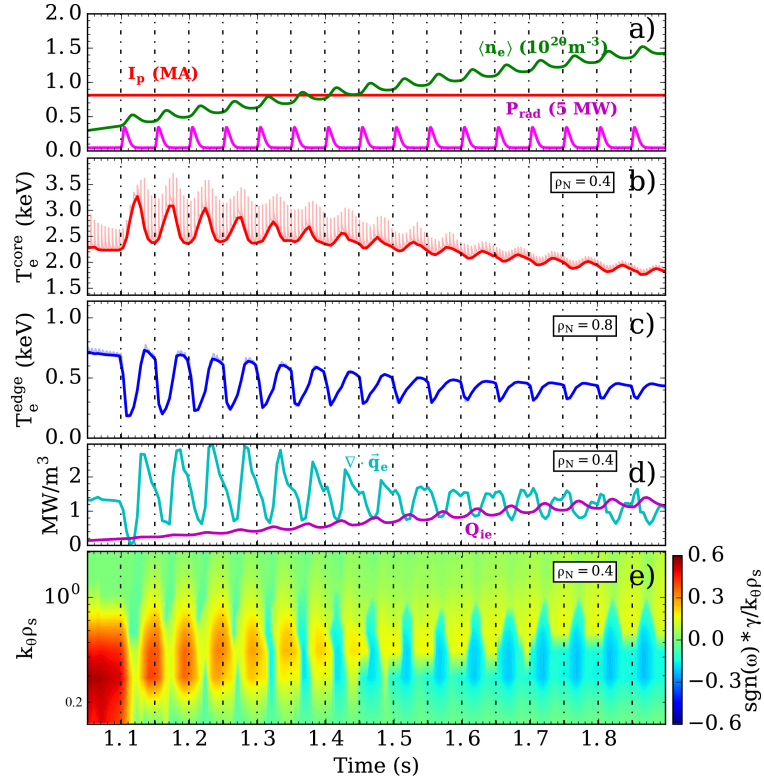


Figure 5.8: Simulation of density scan. (a) Plasma current, volume-averaged density and total radiated power. (b) Electron temperature trace at $\rho_N = 0.4$. (c) Electron temperature trace at $\rho_N = 0.8$. (d) Electron-ion collisional power and electron conducted power at $\rho_N = 0.4$. (e) Low-k linear growth rates spectrum at $\rho_N = 0.4$, with sign representing direction of propagation (blue: ion diamagnetic direction; red: electron diamagnetic direction). Vertical dashed lines represent cold-pulse injection times. Spectrum, temperatures and power densities have been down-sampled to before-sawtooth-crash times.

As we describe next, Figure 5.8 demonstrates that the cold pulse behavior transitions smoothly from exhibiting temperature inversions at low density to purely diffusive response at high density. Injections are introduced every 50 ms during a linear density ramp with constant plasma current. The magnitude of the core temperature inversions (Figure 5.8b) following edge temperature drops (Figure 5.8c) decreases and the inversion appears later in time as density is increased. Concurrently, electron-ion collisional power becomes closer to the electron heat conduction power (Figure 5.8d), indicating that the plasma becomes more thermally coupled, and TEM as the dominant linear micro-instability gets weaker (Figure 5.8e). At low densities, the electron conducted power is quickly reduced following the laser blow-off (LBO) injection, a consequence of the stabilization of TEM modes when they are the primary electron heat exhaust mechanism. The electron conducted power starts to increase following the injection at around $t = 1.4\text{s}$, and consequently the core electron temperature starts exhibiting a temperature drop. The increase in conducted power density $\nabla \cdot \vec{q}_e$ (and thus decrease in core temperature) gets larger as density increases. Interestingly, the core electron temperature rises above the pre-injection value later in the simulation following the temperature drop. We believe this could be a consequence of the simplified shape of the density

pulse, which does not properly capture the relaxation of the density profile.

The smoothly varying response of the core temperature with density and the continuous (instead of abrupt) transition has been observed experimentally, as described in Chapter 4. Our simulation captures this behavior, which is fundamentally different from other abrupt transport phenomena, such as the core intrinsic rotation reversal or hollowing [36]. For some years, a causal relationship between rotation reversal density and the disappearance of the temperature inversion effect was suggested, but here it is shown that the temperature inversions can happen at fixed direction of the toroidal rotation (in all cases, co-current rotation is assumed), and that the disappearance is not abrupt. Instead, a weakening of the core temperature inversion is clearly observed. While here we provide evidence that the phenomenology of the heat transport channel does not require changes in plasma rotation and its gradients, it is likely that intrinsic rotation is affected by the turbulence state of the plasma core [36, 37].

Having shown that the model captures the trend with line-averaged density (i.e. temperature inversion disappears at high density), next section investigates the effect of current on the temperature inversion, particularly on the flex-point.

5.5 Simulation of Plasma Current Scan

Cold-pulse experiments in several machines (RTP [38–40], ASDEX-U [21] and Alcator C-Mod [8]) revealed an important trend, that the electron temperature “flex point” (the radial location where the electron temperature remains the same before and during the cold-pulse propagation) was linked to the safety factor profile, and that the location moves along with the rational surfaces. For sawtoothed plasmas ($q_0 \approx 1.0$) at high plasma current (low q_{95}), the safety factor profile becomes flatter at the plasma core and the locations of rational surfaces generally move outwards.

In order to test this experimental property of the cold-pulse paradigm, we ran a simulation at three currents ($I_p = 0.55 \text{ MA}, 0.8 \text{ MA}, 1.1 \text{ MA}$) and low enough density ($\langle n_e \rangle \approx 0.5 \cdot 10^{20} \text{ m}^{-3}$) so that inversions happen at the three currents, as depicted in Figure 5.9a and Figure 5.9b.

Figure 5.9c plots the normalized linear growth rate of low-k modes ($k_\theta \rho_s = 0.6$) only for electron-direction modes when they are dominant. One can see how, by raising the current, electron modes become more unstable, covering larger portions of the plasma. The consequence of this behavior is that, for a given location in the plasma, TEMs are more unstable as we raise the current, and the inversion happens in outer positions because electron heat flux becomes more sensitive to the TEM drives at those outer locations. Such change of microturbulence in the outer portions of the plasma volume is likely related to the reduction of collisionality that happens when the electron temperature increases (as more Ohmic power is provided) at constant density. Lower collisionality favors the completion of trapped electron orbits before de-trapping, and consequently leads to more TEM activity [41]. The lower magnetic shear associated with the increase in plasma current

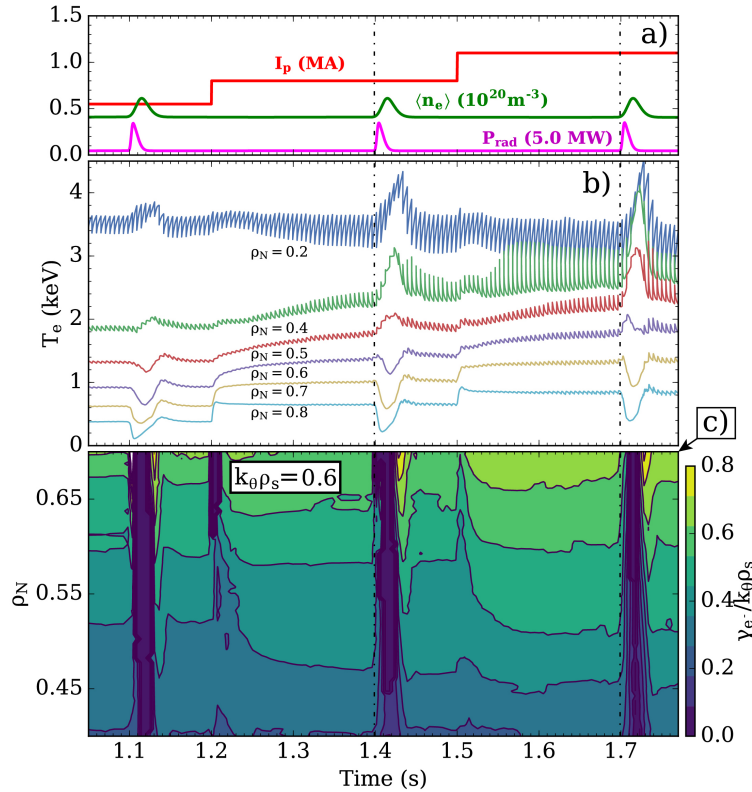


Figure 5.9: Simulation of current scan. (a) Plasma current, volume-averaged density and total radiated power. (b) Electron temperature traces at several radial locations. (c) Linear growth rates at $k_{\theta} \rho_s = 0.6$ in the electron diamagnetic direction. Vertical dashed lines represent cold-pulse injection times. Spectrum has been down-sampled to before-sawtooth-crash times.

in sawtoothing plasmas (i.e. with $q_0 \approx 1.0$) also contributes to higher transport levels.

Figure 5.10a shows the electron temperature profiles before and after cold-pulse injections, and the temperature flex point is also plotted explicitly. Figure 5.10b shows that the qualitative trends are captured by the simulation: the temperature flex point moves outwards with increasing plasma current, like the motion of the rational surfaces. However, the temperature flex point in the simulation is systematically over-predicted (location of the simulated flex point is more radially outward than in experiment), which could be related to the simplified density gradient evolution (assumed here to be the same for the three plasma currents) or the over-prediction of steady-state core electron temperature and consequent underprediction of collisionality. Such core temperature over-prediction could be due to two main reasons. On the one hand, effective ion charge and main ion dilution, among other steady-state plasma parameters, are not well constrained from experiment and can have a significant effect on the TEM instability. On the other hand, the over-prediction of core electron temperature could be related to the under-prediction of heat fluxes by the saturation rule in TGLF. To compensate this under-prediction, the transport solver increases a/L_{T_e} until the fluxes that result from the power balance calculation and the fluxes from the transport model are matched in steady-state (typical flux-matching approach). Given that the saturation

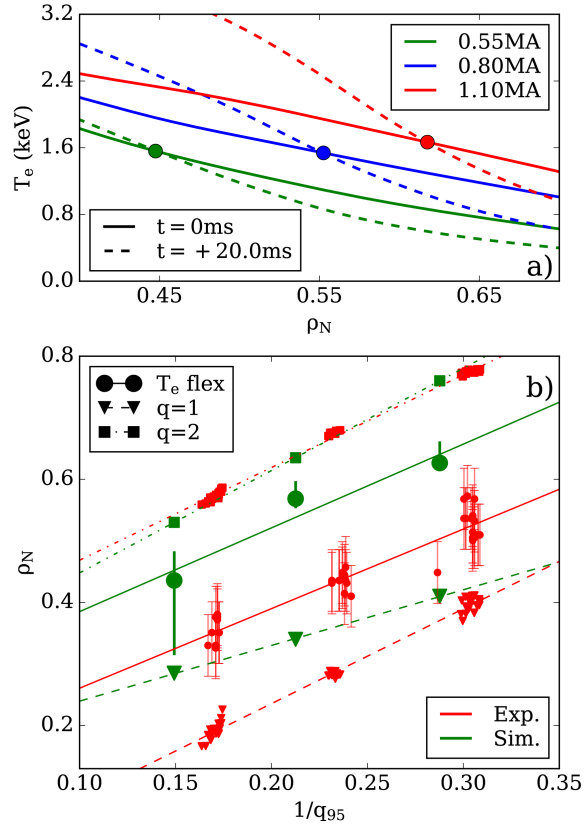


Figure 5.10: (a) Simulated core temperature profile (solid) before and (dashed) 20 ms after the cold-pulse injection for the three plasma currents: 0.55 MA (green), 0.8 MA (blue) and 1.1 MA (red). (b) Simulated and experimental temperature flex point and location of $q = 1$ and $q = 2$ for different values of q_{95} . Green data points for the simulated flex point correspond to the average in the interval 10 – 30 ms after injection, and vertical lines indicate covered range in the simulation. Experimental flex points adapted from Ref. [8].

rule is constructed from linear physics, the flux compensation results in a situation with more unstable linear modes than in experiment. As the integration of "over-predicted" gradients leads to lower collisionality (higher core temperatures for constant density), trapped electron modes will be particularly over-excited in relation to ion temperature gradient modes. In any case, if one takes into account that there might be a threshold in the ratio of TEM to ITG turbulence levels to have temperature inversions (as the data and the simulations suggest), the stronger TEM turbulence resulting from the over-prediction of the steady-state profiles in TGLF could be leading to temperature inversions in outer radii and with larger magnitude than in experiment.

Having shown in Section 5.4 that the model captures the trend with line-averaged density (i.e. temperature inversion disappears at high density), next section investigates whether the temperature inversion effect is recovered at high density by increasing the net plasma current.

5.6 Combined Effect of Density and Plasma Current

The disappearance of temperature inversions at high-density has been well-documented in several experimental studies [26, and references therein]. However, Section 4.4.1 showed experimental evidence of core temperature inversions at very high densities when the plasma current is raised. Such modification of the “transition density” (transition from temperature inversion to standard cold-pulse behavior) by plasma current had also been observed in Tore Supra [42].

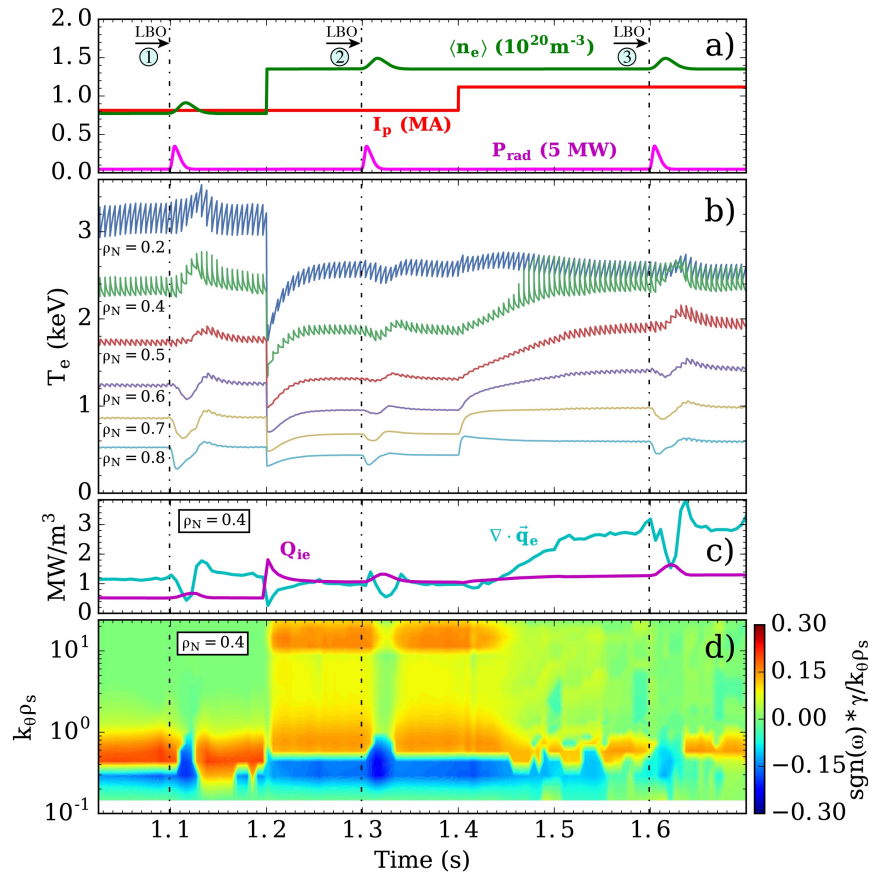


Figure 5.11: Simulation of combined density and current scan. (a) Plasma current, volume-averaged density and total radiated power. (b) Electron temperature traces at several radial locations. (c) Electron-ion collisional power and electron conducted power at $\rho_N = 0.4$. (d) Linear growth rates spectrum at $\rho_N = 0.4$, with sign representing direction of propagation (blue: ion diamagnetic direction; red: electron diamagnetic direction). Vertical dashed lines represent cold-pulse injection times. Spectrum and power densities have been down-sampled to before-sawtooth-crash times.

Figure 5.11a and Figure 5.11b demonstrate that the simulation captures the full phenomenology: (1) temperature inversion at low-density, (2) disappearance following a density increase, (3) re-appearance after increasing the plasma current. Figure 5.11c shows that the LBO injection that does

not exhibit a temperature inversion (injection #2) features a collisional equilibration power roughly equal to the electron heat conduction power, whereas the latter is much larger for injections #1 and #3. This is consistent with past work [2, 39] suggesting that temperature inversions correlate with the ratio of collisional electron-ion power transfer to electron heat conduction, i.e. temperature inversions take place in thermally decoupled (or weakly coupled) plasmas. Figure 5.11d shows the linear growth rates spectrum at $\rho_N = 0.4$, whose sign indicates the direction of propagation. The linear stability spectrum is dominated at long wavelengths ($k_\theta \rho_s \leq 1.0$) by electron modes for those conditions where the temperature inversion takes place. The plasma at the time of injection #2, which exhibits a standard core drop, is dominated by ITG modes at long wavelengths and Electron Temperature Gradient (ETG) modes at short wavelengths. Even though TEMs are indeed stabilized by the flattening of density gradients and increase in collisionality (Figure 5.11d), the loss of TEM dominance in exhausting electron heat flux prevents the prompt reduction of electron transport, as it will be discussed in greater detail in the next sections.

The investigations presented in Sections 5.4 and 5.5, along with the combined density and current scan shown in this section, suggest that the existence (and magnitude) of the temperature inversion effect depends on the strength of trapped electron mode turbulence. Next section quantifies this strength in terms of a metric that represents the dominance of TEM over ITG turbulence in the plasmas studied here.

5.6.1 Analysis of the Inversion Condition from Linear Characteristics

Simulations of cold-pulse propagation suggest that the existence of the temperature inversion effect is somehow related to the dominant linear micro-instability in the plasma core. In order to quantify this, a metric is constructed based on the relative strength of the estimated mixing length transport of TEM v.s. ITG. For every cold pulse simulated in this work, the TGLF gyrofluid model is used to calculate the dominant linear modes for each sign of the frequency (electron and ion diamagnetic directions), and a dominance metric at long wavelengths ($k_\theta \rho_s \leq 3$) is formulated here as $\eta_{TEM/ITG} = D_{TEM}/D_{ITG}$, where $D_{TEM} = \max[\gamma_{TEM}/k_{TEM}^2]$ and $D_{ITG} = \max[\gamma_{ITG}/k_{ITG}^2]$.

Because cold pulses are introduced during continuous density ramps (i.e. with changes in background temperature) and a small temperature drop may happen before the temperature increase (as seen in Figure 5.8), a metric for the strength of the temperature inversion must also be constructed. In this study we use $\Delta T_e^{core} = \frac{1}{t_f - t_0} \int_{t_0}^{t_f} (T_e - T_{e,0}) dt$, where $T_{e,0}$ is the linear interpolation of the temperature without a cold pulse, t_0 is the cold-pulse injection time, and t_f is the time after the effect disappears. This means that, if the plasma exhibits a core temperature increase larger than the initial core temperature drop, the plasma is considered to exhibit a temperature inversion. Figure 5.12 depicts the relationship between these two metrics at $\rho_N = 0.4$ for all plasmas in these scans. It is clearly observed that temperature inversions get stronger as the TEMs are more dominant in relation to the ITG modes. Using this metric, temperature inversions disappear when the TEM transport (estimated with D_{TEM}) becomes lower than 70% of ITG (estimated with D_{ITG}).

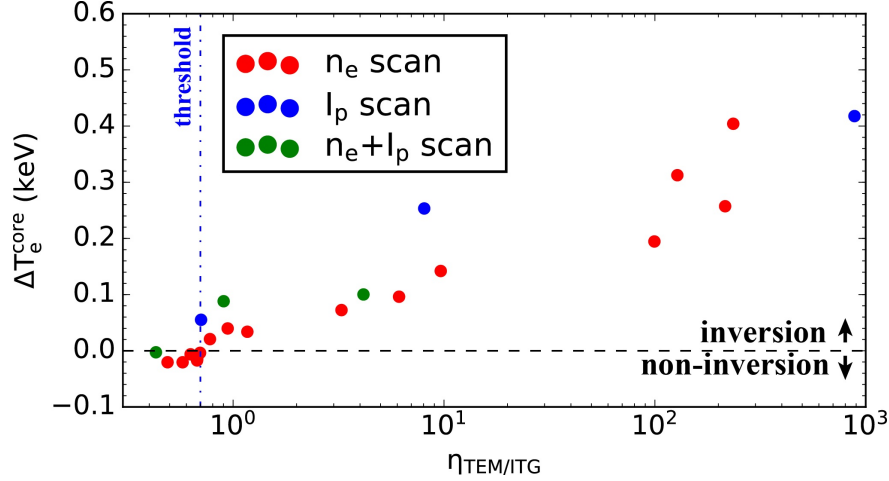


Figure 5.12: Change in core electron temperature as a function of TEM v.s. ITG dominance for all cold pulses simulated in this Chapter: cold pulses from (red) Figure 5.8, (blue) Figure 5.9, and (green) Figure 5.11.

Next section explores in detail the plasma parameters that drive the changes in core turbulence for the conditions presented in Figure 5.11.

5.6.2 Analysis of Driving Terms of TEM v.s. ITG Dominated Regimes

In the previous section, the existence of temperature inversions or lack thereof is shown to be correlated with the dominant micro-instability at the plasma core. However, the details of how the turbulence state can give rise to such different core temperature dynamics remained unclear. In order to address this, detailed linear stability analysis at a time before and after the cold-pulse injection is performed for the three injections in Figure 5.11.

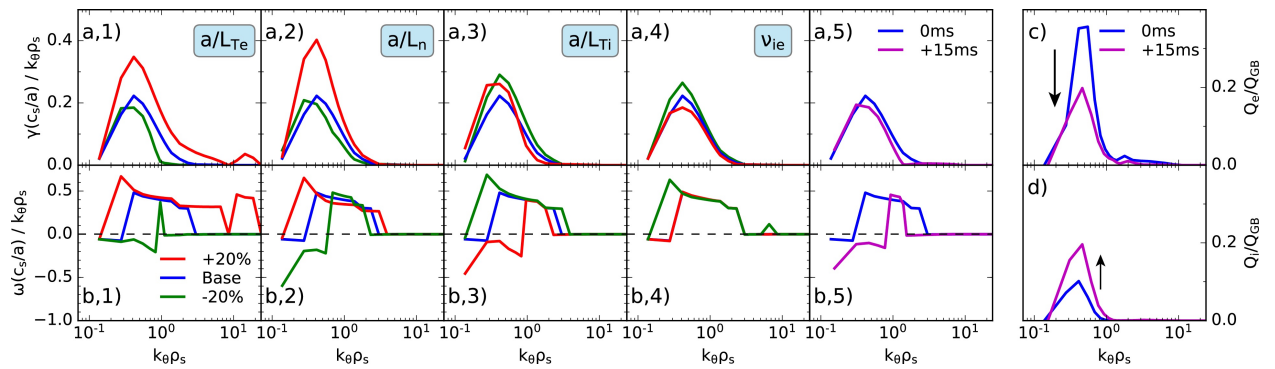


Figure 5.13: Analysis of Injection #1 from Figure 5.11. (a) Linear growth rates and (b) frequencies of the most unstable mode (positive frequency indicates modes in the electron diamagnetic drift direction) at $\rho_N = 0.4$. Scans for 4 main driving terms are shown in red (+20%) and green (-20%), with respect to the baseline (blue). The spectrum after the cold-pulse arrival (magenta) is also plotted. (c) Electron and (d) ion heat flux spectra before and after the cold-pulse arrival.

As shown in Figure 5.13, this analysis confirms that TEMs are the dominant micro-instability in

the core of the low-density, medium-current plasma (injection #1 in Figure 5.11). In the subset of Figure 5.13a and 5.13b, linear stability is most sensitive to changes in both electron temperature and density gradients, as indicated by a larger increase in the growth rate with 20% changes in those drives (red curves). Ion temperature gradient, on the other hand, is shown to destabilize modes in the ion direction but stabilize modes in the electron direction, which is a known feature of TEMs [43–45]. After the injection (15 ms), TEMs are stabilized and the dominant micro-instability is in the ion diamagnetic drift direction at low- k , as shown in Figure 5.13a,5) and Figure 5.13b,5). As TEMs are more efficient at exhausting electron heat flux than ITG modes at low collisionality, electron heat flux is reduced (Figure 5.13c), leading to the increase of core electron temperature. Even though it is difficult to discern what plasma parameter most contributes to the changes in turbulence (because everything changes at the same time), standalone TGLF simulations indicate that a/L_n has a stabilizing effect on the trapped electron modes.

Next, we study injection #2 in Figure 5.11 (high-density medium-current), where it is observed that the spectrum becomes ITG-dominated at long wavelengths and ETG-dominated at short wavelengths by raising the density, leaving a small window in between for existence of TEMs. Because of this, after the pulse arrives ITG modes are destabilized whereas TEM/ETG modes are stabilized (Figure 5.14a and Figure 5.14b), but not enough to compensate the increase in long wavelength electron transport due to the ITG enhancement. In this high-density condition, electron transport is dominantly driven at low- k by ITG modes, which become more unstable and drive more turbulence (hence, higher electron transport as well), as shown in Figure 5.14c.

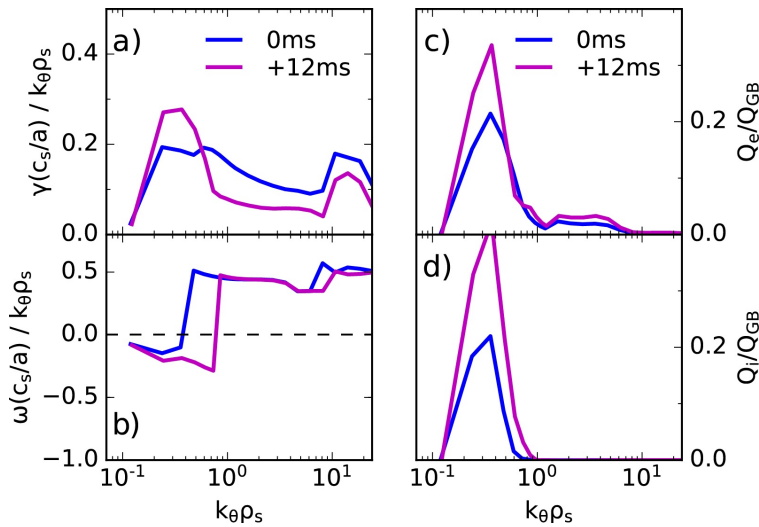


Figure 5.14: Analysis of injection #2 from Figure 5.11. (a) Linear growth rates, (b) mode frequencies (positive frequency indicates modes in the electron diamagnetic drift direction), (c) electron and (d) ion heat flux spectra (blue) before and (magenta) after the cold-pulse arrival.

Lastly, by raising the plasma current (injection #3 in Figure 5.11), transport is dominated by low- k TEMs, as shown in Figure 5.15a and Figure 5.15b. The linear spectrum is now mostly affected by density gradients, which suppress electron modes after the cold-pulse arrival. In this case, the

electron heat flux spectrum shifts to longer wavelengths, but the total electron heat flux decreases.

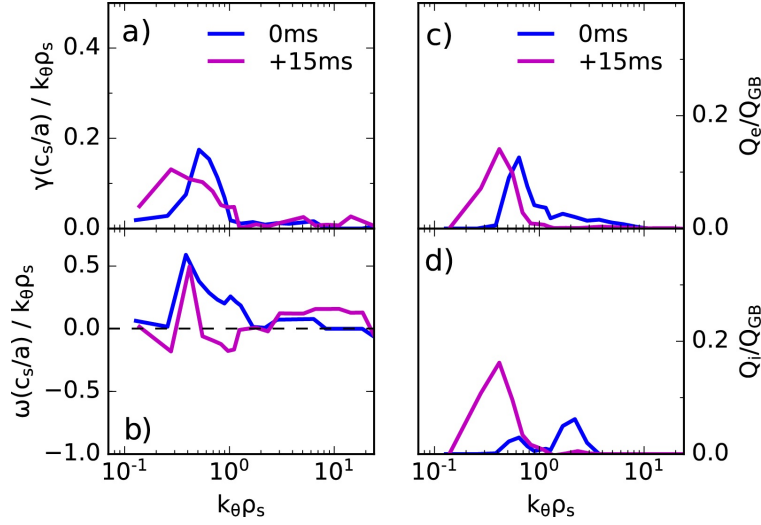


Figure 5.15: Analysis of injection #3 from Figure 5.11. (a) Linear growth rates, (b) mode frequencies (positive frequency indicates modes in the electron diamagnetic drift direction), (c) electron and (d) ion heat flux spectra (blue) before and (magenta) after the cold-pulse arrival.

From the linear stability analysis of Figure 5.14, one can see that changes in the ion temperature gradient are the cause of the core electron temperature drop in the high-density cases, since ITG modes dominate the linear spectrum at long wavelengths. Contrary to the density evolution, which is manually imposed in these simulations, ion temperature dynamics are a consequence of changes in turbulent transport. From Figure 5.13d, Figure 5.14d and Figure 5.15d, we can see that ion heat flux is enhanced in all cases (even in those cases that exhibit an electron heat flux reduction). This increase in ion transport is related to the reduction of impurity density gradient, which leads to the destabilization of ITG [44], amplified in some cases by the self-consistent increase in aL_{Ti} .

5.7 Discussion on Modeling Results in Alcator C-Mod Plasmas

Past results [20, 21, 25] with different quasilinear models were unable to achieve the level of agreement with all the experimentally observed cold-pulse phenomena that is now achieved with TGLF-SAT1. For this reason, cold-pulse propagation had been considered a primary example of the existence of non-local transport effects, not encapsulated in the local transport paradigm [3]. In this work, we have shown that the recently developed trapped gyro-landau fluid model TGLF-SAT1 [6, 7] includes the key physics required to reproduce the experimental cold-pulse dynamics in tokamaks. Parametric studies and linear analyses of the dominant micro-instabilities present in the plasma core reveal that the appearance of the temperature inversion effect is strongly correlated with the strength of trapped electron modes, which are more efficient at exhausting electron heat flux than ion temperature gradient modes at low collisionality.

The model presented here is able to reproduce the experimentally measured timescale associated with cold-pulse-induced temperature inversions. Furthermore, the magnitude is qualitatively consistent with experimental trends, and the well-documented current and density dependencies of cold pulses can be recovered. The study presented here makes use of the TGLF gyrofluid model, which was developed to include both passing and trapped particles dynamics [13]. Trapped particle modes are indeed shown here to be critical to explain the behavior at low collisionality. These modeling results reveal that ion heat pulses are not needed to explain the electron core temperature increase, consistent with experimental observations in other machines [21]. Further work is needed to investigate the conditions that lead to the increase in ion temperature, observed in some experiments [26].

Cold-pulse experiments have been extensively described in the literature, and many different features have been reported. This work does not aim to explain all observations from cold-pulse experiments, but provides confidence that our modeling assumptions are appropriate to reproduce all experimental trends from Alcator C-Mod that have so far been discussed. Future work should address whether the model can capture the behavior of cold-pulse propagation with application of different heating schemes. In the work presented here, only Ohmic discharges were analyzed. It is found experimentally that temperature inversions are enhanced by predominantly electron heating schemes such as electron cyclotron heating (ASDEX-U [21], HL-2A [46]) and Lower Hybrid (Tore Supra [42]), and weakened in ion heating scenarios with neutral beam injections (TFTR [47], JET [25]). These observations are also consistent with the idea of dominance of electron versus ion micro-instabilities at the plasma core, and with the correlation of the magnitude of the inversion with the ratio of electron to ion heat flux.

In this modeling study in Alcator C-Mod, an inwardly propagating pulse was constructed to match the line-averaged measurements of the density perturbation (see Figure 5.2). However there are many different forms of density pulses that match the same constraint, i.e. there are too many free parameters in this problem. It is because of this that new predict-first experiments were

performed in DIII-D, as it will be described in the next Chapter. A density profile reflectometer is used in DIII-D to measure the propagation of particles from edge to core with high time resolution, to further constrain the local modeling with TGLF.

Bibliography

- [1] E.J. Doyle et al. Chapter 2: Plasma confinement and transport. *Nucl. Fusion*, 46:B557–B574, 2007. URL <http://stacks.iop.org/0029-5515/47/i=6/a=S02>.
- [2] J D Callen and M W Kissick. Evidence and concepts for non-local transport. *Plasma Phys. Control. Fusion*, 39(12B):B173, 1997. URL <http://stacks.iop.org/0741-3335/39/i=12B/a=014>.
- [3] K. Ida et al. Towards an emerging understanding of non-locality phenomena and non-local transport. *Nucl. Fusion*, 55(1):013022, 2015. URL <http://stacks.iop.org/0029-5515/55/i=1/a=013022>.
- [4] R.V. Budny et al. Core fusion power gain and alpha heating in jet, tftr, and iter. *Nucl. Fusion*, 56(5):056002, 2016. URL <http://stacks.iop.org/0029-5515/56/i=5/a=056002>.
- [5] Hyun-Tae Kim et al. Statistical validation of predictive transp simulations of baseline discharges in preparation for extrapolation to jet d-t. *Nucl. Fusion*, 57(6):066032, 2017. URL <http://stacks.iop.org/0029-5515/57/i=6/a=066032>.
- [6] G. M. Staebler et al. The role of zonal flows in the saturation of multi-scale gyrokinetic turbulence. *Phys. Plasmas*, 23(6):062518, 2016. URL <http://dx.doi.org/10.1063/1.4954905>.
- [7] Gary M Staebler et al. A model of the saturation of coupled electron and ion scale gyrokinetic turbulence. *Nucl. Fusion*, 2017. URL <http://iopscience.iop.org/10.1088/1741-4326/aa6bee>.
- [8] J.E. Rice et al. Non-local heat transport, rotation reversals and up/down impurity density asymmetries in alcator c-mod ohmic l-mode plasmas. *Nucl. Fusion*, 53(3):033004, 2013. URL <http://stacks.iop.org/0029-5515/53/i=3/a=033004>.
- [9] X. Yuan et al. Parallel computing aspect in TRANSP with PT-SOLVER. In *APS Meeting Abstracts*, page JP8.119, October 2013. URL <http://adsabs.harvard.edu/abs/2013APS..DPPJP8119Y>.
- [10] R. J. Hawryluk. An empirical approach to tokamak transport. *Physics of Plasmas Close to Thermonuclear Conditions*, 1:19–46, 1980. URL <http://www.sciencedirect.com/science/article/pii/B9781483283852500091>.
- [11] Joshua Breslau et al. Transp. [Computer Software] <https://doi.org/10.11578/dc.20180627.4>, jun 2018. URL <https://doi.org/10.11578/dc.20180627.4>.
- [12] C. S. Chang and F. L. Hinton. Effect of finite aspect ratio on the neoclassical ion thermal conductivity in the banana regime. *The Physics of Fluids*, 25(9):1493–1494, 1982. doi: 10.1063/1.863934. URL <https://aip.scitation.org/doi/abs/10.1063/1.863934>.

- [13] G. M. Staebler et al. Gyro-landau fluid equations for trapped and passing particles. *Phys. Plasmas*, 12(10), 2005. URL <http://dx.doi.org/10.1063/1.2044587>.
- [14] G. M. Staebler et al. A theory-based transport model with comprehensive physics. *Phys. Plasmas*, 14(5):055909, 2007. URL <http://dx.doi.org/10.1063/1.2436852>.
- [15] L. L. LoDestro and L. D. Pearlstein. On the grad-shafranov equation as an eigenvalue problem, with implications for q solvers. *Physics of Plasmas*, 1(1):90–95, 1994. doi: 10.1063/1.870464. URL <https://doi.org/10.1063/1.870464>.
- [16] K. W. Gentle et al. Strong nonlocal effects in a tokamak perturbative transport experiment. *Phys. Rev. Lett.*, 74:3620–3623, 1995. URL <https://link.aps.org/doi/10.1103/PhysRevLett.74.3620>.
- [17] M.W. Kissick et al. Non-local component of electron heat transport in tfr. *Nucl. Fusion*, 36(12): 1691, 1996. URL <http://stacks.iop.org/0029-5515/36/i=12/a=I09>.
- [18] C. Angioni et al. The local nature of the plasma response to cold pulses with electron and ion heating at asdex upgrade. (*submitted to Nuclear Fusion*).
- [19] Yuejiang Shi et al. Observation of multi-channel non-local transport in j-text plasmas. *Nuclear Fusion*, 58(4):044002, 2018. URL <http://stacks.iop.org/0029-5515/58/i=4/a=044002>.
- [20] J. E. Kinsey et al. Theoretical transport modeling of ohmic cold pulse experiments. *Phys. Plasmas*, 5(11):3974–3981, 1998. URL <http://dx.doi.org/10.1063/1.873117>.
- [21] F. Ryter et al. Propagation of cold pulses and heat pulses in asdex upgrade. *Nucl. Fusion*, 40(11):1917, 2000. URL <http://stacks.iop.org/0029-5515/40/i=11/a=311>.
- [22] R. L. Boivin et al. High resolution bolometry on the alcator c-mod tokamak (invited). *Rev. Sci. Instrum*, 70(1):260–264, 1999. doi: 10.1063/1.1149309. URL <http://dx.doi.org/10.1063/1.1149309>.
- [23] R. E. Waltz et al. A gyro-landau-fluid transport model. *Phys. Plasmas*, 4(7):2482–2496, 1997. doi: 10.1063/1.872228. URL <https://doi.org/10.1063/1.872228>.
- [24] P. Rodriguez-Fernandez et al. On the correlation between non-local effects and intrinsic rotation reversals in alcator c-mod. *Nucl. Fusion*, 57(7):074001, 2017. URL <http://stacks.iop.org/0029-5515/57/i=7/a=074001>.
- [25] P Mantica et al. Perturbative transport experiments in jet low or reverse magnetic shear plasmas. *Plasma Phys. Control. Fusion*, 44(10):2185, 2002. URL <http://stacks.iop.org/0741-3335/44/i=10/a=308>.
- [26] C. Gao et al. Non-local heat transport in alcator c-mod ohmic l-mode plasmas. *Nucl. Fusion*, 54(8):083025, 2014. URL <http://stacks.iop.org/0029-5515/54/i=8/a=083025>.

- [27] S Inagaki et al. Abrupt reduction of core electron heat transport in response to edge cooling on the large helical device. *Plasma Phys. Control. Fusion*, 48(5A):A251, 2006. URL <http://stacks.iop.org/0741-3335/48/i=5A/a=S23>.
- [28] C. Sung et al. Quantitative comparison of electron temperature fluctuations to nonlinear gyrokinetic simulations in c-mod ohmic l-mode discharges. *Phys. Plasmas*, 23(4):042303, 2016. doi: 10.1063/1.4945620. URL <http://dx.doi.org/10.1063/1.4945620>.
- [29] F. Romanelli et al. Anomalous thermal confinement in ohmically heated tokamaks. *Nuclear Fusion*, 26(11):1515–1528, nov 1986. doi: 10.1088/0029-5515/26/11/007. URL <https://doi.org/10.1088%2F0029-5515%2F26%2F11%2F007>.
- [30] C. Angioni et al. Relationship between density peaking, particle thermodiffusion, ohmic confinement, and microinstabilities in asdex upgrade l-mode plasmas. *Physics of Plasmas*, 12(4):040701, 2005. doi: 10.1063/1.1867492. URL <https://doi.org/10.1063/1.1867492>.
- [31] C. Sung et al. Changes in core electron temperature fluctuations across the ohmic energy confinement transition in alcator c-mod plasmas. *Nuclear Fusion*, 53(8):083010, jul 2013. doi: 10.1088/0029-5515/53/8/083010. URL <https://doi.org/10.1088%2F0029-5515%2F53%2F8%2F083010>.
- [32] N.T. Howard et al. Multi-scale gyrokinetic simulation of tokamak plasmas: enhanced heat loss due to cross-scale coupling of plasma turbulence. *Nucl. Fusion*, 56(1):014004, 2016. URL <https://doi.org/10.1088/0029-5515/56/1/014004>.
- [33] P. Rodriguez-Fernandez et al. Vitals: A surrogate-based optimization framework for the accelerated validation of plasma transport codes. *Fusion Science and Technology*, 74(1-2):65–76, 2018. doi: 10.1080/15361055.2017.1396166. URL <https://doi.org/10.1080/15361055.2017.1396166>.
- [34] S. Maeyama et al. Cross-scale interactions between turbulence driven by electron and ion temperature gradients via sub-ion-scale structures. *Nucl. Fusion*, 57(6):066036, 2017. URL <http://stacks.iop.org/0029-5515/57/i=6/a=066036>.
- [35] I. Erofeev et al. Theory-based modeling of LOC–SOC transitions in ASDEX upgrade. *Nuclear Fusion*, 57(12):126067, nov 2017. doi: 10.1088/1741-4326/aa8e32. URL <https://doi.org/10.1088%2F1741-4326%2Faa8e32>.
- [36] Y Camenen et al. Experimental observations and modelling of intrinsic rotation reversals in tokamaks. *Plasma Physics and Controlled Fusion*, 59(3):034001, jan 2017. doi: 10.1088/1361-6587/aa543a. URL <https://doi.org/10.1088%2F1361-6587%2Faa543a>.
- [37] Y. Camenen et al. Consequences of profile shearing on toroidal momentum transport. *Nuclear Fusion*, 51(7):073039, jun 2011. doi: 10.1088/0029-5515/51/7/073039. URL <https://doi.org/10.1088%2F0029-5515%2F51%2F7%2F073039>.

- [38] P. Mantica et al. Nonlocal transient transport and thermal barriers in rijnhuizen tokamak project plasmas. *Phys. Rev. Lett.*, 82:5048–5051, 1999. URL <https://link.aps.org/doi/10.1103/PhysRevLett.82.5048>.
- [39] P Galli et al. Non-local response of rtp ohmic plasmas to peripheral perturbations. *Nuclear Fusion*, 39(10):1355–1368, oct 1999. doi: 10.1088/0029-5515/39/10/301. URL <https://doi.org/10.1088%2F0029-5515%2F39%2F10%2F301>.
- [40] G M D Hogeweij et al. Recording non-local temperature rise in the RTP tokamak. *Plasma Physics and Controlled Fusion*, 42(10):1137–1144, oct 2000. doi: 10.1088/0741-3335/42/10/310. URL <https://doi.org/10.1088%2F0741-3335%2F42%2F10%2F310>.
- [41] F. Ryter et al. Experimental study of trapped-electron-mode properties in tokamaks: Threshold and stabilization by collisions. *Phys. Rev. Lett.*, 95:085001, Aug 2005. doi: 10.1103/PhysRevLett.95.085001. URL <https://link.aps.org/doi/10.1103/PhysRevLett.95.085001>.
- [42] X L Zou et al. *Plasma Physics and Controlled Fusion*, 42(10):1067–1076, oct 2000. doi: 10.1088/0741-3335/42/10/305. URL <https://doi.org/10.1088%2F0741-3335%2F42%2F10%2F305>.
- [43] N. Bonanomi et al. Effects of nitrogen seeding on core ion thermal transport in JET ILW l-mode plasmas. *Nuclear Fusion*, 58(2):026028, jan 2018. doi: 10.1088/1741-4326/aa9e7c. URL <https://doi.org/10.1088%2F1741-4326%2Faa9e7c>.
- [44] Huarong Du et al. Coupling of ion temperature gradient and trapped electron modes in the presence of impurities in tokamak plasmas. *Physics of Plasmas*, 21(5):052101, 2014. doi: 10.1063/1.4875342. URL <https://doi.org/10.1063/1.4875342>.
- [45] J. Y. Kim and H. S. Han. Linear interaction and relative role of the ion temperature gradient and trapped electron modes in the reactor-relevant finite beta plasma condition. *Physics of Plasmas*, 24(7):072501, 2017. doi: 10.1063/1.4990071. URL <https://doi.org/10.1063/1.4990071>.
- [46] Hong-Juan Sun et al. Experiment of non-local effect with smbi on hl-2a. *Plasma Phys. Control. Fusion*, 52(4):045003, 2010. URL <http://stacks.iop.org/0741-3335/52/i=4/a=045003>.
- [47] M.W. Kissick et al. Conditions and behaviour related to non-local electron heat transport on tfr. *Nucl. Fusion*, 38(6):821, 1998. URL <http://stacks.iop.org/0029-5515/38/i=6/a=304>.

Chapter 6

Predict-first Cold-pulse Experiments in DIII-D

“Science walks forward on two feet, namely theory and experiment... Sometimes it is one foot which is put forward first, sometimes the other, but continuous progress is only made by the use of both- by theorizing and then testing, or by finding new relations in the process of experimenting and then bringing the theoretical foot up and pushing it on beyond, and so on in unending alternations.”

R.A. Millikan, *Nobel Lecture*, 1923

The study presented in Chapter 5 provided an explanation to the cold-pulse phenomena from a local transport perspective. Under the assumptions that (1) the plasma core at low collisionality is dominated by TEM-type turbulence, and (2) a density perturbation exists and propagates inwards after the injection of particles at the edge, then the core electron temperature could increase as a result of turbulence stabilization. While the former assumption fits within many experimental observations and simulations of low collisionality plasmas [1–3], the latter remains to be validated. Because of the rapid cold-pulse behavior, experiments in Alcator C-Mod could only provide line-integrated measurements of electron density, and that was used as the only constraint on the modeled density perturbation.

The model has been successful in explaining many experimental trends in Alcator C-Mod plasmas, as shown in Chapter 5, but the phenomenology of cold-pulse propagation is very rich and other experimental observations still remain to be addressed. Among them, the transition condition for cold-pulse behavior seems to be affected by a $1/R$ dependence [4, 5], with R as the major radius. Using unique pre-experiment predictions with TGLF, and new LBO-enabled experiments and analysis, this Chapter aims to answer the open question of whether simulations in a device other than Alcator C-Mod can reproduce the transition condition (thus able to capture the $1/R$ dependence of the empirical scaling), as well as to address the open question of the propagation of density perturbations in experiments.

This chapter starts by introducing how the predictions of core heat transport behavior in DIII-D were made, in preparation for the experiments.

6.1 Predictions of Cold-Pulse Behavior in Ohmic DIII-D Plasmas

A database of cold-pulse experiments in different machines [4, 5] suggests that the transition in core transport behavior (from “temperature inversion effect” to “standard temperature drop”) happens at constant collisionality (as given by $n_e q_{95} R = \text{const}$). Machines with similar size as DIII-D ($R = 1.67$ m) experience temperature inversions below $n_e q_{95} \approx 12.0 \cdot 10^{19} \text{m}^{-3}$ for ASDEX Upgrade [6] ($R = 1.65$ m) and below $n_e q_{95} \approx 6.0 \cdot 10^{19} \text{m}^{-3}$ for HL-2A [7] ($R = 1.64$ m). Such large uncertainty in the transition condition in DIII-D motivated the use of predict-first theory-based simulations of the core transport behavior.

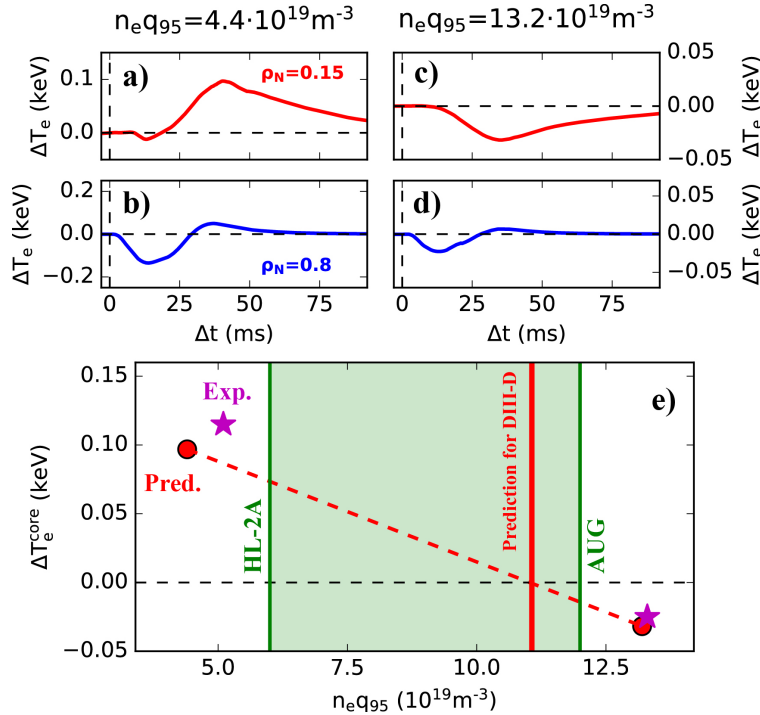


Figure 6.1: Prediction of changes in edge and core electron temperature at low (a,b) and high (c,d) collisionality in DIII-D. (e) Comparison between empirical and theory-based prediction of the transition condition for DIII-D. Green area indicates the uncertainty in the empirical scaling of the transition for DIII-D. Experiment (run after the predictions were made) is also plotted.

An extensive search over recent Ohmic low-density DIII-D plasmas leads to the identification of a discharge with $n_e q_{95}$ below both ASDEX Upgrade and HL-2A thresholds. Specifically, a DIII-D plasma with $n_e q_{95} \approx 4.4 \cdot 10^{19} \text{m}^{-3}$ is selected as the baseline. Next, perturbations in density and radiation are introduced in the simulation to mimic a laser blow-off injection. Lacking experimental data of the perturbations in DIII-D, we scaled down the pulses in density and radiation profiles from Alcator C-Mod. In particular, given that this DIII-D plasma had 8-fold lower absolute density

than the low-collisionality plasma in Alcator C-Mod, the perturbations were reduced accordingly (8 times smaller density perturbation and 8^2 lower radiation). A perturbative transport simulation identical to those in Chapter 5 was performed with the baseline discharge ($n_e q_{95} \approx 4.4 \cdot 10^{19} \text{m}^{-3}$). A higher collisionality version ($n_e q_{95} \approx 13.2 \cdot 10^{19} \text{m}^{-3}$) was also run with a density profile that was simply scaled from the low-density case.

Figure 6.1 shows that these simulations confirm the existence of the two different core transport behaviors in DIII-D: inversion versus non-inversion of the core electron temperature. Following the edge temperature drop (Figure 6.1b and Figure 6.1d), the core temperature increases at low collisionality (Figure 6.1a) and decreases at higher collisionality (Figure 6.1c). Under the assumption that the magnitude of the temperature inversion decreases linearly with density (Section 4.4.1), a theory-based predict-first transition is obtained by linearly interpolating the magnitude of the core temperature change for the two simulations. A transition condition of $n_e q_{95} \approx 11.1 \cdot 10^{19} \text{m}^{-3}$ is found for DIII-D. Figure 6.1e illustrates the transition conditions for ASDEX Upgrade and HL-2A (in green) and the predict-first transition for DIII-D (in red).

Having predicted the conditions to observe the different core transport behavior in DIII-D, next section presents the first experimental observations of the temperature inversion effect in this machine.

6.2 Experiments in Ohmic DIII-D Plasmas

Based on the predictions, two experimental conditions were designed that would exhibit both core transport behaviors in the DIII-D tokamak. The two plasmas presented here had lower-single-null diverted geometry, plasma current $I_p = 1.0 \text{MA}$, magnetic field $B_T = 2.0 \text{T}$, and safety factor $q_{95} = 5.1$. Both plasmas were Ohmic, with laser blow-off injections (using aluminum as impurity) at $t = 1800 \text{ms}$, and diagnostic neutral beams at $t = 1980 \text{ms}$. As shown in Figure 6.2a, at the moment of the LBO injection, the first plasma had a line-averaged density $\tilde{n}_e \approx 1.0 \cdot 10^{19} \text{m}^{-3}$ (from now on, “low density” plasma) and the second one had $\tilde{n}_e \approx 2.6 \cdot 10^{19} \text{m}^{-3}$ (“high density”). This choice of parameters provided plasmas with $n_e q_{95} \approx 5.1 \cdot 10^{19} \text{m}^{-3}$ at low density and $n_e q_{95} \approx 13.3 \cdot 10^{19} \text{m}^{-3}$ at high density, thus covering the empirical and the theory-based predictions of the transition condition. This choice of line-averaged densities also covered the transitions from linear ohmic confinement (LOC) to saturated ohmic confinement (SOC), and from flat to hollow intrinsic rotation profile. Neutral beams were not used during the cold-pulse propagation so that the temperature inversion does not vanish, which is observed in experimental [8, 9] and modeling [10] studies.

Figure 6.2b demonstrates that the discharges exhibit two different core transport behaviors. Following the edge cold-pulse injections (Figure 6.2c), the core temperature abruptly increases in the experiment at low density and decreases at high density. At high density, the edge perturbation is smaller ($\Delta T_e \approx -30 \text{eV}$ versus $\Delta T_e \approx -75 \text{eV}$ at low-density), which could be related to the higher collisional coupling between plasma species, and the lower radiative losses relative to the

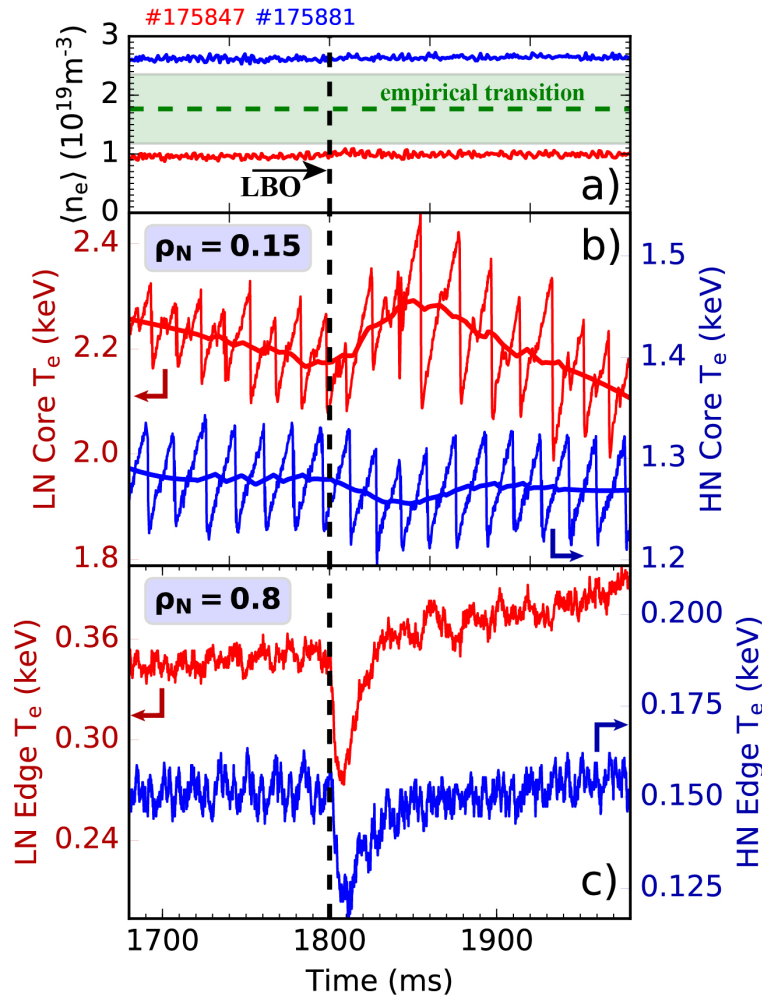


Figure 6.2: a) Line-average density, b) Core temperature ($\rho_N = 0.15$), and c) Edge temperature ($\rho_N = 0.8$) for low (red, LN) and high density (blue, HN) shots. Core temperatures have also been filtered for visualization purposes. Green dashed line in a) indicates the expected transition density as given in [5] for $q_{95} = 5.1$. Shaded green area covers range of transition density for similar size machines, AUG and HL-2A.

plasma stored energy, as the same amount of aluminum impurities was introduced in both plasmas. However, work in Alcator C-Mod (Section 4.3) suggests that the amount of impurities should not significantly change the qualitative features (i.e. inversion versus non-inversion) of the core electron temperature behavior. At low density, the core temperature increases $\Delta T_e \approx 115$ eV, while at high density it drops by $\Delta T_e \approx -25$ eV. The peak of the temperature rise at low density is reached $\Delta t \approx 50$ ms after the injection, which is approximately an energy confinement time (estimated to be in this plasma $\tau_E \approx 60$ ms). The lowest point of the core temperature drop at high density is reached $\Delta t \approx 50$ ms after injection, which instead is significantly shorter than an energy confinement time (estimated as $\tau_E \approx 120$ ms). Notably, the magnitudes of the temperature increase at low density

and temperature drop at high density follow closely the behavior predicted by the model before the experiment was performed (including very similar edge temperature drops), as depicted in Figure 6.1e (magenta stars).

As presented in Chapter 5, the temperature inversion effect arises from the flattening of core density gradients. Next section presents high-time resolution measurements of the density pulse that led to the temperature inversion effect in this DIII-D experiment.

6.2.1 Evidence of Fast Density Pulse

Direct measurements of the density evolution following the edge cold pulse were made by a high time resolution density profile reflectometer system [11], as depicted in Figure 6.3 for the low density discharge discussed in the previous section. A perturbation in electron density is observed to travel from edge (where impurities are deposited) to core in a remarkably fast time-scale. The inner core of the plasma ($\rho_N = 0.15$) starts to experience the arrival of the density pulse only $\Delta t \approx 7$ ms after the injection, reaching its peaked value at a similar time-scale as the electron temperature response ($\Delta t \approx 50$ ms), as depicted in Figure 6.3c.

The change in core electron density is $\Delta n_e \approx 6.0 \cdot 10^{17} \text{ m}^{-3}$, which represents only $\sim 4\%$ of the absolute steady state density. This measurement of electron density in fast time resolution provides evidence to help validate the model discussed in Chapter 5. A fast increase in the core density, even small in magnitude (and usually difficult to measure), would quickly reduce density gradients and potentially stabilize TEM turbulence, leading to seemingly “nonlocal” transport effects.

Next section presents turbulence measurements performed with a Doppler Backscattering

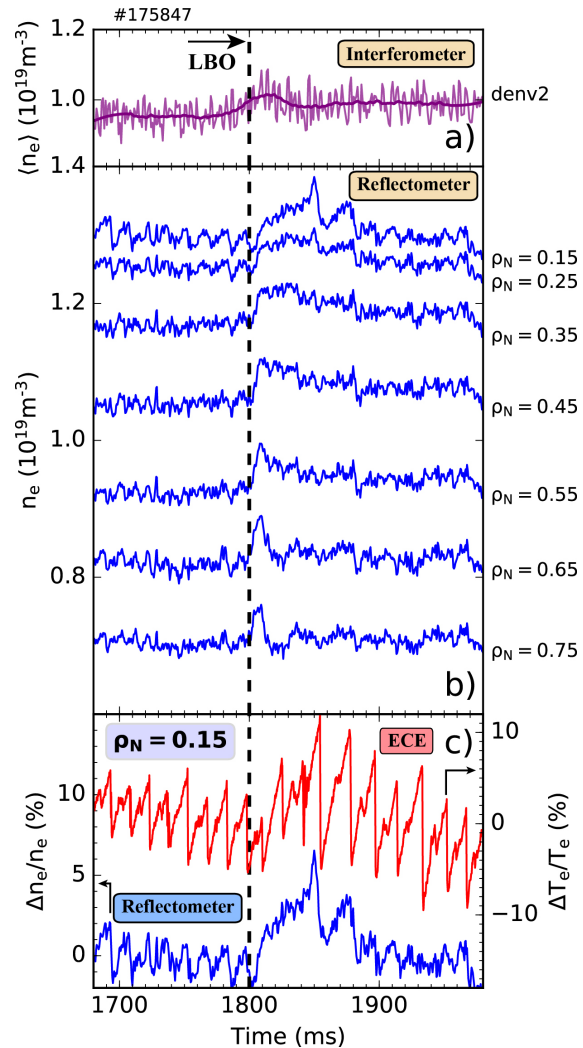


Figure 6.3: a) Line-average density from vertical ($R = 1.94$ m) CO₂ interferometer, b) local density from reflectometer at several radial locations after the injection of impurities at the edge, c) relative change of core electron temperature and density plotted together.

System, and investigates the relationship of changes in turbulence with the core temperature inversion.

6.2.2 Turbulence Measurements

Changes in local turbulence were measured using a multi-channel Doppler Backscattering System (DBS) [12]. The left side of Figure 6.4 plots the normalized amplitude of the scattering signals measured by DBS at four different radial locations simultaneously in the plasma core for the low density condition. These scattering signals are proportional to electron density fluctuations. The right side of the figure displays the evolution of the turbulence perpendicular velocity, extracted from Doppler shift of the DBS measurements. In principle, this turbulence velocity is the sum of the plasma flow velocity in the lab frame and the phase velocity of density fluctuations in the plasma frame. However, because of the lack of plasma flow measurements in time during the cold-pulse propagation (the charge exchange recombination, CER, system was only enabled with NBI blips at one time during the steady-state portion of the discharge), we cannot truly separate the evolution of the phase velocity of the density fluctuations in the plasma frame.

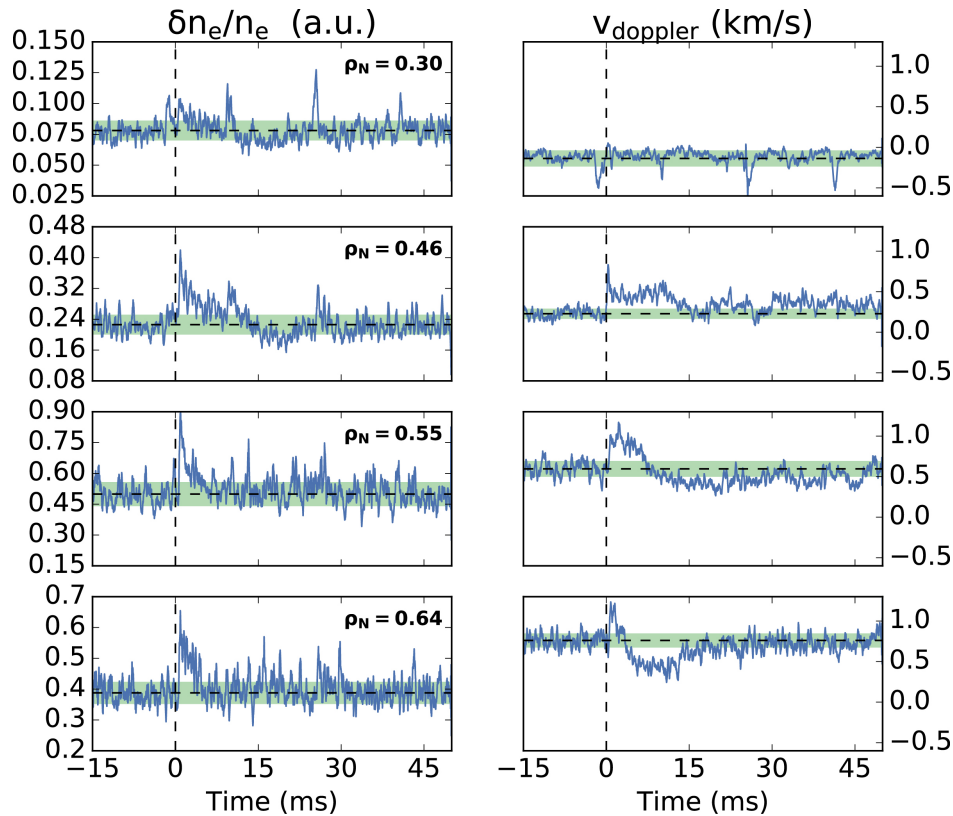


Figure 6.4: Turbulence measurements with DBS for low-density shot #175847: Time-evolution of (left) density fluctuation levels, and (right) Doppler velocity. Black dashed line indicates mean value before injection and green shaded regions indicate $\pm\sigma$ before injection.

In the cases displayed in Figure 6.4, the DBS system measures density fluctuations at (from top

to bottom) $k_{\perp} = 8.0 \pm 1.0 \text{cm}^{-1}$, $k_{\perp} = 6.0 \pm 1.0 \text{cm}^{-1}$, $k_{\perp} = 5.0 \pm 1.0 \text{cm}^{-1}$, and $k_{\perp} = 4.5 \pm 1.0 \text{cm}^{-1}$, which covers a range of $k_{\perp} \rho_s \sim 1.0 - 3.0$. Figure 6.4 indicates that medium-k turbulence as measured by DBS changes on a very fast time-scale following the cold-pulse injection. Density fluctuation levels increase abruptly right after the injection ($< 1 \text{ms}$), but interestingly they decrease slightly below pre-injection values for inner channels ($\rho_N < 0.5$) on a longer time-scale ($\sim 15 \text{ms}$). At this longer time-scale, perpendicular velocity decreases (more towards electron diamagnetic drift direction) in the outer channels and increases (more towards ion diamagnetic drift direction) in the inner channels.

Figure 6.5a and 6.5b depict 10 ms-averaged profiles of density fluctuations and Doppler velocity before and after the cold-pulse injection. In the inner channels and $\sim 20 \text{ms}$ after the injection, density fluctuation levels decrease below pre-injection values. At the same locations, Doppler velocity increases towards ion diamagnetic direction. The temperature flex point (radial location where the temperature remains the same before and after the cold-pulse injection) is located at this same radial location, as shown in Figure 6.5c.

We speculate that this picture is somewhat consistent with the stabilization of electron-direction modes (medium-k turbulence) in the plasma core following the arrival of a density pulse. Reduction of medium-k electron density fluctuations could be an indication of stabilization of trapped electron modes in the core of the plasma, which would in turn lead to the core temperature increase. However, because of lack of transient measurements of plasma flow velocity we cannot provide a true comparison and further analysis is left for future work.

Having shown evidence of an electron density pulse in Section 6.2.1 and fast changes in turbulence, next section explores whether the increase in core electron density is accompanied by an increase in impurity content.

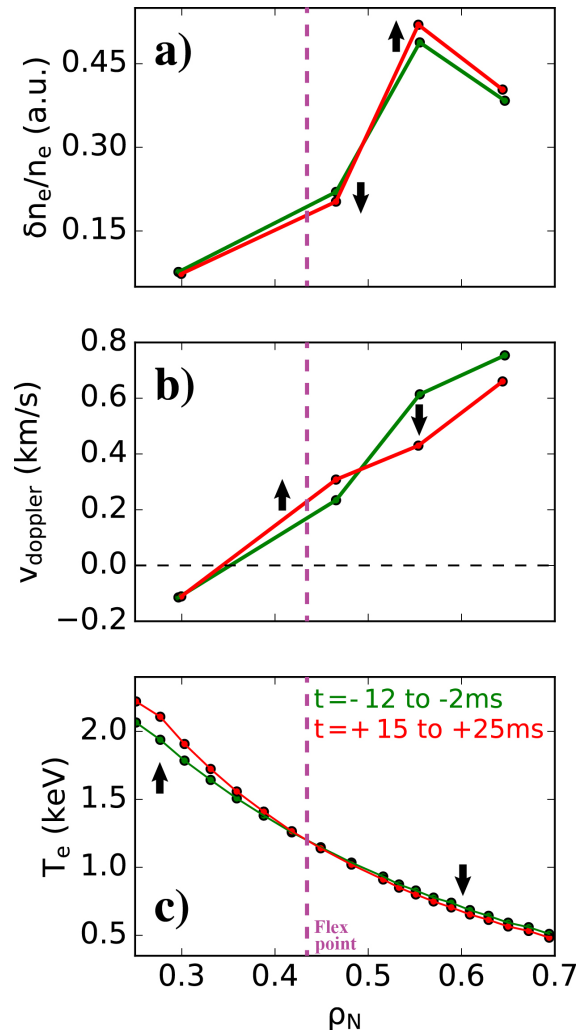


Figure 6.5: Turbulence measurements with DBS for shot #175847. Before and after injection profiles of (a) density fluctuation levels, and (b) Doppler velocity. (c) Electron temperature from ECE. Profiles plotted correspond to the time-average indicated in the legend. Dashed magenta line indicates radial location of temperature flex point.

6.2.3 Behavior of Impurities

Neutral aluminum particles ($\sim 10^{18}$) reach the edge of DIII-D plasmas and get ionized shortly after crossing the last closed flux surface. This local deposition causes a peaked impurity density profile at the edge ($\rho_N \gtrsim 0.8$). The large reversed gradients that build up lead to a strong inward flux of impurities, which reach the core in a very short time, as studied in detail in modeling work at ASDEX Upgrade [10]. The evolution of impurity density following the edge injection can be estimated experimentally using the emission of impurities via soft x-ray diagnostics and the STRAHL impurity transport code [13].

Figure 6.6b shows the contribution of the injected impurities to the electron density by quasineutrality (accounting for the evolution of all charge states, $\Delta n_e = \sum_Z Z \cdot n_{Al,Z}$) compared to the traces of electron density from the reflectometer. Here, impurity density evolution is obtained by running STRAHL simulations within an optimization code to determine maximum likelihood D and V impurity transport coefficients (Figure 6.6a) that match measured absolute levels of soft x-ray emission. The notably good agreement between the two traces in Figure 6.6 indicates that the core electron density perturbation can be explained by the arrival of impurities at the core (i.e. deuterium density remains approximately constant). Impurity radiation is only measured for $\rho_N < 0.6$, and therefore further work is needed to explain changes in electron density in the outer radii. At high density, impurity diffusion is significantly smaller than at low density, further suppressing the stabilization effect of the density gradient reduction.

Cold-pulses (and associated density perturbation) were also triggered by the injection of tungsten in Ohmic DIII-D discharges, but they did not lead to the characteristic temperature inversion at low collisionality observed with aluminum. This could be due to much stronger core radiation and ionization power losses for tungsten injections, which dominates core temperature evolution and thus prevents the temperature increase driven by turbulence stabilization. In these experiments, the impurity atoms that reach the plasma become ionized as they travel to the plasma core. For low-Z impurities, most of

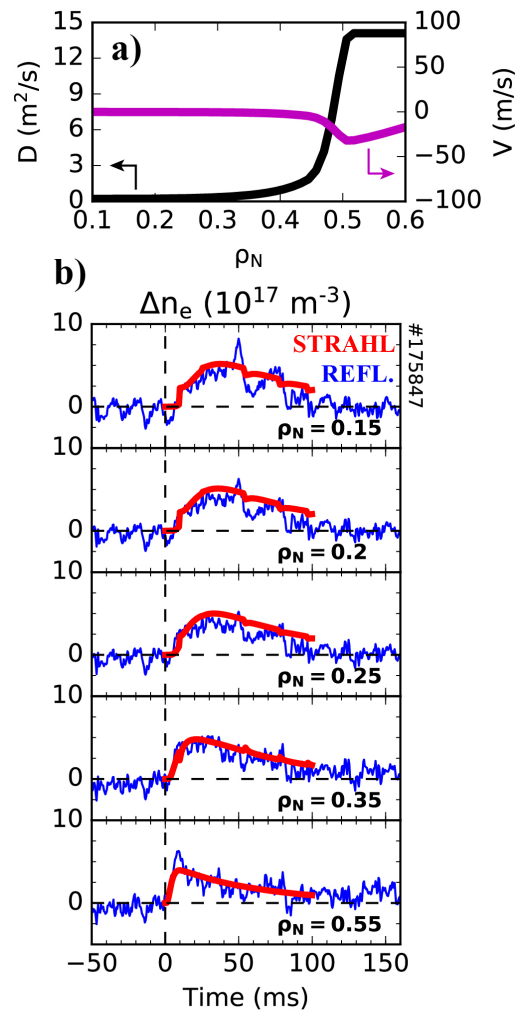


Figure 6.6: (a) Maximum likelihood D and V impurity transport coefficients. (b) Electron density evolution (blue) from reflectometer and (red) inferred from impurity radiation and STRAHL modeling

the radiation from partially ionized states is concentrated at the edge, but high-Z impurities radiate a significant amount of energy in the inner core. Perturbative transport studies then become more complicated because the plasma core is not a source-free region anymore. For this reason, those tungsten injections will not be included in this paper and are left for future work.

Following the experimental observations introduced in this section, extensive postdictive modeling (both steady-state and perturbative transport simulations) of the low-density DIII-D plasma is presented in the next section.

6.3 Postdictive Modeling of DIII-D Cold-Pulses

Steady state electron and ion (Carbon) temperature, and density and toroidal rotation profiles were fitted from experimental measurements with Gaussian Process Regression [14] using the OMFIT framework [15]. CER measurements (via diagnostic neutral beams) were taken after the injection but enough time was allowed, $\Delta t = 280$ ms, for the profiles to relax back to pre-injection steady-state values. A long time window for the radiation signals ($t = 1400 - 2000$ ms) was used to compensate the high noise levels in the bolometer data.

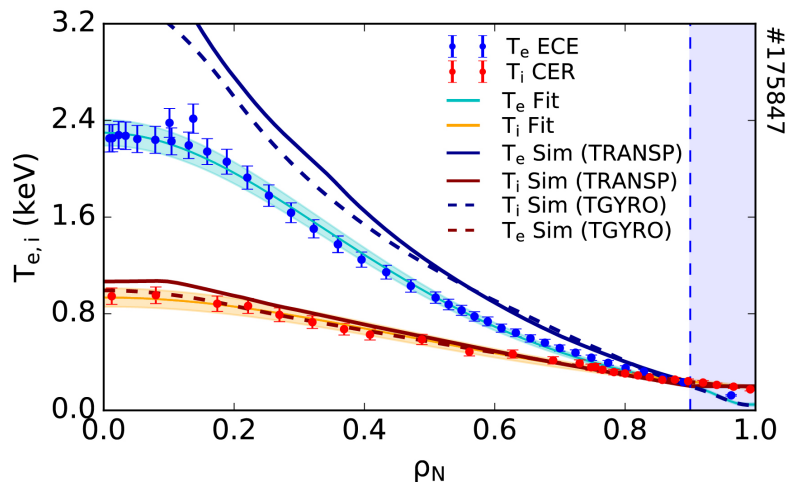


Figure 6.7: Simulated (with TGYRO and TRANSP) and experimental electron and ion temperature profiles in steady-state before the cold-pulse injection. Experimental electron temperature is inferred experimentally using an ECE radiometer, and ion temperature is obtained using a CER system via diagnostic neutral beam injections.

Steady-state predictions were performed using the PT_SOLVER numerical scheme [16] integrated with the TRANSP power balance code [17, 18]. All simulation settings are identical to those reported in Chapter 5. Figure 6.7 shows that the model over-predicts the steady-state electron temperature. This mismatch did not improve by changes in the boundary conditions nor by enabling density evolution. For completeness, the TGYRO code [19], which uses a different flux-matching solver, was also tested and gave similar predictions (dashed lines in Figure 6.7). These results in

steady-state motivate further work to improve the capabilities of TGLF to predict low-collisionality TEM-dominated regimes.

Once steady-state profiles are obtained, we proceed to introduce perturbations that mimic the injection of impurities at the edge of the plasma (increase in radiation and impurity density pulse).

6.3.1 Perturbative Transport Calculations

As done in the modeling of Alcator C-Mod plasmas, the cold-pulse injection is accompanied by an electron density perturbation. In DIII-D, the fast time resolution reflectometer measurements of electron density can be used to constrain the density pulse that travels from edge to core. Motivated by the results of the impurity transport inferences with STRAHL presented in Section 6.2.3, deuterium density will be assumed constant during the cold-pulse propagation.

In this study, the reflectometer core density perturbation is fitted to a skewed-Gaussian pulse in space and time. This approach ensures that the density at the plasma core does not increase before edge and middle channels do. This is justified by the fact that the impurities are injected at the edge of the plasma and propagate inwards, thus increasing core density. Interestingly, it is found that the edge and core channels cannot be fitted by a single Gaussian pulse. To resolve this, a correction has been implemented to keep edge density evolution within error bars. The left side of Figure 6.8 depicts the raw density data (blue) and the result of two different fits that use corrections adjusted manually: 1) an edge correction that ensures that the edge density perturbation is within measurement error bars (green, “model A”),

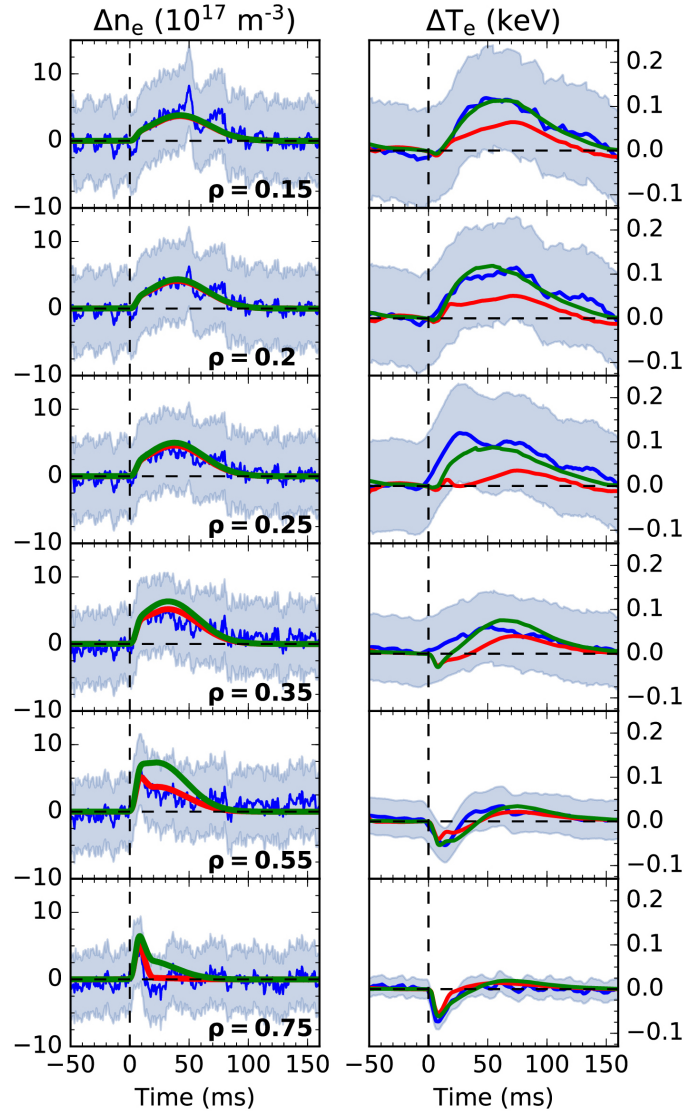


Figure 6.8: (left) Electron density and (right) temperature for (blue) experiment and (green, red) two different Gaussian-pulse fits. Light blue shaded areas indicate estimated error bars. A better agreement with core temperature evolution is achieved when edge density pulse is larger than the mean of the measurement (yet within error bars). This analysis corresponds to shot #175847.

and 2) an edge correction that guarantees that density evolution follows the mean of the measurement (red, “model B”).

The right side of Figure 6.8 shows the transient evolution of electron temperature for the two choices of density perturbation. Simulation and experiment are both depicted, evidencing that a experimentally-constrained density perturbation can produce a temperature inversion effect that is close to experimental measurements. Both density pulses give rise to a core temperature increase, but model A provided a larger core temperature increase. This discrepancy between the two is a consequence of a series of events. Around the middle channels ($\rho_N \sim 0.5 - 0.3$), the reduction of the density gradient is smaller for model B, which prevents the electron temperature from recovering after the initial drop (as depicted in Figure 6.8 at $\rho_N \sim 0.35$). As a consequence, the inner core of the plasma ($\rho_N \sim 0.2 - 0.3$) sees the arrival of higher a/L_{Te} , which increases transport and balances the stabilization effect of a/L_n . Details of the comparison between the two models are presented in the next Section (particularly in Figure 6.10).

6.3.2 Quasilinear Analysis of Main Turbulence Drives

During the cold-pulse propagation, TGLF provides electron and ion heat fluxes at all times in order to evolve kinetic profiles self-consistently. Figure 6.9 shows the relative importance of each turbulence drive in reducing electron and ion heat fluxes at $\rho_N = 0.2$ ($\Delta t = 10$ ms after the edge injection). All the qualitative trends are consistent with TEMs as the primary exhaust mechanism for electron heat flux [20, 21]: less transport with the reduction of a/L_n and n_D/n_e and more transport with the reduction of a/L_{Ti} . On the other hand, ITG-driven modes are the main ion heat exhaust mechanism in this plasma (stabilizing effect of a/L_{Ti} reduction). Other parameters that have an effect on TEM and ITG mode turbulence, such as v_{ie} , a/L_{Te} and T_i/T_e [22, 23], did not significantly change at this radial location ($\rho_N = 0.2$) at the time plotted ($\Delta t = 10$ ms).

Most of the TEM stabilization at $\rho_N = 0.2$ comes from the reduction of density gradients: $\sim 19\%$ reduction in a/L_{ne} leads to $\sim 65\%$ lower electron heat flux. During the simulation and these scans, the deuterium density gradient is kept constant and the impurity density gradient changes to fulfill quasineutrality at all times. In order for this to happen, impurities transiently develop a hollowed profile with reversed density gradient $a/L_{nz} \approx -1.0$ ($L_{ez} \equiv L_{ne}/L_{nz} \approx -3.0$), which acts towards stabilizing TEMs and destabilizing ITG modes. This is consistent with past work on impurity gradient effects on linear gyrokinetic simulations of ITG mode and TEM plasmas [24]. An additional scan was run where $a/L_{ne} = a/L_{nD} = a/L_{nz}$, but it could only account for $\sim 30\%$ of the total electron heat flux reduction (green dashed line in Figure 6.9).

Therefore, the strong impurity density gradients that arise as a consequence of the local deposition at the edge and subsequent inward propagation can be an important stabilization mechanism for TEM turbulence, particularly for plasmas with relatively flat density profiles (as in this case, $\eta_e \equiv L_{ne}/L_{Te} \approx 5.0$, $\epsilon_n \equiv L_{ne}/R \approx 1.0$) [25].

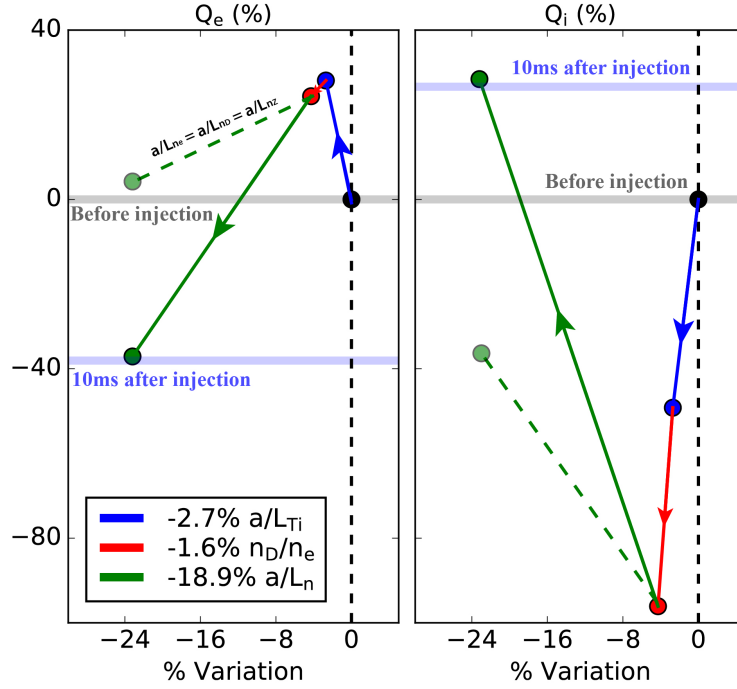


Figure 6.9: Evolution of the (left) electron and (right) ion heat fluxes (relative to the pre-injection time) as a function of a selection of turbulence drives. Each drive is varied the same amount as in the simulation, 10ms after the injection. Impurity dilution and normalized density gradient are also varied to fulfill quasineutrality during the scans. This analysis corresponds to low-density shot #175847.

We must highlight that, even though reversed impurity density gradients form after laser blow-off injections, their existence is, in general, not essential for the change in core impurity density gradient to contribute to the temperature inversion. Linear gyrokinetic simulations showed a stabilizing effect of impurity ions on the TEMs regardless of the peaking direction in the small $\eta_i = L_{ni}/L_{Ti}$ regime [24].

In order to compare model A and model B (results of the temperature evolution in Figure 6.8), we explore the behavior of the heat flux with respect to driving gradients at $\rho_N = 0.35$ (radial position where the differences between models start to become significant). Figures 6.10a and 6.10b show that the primary difference between the two is the stabilization effect of density gradients. For model B, a/L_{ne} is reduced by $\sim 8\%$ at $\Delta t = 30$ ms, while for model A the gradient is reduced by $\sim 18\%$. Such difference in the gradient is caused by $\sim 4\%$ absolute density change in model B and $\sim 5\%$ in model A, highlighting the high sensitivity to small changes in plasma parameters. As shown in Figures 6.10c and 6.10d, the reduction of a/L_{ne} in model A causes a shift in real frequency of the most unstable linear mode at long wavelength (transition to ITG dominance due to the suppression of low-k TEMs), while for model B there is only a reduction of the TEM linear growth rate, without a dominance transition. Consequently, the reduction of electron heat flux driven at low-k is stronger for model A than model B (Figure 6.10e). Figures 6.10a and 6.10b also

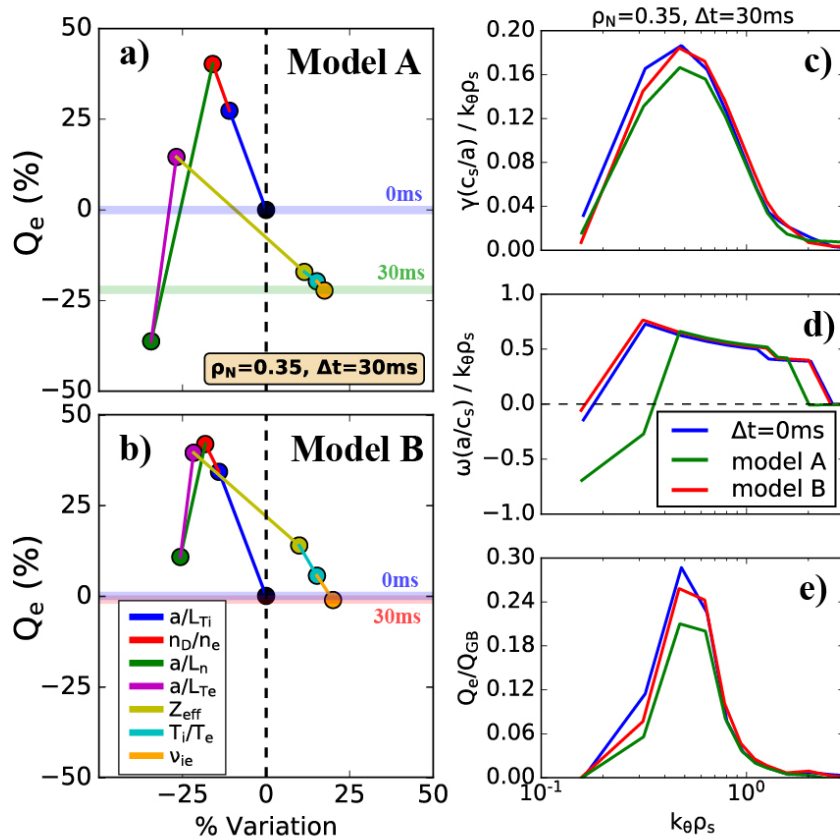


Figure 6.10: Evolution of the electron heat flux (relative to the pre-injection time) as a function of turbulence drives for a) model A and b) model B at $\rho_N = 0.35$ and 30 ms after the injection. Evolution of c) growth rate and d) frequency of the most unstable mode, and e) evolution of the electron heat flux spectrum. This analysis corresponds to low-density shot #175847.

confirm the stabilizing role of the increase in T_i/T_e , Z_{eff} and v_{ie} at $\rho_N = 0.35$ for both models, which helps compensate the destabilization caused by the increased electron temperature gradient at this position.

6.4 Discussion on Modeling Results in DIII-D Plasmas

In preparation for new DIII-D experiments, empirical predictions and predict-first simulations were both used to identify conditions that would exhibit the two distinct perturbative transport behaviors. The empirical scaling from Refs. [4, 5] was constructed with experimental data from devices other than DIII-D, since no evidence of temperature inversions had been reported in this machine. For this reason, theory-based predictions with TGLF were very valuable and helped build confidence that the perturbative transport experiment would run successfully.

The model presented here has been successful in explaining many of the trends observed in Alcator C-Mod cold-pulse experiments, such as the disappearance of the temperature inversion effect at high density, the trend with plasma current, why the temperature flex point seems to move along with rational surfaces, the connection with the thermal coupling between ions and electrons and the effect of auxiliary heating and heat flux ratio [10]. This Chapter also demonstrates that the model successfully captures the collisionality scaling proposed by [4], and was capable of predicting the cold-pulse behavior in a new machine.

High time resolution reflectometer measurements revealed the existence of a density pulse that travels from edge to core, consistent with the inward propagation of impurities after their deposition at the plasma edge. The presence of such a density perturbation was a key element of the original model proposed for Alcator C-Mod to explain the seemingly nonlocal effect observed for many years in magnetically confined plasmas (Chapter 5). Not only does this Chapter provide experimental evidence of rapid impurity and electron density pulses, but it also demonstrates that a large density perturbation is not needed to give rise to the core temperature increase.

Bibliography

- [1] C. Angioni et al. Relationship between density peaking, particle thermodiffusion, ohmic confinement, and microinstabilities in asdex upgrade l-mode plasmas. *Physics of Plasmas*, 12(4):040701, 2005. doi: 10.1063/1.1867492. URL <https://doi.org/10.1063/1.1867492>.
- [2] G.D. Conway et al. Observations on core turbulence transitions in asdex upgrade using doppler reflectometry. *Nuclear Fusion*, 46(9):S799, 2006. URL <http://stacks.iop.org/0029-5515/46/i=9/a=S15>.
- [3] J Citrin et al. Tractable flux-driven temperature, density, and rotation profile evolution with the quasilinear gyrokinetic transport model qualikiz. *Plasma Physics and Controlled Fusion*, 59(12):124005, 2017. URL <http://stacks.iop.org/0741-3335/59/i=12/a=124005>.
- [4] J.E. Rice et al. Non-local heat transport, rotation reversals and up/down impurity density asymmetries in alcator c-mod ohmic l-mode plasmas. *Nucl. Fusion*, 53(3):033004, 2013. URL <http://stacks.iop.org/0029-5515/53/i=3/a=033004>.
- [5] C. Gao et al. Non-local heat transport in alcator c-mod ohmic l-mode plasmas. *Nucl. Fusion*, 54(8):083025, 2014. URL <http://stacks.iop.org/0029-5515/54/i=8/a=083025>.
- [6] F. Ryter et al. Propagation of cold pulses and heat pulses in asdex upgrade. *Nucl. Fusion*, 40(11):1917, 2000. URL <http://stacks.iop.org/0029-5515/40/i=11/a=311>.
- [7] H.J. Sun et al. Experimental evidence of the non-local response of transport to peripheral perturbations. *Nuclear Fusion*, 51(11):113010, oct 2011. doi: 10.1088/0029-5515/51/11/113010. URL <https://doi.org/10.1088/0029-5515/51/11/113010>.
- [8] M.W. Kissick et al. Conditions and behaviour related to non-local electron heat transport on tftr. *Nucl. Fusion*, 38(6):821, 1998. URL <http://stacks.iop.org/0029-5515/38/i=6/a=304>.
- [9] P Mantica et al. Perturbative transport experiments in jet low or reverse magnetic shear plasmas. *Plasma Phys. Control. Fusion*, 44(10):2185, 2002. URL <http://stacks.iop.org/0741-3335/44/i=10/a=308>.
- [10] C. Angioni et al. The local nature of the plasma response to cold pulses with electron and ion heating at asdex upgrade. (*submitted to Nuclear Fusion*).
- [11] L. Zeng et al. Fast automated analysis of high-resolution reflectometer density profiles on diiii-d. *Nuclear Fusion*, 46(9):S677, 2006. URL <http://stacks.iop.org/0029-5515/46/i=9/a=S03>.
- [12] W. A. Peebles et al. A novel, multichannel, comb-frequency doppler backscatter system. *Review of Scientific Instruments*, 81(10):10D902, 2010. doi: 10.1063/1.3464266. URL <https://doi.org/10.1063/1.3464266>.

- [13] R. Dux. Report ipp 9/82. *MPI fur Plasmaphysik, Garching*, 2007.
- [14] M.A. Chilenski et al. Improved profile fitting and quantification of uncertainty in experimental measurements of impurity transport coefficients using gaussian process regression. *Nuclear Fusion*, 55(2):023012, jan 2015. doi: 10.1088/0029-5515/55/2/023012. URL <https://doi.org/10.1088/0029-5515/55/2/023012>.
- [15] O. Meneghini et al. Integrated modeling applications for tokamak experiments with omfit. *Nucl. Fusion*, 55(8):083008, 2015. URL <http://iopscience.iop.org/article/10.1088/0029-5515/55/8/083008/meta>.
- [16] X. Yuan et al. Parallel computing aspect in TRANSP with PT-SOLVER. In *APS Meeting Abstracts*, page JP8.119, October 2013. URL <http://adsabs.harvard.edu/abs/2013APS..DPPJP8119Y>.
- [17] R. J. Hawryluk. An empirical approach to tokamak transport. *Physics of Plasmas Close to Thermonuclear Conditions*, 1:19–46, 1980. URL <http://www.sciencedirect.com/science/article/pii/B9781483283852500091>.
- [18] Joshua Breslau et al. Transp. [Computer Software] <https://doi.org/10.11578/dc.20180627.4>, jun 2018. URL <https://doi.org/10.11578/dc.20180627.4>.
- [19] J. Candy et al. Tokamak profile prediction using direct gyrokinetic and neoclassical simulation. *Phys. Plasmas*, 16(6):060704, 2009. doi: 10.1063/1.3167820. URL <http://dx.doi.org/10.1063/1.3167820>.
- [20] A. G. Peeters et al. Linear gyrokinetic stability calculations of electron heat dominated plasmas in asdex upgrade. *Physics of Plasmas*, 12(2):022505, 2005. doi: 10.1063/1.1848111. URL <https://doi.org/10.1063/1.1848111>.
- [21] N. Bonanomi et al. Effects of nitrogen seeding on core ion thermal transport in JET ILW l-mode plasmas. *Nuclear Fusion*, 58(2):026028, jan 2018. doi: 10.1088/1741-4326/aa9e7c. URL <https://doi.org/10.1088/1741-4326/aa9e7c>.
- [22] J. E. Kinsey et al. Theoretical transport modeling of ohmic cold pulse experiments. *Phys. Plasmas*, 5(11):3974–3981, 1998. URL <http://dx.doi.org/10.1063/1.873117>.
- [23] Alessandro Casati et al. Temperature ratio dependence of ion temperature gradient and trapped electron mode instability thresholds. *Physics of Plasmas*, 15(4):042310, 2008. doi: 10.1063/1.2906223. URL <http://aip.scitation.org/doi/abs/10.1063/1.2906223>.
- [24] Huarong Du et al. Coupling of ion temperature gradient and trapped electron modes in the presence of impurities in tokamak plasmas. *Physics of Plasmas*, 21(5):052101, 2014. doi: 10.1063/1.4875342. URL <https://doi.org/10.1063/1.4875342>.

- [25] Huarong Du et al. Impurity effects on trapped electron mode in tokamak plasmas. *Physics of Plasmas*, 23(7):072106, 2016. doi: 10.1063/1.4955324. URL <https://doi.org/10.1063/1.4955324>.

Chapter 7

Conclusions and Future Work

Understanding turbulence and transport in magnetically confined plasmas is very important to predict performance of future burning plasmas, such as ITER and SPARC. For many years, cold-pulse experiments, extensively described in the literature, seemed to indicate that our current understanding of how local drift-wave-type turbulence is the dominant mechanism of “anomalously” high levels of transport in tokamak plasmas is incomplete. These cold-pulse experiments and associated phenomena have been puzzling plasma transport physicists for more than twenty years. In 1995, an experimental study in the TEXT tokamak [1] showed evidence of rapid core temperature increases following the injection of perturbative cold pulses at the edge of low-collisionality plasmas. Such unexplained behavior was reproduced in many other tokamaks and helical devices (TFTR [2, 3], Tore Supra [4, 5], RTP [6–8], ASDEX Upgrade [9], JET [10], LHD [11–18], HL-2A [19–25], Alcator C-Mod [26, 27], KSTAR [28], J-TEXT [29, 30] and EAST [31]).

The importance of whether or not transport models can explain and reproduce cold-pulse propagation is clear: *why should a transport model be trusted for prediction of future burning plasmas if it fails to explain such a robust and reproducible experiment?* The speed and the change of sign of the perturbation led transport physicists to consider these phenomena as evidence of nonlocal transport. In the framework of turbulence, nonlocal effects refer to mechanisms that allow transport fluxes at a given position in the plasma to be driven by pressure gradients and other parameters at a distance longer than a few radial correlation lengths of the turbulence [32, 33]. As such, nonlocal effects could, in principle, allow for core transport responses that are independent from mean local plasma parameters at the same position in space and at the same time [34]. The violation of the local closure could potentially give rise to transport hysteresis [12, 13], and was justified by the fact that the core temperature increase happens faster than the change on any other plasma quantity. Furthermore, the “reversed polarity” of the core response (temperature increase rather than a drop) appeared to violate the assumption of diffusive heat transport driven by local temperature gradients.

However, while nonlocal effects may exist in certain regimes, such a strong and robust response of the plasma core being driven by nonlocal phenomena would mean that the fundamental assumptions of turbulent transport models would need to be revisited [34, 35]. Such models, like TGLF [36] and QuaLiKiz [37], among others, are widely used to predict plasma performance and profiles in ITER and future reactors [38–48], and have been extensively validated against experiments [42, 49–53]. Turbulent heat transport, as provided by these models, may be driven by plasma parameters other than temperature gradients, exhibit critical-gradient behavior and may be strongly nonlinear (e.g. stiff transport [54]). An example of this is the case of Trapped Electron Mode turbulence, which is well known to drive large amounts of electron heat flux and can lead to hysteresis with respect to the electron temperature gradient. The possibility of such multi-channel interactions and high transport stiffness opens new pathways for understanding perturbative transport phenomena.

In this Thesis, cold pulses have been revisited from the standpoint of both modeling and experiment. This work provides the strongest evidence to date that the cold-pulse phenomena in tokamaks can be captured by the standard paradigm of local transport. It is found that stabilization of Trapped Electron Modes (TEMs) resulting from multiple small changes in local plasma quantities (mostly core electron and impurity density gradients, main ion dilution, effective ion charge and collisionality) leads to an increase in core temperature. These effects can be viewed as the consequence of the injection of impurities, subsequent propagation to the plasma core, and quasineutrality. Results in Alcator C-Mod and DIII-D demonstrate that such a density pulse can lead to the observed temperature behavior.

Not only was the inversion of temperature reproduced in simulations, but also the model has been successful in explaining the transition from temperature inversion to standard response with density and the observed trends in the cold pulse response with changes in plasma current. At high density, three main effects are known to contribute to the transition to dominant Ion Temperature Gradient (ITG) driven turbulence: higher collisionality, reduction in impurity content and increase in normalized ion temperature gradient. The dominance of ITG turbulence suppresses the stabilizing effect of core density gradients following the cold-pulse injection. Consequently, the electron temperature drop can propagate to the core without any “inversion”. At high plasma current, collisionality decreases due to increased Ohmic heating and a broadened temperature profile (at constant density), leading to less de-trapping and more TEM activity, which covers larger portions of the plasma. Other effects, such as the reduction of normalized ion temperature gradient a/L_{T_i} (less collisional exchange, only source of heat for the ions in Ohmic plasmas, generally leads to flatter T_i) may also result in prevalence of TEM over ITG turbulence. This dependence of dominant microinstability on plasma current is also compatible with the upshift of the critical density for ohmic confinement saturation [26, 55, 56], and explains the existence of temperature inversions at high density when the plasma current is increased. Such a model could also explain why the temperature flex point moves outwards (like the rational surfaces) when the current increases.

7.1 Future Work

While other models (mostly based on phenomenological and nonlocal contributions) have been proposed in past work, this modeling exercise has been able to reproduce experimental observations with greater detail than ever, using a model based on first-principle physics that has been extensively validated and is used to reproduce and predict steady-state plasmas in many machines. However, there are still a number of experimental features of cold-pulse phenomena that have not been addressed in this work. Some of these are detailed next.

This work has shown, thanks to experiments in DIII-D with high-time resolution density measurements and STRAHL inferences of impurity density evolution, that the core temperature inversion is a consequence of the rapid inward propagation of particles from edge to core. The fast inward propagation of a density pulse was experimentally confirmed and was consistent with the propagation of laser blow-off impurities. However, this Thesis has not addressed whether the fast inward propagation of particles can be reproduced with a local drift-wave turbulence model. Very recent work with our collaborators at the ASDEX Upgrade tokamak has been devoted to investigating this issue [57], confirming that the density pulse propagation is indeed captured in TGLF simulations. In ASDEX Upgrade simulations, the fast influx of impurities is triggered by an impurity mode, which is destabilized by strong reversed edge impurity gradients. Such impurity mode drives a large inward flux of impurities, which quickly flattens the density profile (as shown experimentally in the DIII-D work presented in this Thesis) and thus leads to the temperature increase.

In Ohmic DIII-D discharges cold-pulses were also triggered by the injection of tungsten, but they did not lead to the characteristic temperature inversion at low collisionality observed with aluminum. In Chapter 6, it was argued that the reason for this different behavior could be the stronger core radiation and ionization power losses for tungsten injections. However, comprehensive simulations of such injections could reveal new physics of cold-pulse dynamics.

A direct role of integer values of the q -profile in the phenomenology of cold pulses was suggested after experiments in RTP [8], but such observations have not been addressed in this Thesis. In Alcator C-Mod current scan simulations (Section 5.5), a direct role of integer q -values was not required to capture the experimental trend of the temperature flex point but instead it can be explained by the radial region where TEM turbulence dominates over ITG. However, experiments in RTP found that exceptionally large core temperature increases happened when off-axis electron cyclotron heating was aimed at the $q = 1$ surface. These experiments were not addressed here and therefore the direct role of integer values of the q -profile on the temperature inversion effect still remains unknown.

7.2 Final Remarks

The difficulty of drift-wave-type turbulence driven by local gradients to explain cold-pulse behavior had been considered one of the outstanding flaws of modern transport models based on local gyrokinetics [34]. This work represents a validation exercise for the TGLF turbulent transport model, which is shown here to reproduce satisfactorily all experimental trends that have been tested so far. Reproducing such complex turbulent transport dynamics with the TGLF model is remarkable, and gives us confidence that the fundamental assumptions of local reduced models alike are sufficient to predict transport and confinement in magnetic-confinement fusion devices.

To the author's knowledge, these results provide the strongest evidence to date that the cold-pulse phenomena in tokamaks can be captured by the standard paradigm of local transport, without the need to invoke non-local transport effects. By means of experimentally-constrained self-consistent modeling of cold-pulse experiments, we have shown that the existence of non-local transport phenomena is not necessary for explaining the behavior and timescales of cold-pulse experiments in tokamak plasmas.

Other models have been proposed in past work [17, 18, 58, 59], but their validity to reproduce quantitatively the core temperature behavior and the experimental trends with plasma parameters still remains to be explored. The success of local quasilinear transport models based on nonlinear gyrokinetics (e.g. TGLF and QuaLiKiz) in reproducing multichannel steady-state profiles has been evident for many years [42, 49–53]. Our predictive capabilities for future burning plasmas based on these transport models are becoming increasingly accurate thanks to extensive validation studies, and this work provides further confidence that the fundamental assumptions of integrated modeling frameworks based on local physics are enough to reproduce heat transport in tokamak plasmas.

Bibliography

- [1] K. W. Gentle et al. Strong nonlocal effects in a tokamak perturbative transport experiment. *Phys. Rev. Lett.*, 74:3620–3623, 1995. URL <https://link.aps.org/doi/10.1103/PhysRevLett.74.3620>.
- [2] M.W. Kissick et al. Non-local component of electron heat transport in tfr. *Nucl. Fusion*, 36(12): 1691, 1996. URL <http://stacks.iop.org/0029-5515/36/i=12/a=I09>.
- [3] M.W. Kissick et al. Conditions and behaviour related to non-local electron heat transport on tfr. *Nucl. Fusion*, 38(6):821, 1998. URL <http://stacks.iop.org/0029-5515/38/i=6/a=304>.
- [4] T. Dudok de Wit et al. Self-consistent removal of sawtooth oscillations from transient plasma data by generalized singular value decomposition. *Phys. Plasmas*, 5(5):1360–1368, 1998. URL <https://doi.org/10.1063/1.872796>.
- [5] X L Zou et al. *Plasma Physics and Controlled Fusion*, 42(10):1067–1076, oct 2000. doi: 10.1088/0741-3335/42/10/305. URL <https://doi.org/10.1088%2F0741-3335%2F42%2F10%2F305>.
- [6] P. Mantica et al. Nonlocal transient transport and thermal barriers in rijnhuizen tokamak project plasmas. *Phys. Rev. Lett.*, 82:5048–5051, 1999. URL <https://link.aps.org/doi/10.1103/PhysRevLett.82.5048>.
- [7] P Galli et al. Non-local response of rtp ohmic plasmas to peripheral perturbations. *Nuclear Fusion*, 39(10):1355–1368, oct 1999. doi: 10.1088/0029-5515/39/10/301. URL <https://doi.org/10.1088%2F0029-5515%2F39%2F10%2F301>.
- [8] G M D Hogewei et al. Recording non-local temperature rise in the RTP tokamak. *Plasma Physics and Controlled Fusion*, 42(10):1137–1144, oct 2000. doi: 10.1088/0741-3335/42/10/310. URL <https://doi.org/10.1088%2F0741-3335%2F42%2F10%2F310>.
- [9] F. Ryter et al. Propagation of cold pulses and heat pulses in asdex upgrade. *Nucl. Fusion*, 40(11):1917, 2000. URL <http://stacks.iop.org/0029-5515/40/i=11/a=311>.
- [10] P Mantica et al. Perturbative transport experiments in jet low or reverse magnetic shear plasmas. *Plasma Phys. Control. Fusion*, 44(10):2185, 2002. URL <http://stacks.iop.org/0741-3335/44/i=10/a=308>.
- [11] N. Tamura et al. Observation of core electron temperature rise in response to an edge cooling in toroidal helical plasmas. *Physics of Plasmas*, 12(11):110705, 2005. doi: 10.1063/1.2131047. URL <https://doi.org/10.1063/1.2131047>.
- [12] S Inagaki et al. Abrupt reduction of core electron heat transport in response to edge cooling on the large helical device. *Plasma Phys. Control. Fusion*, 48(5A):A251, 2006. URL <http://stacks.iop.org/0741-3335/48/i=5A/a=S23>.

- [13] N. Tamura et al. Impact of nonlocal electron heat transport on the high temperature plasmas of lhd. *Nucl. Fusion*, 47(5):449, 2007. URL <http://stacks.iop.org/0029-5515/47/i=5/a=009>.
- [14] N. Tamura et al. Edge-core interaction revealed with dynamic transport experiment in lhd (exc/p8-16). *International Atomic Energy Agency (IAEA)*, (IAEA-CN-180), 2010. URL http://www-pub.iaea.org/MTCD/Meetings/PDFplus/2010/cn180/cn180_BookOfAbstracts.pdf.
- [15] S Inagaki et al. Characterization of bifurcation induced by long distance correlation between heat flux and temperature gradient in toroidal plasmas. *Plasma Physics and Controlled Fusion*, 52(7):075002, may 2010. doi: 10.1088/0741-3335/52/7/075002. URL <https://doi.org/10.1088%2F0741-3335%2F52%2F7%2F075002>.
- [16] S. Inagaki et al. Observation of long-distance radial correlation in toroidal plasma turbulence. *Phys. Rev. Lett.*, 107:115001, 2011. URL <https://link.aps.org/doi/10.1103/PhysRevLett.107.115001>.
- [17] R O Dendy et al. Modelling the measured local time evolution of strongly nonlinear heat pulses in the large helical device. *Plasma Physics and Controlled Fusion*, 55(11):115009, oct 2013. doi: 10.1088/0741-3335/55/11/115009. URL <https://doi.org/10.1088%2F0741-3335%2F55%2F11%2F115009>.
- [18] H. Zhu et al. A quantitative model for heat pulse propagation across large helical device plasmas. *Physics of Plasmas*, 22(6):062308, 2015. doi: 10.1063/1.4923307. URL <https://doi.org/10.1063/1.4923307>.
- [19] H.J. Sun et al. Observation of non-local transport phenomena with SMBI in HL-2a. *Chinese Physics Letters*, 24(9):2621-2623, aug 2007. doi: 10.1088/0256-307x/24/9/044. URL <https://doi.org/10.1088%2F0256-307x%2F24%2F9%2F044>.
- [20] X.R. Duan et al. Overview of experimental results on hl-2a. *Nucl. Fusion*, 49(10):104012, 2009. URL <http://stacks.iop.org/0029-5515/49/i=10/a=104012>.
- [21] Hong-Juan Sun et al. Experiment of non-local effect with smbi on hl-2a. *Plasma Phys. Control. Fusion*, 52(4):045003, 2010. URL <http://stacks.iop.org/0741-3335/52/i=4/a=045003>.
- [22] H.J. Sun et al. Experimental evidence of the non-local response of transport to peripheral perturbations. *Nuclear Fusion*, 51(11):113010, oct 2011. doi: 10.1088/0029-5515/51/11/113010. URL <https://doi.org/10.1088%2F0029-5515%2F51%2F11%2F113010>.
- [23] O. Pan et al. Evidence of enhanced self-organized criticality (soc) dynamics during the radially non-local transient transport in the hl-2a tokamak. *Nucl. Fusion*, 55(11):113010, 2015. URL <http://stacks.iop.org/0029-5515/55/i=11/a=113010>.
- [24] W. Chen et al. Dynamics between the fishbone instability and nonlocal transient transport in hl-2a nbi plasmas. *Nucl. Fusion*, 56(4):044001, 2016. URL <http://stacks.iop.org/0029-5515/56/i=4/a=044001>.

- [25] X Q Ji et al. On the interplay between neoclassical tearing modes and nonlocal transport in toroidal plasmas. *Scientific Reports*, 6:32697, 2016. URL <https://www.nature.com/articles/srep32697>.
- [26] J.E. Rice et al. Non-local heat transport, rotation reversals and up/down impurity density asymmetries in alcator c-mod ohmic l-mode plasmas. *Nucl. Fusion*, 53(3):033004, 2013. URL <http://stacks.iop.org/0029-5515/53/i=3/a=033004>.
- [27] C. Gao et al. Non-local heat transport in alcator c-mod ohmic l-mode plasmas. *Nucl. Fusion*, 54(8):083025, 2014. URL <http://stacks.iop.org/0029-5515/54/i=8/a=083025>.
- [28] Y.J. Shi et al. Intrinsic rotation reversal, non-local transport, and turbulence transition in kstar l-mode plasmas. *Nuclear Fusion*, 57(6):066040, 2017. URL <http://stacks.iop.org/0029-5515/57/i=6/a=066040>.
- [29] Yuejiang Shi et al. Observation of multi-channel non-local transport in j-text plasmas. *Nuclear Fusion*, 58(4):044002, 2018. URL <http://stacks.iop.org/0029-5515/58/i=4/a=044002>.
- [30] Y. J. Shi et al. Observation of non-local effects in ion transport channel in j-text plasmas. *arXiv:1810.07529*, 2018. URL <https://arxiv.org/abs/1810.07529>.
- [31] Yong Liu et al. Dynamics of cold pulses induced by super-sonic molecular beam injection in the EAST tokamak. *Nuclear Fusion*, 59(4):044005, mar 2019. doi: 10.1088/1741-4326/ab0665. URL <https://doi.org/10.1088%2F1741-4326%2Fab0665>.
- [32] J D Callen and M W Kissick. Evidence and concepts for non-local transport. *Plasma Phys. Control. Fusion*, 39(12B):B173, 1997. URL <http://stacks.iop.org/0741-3335/39/i=12B/a=014>.
- [33] K Ida. New concepts of transport physics in toroidal plasmas. *Plasma Physics and Controlled Fusion*, 57(4):044007, mar 2015. doi: 10.1088/0741-3335/57/4/044007. URL <https://doi.org/10.1088%2F0741-3335%2F57%2F4%2F044007>.
- [34] K. Ida et al. Towards an emerging understanding of non-locality phenomena and non-local transport. *Nucl. Fusion*, 55(1):013022, 2015. URL <http://stacks.iop.org/0029-5515/55/i=1/a=013022>.
- [35] E.J. Doyle et al. Chapter 2: Plasma confinement and transport. *Nucl. Fusion*, 46:B557–B574, 2007. URL <http://stacks.iop.org/0029-5515/47/i=6/a=S02>.
- [36] G. M. Staebler et al. A theory-based transport model with comprehensive physics. *Phys. Plasmas*, 14(5):055909, 2007. URL <http://dx.doi.org/10.1063/1.2436852>.
- [37] C. Bourdelle et al. A new gyrokinetic quasilinear transport model applied to particle transport in tokamak plasmas. *Phys. Plasmas*, 14(11):112501, 2007. doi: 10.1063/1.2800869. URL <http://dx.doi.org/10.1063/1.2800869>.

- [38] R.V. Budny et al. Predictions of h-mode performance in iter. *Nuclear Fusion*, 48(7):075005, 2008. URL <http://stacks.iop.org/0029-5515/48/i=7/a=075005>.
- [39] F Wagner et al. On the heating mix of iter. *Plasma Physics and Controlled Fusion*, 52(12):124044, 2010. URL <http://stacks.iop.org/0741-3335/52/i=12/a=124044>.
- [40] M. Murakami et al. Integrated modelling of steady-state scenarios and heating and current drive mixes for iter. *Nuclear Fusion*, 51(10):103006, 2011. URL <http://stacks.iop.org/0029-5515/51/i=10/a=103006>.
- [41] A.H. Kritz et al. Integrated modelling for prediction of optimized iter performance. *Nuclear Fusion*, 51(12):123009, 2011. URL <http://stacks.iop.org/0029-5515/51/i=12/a=123009>.
- [42] J.E. Kinsey et al. Iter predictions using the gyro verified and experimentally validated trapped gyro-landau fluid transport model. *Nuclear Fusion*, 51(8):083001, 2011. URL <http://stacks.iop.org/0029-5515/51/i=8/a=083001>.
- [43] K Besseghir et al. Achieving and sustaining advanced scenarios in iter modelled by cronos and dina-ch. *Plasma Physics and Controlled Fusion*, 55(12):125012, 2013. URL <http://stacks.iop.org/0741-3335/55/i=12/a=125012>.
- [44] V. Parail et al. Self-consistent simulation of plasma scenarios for iter using a combination of 1.5d transport codes and free-boundary equilibrium codes. *Nuclear Fusion*, 53(11):113002, 2013. URL <http://stacks.iop.org/0029-5515/53/i=11/a=113002>.
- [45] R.V. Budny et al. Core fusion power gain and alpha heating in jet, tftr, and iter. *Nucl. Fusion*, 56(5):056002, 2016. URL <http://stacks.iop.org/0029-5515/56/i=5/a=056002>.
- [46] O. Meneghini et al. Integrated fusion simulation with self-consistent core-pedestal coupling. *Physics of Plasmas*, 23(4):042507, 2016. doi: 10.1063/1.4947204. URL <https://doi.org/10.1063/1.4947204>.
- [47] C. Chrystal et al. Predicting rotation for iter via studies of intrinsic torque and momentum transport in diiii-d. *Physics of Plasmas*, 24(5):056113, 2017. doi: 10.1063/1.4979194. URL <https://doi.org/10.1063/1.4979194>.
- [48] Jiale Chen et al. Self-consistent modeling of cfetr baseline scenarios for steady-state operation. *Plasma Physics and Controlled Fusion*, 59(7):075005, 2017. URL <http://stacks.iop.org/0741-3335/59/i=7/a=075005>.
- [49] Hyun-Tae Kim et al. Statistical validation of predictive transp simulations of baseline discharges in preparation for extrapolation to jet d-t. *Nucl. Fusion*, 57(6):066032, 2017. URL <http://stacks.iop.org/0029-5515/57/i=6/a=066032>.

- [50] J Citrin et al. Tractable flux-driven temperature, density, and rotation profile evolution with the quasilinear gyrokinetic transport model qualikiz. *Plasma Physics and Controlled Fusion*, 59(12):124005, 2017. URL <http://stacks.iop.org/0741-3335/59/i=12/a=124005>.
- [51] O. Meneghini et al. Self-consistent core-pedestal transport simulations with neural network accelerated models. *Nuclear Fusion*, 57(8):086034, 2017. URL <http://stacks.iop.org/0029-5515/57/i=8/a=086034>.
- [52] P. Rodriguez-Fernandez et al. Vitals: A surrogate-based optimization framework for the accelerated validation of plasma transport codes. *Fusion Science and Technology*, 74(1-2):65–76, 2018. doi: 10.1080/15361055.2017.1396166. URL <https://doi.org/10.1080/15361055.2017.1396166>.
- [53] O. Linder et al. Flux-driven integrated modelling of main ion pressure and trace tungsten transport in asdex upgrade. *Nuclear Fusion*, 59(1):016003, 2019. URL <http://stacks.iop.org/0029-5515/59/i=1/a=016003>.
- [54] N T Howard et al. Multi-scale gyrokinetic simulations of an alcator c-mod, ELM-y h-mode plasma. *Plasma Physics and Controlled Fusion*, 60(1):014034, nov 2017. doi: 10.1088/1361-6587/aa9148. URL <https://doi.org/10.1088%2F1361-6587%2Faa9148>.
- [55] J. E. Rice et al. Ohmic energy confinement saturation and core toroidal rotation reversal in alcator c-mod plasmas. *Physics of Plasmas*, 19(5):056106, 2012. doi: 10.1063/1.3695213. URL <https://doi.org/10.1063/1.3695213>.
- [56] H. Arnichand et al. Discriminating the trapped electron modes contribution in density fluctuation spectra. *Nuclear Fusion*, 55(9):093021, aug 2015. doi: 10.1088/0029-5515/55/9/093021. URL <https://doi.org/10.1088%2F0029-5515%2F55%2F9%2F093021>.
- [57] C. Angioni et al. The local nature of the plasma response to cold pulses with electron and ion heating at asdex upgrade. (*submitted to Nuclear Fusion*).
- [58] V D Pustovitov. Nonlocal effects in energy balance in an equilibrium plasma during its fast heating/cooling in tokamaks and stellarators. *Plasma Physics and Controlled Fusion*, 54(12):124036, nov 2012. doi: 10.1088/0741-3335/54/12/124036. URL <https://doi.org/10.1088%2F0741-3335%2F54%2F12%2F124036>.
- [59] F. Hariri et al. Cold pulse and rotation reversals with turbulence spreading and residual stress. *Phys. Plasmas*, 23(5), 2016. URL <http://dx.doi.org/10.1063/1.4951023>.

Appendix A

Derivations

A.1 Definitions of Stiffness

In the following, and with the purpose of a compilation on a single document, various definitions of stiffness are derived. An example of their application is discussed in Section 2.2.2.

In the following, it is assumed that steady-state heat flux follows a diffusion-convection form: $Q = -n\chi\nabla T + VnT$. Diffusivity is assumed to take positive values, and therefore, positive heat flux requires negative temperature gradient.

Incremental diffusivity as a measure of stiffness

In many cases, χ^{inc} alone is referred to as the “plasma stiffness”:

$$S_{\chi^{inc}} = \frac{1}{n} \left| \frac{\partial Q}{\partial \nabla T} \right| \quad (\text{A.1})$$

It is important to be aware that, even though χ^{inc} provides a metric to characterize the stiffness of the plasma profile to small changes in gradients, the incremental diffusivity given in Eq A.1 has units of diffusivity, m^2/s . The following stiffness definitions attempt to provide a dimensionless quantity that can be used for cross-machine comparison.

Departure from steady-state diffusivity

One may use as a measure of the plasma stiffness the relative departure from steady-state diffusivity:

$$S_{\chi} = \frac{\chi^{inc} - \chi}{\chi} \quad (\text{A.2})$$

By plugging in the incremental and power balance diffusivities, and using that $\frac{\partial \ln A}{\partial \ln B} = \frac{B}{A} \frac{\partial B}{\partial A}$

with $A > 0, B > 0$:

$$S_\chi = \frac{\chi + \frac{\partial \chi}{\partial \nabla T} \nabla T - \chi}{\chi} = \frac{\nabla T}{\chi} \frac{\partial \chi}{\partial \nabla T} = \frac{\partial \ln \chi}{\partial \ln |\nabla T|} = \frac{\partial \ln (VT - Q/n\nabla T)}{\partial \ln |\nabla T|} \quad (\text{A.3})$$

$$\boxed{S_\chi = -\frac{\partial \ln (VT - Q/n\nabla T)}{\partial \ln |\nabla T|}} \quad (\text{A.4})$$

where we have assumed that, by writing $Q = -n\chi\nabla T + nVT$, heat flux is positive for negative gradient. It is also important to notice that this definition is a diffusion-like stiffness, since only the increment on the diffusive heat flux is considered.

Relative flux increase

Another definition for stiffness refers to the resistance to change that the profile presents with the addition of heating power. We can then describe the stiffness as the ratio of relative change in heat flux to relative change in temperature gradient:

$$S_T = \frac{\frac{1}{Q} \partial Q}{\frac{1}{\nabla T} \partial \nabla T} = \frac{\nabla T}{Q} \frac{\partial Q}{\partial \nabla T} = \frac{\partial \ln Q}{\partial \ln |\nabla T|} \quad (\text{A.5})$$

$$\boxed{S_T = \frac{\partial \ln Q}{\partial \ln |\nabla T|}} \quad (\text{A.6})$$

Stiffness as in Eq A.6 considers incremental heat loss without separating the diffusion and convection terms. Actually, this definition is equivalent to calculating the ratio with respect to an effective steady-state diffusivity ($S_T = \frac{\chi^{inc}}{\chi_{eff}}$) that also captures the convective component, i.e. $Q = n\chi_{eff}\nabla T$. Note that, in Eq. A.5 we could have then written that [1]:

$$S_T = \frac{\chi^{inc}}{\chi_{eff}} = \frac{\nabla T}{Q} \frac{\partial Q}{\partial \nabla T} = \frac{\nabla T}{n\chi_{eff}\nabla T} \frac{\partial (n\chi_{eff}\nabla T)}{\partial \nabla T} = 1 + \frac{\nabla T}{\chi_{eff}} \frac{\partial \chi_{eff}}{\partial \nabla T} \quad (\text{A.7})$$

Normalized incremental diffusivity

In transport theory, it is a common convention to assume that transport equations are invariant under gyro-radius transformations, and thus are normalized to the so-called gyro-Bohm units. Likewise, the driving gradients are normalized as scale lengths. A definition of stiffness using these units would look like [1]:

$$\boxed{S^* = \frac{\partial Q_{GB}}{\partial a/L_T}} \quad (\text{A.8})$$

The definition of gyro-Bohm heat flux unit is $Q_{GB,unit} = nTc_s(\rho_s/a)^2 = CnT^{5/2}$ and the gyro-Bohm diffusivity unit is $\chi_{GB,unit} = c_s/a\rho_s^2 = CaT^{3/2}$. Using these normalizations ($Q_{GB} =$

$Q/Q_{GB,unit}$ and $\chi_{GB} = \chi_{eff}/\chi_{GB,unit}$ and $a/L_T = \nabla T \cdot a/T$, we can write:

$$S^* = C \frac{\partial}{\partial (\nabla T \cdot a/T)} \left(Q / (CnT^{5/2}) \right) = \frac{1}{a \cdot Cn} \frac{\partial (Q \cdot T^{-5/2})}{\partial (\nabla T/T)} = \quad (\text{A.9})$$

$$= \frac{1}{a \cdot Cn} \left(T^{-3/2} \frac{\partial Q}{\partial \nabla T} + QT \frac{\partial (T^{-5/2})}{\partial \nabla T} \right) = \quad (\text{A.10})$$

$$= \frac{1}{a \cdot CnT^{3/2}} \frac{\partial Q}{\partial \nabla T} = \frac{1}{\chi_{GB,unit} \cdot n} \frac{\partial Q}{\partial \nabla T} = \quad (\text{A.11})$$

$$= \chi_{GB} \frac{\chi^{inc}}{\chi_{eff}} = \chi_{GB} \cdot S_T \quad (\text{A.12})$$

where we have used the fact that a is not a coordinate but a constant and that, again, ∇T , T and n are treated as independent variables. We have also used that $Q = -n\chi_{eff}\nabla T$ and therefore $Q \neq Q(T)$ in this framework.

A.2 1.5D Governing Equations for Transport Codes

Starting from the full set of Maxwell's equations coupled to the Boltzmann kinetic model, one can derive a set of fluid equations [2]. The first three moments result, for each plasma species α , along with Maxwell's equations, in:

$$\begin{aligned}
 \frac{\partial n_\alpha}{\partial t} + \nabla \cdot (\vec{u}_\alpha n_\alpha) &\equiv \frac{Dn_\alpha}{Dt} + n_\alpha \nabla \cdot \vec{u}_\alpha = S_\alpha \\
 m_\alpha n_\alpha \frac{D\vec{u}_\alpha}{Dt} + \nabla \cdot \bar{\bar{P}}_\alpha - Z_\alpha e n_\alpha (\vec{E} + \vec{u}_\alpha \times \vec{B}) - \vec{R}_\alpha &= S_{M,\alpha} \\
 \frac{3}{2} n_\alpha \frac{DT_\alpha}{Dt} + \bar{\bar{P}}_\alpha : \nabla \vec{u}_\alpha + \nabla \cdot \vec{q}_\alpha - Q_\alpha &= S_{E,\alpha}
 \end{aligned}
 \quad \left| \begin{aligned}
 \nabla \times \vec{E} &= -\frac{\partial \vec{B}}{\partial t} \\
 \nabla \times \vec{B} &= \mu_0 e (n_i \vec{u}_i - n_e \vec{u}_e) + \frac{1}{c} \frac{\partial \vec{E}}{\partial t} \\
 \nabla \cdot \vec{E} &= \frac{e}{\epsilon_0} (n_i - n_e) \\
 \nabla \cdot \vec{B} &= 0
 \end{aligned} \right.
 \tag{A.13}$$

where S_α , $S_{M,\alpha}$ and $S_{E,\alpha}$ refer to external sources of particle, momentum and energy, respectively. $\bar{\bar{P}}_\alpha$ is the total pressure tensor ($\bar{\bar{P}}_\alpha = p_\alpha \bar{\bar{I}} + \bar{\bar{\Pi}}_\alpha$), \vec{R}_α is the mean momentum transferred between unlike particles due to friction of collisions, and Q_α is the heat generated and transferred between unlike particles due to collisional dissipation.

The derivation that follows is a summary of that presented in Refs. [3–5] and complements the formulations with specific approaches of different power balance codes, namely TRANSP [6], ASTRA [7], JETTO [8], CRONOS [9] and FASTRAN [10]. Here, only energy and particle conservation equations are converted into the proper formalism. Momentum governing equation would follow a similar procedure, and the interested reader is invited to read Ref [4].

We can define the absolute spatial coordinate based on the toroidal flux and with arbitrary normalization as $\rho = \frac{\sqrt{\Phi}}{\pi B_0}$ and a relative spatial coordinate $\zeta = \rho / \rho_{lim}$. The objective is to convert transport equations, $\frac{\partial F}{\partial t} + \nabla \cdot \vec{q} = P$, into a coordinate system independent on the normalization and where the boundary is always prescribed and not time-varying (e.g. $\zeta_{lim} = 1$). The procedure starts by volume-integrating the transport equations and differentiating in the coordinate ρ :

$$\frac{\partial}{\partial \rho} \int_V dV \left[\frac{\partial F}{\partial t} + \nabla \cdot \vec{q} = P \right] \tag{A.14}$$

where V is the volume of the interior of the flux surface with $\rho = const$.

First, by integrating over the region interior to a surface with $\rho = const$, and defining $\langle \cdot \rangle$ as the flux-surface average, we have [5]:

$$\int_V P dV = \int_0^\rho \langle P \rangle \frac{\partial V}{\partial \rho} d\rho \tag{A.15}$$

Defining the differential volume element as $V' = \frac{\partial V}{\partial \rho}$ and using the assumption that kinetic

profiles are constant over flux-surfaces, we can differentiate both sides with respect to ρ :

$$\frac{\partial}{\partial \rho} \left[\int_V P dV \right] = V' \langle P \rangle \quad (\text{A.16})$$

Defining $\vec{u}_{S,\rho}$ as the speed of the moving coordinate ρ (i.e. velocity of the flux surface), such that $\frac{\partial \rho}{\partial t} + \vec{u}_{S,\rho} \cdot \nabla \rho = 0$, the time derivative on a moving grid results:

$$\frac{\partial}{\partial t} \int_{V,\rho} P dV = \int_{V,\rho} \frac{\partial P}{\partial t} dV + \oint P \vec{u}_{S,\rho} \cdot d\vec{S}_\rho \quad (\text{A.17})$$

Using the divergence theorem and realizing that $d\vec{S}_\rho = dS \frac{\nabla \rho}{|\nabla \rho|}$ we can write the terms that follow a flux-form as:

$$\int_V (\nabla \cdot \vec{f}) dV = \oint_S \vec{f} \cdot d\vec{S}_\rho = \oint_S \vec{f} \cdot \nabla \rho \frac{dS}{|\nabla \rho|} = \langle \vec{f} \cdot \nabla \rho \rangle V' \quad (\text{A.18})$$

Differentiating both sides with respect to ρ we find that:

$$\frac{\partial}{\partial \rho} \left[\int_V (\nabla \cdot \vec{f}) dV \right] = \frac{\partial}{\partial \rho} (\langle \vec{f} \cdot \nabla \rho \rangle V') \quad (\text{A.19})$$

In terms of the energy conservation equation (Equation A.13), viscous stresses are usually neglected, that is $\bar{\bar{P}} : \nabla \vec{u} \approx p \nabla \cdot \vec{u}$. If we define a particle velocity as $\vec{u} = \vec{\Gamma}/n$, we can rewrite the energy transport equation as:

$$\frac{\partial}{\partial t} \left(\frac{3}{2} nT \right) = -p \nabla \cdot \vec{u} - \nabla \cdot \left(\vec{q} + \frac{3}{2} \vec{\Gamma} T \right) + Q + S_E \quad (\text{A.20})$$

where the species subscript α has been dropped to simplify notation. Performing a volume-integration, differentiating in the coordinate ρ and using the properties above, each term then becomes:

$$\frac{\partial}{\partial \rho} \int \left[\frac{\partial}{\partial t} \left(\frac{3}{2} nT \right) \right] dV = \frac{\partial}{\partial t} \Big|_\rho \left(\frac{3}{2} \langle nT \rangle V' \right) - \frac{\partial}{\partial \rho} \left(\frac{3}{2} \langle nT \vec{u}_{S,\rho} \cdot \nabla \rho \rangle V' \right) \quad (\text{A.21})$$

$$\begin{aligned} \frac{\partial}{\partial \rho} \left(\int \left[\nabla \cdot \left(\frac{3}{2} nT \vec{u} \right) \right] dV + \int [nT \nabla \cdot \vec{u}] dV \right) &= \frac{\partial}{\partial \rho} \left(\left\langle \frac{5}{2} nT (\vec{u} - \vec{u}_{S,\rho}) \cdot \nabla \rho \right\rangle V' \right) - \\ &- \langle (\vec{u} - \vec{u}_{S,\rho}) \cdot \nabla (nT) \rangle V' + \langle nT \nabla \cdot \vec{u}_{S,\rho} \rangle V' \end{aligned} \quad (\text{A.22})$$

$$\frac{\partial}{\partial \rho} \int [\nabla \cdot \vec{q}] dV = \frac{\partial}{\partial \rho} (\langle \vec{q} \cdot \nabla \rho \rangle V') \quad (\text{A.23})$$

$$\frac{\partial}{\partial \rho} \int [Q + S_E] dV = \langle Q \rangle V' + \langle S_E \rangle V' \quad (\text{A.24})$$

Finally, using the relationship $\langle nT \nabla \cdot \vec{u}_{S,\rho} \rangle V' = \langle nT \rangle \oint \vec{u}_{S,\rho} \cdot d\vec{S}_\rho = \langle nT \rangle \frac{\partial V'}{\partial t}$ [3], we can write¹:

$$\begin{aligned} \frac{1}{V'} \left[\frac{\partial}{\partial t} \Big|_\rho \left(\frac{3}{2} \langle nT \rangle V' \right) + \langle nT \rangle \frac{\partial V'}{\partial t} \right] = \\ - \frac{1}{V'} \frac{\partial}{\partial \rho} \left(\left[\langle \vec{q} \cdot \nabla \rho \rangle + \frac{5}{2} \langle nT (\vec{u} - \vec{u}_{S,\rho}) \cdot \nabla \rho \rangle \right] V' \right) + \langle (\vec{u} - \vec{u}_{S,\rho}) \cdot \nabla (nT) \rangle + \langle Q \rangle + \langle S_E \rangle \end{aligned} \quad (\text{A.25})$$

Using neoclassical theory analysis and conservation of momentum, it can be shown [5] that, for electron and ion species:

$$\langle (\vec{u}_e - \vec{u}_{S,\rho}) \cdot \nabla (n_e T_e) \rangle + \langle Q_e \rangle \approx \langle \vec{J} \cdot \vec{E} \rangle - (\langle Q_{ei} \rangle + \langle Q_\Gamma \rangle) \quad (\text{A.26})$$

$$\langle (\vec{u}_i - \vec{u}_{S,\rho}) \cdot \nabla (n_i T_i) \rangle + \langle Q_i \rangle \approx \langle Q_{ei} \rangle + \langle Q_\Gamma \rangle \quad (\text{A.27})$$

where $Q_\Gamma = \vec{u}_e \cdot \nabla (n_i T_i)$, Q_{ei} is the electron-ion collisional energy exchange, and $\vec{J} \cdot \vec{E} = Q_{OH}$ is the Ohmic power density. In the rest of this formulation, we will include the Ohmic power density inside the electron energy sources, $S_{E,e}$, and Q_Γ will be included in the electron-ion exchange term.

Therefore:

$$\begin{aligned} \frac{1}{V'} \left[\frac{\partial}{\partial t} \Big|_\rho \left(\frac{3}{2} \langle n_e T_e \rangle V' \right) + \langle n_e T_e \rangle \frac{\partial V'}{\partial t} \right] = \\ - \frac{1}{V'} \frac{\partial}{\partial \rho} \left(\left[\langle \vec{q}_e \cdot \nabla \rho \rangle + \frac{5}{2} \langle n_e T_e (\vec{u}_e - \vec{u}_{S,\rho}) \cdot \nabla \rho \rangle \right] V' \right) - \langle Q_{ei} \rangle + \langle S_{E,e} \rangle \\ \frac{1}{V'} \left[\frac{\partial}{\partial t} \Big|_\rho \left(\frac{3}{2} \langle n_i T_i \rangle V' \right) + \langle n_i T_i \rangle \frac{\partial V'}{\partial t} \right] = \\ - \frac{1}{V'} \frac{\partial}{\partial \rho} \left(\left[\langle \vec{q}_i \cdot \nabla \rho \rangle + \frac{5}{2} \langle n_i T_i (\vec{u}_i - \vec{u}_{S,\rho}) \cdot \nabla \rho \rangle \right] V' \right) + \langle Q_{ei} \rangle + \langle S_{E,i} \rangle \end{aligned} \quad (\text{A.28})$$

Recognizing that $\vec{\Gamma} = n (\vec{u} - \vec{u}_{S,\rho})$, we can write the convection term contribution to the heat flux as:

$$\frac{5}{2} \langle nT (\vec{u} - \vec{u}_{S,\rho}) \cdot \nabla \rho \rangle V' = \frac{5}{2} \langle T \vec{\Gamma} \cdot \nabla \rho \rangle V' \quad (\text{A.29})$$

Using the same properties, we can write the particle conservation equation (from Eq. A.20):

$$\frac{\partial}{\partial \rho} \int_V \left[\frac{\partial n}{\partial t} + \nabla \cdot (n \vec{u}) = S \right] dV \quad (\text{A.30})$$

$$\frac{\partial}{\partial t} \Big|_\rho (\langle n \rangle V') = - \frac{\partial}{\partial \rho} (\langle n (\vec{u} - \vec{u}_{S,\rho}) \cdot \nabla \rho \rangle V') + \langle S \rangle V' \quad (\text{A.31})$$

¹Please note that some authors [3, 5, 7] prefer to include the compression power density due to the changing volume in the first derivative, thus $\frac{1}{V'} \frac{\partial}{\partial t} \Big|_\rho \left(\frac{3}{2} \langle nT \rangle V' \right) + \frac{1}{V'} \langle nT \rangle \frac{\partial V'}{\partial t} \rightarrow \frac{1}{(V')^{5/3}} \frac{\partial}{\partial t} \Big|_\rho \left(\frac{3}{2} \langle nT \rangle (V')^{5/3} \right)$, but here we will leave the compression term explicit.

Therefore, we can write electron density and electron and ion energy equations:

$$\begin{aligned}
 \frac{1}{V'} \frac{\partial}{\partial t} \Big|_{\rho} (\langle n_e \rangle V') &= -\frac{1}{V'} \frac{\partial}{\partial \rho} (\langle \Gamma_e \cdot \nabla \rho \rangle V') + \langle S_e \rangle \\
 \frac{1}{V'} \left[\frac{\partial}{\partial t} \Big|_{\rho} \left(\frac{3}{2} \langle n_e T_e \rangle V' \right) + \langle n_e T_e \rangle \frac{\partial V'}{\partial t} \right] &= -\frac{1}{V'} \frac{\partial}{\partial \rho} \left(\left[\langle \vec{q}_e \cdot \nabla \rho \rangle + \frac{5}{2} \langle T_e \Gamma_e \cdot \nabla \rho \rangle \right] V' \right) - \langle Q_{ei} \rangle + \langle S_{E,e} \rangle \\
 \frac{1}{V'} \left[\frac{\partial}{\partial t} \Big|_{\rho} \left(\frac{3}{2} \langle n_i T_i \rangle V' \right) + \langle n_i T_i \rangle \frac{\partial V'}{\partial t} \right] &= -\frac{1}{V'} \frac{\partial}{\partial \rho} \left(\left[\langle \vec{q}_i \cdot \nabla \rho \rangle + \frac{5}{2} \langle T_i \Gamma_i \cdot \nabla \rho \rangle \right] V' \right) + \langle Q_{ei} \rangle + \langle S_{E,i} \rangle
 \end{aligned}
 \tag{A.32}$$

This is a convenient form of writing transport equations, because transport fluxes in real units (\vec{q} [W/m²]) can be evaluated very easily in the ρ -grid:

$$\vec{q} = -n\chi_{eff}\nabla T \implies \langle \vec{q} \cdot \nabla \rho \rangle = -\langle \chi_{eff} n \nabla T \cdot \nabla \rho \rangle = -\left\langle \chi_{eff} n \frac{\partial T}{\partial \rho} \|\nabla \rho\|^2 \right\rangle \tag{A.33}$$

$$\vec{\Gamma} = -D_{eff}\nabla n \implies \langle \vec{\Gamma} \cdot \nabla \rho \rangle = -\langle D_{eff} \nabla n \cdot \nabla \rho \rangle = -\left\langle D_{eff} \frac{\partial n}{\partial \rho} \|\nabla \rho\|^2 \right\rangle \tag{A.34}$$

Bibliography

- [1] T.C. Luce et al. Experimental challenges to stiffness as a transport paradigm. *Nuclear Fusion*, 58(2):026023, jan 2018. doi: 10.1088/1741-4326/aa9af7. URL <https://doi.org/10.1088/2F1741-4326%2Faa9af7>.
- [2] Jeffrey P. Freidberg. *Ideal MHD*. Cambridge University Press, 2014. doi: 10.1017/CBO9780511795046. URL <https://doi.org/10.1017/CBO9780511795046>.
- [3] M. Kikuchi. *Frontiers in Fusion Research: Physics and Fusion*. Springer London, 2011. ISBN 9781849964111. URL <https://books.google.com/books?id=imkzzTW-Ns4C>.
- [4] B.A. Grierson. Basic transp equations. 2017. URL <https://drive.google.com/file/d/0B3rL-PK3cqQ3cmU2WTNpWlFOVVk/view>.
- [5] F. L. Hinton and R. D. Hazeltine. Theory of plasma transport in toroidal confinement systems. *Rev. Mod. Phys.*, 48:239–308, Apr 1976. doi: 10.1103/RevModPhys.48.239. URL <https://link.aps.org/doi/10.1103/RevModPhys.48.239>.
- [6] D McCune et al. Generalization of pppl transport analysis code transp for time dependent magnetic flux geometry. *Division of Plasma Physics Annual Meeting*, 1984. URL http://w3.pppl.gov/transp/papers/APS_1984_TRANSP.pdf.
- [7] G.V. Pereverzev and P.N. Yushmanov. *ASTRA: Automated System for Transport Analysis in a Tokamak*. Bericht / 5: Bericht. IPP, 2002. URL <https://books.google.com/books?id=iBi0mgEACAAJ>.
- [8] G Cenacchi and A Taroni. *JETTO: A free-boundary plasma transport code*. IAEA, 1988. URL http://www.iaea.org/inis/collection/NCLCollectionStore/_Public/19/097/19097143.pdf?r=1.
- [9] J.F. Artaud et al. The cronos suite of codes for integrated tokamak modelling. *Nuclear Fusion*, 50(4):043001, 2010. URL <http://stacks.iop.org/0029-5515/50/i=4/a=043001>.
- [10] J.M. Park et al. An efficient transport solver for tokamak plasmas. *Computer Physics Communications*, 214(Supplement C):1 – 5, 2017. ISSN 0010-4655. doi: <https://doi.org/10.1016/j.cpc.2016.12.018>. URL <http://www.sciencedirect.com/science/article/pii/S0010465516303976>.

Appendix B

Steady-State Transport Model Validation

“Validation is the process by which it is determined that the mathematical model faithfully represents stipulated physical processes, [...] within prescribed limits.”

Terry et al. (Physics of Plasmas, 2008).

Understanding transport in magnetically confined plasmas is critical for developing predictive models for future devices, such as ITER and SPARC. Thanks to recent progress in simulation and theory, along with enhanced computational power and better diagnostic systems, direct and quantitative comparisons between experimental results and models is possible. However, validating transport models using additional constraints and accounting for experimental uncertainties still remains a formidable task.

Here, a new optimization framework is developed to address the issue of constrained validation of transport models. The VITALS (Validation via Iterative Training of Active Learning Surrogates) framework exploits surrogate-based strategies using Gaussian processes and sequential parameter updates to achieve the combination of plasma parameters that matches experimental transport measurements within diagnostic error bars.

Section [B.1](#) introduces the concept of transport model validation and the main difficulties encountered in the field of tokamak plasma physics. Section [B.2](#) describes how VITALS is capable of handling these difficulties. Section [B.3](#) contains details on the machine learning framework used within VITALS to tackle the optimization problem. The possible transport metrics that can be used to validate models within VITALS are presented in Section [B.4](#). Section [B.5](#) presents the application of VITALS to a set of Alcator C-Mod L-mode plasma conditions. Lastly, Section [B.6](#) provides a discussion of the results, as well as advantages with respect to typical heat-flux matching simulation codes.

B.1 Motivation: Difficulties in Transport Model Validation

Validating computer simulations of plasma behavior is critical for the further development of theory and the better design of targeted experiments [2]. The plasma physics community defines transport validation as the process of determining if numerical simulations faithfully capture the physical processes that govern transport in confined plasmas [1]. Nonlinear gyrokinetic theory as encapsulated by modern codes such as GYRO [3] and GENE [4], and the associated gyrofluid model used by TGLF [5], is the leading model for core turbulence and transport and also the most extensively validated. So much so, that the codes have been used successfully to design new experiments and predict changes in turbulence before measurements are available [6–8].

Many validation efforts with gyrokinetic codes have focused on comparisons with heat fluxes [9–12]. Comparison against measured turbulence has become more common [8, 13–19], and very recently additional constraints such as impurity transport [20] and perturbative diffusivity [21, 22] have been included as well. The highly nonlinear nature of plasmas and plasma turbulence means that these simulations are very sensitive to small changes in input parameters. It is therefore widely recognized that many careful sensitivity scans must be performed, changing input parameters within experimental error bars, in order to ensure that any agreement (or disagreement) is not fortuitous [1, 2, 23].

To the best of our knowledge, the aforementioned papers and most validation techniques using codes like GYRO [3] and TGLF [5] have relied on a serial, or “base-case” approach: the code user will modify one or two inputs to the turbulence simulation (e.g. normalized gradient scale lengths of ion and electron temperature, a/L_{T_i} and a/L_{T_e} respectively), and then the user tests whether heat fluxes are in agreement with experiment within error bars [24]. Once a so-called “base-case” simulation is obtained, then the results of that one simulation case are compared with turbulence measurements or other transport quantities. But this serial approach is quite limited. For example, if the same simulation were instead constrained by bringing the turbulence into agreement with the experiment based on changes of input parameters like a/L_{T_i} , it is highly likely that resulting heat fluxes would no longer agree with experiment. To reconcile this, more sensitivity scans would be needed, but the serial nature of the sensitivity scans can quickly become intractable, even when using gyrofluid models, much less a full nonlinear gyrokinetic model. Ideally, one would like to perform many scans of many input parameters simultaneously to probe whether or not a model can match *all the* experimentally measured quantities within error bars *at the same time*. The new framework presented here, VITALS (Validation via Iterative Training of Active Learning Surrogates), accomplishes just this goal. We note that some validation techniques use flux-matching approaches, such as TGYRO [25], where a solution consistent with a given transport model and well defined physics-based relationships is found. This work does not follow the same methodology as the flux-matching approaches, since physics-based relationships and global integration are not yet implemented.

B.2 VITALS Fundamentals

VITALS consists on the implementation of machine learning algorithms to the validation of plasma transport codes, and allows the user to scan many input parameters at once, while also simultaneously constraining the results using heat fluxes, turbulence measurements, and other transport quantities. With the use of actively trained surrogate models, the computational time is greatly reduced and therefore additional constraints based on measurements of transport features can be used during the validation process. Typically, only ion and electron heat fluxes are used to match experiments and simulations with 1D or 2D scans of turbulence drives (i.e. inverse gradient scale lengths), and very often, only one or two inputs are changed, and rarely at the same time [10, 13–15, 17, 20, 22, 24]. This approach is justified if only one type of turbulence is dominant, but is not appropriate in all cases.

The VITALS tool allows the user to apply as much knowledge of the plasma as one can gather, and therefore use many measured parameters, within error bars, to achieve the simultaneous match of several transport quantities. These multi-dimensional scans of plasma parameters are performed using a smart optimization process that exploits machine learning techniques to fit and subsequently refine surrogate models. This toolbox has common elements with Bayesian optimization and adaptive learning, where the parameters of a probabilistic model are updated iteratively.

VITALS does not intend to provide a substitute to flux-matching and time-dependent transport frameworks that evolve temperature, density and rotation profiles self-consistently, thus modifying derived quantities with physics-based relationships. The tool presented here treats plasma input parameters as separate and independent design variables, and therefore it is up to the user to carefully select the uncorrelated parameters that should be allowed to vary independently. Likewise, VITALS performs the validation of transport models locally, hence neglecting the effect of integrating gradients and changes in global parameters. Future work will include correlation between variables, as well as a more comprehensive global treatment of the profiles.

The TGLF model (Section 3.3) is used to benchmark VITALS, and the application of QuaLiKiz [26] has also been successful. In a practical sense, these reduced quasilinear transport models take experimental plasma parameters (electron temperature and density, main ion dilution, toroidal velocities, etc.) and return particle, momentum and energy fluxes (see Figure 3.7). In the following, TGLF and QuaLiKiz runs will be referred to as “high-fidelity” evaluations to be consistent with the machine learning literature. Even though these are reduced models that were built to fit nonlinear gyrokinetic simulations, they are still too expensive for brute force scans of high-dimensional parameter spaces. Because of this, surrogate models will be built from few data points obtained from TGLF and QuaLiKiz (the “high-fidelity”) simulations.

B.3 Optimization Framework

In this work, the transport model of interest is treated as a black-box function, where the input to output behavior is the only piece of information that is used in the entire validation process. This allows one to generalize the implementation of VITALS to the validation of any transport code, as shown in Figure B.1. VITALS receives plasma parameters with uncertainties from experimental data, and transport fluxes from power balance calculations. Additional transport measurements are also incorporated and must be provided as inputs. The combination of plasma parameters that best matches the objective functions is returned, and the likelihood of this choice can be studied.

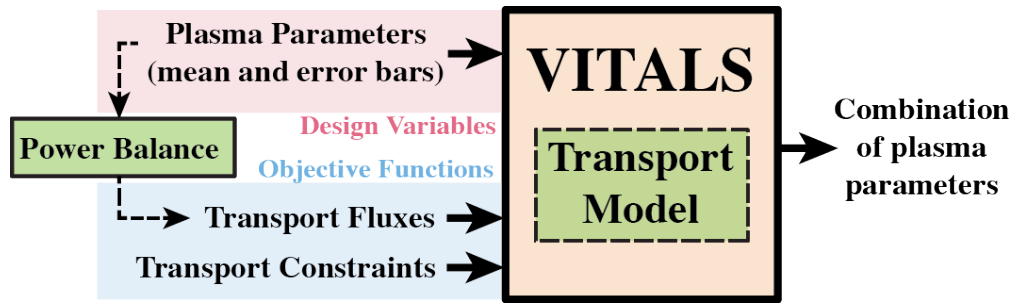


Figure B.1: Schematic view of the optimization problem, where design variables (mean and error bars of plasma parameters) and objective functions (transport fluxes and measurements) are provided to the code. The combination of design variables that give the optimum value of the objective functions is then returned by the code.

The general problem of global optimization, given a set of input parameters $\vec{x} = [x_1, \dots, x_d]$, a function f , and lower and upper bounds (\vec{x}^l, \vec{x}^u) , can be described as:

$$\vec{x}^* = \arg \max_{\vec{x} \in \mathcal{R}^d} f(\vec{x}) \quad \text{s.t.} \quad x_k^l < x_k < x_k^u \quad \text{for} \quad k = 1 \dots d \quad (\text{B.1})$$

When the black-box objective function $f(\vec{x})$ has no analytical form, is non-convex, or when there is no access to gradients, the only piece of information that is available for optimization are evaluations on specific data points, $f(\vec{x}^{(i)})$. Furthermore, when these evaluations are costly, as it usually happens in the case of simulation codes, the query points must be carefully selected. Recently exploited Bayesian optimization methods use sequential search algorithms to choose new query points at each iteration, $\vec{x}^{(i)}$. After selecting a prior belief, the model is refined when new data points are observed (posterior update). The prior distribution with subsequent updates on its parameters is called probabilistic surrogate model, meta-model or emulator.

In this work, Kriging [27] surrogate-based optimization is used, which is a subfield of Bayesian optimization methods [28]. Kriging uses a measure of dissimilarity between samples and their separation distance, and fits a model using conventional regression techniques. Sometimes referred to as Gaussian process prediction, Kriging has provided excellent results in many fields of engineering

and physics where surrogates of deterministic models need to be constructed [29, 30]. In Kriging, the action of drawing random samples assumes errors that are spatially correlated, using a Gaussian process around each sample data point [31]. When an optimization strategy with subsequent model parameters updates is employed, new query points are likely to be clustering near optimal locations or inside “trust-regions”. The spatially correlated response values in Kriging make it very suitable for this application with irregularly spaced data and deterministic simulations.

Mathematically, Kriging assumes that the output of the model consists of a global trend function and a Gaussian process error model:

$$y(\vec{x}) = \vec{g}(\vec{x})^T \vec{\beta} + \epsilon(\vec{x}) \quad (\text{B.2})$$

where $\vec{g}(\vec{x})$ and $\vec{\beta}$ are vectors that contain the trend basis functions and the generalized least squares estimates of the coefficients, respectively. By selecting an appropriate kernel to model a correlation function, $r(\vec{x}, \vec{x}')$, the covariance between the error of two arbitrary points is defined as $\text{cov}[\epsilon(\vec{x}), \epsilon(\vec{x}')] = \sigma^2 r(\vec{x}, \vec{x}')$, where σ^2 is referred as the unadjusted variance. The correlation function is chosen in this work to be a squared exponential, also known as radial basis function kernel:

$$r(\vec{x}^{(i)}, \vec{x}^{(j)}) = \exp \left(- \sum_{k=1}^d \frac{1}{2l_k^2} |x_k^{(i)} - x_k^{(j)}|^2 \right) \quad (\text{B.3})$$

where the vector $\vec{l} = [l_1, \dots, l_d]$ is a set of correlation lengths that expresses the extent of the spatial dissimilarity between samples for each dimension. This implies that variables close in space have errors which are highly correlated. A positive-definite correlation (Kernel) matrix \underline{R} can be constructed with elements $R_{i,j} = r(\vec{x}^{(i)}, \vec{x}^{(j)})$, and the Kriging predictor given observed data can be derived by minimizing the mean square error [31]:

$$\hat{y}(\vec{x}) = \mathbb{E}(y(\vec{x})|\mathcal{D}) = \vec{g}(\vec{x})^T \vec{\beta} + \vec{r}(\vec{x})^T \underline{R}^{-1} (\vec{y} - \underline{G} \vec{\beta}) \quad (\text{B.4})$$

In this expression, a correction to the least squares mean is introduced by $\vec{r}(\vec{x})^T \underline{R}^{-1} (\vec{y} - \underline{G} \vec{\beta})$, where the vector $\vec{r}(\vec{x})$ is defined as $r_i(\vec{x}) = r(\vec{x}, \vec{x}^{(i)})$, constructed from observed data points, $\vec{x}^{(i)}$, and the vector of differences between true outputs and trend function evaluations at all data points is defined as $(\vec{y} - \underline{G} \vec{\beta})$. Here, \underline{G} is a matrix that contains the evaluation of the least squares basis functions at all points in the observed data. The estimator for the unadjusted variance σ^2 and the trend function parameters $\vec{\beta}$ are obtained by generalized least squares, and a reduced quadratic trend function is used, without mixing terms: $\beta g(\vec{x}) = \beta_0 + \sum_{k=1}^d (\beta_{1,k} x_k + \beta_{2,k} x_k^2)$. The correlation lengths, $\{l_k\}_{k=1}^d$, must be determined by maximum likelihood estimation. In this work, the *DiRect* global search algorithm is used because of its robustness, but specific details of these calculations and choice of optimization algorithm are beyond the scope of this paper and can be found in [31, 32].

B.3.1 Sampling and Optimization Techniques

In this work, the Latin Hypercube Sampling (LHS) technique is used to uniformly draw datapoints from the region of interest to ensure space-filling. LHS divides the design space into N segments whose individual size is given by a uniform probability distribution. Then, it randomly draws samples from each region (each sample is d -dimensional, with d being the number of design variables), and this set of N selections of each of the d design variables is shuffled [32, 33]. A database with $(d + 1)(d + 2)/2$ data points is used to build the surrogate models with reduced quadratic trend functions, as suggested in the literature [34].

For optimization problems where accuracy is not the important factor, with multiple local optima and with cheap function evaluations, the application of heuristic methods is particularly attractive. Within the class of heuristic methods, Genetic Algorithms (GAs) have become very useful in a wide range of applications, due to many advantages that make them outperform other optimization methods [29, 30]. GAs can readily deal with oscillating or non-smooth multi-objective functions in constrained optimization. The global search capabilities of GAs make them well suited for optimization problems with multiple local optima, for which gradient methods are not readily available. In many optimization problems, GAs quickly identify promising regions of the design space where the global optimum could be located. Given that the optimization is performed over a surrogate model that only captures global trends, accuracy in the optimization is unimportant and only regions with possible optimality are needed. The preservation of diversity that genetic algorithms offer makes them very suited for an exploratory role. The interested reader is invited to consult Ref. [35] and the *JEGA* library [36] for a complete description of different GA approaches.

The genetic algorithm employed in this study used a population size of 50 members, a 10% mutation rate with uniform single-variable replacing, a 80% crossover rate between design variables and elitist (best designs) replacement. Population members are ranked by how many designs dominate them, i.e. how many other members have better values in more than one objective function. This method avoids issues with the aggregation into a pseudo single-objective function, which is very convenient in cases where it is more important to find a solution that matches all objectives simultaneously. Aggregation into a pseudo single-objective function could drive the minimization of one of the objectives below experimental uncertainties with the unfortunate worsening of another objective. A radial niche pressure of 1% is applied in the performance space to enforce a minimum Euclidean distance between members of the population at each GA iteration. Further details about the terminology and usage of genetic algorithms can be consulted in Ref. [35].

B.3.2 Surrogate-Based Local Optimization

This optimization problem has been assembled in the object-oriented framework *Dakota* [32]; *Surfpack* is used for the Kriging model [31, 34] and *JEGA* for the genetic algorithms [36]. In the following, Surrogate-Based Local Optimization (SBLO) is described, as also summarized in Figure

B.2.

The workflow of SBLO starts by selecting a region of the design variables space (the “trust-region”), where individual points are selected using the sampling techniques described in Section B.3.1. Each of those individual points are then evaluated with the transport model and objective functions are built with user-defined metrics, such as incremental diffusivities, fluctuation levels or the relative error with respect to experimental heat fluxes. With such mapping between inputs and outputs, the surrogate Kriging model is then constructed. Once the surrogate model is built, the multi-objective GA optimization method is applied to find the combination of input parameters that provides the optimum set of objective functions. The optimum of the surrogate is then passed to the real transport model for the high-fidelity evaluation.

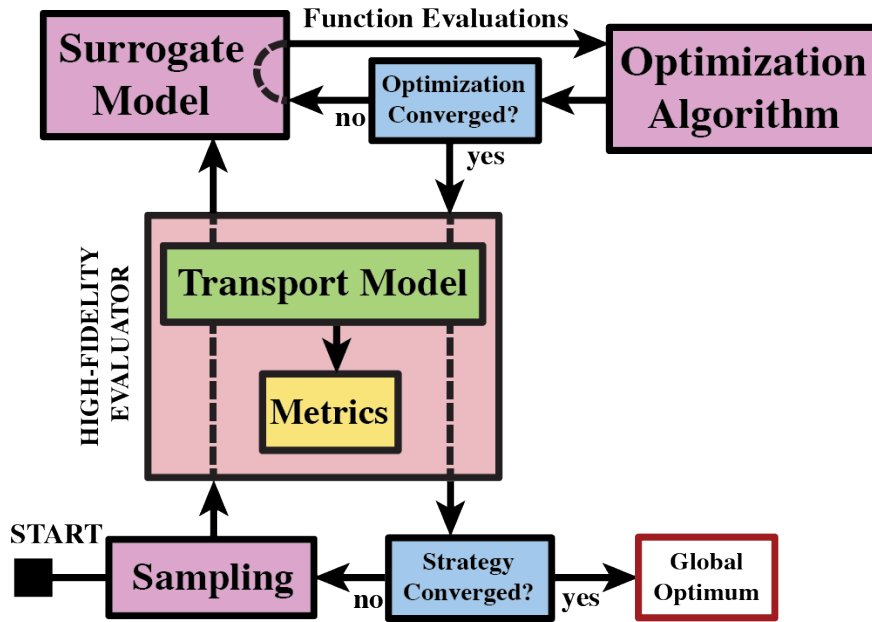


Figure B.2: Scheme of surrogate-based optimization. An initial database is built using TGLF or QuaLiKiz evaluations of selected data points, and a surrogate model is constructed. The optimization acts on the surrogate, and the optimum is then used to improve the model for the next iteration.

The step acceptance is determined by assessing if the new optimum is not dominated by any previous iteration, and a metric assessing how well the surrogate matches the real model is then used to select the new trust-region. This performance metric is called *trust-region ratio* and determines the trust-region size and position of the next iteration:

$$\rho_t = \frac{f(x_{t-1}^*) - f(x_t^*)}{\tilde{f}(x_{t-1}^*) - \tilde{f}(x_t^*)} \quad (\text{B.5})$$

where x_{t-1}^* is the center of the trust-region (which was the optimum of the previous step) and x_t^* is the optimum in the current step. Therefore, ρ_t is a ratio between the improvement in the high-fidelity model ($f(x)$) and the improvement in the surrogate model ($\tilde{f}(x)$). The trust-region

ratio can be understood as a measure of the accuracy of the surrogate and it is used to determine the size of the region where the model is trained. In general, a small trust-region size would provide more accurate results but the global optimization capabilities are compromised. A balance between these two situations is found by using the logic in Table B.1 [32].

Trust-region ratio	Next trust-region size
$\rho_t \leq 0.25$	Shrink ($\div 2$)
$0.25 \leq \rho_t \leq 0.75$	Retain
$0.75 \leq \rho_t \leq 1.25$	Retain if $x_t^* \in \mathcal{U}_t$ Expand ($\times 2$) if $x_t^* \notin \mathcal{U}_t$
$1.25 \leq \rho_t$	Retain

Table B.1: Trust region ratio logic for SBLO optimization. \mathcal{U}_t stands for the current trust-region and x_t^* for the optimum found in the current iteration.

The trade-off between over-fitting and under-fitting is always critical when building models from data. If the initial database is too big, then the model will likely overfit the transport model response and further improvement in unexplored areas will not be achieved. If, instead, small databases are built around small regions of the space with few parameters and with a surrogate model that accounts for data clustering, there is little risk of over-fitting. Even though the surrogate is built with data that belongs to small regions of the space, optimization is performed globally, permitting exploration of regions that may contain optimal points. This is the main feature of SBLO that makes it very suitable for the application explored here. Algorithm 1 shows, schematically, the workflow of SBLO.

Algorithm 1 Surrogate-Based Local Optimization

- 1: Select initial trust-region bounds in the design variables space $\rightarrow \mathcal{U}_{t=0} \subset \mathcal{R}^d$
 - 2: Build database by sampling trust-region $\rightarrow \{x^{(i)}\} \in \mathcal{U}_t$
 - 3: Evaluate each point in database with real transport model $\rightarrow \{x^{(i)}, y^{(i)}\}$
 - 4: Build surrogate prediction model with data points $\rightarrow \tilde{f}(x)$
 - 5: Find optimum of surrogate model $\rightarrow x^* = \arg \max \tilde{f}(x), \hat{y}^* = \tilde{f}(x^*)$
 - 6: Evaluate optimum with real model $\rightarrow y^* = f(x^*)$
 - 7: Calculate step acceptance and trust-region ratio (ρ_t) using y^* and \hat{y}^*
 - 8: Accept or reject iteration and select next region $\rightarrow \mathcal{U}_{t+1} \subset \mathcal{R}^d$
 - 9: Back to step 2 until stopping criterion is met
-

One of the important advantages of this approach is the high degree of parallelization that can be applied. Once a trust-region is chosen and the points are randomly drawn, several high-fidelity evaluations (i.e. several TGLF or QuaLiKiz calls) can be launched simultaneously, greatly reducing the computational time of the validation process.

B.4 Validation Metrics

As presented earlier, VITALS allows the user to apply as much knowledge of the plasma as one can gather. However, this is limited to the ability of the specific model to provide the transport quantity of interest. In the following, a list of available metrics by the time of writing this Thesis is presented.

- **Transport fluxes** (energy, particle and momentum)

Here, transport fluxes are approximated by using quasilinear theory and a saturation rule that has been fitted to nonlinear gyrokinetic simulations (see Section 3.3). Gyro-Bohm normalized fluxes are converted into real units and compared with the experimentally inferred fluxes from interpretive TRANSP power balance calculations (see Section 3.4.1).

- **Incremental diffusivity**

Experimentally, electron incremental thermal diffusivity measurements are obtained via partial sawtooth heat pulse propagation analysis, as described in Ref. [21], or via modulated electron cyclotron heating (mECH), as in Ref. [37].

In simulations, χ_e^{inc} is determined by the numerical derivative of the Q_e v.s. $n_e \nabla T_e$. In this work, a central differences scheme is applied at each point to determine χ_e^{inc} . In other words, for each high-fidelity evaluation, two additional simulations are performed with small variations of a/L_{T_e} . If we define the normalized incremental diffusivity at position j as $\bar{\chi}_{e,j}^{inc} \approx \frac{Q_{e,j+1}^{GB} - Q_{e,j-1}^{GB}}{(a/L_{T_e})_{j+1} - (a/L_{T_e})_{j-1}}$, where the grid spacing in the inverse electron temperature gradient scale length is equal to 15% of $(a/L_{T_e})^{exp}$, we can write $\chi_e^{inc} = \bar{\chi}_e^{inc} \frac{\rho_s^2}{(a/c_s)}$. This choice of grid spacing is made to be consistent with partial sawtooth and mECH measurements and avoid problems with nonlinearities in the Q_e v.s. $n_e \nabla T_e$ relationship.

Despite being much harder to measure, the same methodology can be applied to compare experiment and simulation of ion incremental thermal diffusivity, χ_i^{inc} .

- **Temperature and density fluctuations**

Long wavelength electron temperature fluctuations can be measured with a correlation electron cyclotron emission (CECE) radiometer (e.g. [38, 39]), and reflectometers can be used to measure density fluctuations. The amplitude of temperature and density fluctuations is given by TGLF at each wavenumber, $A_{(k_y)} = \sqrt{dI_{(k_y)}/dk_y}$. The fluctuation levels, $|\tilde{T}_e/T_{e,0}|$ or $|\tilde{n}_e/n_{e,0}|$, can be compared with experiment by taking into account the normalization factor and integrating the low- k part of the spectrum.

In this work, the standard k_y -grid for transport simulations is used, where the resolution of the low- k part of the spectrum (up to $k_y = 1.0$) defaults to $\Delta k_y \sim 0.11$ and the rest of the spectrum, up to $k_y = 24.0$, are separated by linearly-increasing steps. This very coarse grid makes the integration of the low- k fluctuation spectrum slightly unphysical. Future work

will suggest an increase in resolution of the low- k part of the spectrum while maintaining the high- k contributions.

At the moment of writing this Thesis, QuaLiKiz does not provide fluctuation levels as outputs and therefore cannot be used in the validation process.

- **n-T Cross-phase angle**

As discussed in Section 3.3.1, TGLF also provides the cross-phase angle between density and temperature fluctuations, $\alpha_{n_e T_e}$ (see Figure ?? for an example), which can be compared to experimental measurements [7]. Usually, $\alpha_{n_e T_e}$ can be used to differentiate between ITG v.s. TEM dominated plasmas.

As with fluctuation levels, the cross-phase angle between density and temperature fluctuations is given by TGLF at each wavenumber, $\alpha_{n_e T_e}(k_y)$, which can be properly averaged in the low- k part of the spectrum to compare with experiment.

- **D and V impurity transport coefficients**

Experimentally, impurities can be injected at the edge of magnetically confined plasmas using a laser blow-off system [20], and impurity diffusion and convection coefficients can be inferred from the soft x-ray emission and the STRAHL impurity transport code [40].

In simulations, D and V are determined by the numerical derivative and offset of the Γ_{imp} v.s. ∇n_{imp} . Similarly to the thermal incremental diffusivity, a central differences scheme is applied at each point using small variations of ∇n_{imp} .

B.4.1 Notes on Regularization

Regularization prevents the variables to deviate from the mean of the distribution and thus acts as a further constraint to the optimization. In short, regularization formulas add penalties that prevent design variables with little to no influence in the objective functions to deviate from the mean of the distribution. If no regularization penalty is applied, usually an early stopping criterion would need to be implemented case by case, complicating the automation and generalization of the tool.

In this work, either an L_1 or L_2 norm can be applied to the design variables deviation from the mean. In particular, application of L_1 -norm is similar with the least absolute selection and shrinkage (*lasso*) regularization that is used in regression problems. *Lasso* tends to drive some of the regression coefficients to 0, thus resulting in sparse solutions. In the case of L_1 -norm, for each data point $x^{(i)}$ in the design variable space, we define an extra objective function as:

$$w_{L_1}^{(i)} = \sum_{j=1}^d |x_j^{(i)} - 1| \quad (\text{B.6})$$

Regularization of objective functions can also be applied to resolve situations where the final

converged solution indicates that one objective is barely outside error bars and other objective reaches the mean of the measurement.

B.5 Application to Study Validation of Quasilinear Transport Models

In the following examples, design variables are constructed using deviations from the experimentally measured values, e.g. $v_{ei} \equiv (v_{ei}^{sim} - v_{ei}^{exp}) / v_{ei}^{exp}$, to ease the implementation of error bars as design variables bounds. Specifically, $1-\sigma$ deviation from the mean value of each individual parameter is chosen as upper and lower bounds. All objective functions are also defined as the relative error with respect to the experimentally inferred parameters.

B.5.1 Benchmark with Alcator C-Mod L-mode plasmas

In this preliminary study, validation of TGLF is performed using data from the core of a conventional L-mode Alcator C-Mod plasma (shot #1120921008). Further information about this plasma can be found in Ref. [22]. A set of 9 input plasma parameters is used: a/L_{Te} , a/L_{Ti} , v_{ei} , Z_{eff} , a/L_n , V_{tor} , T_i/T_e , n_i/n_e and V'_{ExB} . Lacking accurate data of impurities in Alcator C-Mod plasmas, temperature, density, toroidal velocity and gradients of the average impurity are approximated as those of the main ion species. Because of this, changes in the main ion parameters during the optimization also changes the impurity parameters, to be consistent with past validation studies in Alcator C-Mod [22]. Future implementation of VITALS in tokamaks with better impurity diagnostics will allow to treat the impurities parameters as independent variables. Likewise, a/L_n is considered to be the same for both electron and ion species. Future work would also consider a more comprehensive consistency check (e.g. v_{ei} changing when T_i/T_e or a/L_{Te} change), where the free parameters in the optimization are reduced.

As objectives, the electron and ion heat fluxes (Q_e , Q_i), the low-k electron temperature fluctuation level (\tilde{T}_e/T_e) and electron temperature incremental diffusivity (χ_e^{inc}) are used with the same relative weights. A regularization function, constructed from the individual deviations of the design variables with respect to the mean of the statistical distribution is also used.

VITALS Optimization Results

An optimization problem with 9 variables and 5 objectives is very challenging if approached with direct methods and gradient-based optimization techniques. The use of active learning surrogate models and trust-regions permits to tackle this problem with ease. As suggested in Section B.3.1, $(d+1)(d+2)/2 = 55$ samples will be drawn in each trust-region iteration, permitting to launch 55 TGLF simulations in parallel. The optimization will stop when either the trust-region bounds become too small or when the progress between 5 successive iterations falls below a soft

convergence tolerance. The entire space is used as the initial trust-region.

In this benchmark case, plasma parameters and transport quantities are calculated at $\rho_{tor} = 0.8$. The transport quantities to validate the transport models are listed in Table B.2. Error bars in the heat fluxes (TRANSP outputs) are obtained by propagating the uncertainties in the plasma parameters. Uncertainty in the CECE fluctuation level measurement is given by the sensitivity of the diagnostic. The value of χ_e^{inc} is obtained as an average from $\rho_{tor} = 0.64$ to 0.84. The error bar that is provided in Table B.2 is therefore an error bar on the average value and not strictly on the local quantity.

$Q_e = 0.30 \text{ MW/m}^2 \pm 25\%$	$\tilde{T}_e/T_e = 0.0085 \pm 25\%$
$Q_i = 0.12 \text{ MW/m}^2 \pm 25\%$	$\chi_e^{inc} = 4.0 \text{ m}^2/\text{s} (\pm 15\%)$

Table B.2: Transport quantities (Objectives)

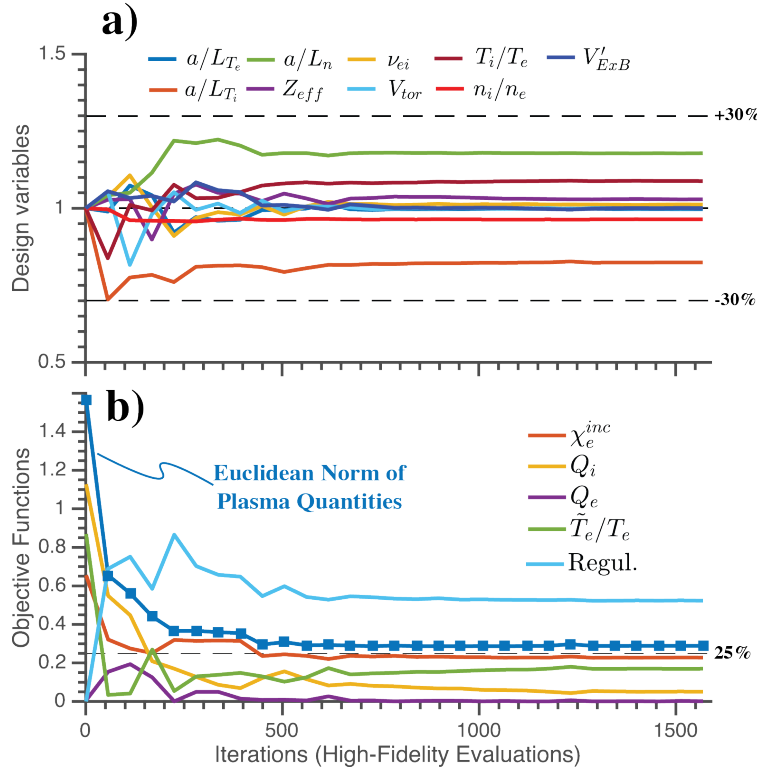


Figure B.3: Evolution of *a)* design variables and *b)* objective functions during the optimization at each trust-region iteration. Euclidean norm of plasma transport quantities (excluding regularization) is also plotted as a metric for the optimization performance.

From Figure B.3, one can see that none of the design variables except the electron temperature and density gradient scale lengths (a/L_{T_e} , a/L_n) and T_i/T_e affected the selected outputs; the rest were not needed to minimize the error in the transport quantities. Because of the regularization, those variables tend to 1 (mean value) because of the added penalty if they deviate with no

improvement in the objectives. Therefore, the solution can be considered to be *sparse*, with only a/L_{T_e} , a/L_n , T_i/T_e supporting the objective functions. One can also see that the optimization started with very high values of the errors ($> 65\%$ error in all physical quantities except Q_e). This means that drawing conclusions about transport model validation with only evaluations of the mean values of the plasma parameters is misleading. It is important to note that a previous validation study [22] showed that it is not possible to match experimental transport fluxes and incremental diffusivity with only scans of a/L_{T_i} , using the same plasma conditions and transport model. Only three trust-region iterations of the optimization tool provided errors below 25% of all physical quantities. Further optimization helped regularize the solution.

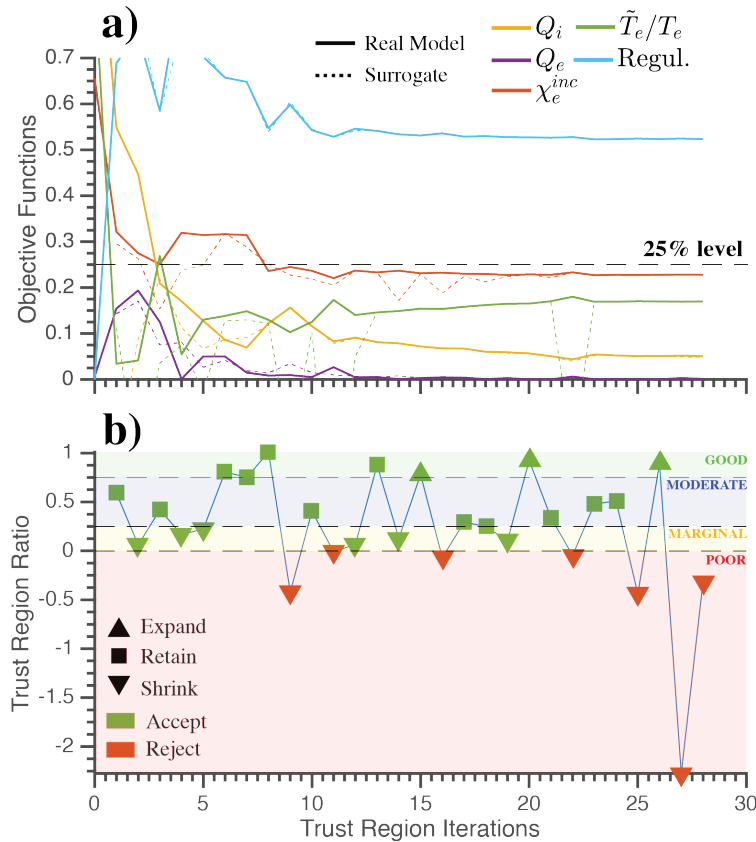


Figure B.4: *a)* Objective functions evaluations with high-fidelity and surrogate models for each trust-region iteration. *b)* Trust region ratio evolution and logic for trust-region size selection and step acceptance. Shaded regions represent accuracy of the surrogate model.

Figure B.4 shows the performance of the surrogate-based approach. As seen in the upper part of the figure, the Kriging surrogate model is able to accurately reproduce all outputs of TGLF with ease, thus quickly driving the minimization. Resizing logic is performed according to Table B.1 and the step acceptance is determined by iterates dominance. In the lower part, the trust-region ratio shows that accuracy is overall satisfactory. Whenever the accuracy worsens (e.g. iteration 2), the trust-region size shrinks to half its size to improve the fidelity of the surrogate. If the accuracy is

very bad such that there is a worsening in the objective functions or the surrogate v.s. real model follow opposite directions (e.g. iteration 9), the iteration is rejected, the trust-region center is not updated and the size is decreased.

TGLF-SAT0 v.s. TGLF-SAT1

The differentiating feature that introduces TGLF-SAT1 with respect to TGLF-SAT0 is the enhancement of electron heat flux near the marginal stability for ion temperature gradient turbulence, which comes from a new model for the saturated turbulence potential amplitude peak [41]. VITALS can be used to test if the incorporation of multi-scale effects through the new saturation rule was needed to reproduce the transport characteristics in Alcator C-Mod L-modes.

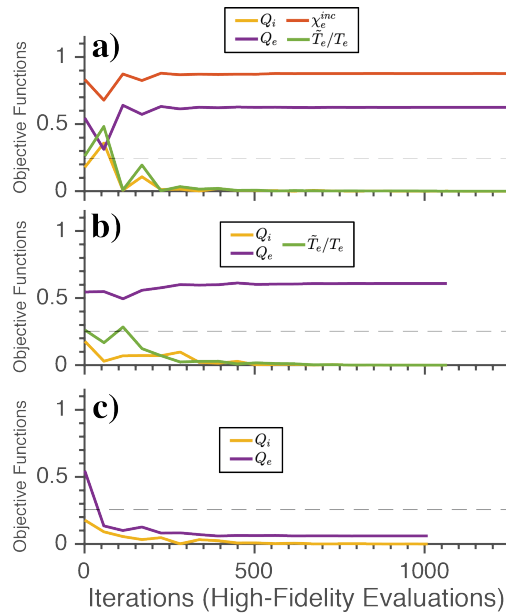


Figure B.5: Summary of VITALS optimizations using TGLF-SAT0: (a) Complete optimization using Q_i , Q_e , \tilde{T}_e/T_e and χ_e^{inc} , (b) without χ_e^{inc} , and (c) only heat fluxes.

Figure B.5a shows that VITALS cannot find a solution that satisfies the objective functions simultaneously using TGLF-SAT0, even with a large number of free plasma input parameters and without regularization, thus providing further evidence that multi-scale effects are needed to capture the complete transport physics in C-Mod L-modes. Particularly, electron transport stiffness, given by χ_e^{inc} , is highly under-predicted with TGLF-SAT0. Eliminating χ_e^{inc} as objective function did not help to find a solution with simultaneous match, as evidenced in Figure B.5b. However, one may wonder whether or not a combination of input parameters can be found such that only the heat fluxes are matched. Figure B.5c shows that, indeed, a combination of plasma input parameters was easily found if only heat fluxes are used as objective functions in the optimization. It is left for the reader to conclude whether or not it is relevant that steady-state heat fluxes can be matched when no other transport quantity constraints the validation. We note however that χ_e^{inc} is an

important parameter to characterize transport in the electron channel, since it measures the shape of Q_e v.s. a/L_{T_e} . The high sensitivity of turbulent transport on plasma input parameters could potentially lead to fortuitous agreement. Not being able to match χ_e^{inc} means that the dependencies of Q_e on plasma parameters are misinterpreted by the the transport code. The community already recognized the need for comparison of other quantities to provide meaningful conclusions on the physics that a transport model can capture [1, 2]. In view of this, VITALS represents a more comprehensive way of constraining the validation of transport models.

B.6 Conclusions and Future Work

This study represents, to the authors' knowledge, the first effort to create a framework to validate plasma transport simulations by simultaneously changing many input parameters and then applying the experimentally inferred heat fluxes *and* turbulence measurements (or other transport quantities) as constraints. As discussed in the introduction, validation techniques have previously relied on a serial approach: modify one or two inputs to the turbulence simulation (e.g. a/L_{T_i} and a/L_{T_e}) to test whether Q_e and Q_i are in agreement with experiment within error bars. Then the outputs of the so-called "base-case" simulation are compared with turbulence measurements or other transport quantities. But this serial approach is quite limited. For example, if the same simulation were instead constrained by bringing the turbulence into agreement with the experiment based on changes of input parameters like a/L_{T_i} , is it highly likely that neither Q_e nor Q_i would agree with experiment. And to perform more simulations and sensitivity scans can quickly become intractable. With the new techniques and tool, VITALS, the simulation code is considered as a "black-box" function and no knowledge of the equations or the model behind the code is needed for the user to simultaneously scan many inputs and constrain the model using many experimental measurements. This allows to use a higher number of input parameters (instead of just a/L_{T_i} and a/L_{T_e}) to reach the desired output, and it enables the future adoption of more complex simulation codes, such as linear and non-linear gyrokinetic simulations, when improved computational resources become available. In the future, VITALS could be run using any transport model in place of TGLF and QuaLiKiz (e.g. GYRO [3]).

The advantages of VITALS with respect to the widely used "flux-matching approach" are both mathematical and practical. First, experimental uncertainties can be implemented as design variables bounds and the most likely solution can be found such that it is consistent with experimental observations. Secondly, metrics that are not directly measured as outputs of the transport model, such as incremental diffusivity and regularization, can be used during the error minimization process. The matching of transient transport behavior through the incremental diffusivity is particularly attractive if integrated modeling techniques are used to study perturbative transport later on. Lastly, the surrogate-based trust-region strategy provides a very high level of parallelization. Figure B.5c already showed that a single trust-region iteration already provides heat fluxes within

error bars. The reason behind this high efficiency is that each trust-region is formed by 55 samples that provide sufficient accuracy and can be run independently.

In future work, consistency checks between design variables will be implemented to ensure that correlated parameters are changed accordingly. Moreover, design variables can also be assigned a probability distribution to determine the likelihood of plasma parameters combinations during the optimization process. This would act as a regularization function, but offering more physical intuition.

Bibliography

- [1] P. W. Terry et al. Validation in fusion research: Towards guidelines and best practices. *Phys. Plasmas*, 15(6), 2008. URL <http://dx.doi.org/10.1063/1.2928909>.
- [2] C. Holland. Validation metrics for turbulent plasma transport. *Phys. Plasmas*, 23(6):060901, 2016. doi: 10.1063/1.4954151. URL <http://dx.doi.org/10.1063/1.4954151>.
- [3] J. Candy and R.E. Waltz. An eulerian gyrokinetic-maxwell solver. *Journal of Computational Physics*, 186(2):545 – 581, 2003. ISSN 0021-9991. doi: [https://doi.org/10.1016/S0021-9991\(03\)00079-2](https://doi.org/10.1016/S0021-9991(03)00079-2). URL <http://www.sciencedirect.com/science/article/pii/S0021999103000792>.
- [4] F. Jenko et al. Electron temperature gradient driven turbulence. *Phys. Plasmas*, 7(5):1904–1910, 2000. doi: 10.1063/1.874014. URL <http://dx.doi.org/10.1063/1.874014>.
- [5] G. M. Staebler et al. A theory-based transport model with comprehensive physics. *Phys. Plasmas*, 14(5):055909, 2007. URL <http://dx.doi.org/10.1063/1.2436852>.
- [6] A E White et al. Feasibility study for a correlation electron cyclotron emission turbulence diagnostic based on nonlinear gyrokinetic simulations. *Plasma Phys. Control. Fusion*, 53(11): 115003, 2011. URL <http://stacks.iop.org/0741-3335/53/i=11/a=115003>.
- [7] A. E. White et al. Measurements of the cross-phase angle between density and electron temperature fluctuations and comparison with gyrokinetic simulations. *Phys. Plasmas*, 17(5): 056103, 2010. doi: 10.1063/1.3323084. URL <http://dx.doi.org/10.1063/1.3323084>.
- [8] S. Leerink et al. Multiscale investigations of drift-wave turbulence and plasma flows: Measurements and total-distribution-function gyrokinetic simulations. *Phys. Rev. Lett.*, 109:165001, Oct 2012. doi: 10.1103/PhysRevLett.109.165001. URL <https://link.aps.org/doi/10.1103/PhysRevLett.109.165001>.
- [9] J. Candy and R. E. Waltz. Anomalous transport scaling in the diii-d tokamak matched by supercomputer simulation. *Phys. Rev. Lett.*, 91:045001. doi: 10.1103/PhysRevLett.91.045001. URL <https://link.aps.org/doi/10.1103/PhysRevLett.91.045001>.
- [10] D. Told et al. Characterizing turbulent transport in asdex upgrade l-mode plasmas via nonlinear gyrokinetic simulations. *Phys. Plasmas*, 20(12):122312, 2013. doi: 10.1063/1.4858899. URL <http://dx.doi.org/10.1063/1.4858899>.
- [11] A. Banon Navarro et al. Comparisons between global and local gyrokinetic simulations of an asdex upgrade h-mode plasma. *Phys. Plasmas*, 23(4):042312, 2016. doi: 10.1063/1.4947557. URL <http://dx.doi.org/10.1063/1.4947557>.

- [12] N. T. Howard et al. Multi-scale gyrokinetic simulations: Comparison with experiment and implications for predicting turbulence and transport. *Phys. Plasmas*, 23(5):056109, 2016. doi: 10.1063/1.4946028. URL <http://dx.doi.org/10.1063/1.4946028>.
- [13] A. E. White et al. Measurements of core electron temperature and density fluctuations in diii-d and comparison to nonlinear gyrokinetic simulations. *Phys. Plasmas*, 15(5):056116, 2008. doi: 10.1063/1.2895408. URL <http://dx.doi.org/10.1063/1.2895408>.
- [14] C. Holland et al. Implementation and application of two synthetic diagnostics for validating simulations of core tokamak turbulence. *Phys. Plasmas*, 16(5):052301, 2009. doi: 10.1063/1.3085792. URL <http://dx.doi.org/10.1063/1.3085792>.
- [15] A. Casati et al. Turbulence in the tore supra tokamak: Measurements and validation of nonlinear simulations. *Phys. Rev. Lett.*, 102:165005, 2009. doi: 10.1103/PhysRevLett.102.165005. URL <https://link.aps.org/doi/10.1103/PhysRevLett.102.165005>.
- [16] T. Goerler et al. A flux-matched gyrokinetic analysis of diii-d l-mode turbulence. *Phys. Plasmas*, 21(12):122307, 2014. doi: 10.1063/1.4904301. URL <http://dx.doi.org/10.1063/1.4904301>.
- [17] C. Sung et al. Quantitative comparison of electron temperature fluctuations to nonlinear gyrokinetic simulations in c-mod ohmic l-mode discharges. *Phys. Plasmas*, 23(4):042303, 2016. doi: 10.1063/1.4945620. URL <http://dx.doi.org/10.1063/1.4945620>.
- [18] D. R. Ernst et al. Role of density gradient driven trapped electron mode turbulence in the h-mode inner core with electron heating. *Phys. Plasmas*, 23(5):056112, 2016. doi: 10.1063/1.4948723. URL <http://dx.doi.org/10.1063/1.4948723>.
- [19] T Happel et al. Comparison of detailed experimental wavenumber spectra with gyrokinetic simulation aided by two-dimensional full-wave simulations. *Plasma Phys. Control. Fusion*, 59(5):054009, 2017. URL <http://stacks.iop.org/0741-3335/59/i=5/a=054009>.
- [20] N.T. Howard et al. Quantitative comparison of experimental impurity transport with nonlinear gyrokinetic simulation in an alcator c-mod l-mode plasma. *Nucl. Fusion*, 52(6):063002, 2012. URL <http://stacks.iop.org/0029-5515/52/i=6/a=063002>.
- [21] A.J. Creely et al. Perturbative thermal diffusivity from partial sawtooth crashes in alcator c-mod. *Nucl. Fusion*, 56(3):036003, 2016. URL <https://doi.org/10.1088/0029-5515/56/3/036003>.
- [22] A. J. Creely et al. Validation of nonlinear gyrokinetic simulations of l- and i-mode plasmas on alcator c-mod. *Phys. Plasmas*, 24(5):056104, 2017. doi: 10.1063/1.4977466. URL <http://dx.doi.org/10.1063/1.4977466>.
- [23] Martin Greenwald. Verification and validation for magnetic fusion. *Phys. Plasmas*, 17(5):058101, 2010. doi: 10.1063/1.3298884. URL <http://dx.doi.org/10.1063/1.3298884>.

- [24] A. E. White et al. Nonlinear gyrokinetic simulations of the i-mode high confinement regime and comparisons with experiment. *Phys. Plasmas*, 22(5):056109, 2015. doi: 10.1063/1.4921150. URL <http://aip.scitation.org/doi/abs/10.1063/1.4921150>.
- [25] J. Candy et al. Tokamak profile prediction using direct gyrokinetic and neoclassical simulation. *Phys. Plasmas*, 16(6):060704, 2009. doi: 10.1063/1.3167820. URL <http://dx.doi.org/10.1063/1.3167820>.
- [26] C. Bourdelle et al. A new gyrokinetic quasilinear transport model applied to particle transport in tokamak plasmas. *Phys. Plasmas*, 14(11):112501, 2007. doi: 10.1063/1.2800869. URL <http://dx.doi.org/10.1063/1.2800869>.
- [27] M. L. Stein et al. *Interpolation of Spatial Data*. Springer Series in Statistics, 1999. ISBN 1402072406. URL <https://www.springer.com/us/book/9780387986296>.
- [28] E. Brochu et al. A tutorial on bayesian optimization of expensive cost functions, with application to active user modeling and hierarchical reinforcement learning. *arXiv:1012.2599*, 2010. URL arxiv.org/abs/1012.2599.
- [29] P. Rodriguez-Fernandez et al. Automatic design of orc turbine profiles by using evolutionary algorithms. *ASME ORC*, 133, 2015. URL http://www.asme-orc2015.be/online/proceedings/display_manuscript/133.htm.
- [30] G Persico et al. High-fidelity shape optimization of non-conventional turbomachinery by surrogate evolutionary strategies. *Journal of Turbomachinery*, 141(8):081010–081010–11, 2019. doi: 10.1115/1.4043252. URL <http://turbomachinery.asmedigitalcollection.asme.org/article.aspx?articleid=2729212>.
- [31] Anthony A. Giunta et al. A comparison of approximation modeling techniques. In *7th AIAA/USAF/NASA/ISSMO Symposium on Multidisciplinary Analysis and Optimization, Multidisciplinary Analysis Optimization Conferences*, 1998. URL <https://doi.org/10.2514/6.1998-4758>.
- [32] B.M. Adams et al. Dakota, a multilevel parallel object-oriented framework for design optimization, parameter estimation, uncertainty quantification, and sensitivity analysis: Version 6.6 user’s manual. *Sandia Tech. Rep. SAND2014, 4633*, Updated May 2017. URL <http://dakota.sandia.gov/documentation.html>.
- [33] M. D. McKay et al. A comparison of three methods for selecting values of input variables in the analysis of output from a computer code. *Technometrics*, 21(2):239–245, 1979. ISSN 00401706. URL <http://www.jstor.org/stable/1268522>.
- [34] A. A. Giunta et al. The surfpack software library for surrogate modeling of sparse irregularly spaced multidimensional data. In *11th AIAA/ISSMO Multidisciplinary Analysis and Optimiza-*

- tion Conference, Portsmouth, Virginia, 2006. URL <https://arc.aiaa.org/doi/abs/10.2514/6.2006-7049>.
- [35] C. R. Reeves et al. *Genetic Algorithms: Principles and Perspectives*. Kluwer Academic Publishers, 2002. ISBN 1402072406. URL <https://www.springer.com/us/book/9781402072406>.
- [36] J. Eddy and K. Lewis. Effective generation of pareto sets using genetic programming. In *ASME International Design Technical Conferences, Design Automation Conference*, 2001. URL http://does.eng.buffalo.edu/index.php?option=com_jresearch&view=publication&task=show&id=59.
- [37] J. C. DeBoo et al. Electron profile stiffness and critical gradient studies. *Physics of Plasmas*, 19(8):082518, 2012. doi: 10.1063/1.4750061. URL <https://doi.org/10.1063/1.4750061>.
- [38] C. Sung et al. Design of a correlation electron cyclotron emission diagnostic for alcator c-mod. *Rev. Sci. Instrum*, 83(10):10E311, 2012. doi: 10.1063/1.4731750. URL <http://dx.doi.org/10.1063/1.4731750>.
- [39] N. T. Howard et al. Measurement of electron temperature fluctuations using a tunable correlation electron cyclotron emission system on alcator c-mod. *Rev. Sci. Instrum*, 85(11):11D811, 2014. doi: 10.1063/1.4886422. URL <http://dx.doi.org/10.1063/1.4886422>.
- [40] R. Dux. Report ipp 9/82. *MPI fur Plasmaphysik, Garching*, 2007.
- [41] G. M. Staebler et al. The role of zonal flows in the saturation of multi-scale gyrokinetic turbulence. *Phys. Plasmas*, 23(6):062518, 2016. URL <http://dx.doi.org/10.1063/1.4954905>.

Appendix C

Code Workflows

Most tools presented here have been developed in Python using the OMFIT [1] integrated modeling framework, except the analysis of Alcator C-Mod experimental data, which has been done using Matlab. The data and scripts used in this Thesis, as well as the complete OMFIT projects, have been stored in the PSFC cmodws cluster. In the following, the paths to the scripts and projects will be relative to the path `/home/pablorf/PRF_Repo_Thesis/Scripts/`. Files containing shot data and simulation results can also be found in `/home/pablorf/PRF_Repo_Thesis/Data/`.

In case that the OMFIT projects do not work, one can get all the simulation results from the corresponding CDF files. One could simply use the python module `netCDF4` to open results files. For example, the following code plots the central ($\rho_N = 0$) electron temperature as a function of time and the electron temperature profile profile at the initial simulation time ($t = 1.08s$) for the results presented in Figure 5.8:

```
1 import netCDF4
2 import matplotlib.pyplot as plt
3 results = netCDF4.Dataset('/home/pablorf/PRF_Repo_Thesis/Data/TRANSP/152895U31_tmp
4 /152895U31.CDF')
5 Te = results.variables['TE'][:]
6 t = results.variables['TIME'][:]
7 rho = results.variables['X'][:, -1, :]
8 plt.figure(); plt.plot(t, Te[:, 0])
9 plt.figure(); plt.plot(rho, Te[0, :])
10 plt.show()
```

Bibliography

- [1] O. Meneghini et al. Integrated modeling applications for tokamak experiments with omfit. *Nucl. Fusion*, 55(8):083008, 2015. URL <http://iopscience.iop.org/article/10.1088/0029-5515/55/8/083008/meta>.

Introduction

- **Figure 1.2**

Alcator C-Mod shot #1160503002, $t = 0.7s$.

Instructions: OMFIT project Introduction, script SCRIPTS/TeECE.py.

Background

- **Figure 2.4**

Alcator C-Mod shot #1120921008, TRANSP #88773 (PSFC MDS+), $t = 0.9s \pm 20ms$, $\rho_N = 0.8$.

Instructions: OMFIT project Background, script SCRIPTS/ChiInc.py.

- **Figure 2.5**

Alcator C-Mod shots #1120607008 and #1120607011, TRANSP #88188 and #88191 (PSFC MDS+), $t = 1.0s \pm 200ms$, $\rho_N = 0.7$.

Instructions: OMFIT project Background, script SCRIPTS/ChiLOCSOC.py.

- **Figure 2.6**

Alcator C-Mod shot #1160503002, $t = 0.7s$.

Instructions: OMFIT project Introduction, script SCRIPTS/TeECE.py.

- **Figure 2.7**

DIII-D shot #175847

Instructions: OMFIT project PRIMA_DIIID, script PLOTS/DBSplots.py.

Experimental and Modeling Techniques

- **Figure 3.4**

Alcator C-Mod shot #1120216030 ($t = 750ms$) and DIII-D shot #175847 ($t = 1750ms$).

Instructions: OMFIT project Background, script SCRIPTS/EFITs.py.

- **Figure 3.5, Figure ?? and Figure 3.6**

Alcator C-Mod shot #1120216030, TRANSP #152895U20, $t = 1.25s \pm 20ms$, $\rho_N = 0.4$.

Instructions: OMFIT project Background, script SCRIPTS/TGLFexplanation.py.

- **Figure 3.11**

OMFIT project PRIMA_DIIID, script SCRIPTS/Thesis_Pulse.py.

Cold-Pulse Experiments in Alcator C-Mod

- **Figure 4.1**
Alcator C-Mod shots #1120216030 ($t = 1304ms$) and #1150903022 ($t = 600ms$) .
Instructions: MATLAB script Phenomenology_1.m.
- **Figure 4.2**
Alcator C-Mod shot #1120216030.
Instructions: OMFIT project PRIMA_DIIID, PRIMA GUI, Plotting, Set of Quick Plots, “Cold-Pulse PRL”.
- **Figure 4.3 and Figure 4.6**
Alcator C-Mod shots #1160429014, #1120216030, #1120106031 and #1120216011.
Instructions: MATLAB scripts Mixing_1_MOD.m and Mixing_1_MOD_SXR.m.
- **Figure 4.4 and Figure 4.7**
Alcator C-Mod shots #1120216017, #1120216011, #1150901021 and #1150901008.
Instructions: MATLAB scripts RotBreak_Ip_2.m, RotBreak_Ip_Te1.m and RotBreak_RF_Te1.m.
- **Figure 4.5, Figure ?? and Figure 4.10**
Alcator C-Mod shots database (stored in /home/pablorf/PRF_Repo_Thesis/Scripts/matlabScripts/InfoShots/).
Instructions: MATLAB script CorrelationsDatabase/Correlations_MAIN.m.
- **Figure 4.6**
Alcator C-Mod shots #1120216030, #1120216031 and #1120216011.
Instructions: MATLAB scripts RotBreak_Ip_2.m and RotBreak_Ip_Te1.m.
- **Figure 4.8**
Alcator C-Mod shots #1160503008 and #1150901010 .
Instructions: MATLAB script RotBreak_Locked_1MOD.m.
- **Figure 4.2**
Alcator C-Mod shot #1120216030.
Instructions: OMFIT project CMODexperiments, script GetEFITS.py.

Modeling of Alcator C-Mod Cold Pulses

- **Figure 5.2, Figure 5.3, Figure 5.4 and Figure 5.5**
Alcator C-Mod shot #1120216030, TRANSP #152895W24.

Instructions: OMFIT project PRIMA_DIIID, PRIMA GUI, Plotting, Set of Quick Plots, “Cold-Pulse PRL”.

▪ **Figure 5.6**

Alcator C-Mod shot #1120216030, TRANSP [#152895W24](#), [#152895W26](#) and [#152895W27](#).

Instructions: OMFIT project PRIMA_DIIID, script PRIMApLotTGLFcomparison.py.

▪ **Figure 5.7**

Alcator C-Mod shot #1120216030, TRANSP [#152895W24](#), [#152895W88](#), [#152895W89](#) and [#152895W90](#).

Instructions: OMFIT project PRIMA_DIIID, script PRIMA/plotDensityStrength.py.

▪ **Figure 5.8**

TRANSP [#152895U31](#) and [#152895U33](#)

Instructions: OMFIT project PRIMA_DIIID, PRIMA GUI, Plotting, Set of Quick Plots, “Cold-Pulse NF”.

▪ **Figure 5.9 and Figure 5.10**

TRANSP [#152895U26](#)

Instructions: OMFIT project PRIMA_DIIID, PRIMA GUI, Plotting, Set of Quick Plots, “Cold-Pulse NF”.

▪ **Figure 5.11**

TRANSP [#152895U20](#)

Instructions: OMFIT project PRIMA_DIIID, PRIMA GUI, Plotting, Set of Quick Plots, “Cold-Pulse NF”.

▪ **Figure 5.12**

TRANSP [#152895U20](#), [#152895U26](#), [#152895U31](#) and [#152895U33](#)

Instructions: OMFIT project PRIMA_DIIID, script PLOTS/PRIMA_plotNF_metric.py.

▪ **Figure 5.13, Figure 5.14 and Figure 5.15**

TRANSP [#152895U20](#)

Instructions: OMFIT project PRIMA_DIIID, PRIMA GUI, Standalone, Type “Scans”.

Predict-first Cold-pulse Experiments in DIII-D

▪ **Figure 6.1**

DIII-D shots #175847 and #175881, TRANSP [#175847C61](#) and [#175847C62](#)

Instructions: OMFIT project PRIMA_DIIID, script PLOTS/PRIMA_plotPoP_predictfirst.py.

▪ **Figure 6.2, Figure 6.3 and Figure 6.6**

DIII-D shots #175847 and #175881

Instructions: OMFIT project PRIMA_DIIID, PRIMA GUI, Plotting, Set of Quick Plots, “Cold-Pulse PoP”.

- **Figure 6.4** and **Figure 6.5**

DIII-D shot #175847

Instructions: OMFIT project PRIMA_DIIID, script PLOTS/DBSplots.py.

- **Figure 6.9** and **Figure 6.10**

DIII-D shot #175847, TRANSP #175847C57 and #175847C58

Instructions: OMFIT project PRIMA_DIIID, PRIMA GUI, Standalone, Type “Scans”.

- **Perturbative W-injections in DIII-D**

The following shot numbers correspond to tungsten injections in DIII-D:

#175890, #175891, #175894, #175895, #175896, #175897.

Appendix: **Steady-State Transport Model Validation**

- **Figure B.3** and **Figure B.4**

Instructions: MATLAB script PlotDakota_Complete_v1.m, using file Opt_PostIAEA_v9.sav

- **Figure B.5**

Instructions: MATLAB script PlotDakota_Complete_v1.m, using files Opt_PostIAEA_v9_SAT0.sav, Opt_PostIAEA_v9_SAT0_fluc.sav and Opt_PostIAEA_v9_SAT0_OnlyQ.sav